Surface Geophysical Exploration of the TX and TY Tank Farms at the Hanford Site

Prepared by
D. Rucker **J. Greenwood** **B. Cubbage**
M. Levitt **G. O'Brien** **R. Mcgill**
M. Bergeron **M. McNeill** **S. Gering**
hydroGEOPHYSICS, Inc.

C. Henderson
Columbia Energy & Environmental Services, Inc.

Prepared for
CH2M HILL Hanford Group, Inc.
Richland, WA 99354
U.S. Department of Energy Contract DE-AC27-99RL14047

EDT/ECN: DRF UC:
Cost Center: Charge Code:
B&R Code: Total Pages: 295

Key Words: Surface Geophysical Exploration, SGE, Characterization

Abstract: This report presents the results of an investigation at TX and TY tank farm at the Hanford Site for areas of potential contamination using electrical resistivity methods. Geophysical exploration involved collecting and analyzing resistivity data using shallow surface electrodes and wells.

TRADEMARK DISCLAIMER. Reference herein to any specific commercial product, process, or service by trade name, trademark, manufacturer, or otherwise, does not necessarily constitute or imply its endorsement, recommendation, or favoring by the United States Government or any agency thereof or its contractors or subcontractors.

Printed in the United States of America. To obtain copies of this document, contact: Document Control Services, P.O. Box 950, Mailstop H6-08, Richland WA 99352, Phone (509) 372-2420; Fax (509) 376-4989.

AUG 27 2008
DATE:
STA: 15
HANFORD RELEASE
ID: 65

Release Approval Date 08/27/08

Release Stamp

Approved For Public Release

EXECUTIVE SUMMARY

This report documents the results of surface geophysical characterization activities performed during fiscal year 2008 for the TX and TY tank farms and the surrounding areas within the 200 West Area at the U.S. Department of Energy Hanford Site in Washington State. The objective of this investigation was to collect and analyze electrical resistivity data in order to identify and locate discrete low resistivity regions (low resistivity targets) in the subsurface to guide future geochemical sampling and analysis efforts.

This geophysical investigation involved the installation and subsequent data collection from permanent surface-to-surface (STS) electrodes spaced 6 meters apart along 26,712 total linear meters of cable arranged 30 meters apart in an orthogonal grid. Investigation within the TX and TY farm fence utilized the Well-to-Well (WTW) long electrode resistivity measurement method. WTW measurements were made using 105 steel cased vadose zone wells, 30 groundwater wells, and 27 point source electrodes.

The STS data were acquired along 47 individual lines of which 23 were oriented in a south-north direction and 24 lines were oriented in an east-west direction (Figure ES-1). The total data coverage area was approximately 82 acres over seven main waste focus areas: the eastern cribs (216-T-26 through 216-T-28), northern cribs (216-T-36-13 and T216-T-13), south tile field (216-T-19), western trenches (216-T-21 through 216-T-25), the area directly east of the TX farm, TX tank farm, and TY tank farm.

Analysis results based on the full TX-TY complex-wide model domain were problematic for both the well-to-well and surface-to-surface data. To address the limitation with the TX-TY Complex-wide model domain, specific focus areas were analyzed using either the well-to-well data or the surface-to-surface data as described in the following paragraphs.

WTW Analysis within the TY Tank Farm area. The WTW resistivity inversion model results for the TY tank farm utilized long electrode resistivity data measured from a dense 3D distribution of steel cased vadose zone wells. The resistivity inversion model results indicate several low resistivity targets which are located in close proximity to underground storage tanks which are assumed to have leaked. (See Figure ES-2). In contrast, no significant low resistivity targets were located near Tank 102, which is not known to have leaked. In addition to the spatial correlation of low resistivity targets with tanks which are assumed to have leaked, the shape of the targets themselves does not follow a strict linear pattern along the locations of pipelines. These WTW results suggest that infrastructure within TY farm does not control the distribution of low resistivity targets found in association with the tanks which are assumed to have leaked.

WTW Analysis within the TX Tank Farm area. The WTW resistivity inversion model results from the TX tank farm utilized long electrode resistivity data measured from a dense 3D distribution of steel vadose zone wells. Resistivity inversion model results within the TX tank farm show more dispersed low resistivity targets which are in some cases linear shaped along locations of known pipelines (See Figure ES-3). The shape and position of the low resistivity targets with respect to known infrastructure suggest that the numerous pipelines may be influencing the size, shape and locations of the low resistivity targets within TX tank farm. Although the more numerous buried infrastructure may be affecting the low resistivity targets

when compared to the TY tank farm results, a clustering of low resistivity targets exist around the 107, 108, 111 and 112 tanks.

The following is a brief discussion of the results from the surface-to-surface (STS) resistivity surveys performed for the entire TX-TY Complex and in selected waste site areas outside of the tank farms.

STS Data Analysis of Waste Site Area outside the Tank Farms. The results from both 2D and 3D inversion of the resistivity data collected in the area of the TX trenches west of the tank farms showed a clear low-resistivity target relative to a background resistivity, directly below the trenches. The primary target in this region was a low (1-30 ohm-m) resistivity target located directly below the 216-T-21 to 216-T-25 trenches (See Figure ES-4). The area of the low-resistivity target was primarily contained within the footprint of the trenches. Analysis of the STS data in the 2D and 3D analysis suggest that the low-resistivity target is isolated from the expected water table depth.

Review of 2D and 3D resistivity models showed that nearly all east-west and north-south lines that cross the 216-T-19 crib and tile field and the 216-Z-7 areas south of TX tank farm were impacted by the presence of buried infrastructure and surface fences. However, review of selected 2D resistivity inversion models in the 216-T-19 crib and tile field area revealed a primary shallow low resistivity target that runs for much of the length of this waste site in the north-south direction. In addition, selected 2D model results near the 216-Z-7 crib area revealed a low resistivity target centered beneath the crib area.

Review of 2D resistivity inversion model results of nearly all east-west and north-south survey lines that cross the TY cribs area and 216-T-31 French drain areas east of the tank farms showed significant impacts from the presence of buried infrastructure and surface fences. The buried infrastructure in this area made it difficult to identify any specific low-resistivity targets below these waste sites. 3D modeling results of the area east of the tank farms that included these waste sites showed primary low-resistivity targets that were linear and along areas of buried infrastructure. However, the size and depth of these targets appears to be too large to be caused by surface and buried infrastructure alone and may also show lower resistivity values due to potential leaks from pipelines.

Selected 2D analysis results of the area north of the TY tank farm identified low-resistivity targets generally located below the 216-T-36 crib, the 216-T-13 trench, and the 216-T-18 Test crib. However, only selected 3D analysis of STS data over the western and eastern part of the northern area yielded low resistivity targets beneath the 216-T-38 and 216-T-18 Test crib area that were consistent with the results of the 2D analysis at the same area (Figure ES-4 and ES-5). 3D analysis of STS data over the western half of the northern area was not able to confirm the results of the 2D analysis for the 216-T-13 trench area.

Areas with substantial infrastructure continue to present the most difficulties with regard to inversion modeling and associated interpretation of estimated resistivity distributions.

An overall review of both 2D and 3D inversion modeling results showed, in particular, that deeper model layers surrounding waste site areas, where infrastructure such as pipelines and groundwater wells are abundant near surface electrodes, showed low-resistivity targets that are dominated by infrastructure. The presence of these low resistivity targets can dominate the

lower parts of model domains and obscure either changes in resistivity due to the effects of waste site discharges or to the expected gradual lowering of resistivity as one approaches the local water table at approximately 80 meters. However, several targets located directly beneath some of the waste site areas cannot be accounted for by known infrastructure alone.

The resolution of low resistivity targets associated with waste sites was improved in some areas of the Complex by shifting the limits of the resistivity inversion model domains away from known locations of buried pipelines and other infrastructure. This was particularly evident by comparing the low resistivity target identified beneath the T-36 crib in the model domain which was shifted to the west of a cluster of pipelines. This same low resistivity target is not resolved when data from the pipeline area is included by shifting the model domain a relatively short distance to the east or by expanding the model domain to include all STS data.

Figure ES-1. HRR Survey Coverage Area, Showing Resistivity Line Locations-TX-TY Complex.

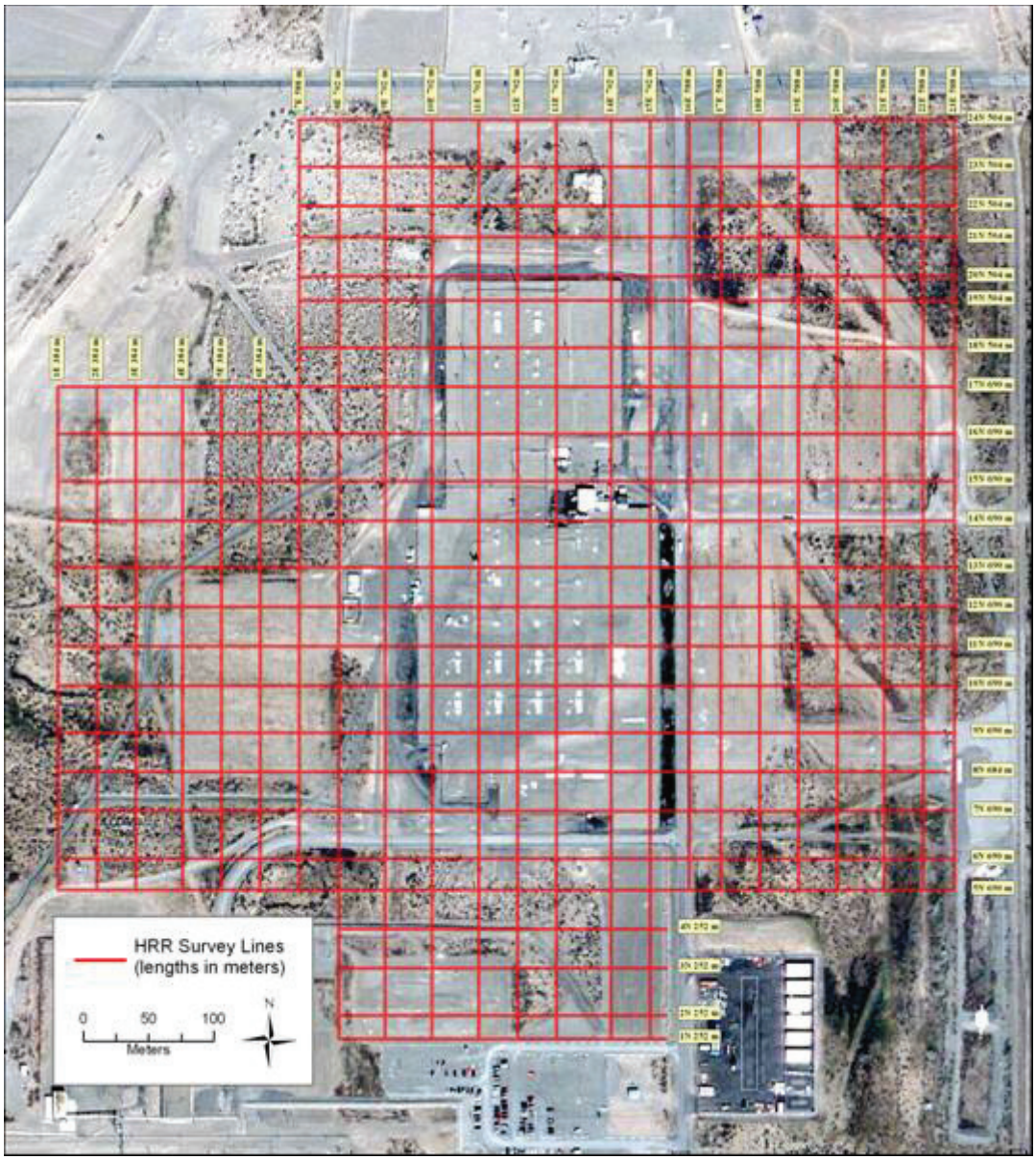

Figure ES-2. WTW Resistivity Inversion Model Results for the TY Tank Farm (TXTY-WTW6 model domain).

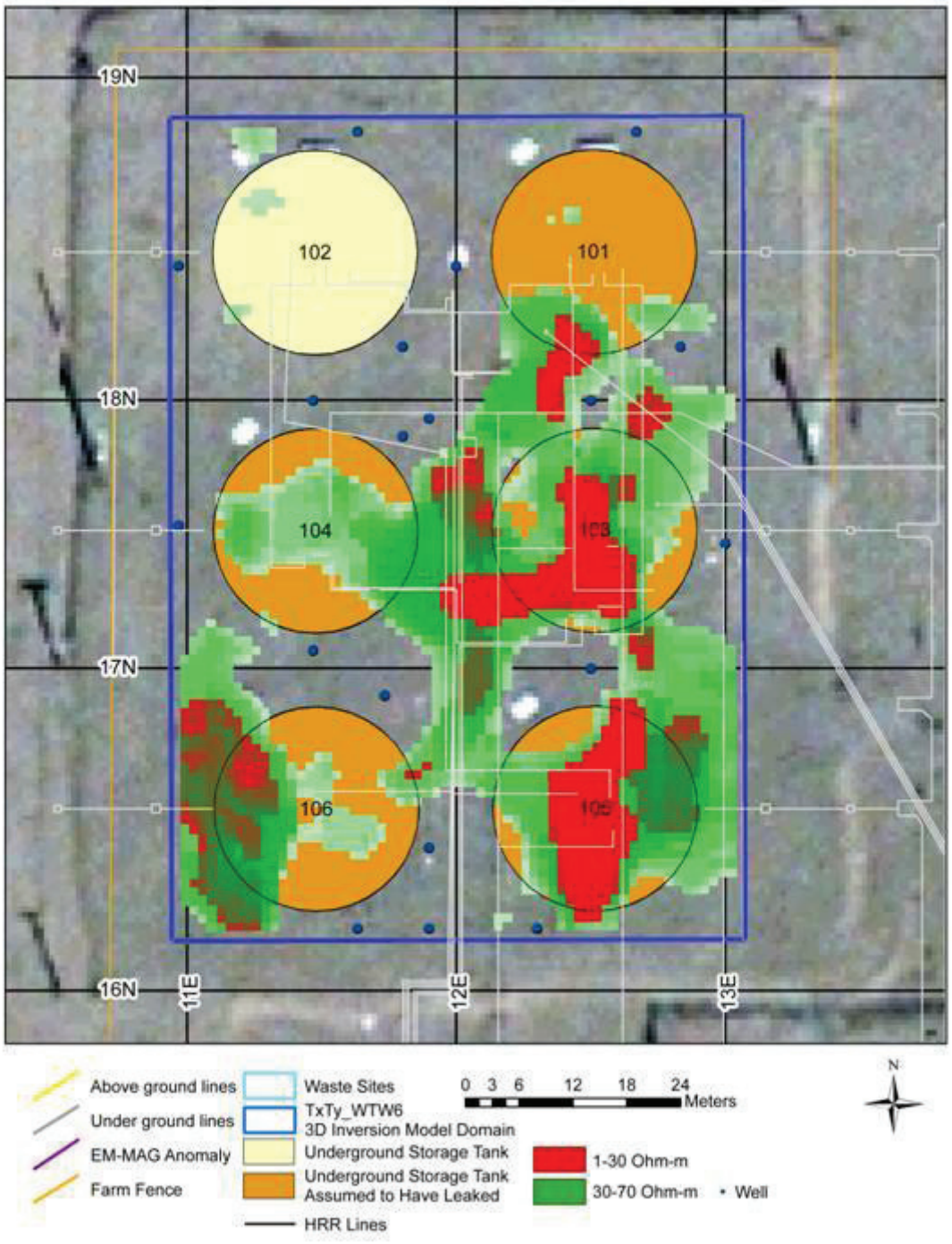

Figure ES-3. WTW Resistivity Inversion Model Results for the TX Tank Farm (TXTY-WTW8 model domain).

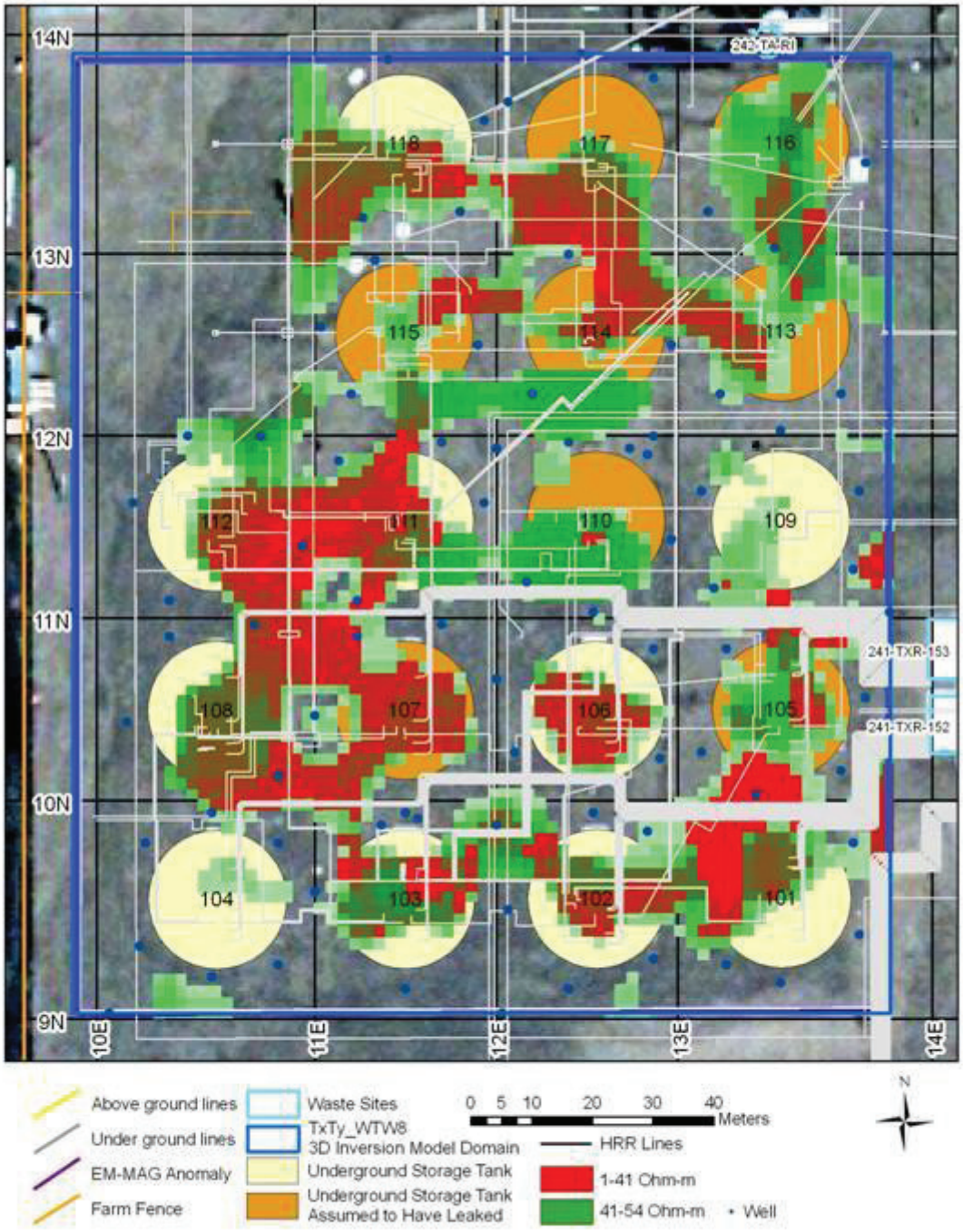

Figure ES-4. Model Results Showing 3D View from the Southeast of Selected Resistivity Levels – TX Trench Area (TXTY-STS1 Inverse Model Domain).

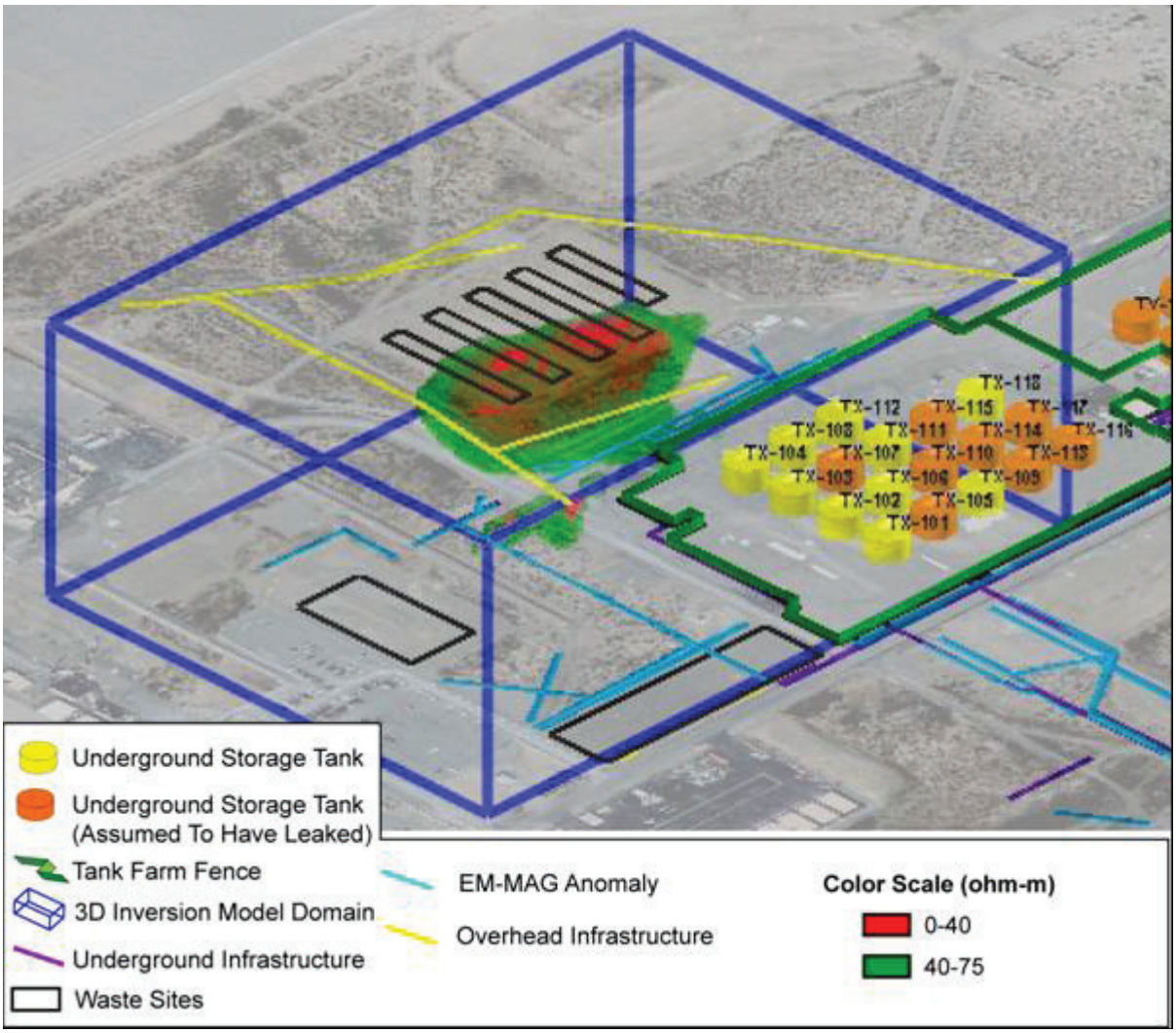

Figure ES-5. View of Model Results from Southwest Direction for Area Northwest of TY Farm - 216-T-36 Crib Area.(TXTY-STS8 Inverse Model Domain).

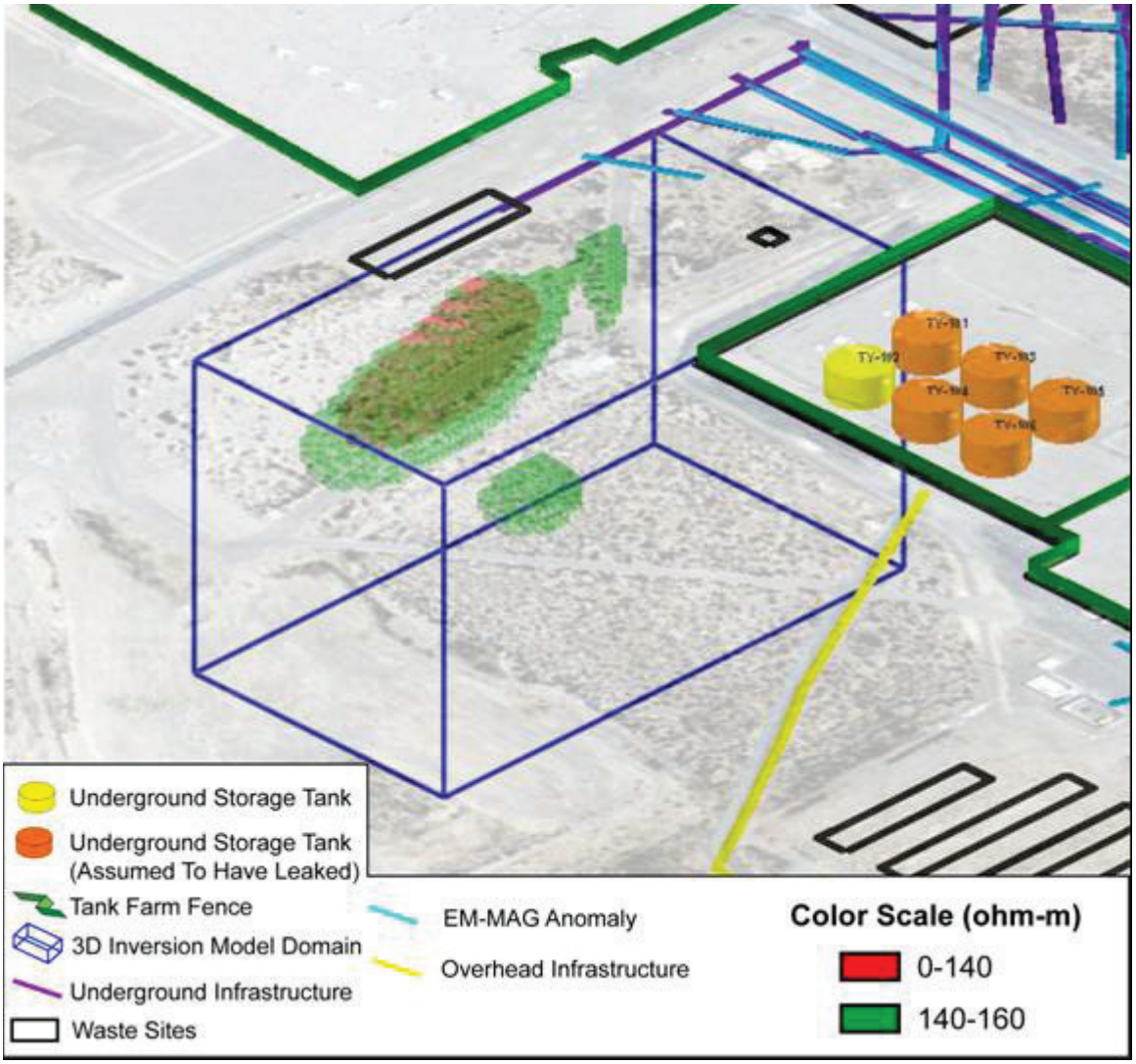

Figure ES-6. Plan View Model Results for Area Northeast of TY Farm - 216-T-18 Test Crib Area. (TXTY-STS7 Inverse Model Domain).

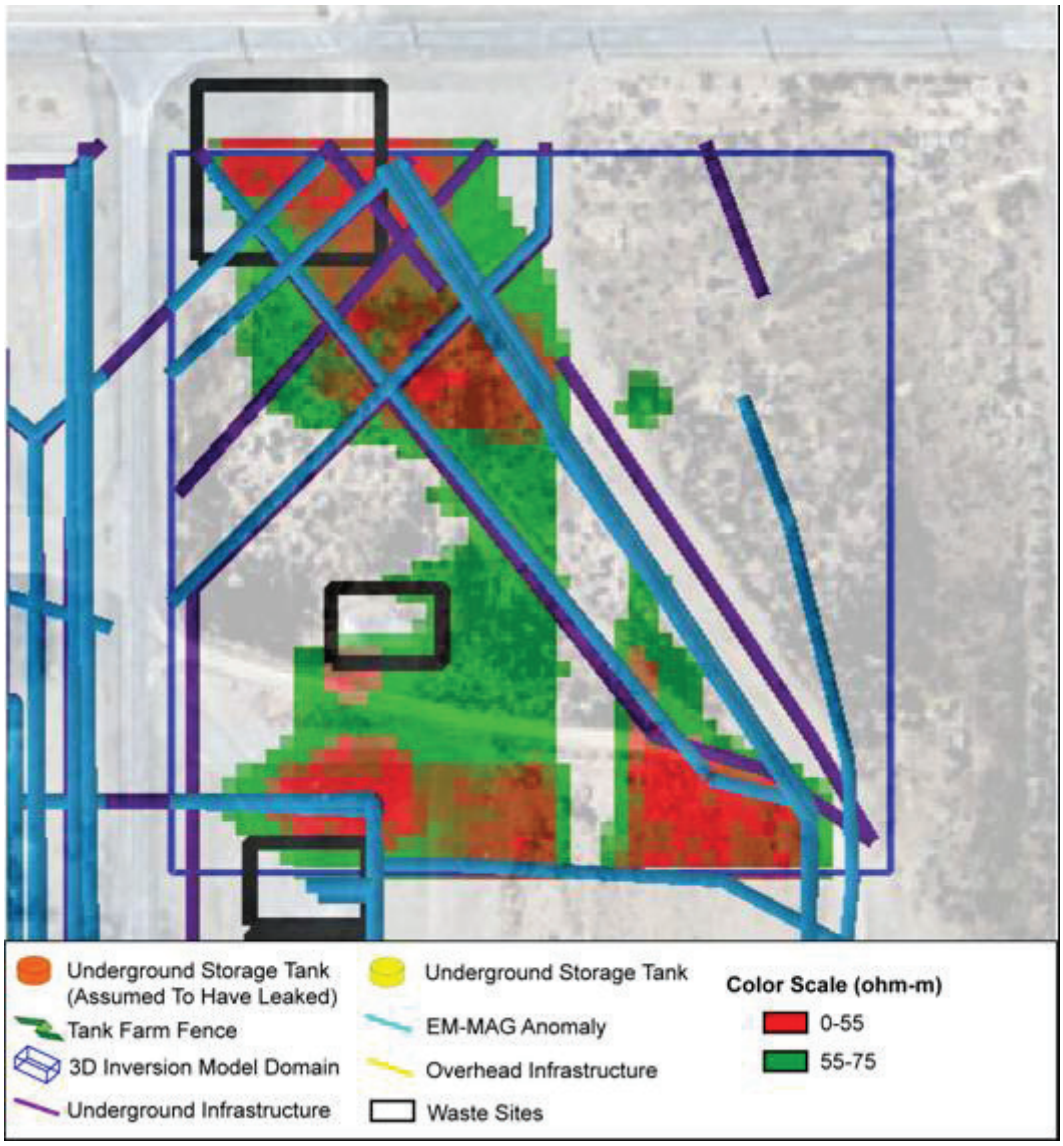

This page is intentionally left blank.

TABLE OF CONTENTS

1.0 INTRODUCTION 1-1
1.1 SCOPE 1-1
1.2 OBJECTIVES 1-2
1.3 REPORT LAYOUT 1-2

2.0 BACKGROUND 2-1
2.1 SITE DESCRIPTION 2-1
2.2 OPERATIONAL HISTORY 2-5
2.2.1 Liquid Waste Releases at TX-TY Complex 2-6
2.2.2 Infrastructure and Waste Delivery to TX-TY Complex 2-11
2.3 ENVIRONMENTAL SETTING 2-14
2.4 HISTORICAL CHARACTERIZATION EFFORTS 2-14
2.4.1 Vadose Zone 2-17

3.0 QUALITY ASSURANCE 3-1
3.1 DATA COLLECTION 3-1
3.2 DATA PROCESSING 3-2

4.0 RESULTS AND INTERPRETATIONS 4-1
4.1 TX TRENCHES (216-T-21 THROUGH 216-T-25) AREA 4-2
4.1.1 2D Inversion Model Results 4-3
4.1.2 3D Inversion Model Results 4-7
4.2 216-T-19 CRIB AND TILE FIELD AREA 4-13
4.2.1 2D Inversion Model Results 4-14
4.2.2 3D Inversion Model Results 4-21
4.3 TY CRIB (216-T-26 THROUGH 216-T-28) AND 216-T-31 FRENCH DRAIN AREA 4-26
4.3.1 2D Inversion Model Results 4-26
4.3.2 3D Inversion Model Results 4-31
4.4 NORTHERN WASTE SITE AREA CONTAINING 216-T-36 CRIB, 216-T-13 TRENCH, AND 216-T-18 TEST CRIB AREA 4-37
4.4.1 2D Inversion Modeling Results 4-39
4.4.2 3D Inversion Model Results 4-43
4.5 TX AND TY TANK FARM AREAS 4-59
4.5.1 WTW Data Analysis of TX-TY Complex area 4-60
4.5.2 WTW Data Analysis of TY Tank farm area 4-61
4.5.3 WTW Data Analysis of TX Tank farm area 4-61
4.6 TX-TY COMPLEX AREA 4-69
4.6.1 3D STS Inversion Model Results 4-69

5.0 CONCLUSIONS 5-1

6.0 LIMITATIONS 6-1
6.1 ELECTRODE GEOMETRY 6-1
6.2 EQUIPMENT 6-1
6.3 DEPLOYMENT LOGISTICS 6-1
6.4 SUBSURFACE INFRASTRUCTURE 6-1
6.5 INVERSION 6-2
6.6 VISUALIZATION 6-3
6.7 INTERPRETATION 6-3
6.7.1 Relating Resistivity Results to Contamination 6-3
6.7.2 Relating Resistivity Results to Other Characterization Methods 6-4

7.0 LESSONS LEARNED AND RECOMMENDATIONS 7-4
7.1 LESSONS LEARNED 7-4
7.1.1 Data Collection/Field Work 7-4
7.1.2 Data Processing 7-6
7.2 RECOMMENDATIONS 7-7
7.2.1 Data Acquisition 7-7
7.2.2 Processing and Modeling 7-8
7.2.3 Verification of Results 7-8

8.0 REFERENCES 8-1

LIST OF APPENDICES

A RESISTIVITY ACQUISITION METHODOLOGY ..... A-i
B DATA PROCESSING AND REDUCTION ..... B-i
C DATA ARCHIVAL ..... C-i
D BACKGROUND GEOPHYSICAL PROPERTIES ..... D-i
E DATA PROCESSING AND REDUCTION ..... E-i

LIST OF FIGURES

2-1. Location of TX and TY Tank Farms in the 200 West Area 2-3
2-2. TX and TY Tank Farms and Surrounding Facilities 2-4
2-3. General Configuration of Tank Construction in Waste Management Area TX-TY 2-5
2-4. Liquid Waste Volumes Discharged Around Waste Management Area TX-TY 2-8
2-5. Major Anions Discharged Around Waste Management Area TX-TY 2-9
2-6. Major Cations Discharged Around Waste Management Area TX-TY 2-10
2-7. Major Radionuclides Discharged Around Waste Management Area TX-TY 2-12

2-8. Infrastructure Map for TX and TY Tank Farms 2-13
2-9. Vertical Distribution of Moisture in Selected Boreholes within the TX Tank Farm..... 2-22
2-10. Vertical Distribution of Nitrate and Sulfate from Selected Boreholes within the TX Tank Farm..... 2-23
2-11. Average Nitrate Concentrations in Central and North 200 West Area, Upper Part of Unconfined Aquifer 2-24
2-12. Average Technetium-99 Concentrations in North 200 West Area, Upper Part of Unconfined Aquifer 2-25
4-1. STS Survey Lines and Model Domain Associated with TX Trench Area 4-3
4-2. 2D Inversion Model Results - Line 5E 4-4
4-3. 2D Inversion Model Results - Line 6E 4-5
4-4. 2D Inversion Model Results - Line 10N 4-6
4-5. 2D Inversion Model Results - Line 11N 4-7
4-6. TXTY-STS1iii Inversion Model Convergence Curve 4-8
4-7. TxTy-TS1iii Inversion Model Results Showing 3D Plan View of Selected Resistivity Levels – TX Trench Area 4-9
4-8. TXTY-STS1iii Inversion Model Results Showing 3D View from Southwest of Selected Resistivity Levels – TX Trench Area 4-10
4-9. TXTY-STS1iii Inversion Model Results Showing 3D View from the Southeast of Selected Resistivity Levels – TX Trench Area 4-11
4-10. TXTY-STS1iii Inversion Model Results Showing 3D View from East of Selected Resistivity Levels – TX Trench Area 4-12
4-11. TXTY-STS1iii Inversion Model Results Showing 3D View from Above and South West of 2D Slices Through the Primary Target and Background Levels - TX Trench Area 4-13
4-12. Model Domain of 216-T-19 Crib and Tile Field and 216-Z-7 Crib Area 4-16
4-13. Model Results for 2D Inverse Model Domain of Resistivity Survey Line 2N 4-17
4-14. Model Results for 2D Inverse Model Domain of Resistivity Survey Line 3N 4-18
4-15. Model Results for 2D Inverse Model Domain of Resistivity Survey Line 14E 4-19
4-16. Model Results for 2D Inverse Model Domain of Resistivity Survey Line 15E 4-19
4-17. Model Results for 2D Inverse Model Domain of Resistivity Survey Line 9E 4-20
4-18. Model Results for 2D Inverse Model Domain of Resistivity Survey Line 10E 4-20
4-19. Model Convergence Chart Showing RMS % and Iteration Number for the 3D Inversion Model of the TXTY-STS5ii Domain 4-22
4-20. 3D Resistivity Inversion Model for the TXTY-STS5ii Domain - View is from above and South-East 4-23
4-21. 3D Resistivity Inversion Model for the TXTY-STS5ii – View is From Above and Southwest Direction 4-24
4-22. Plan View of Model Results for 3D TXTY-STS5ii Inverse Model Domain 4-25
4-23. Cross-sectional View of Model Results from South Direction for 3D TXTY-STS5ii Inverse Model Domain 4-26

4-24. STS Survey Lines and Model Domain Associated with TY Cribs and 216-T-31 French Drain Area 4-28
4-25. Model Results for 2D Inverse Model Domain of Resistivity Survey Line 16N 4-29
4-26. Model Results for 2D Inverse Model Domain of Resistivity Survey Line 18E 4-29
4-27. Model Results for 2D Inverse Model Domain of Resistivity Survey Line 10N 4-30
4-28. Model Results for 2D Inverse Model Domain of Resistivity Survey Line 14E 4-31
4-29. TXTY-STS2iii Inversion Model Convergence Curve 4-32
4-30. View of Model Result from Southeast Direction for 3D TXTY-STS2ii Inverse Model Domain 4-34
4-31. View of Model Results from Southwest Direction for 3D TXTY-STS2ii Inverse Model Domain 4-35
4-32. Plan View of Model Results for 3D TXTY-STS2iii Inverse Model Domain 4-36
4-33. STS Survey Lines and 3D TXTY-STS6 Model Domain Associated with Northern Waste Site Area – TX-TY Complex 4-38
4-34. 2D Inversion Model Results - Line 24N 4-40
4-35. 2D Inversion Model Results - Line 22N 4-41
4-36. 2D Inversion Model Results - Line 12E 4-41
4-37. 2D Inversion Model Results - Line 18E 4-42
4-38. 2D Inversion Model Results - Line 19N. 4-43
4-39. Convergence Curve for 3D TXTY-STS6 Inversion Model 4-44
4-40. View of Model Results from Southeast Direction for 3D TXTY-STS6 Inverse Model Domain. 4-45
4-41. View of Model Results from Southwest Direction for 3D TXTY-STS6 Inverse Model Domain 4-46
4-42. Plan View of Model Results for 3D TXTY-STS6 Inverse Model Domain 4-47
4-43. View of Model Results from Southwest Direction for 3D TXTY-STS6 Inverse Model Domain 4-48
4-44. STS Survey Lines and 3D TXTY-STS7ii Associated with Northern Waste Site Area – TX-TY Complex 4-49
4-45. Convergence Curve for 3D TXTY-STS7ii Inversion Model 4-50
4-46. View of Model Results from Southeast Direction for 3D TXTY-STS7ii Inverse Model Domain 4-51
4-47. Plan View Model Results for 3D TXTY-STS7ii Inverse Model Domain 4-52
4-48. Cross-sectional View of Model Results from East Direction for 3D TXTY-STS7ii Inverse Model Domain 4-53
4-49. STS Survey Lines and 3D TXTY-STS6 and TXTY-STS8i Model Domains Associated with Northern Waste Site Area – TX-TY Complex 4-54
4-50. Convergence Curve for TXTY-STS8i Inversion Model Convergence Curve 4-55
4-51. View of Model Results from Southeast Direction for 3D TXTY-STS8i Inverse Model Domain 4-56
4-52. View of Model Results from Southwest Direction for 3D TXTY-STS8i Inverse Model Domain. 4-57

4-53. Plan View Model Results for 3D TXTY-STS8i Inverse Model Domain 4-58
4-54. Cross-sectional View of Model Results from the North Direction for 3D TXTY-STS8i Inverse Model Domain 4-59
4-55. Model Domains of TX and TY Tank Farm Areas 4-62
4-56. Convergence Chart for WTW Inverse Model Domain TXTY-WTW1i 4-63
4-57. Results For 3D TXTY-WTW1i Inverse Model 4-64
4-58. Convergence Chart for WTW Inversion Model Domain TXTY-WTW6. 4-65
4-59. Model Results for 3D TXTY-WTW6 Inverse Model Domain 4-66
4-60. Convergence Chart for WTW Inversion Model Domain TXTY-WTW8. 4-67
4-61. WTW Resistivity Inversion Model Results for the TXTY-WTW8 Domain 4-68
4-62. Model Domain of TX-TY Complex-Wide Model TXTY-STS3i 4-70
4-63. Model Convergence Showing RMS % and Iteration Number for the 3D Inversion Model of the TXTY-STS3i Domain. 4-72
4-64. Isometric View of Model Results from Southwest Direction for 3D TXTY-STS3i Inverse Model Domain 4-73
4-65. Isometric View of Model Results from Southeast Direction for 3D TXTY-STS3i Inverse Model Domain 4-74
4-66. Plan View of Model Results For 3D TXTY-STS3i Inverse Model Domain 4-75
4-67. Cross-sectional View of Model Results from East Direction for 3D TXTY-STS3i Inverse Model Domain 4-76
6-1. Electrical Resistivity Inversion of a Plume (10 ohm-meters) in a Homogeneous Background Sand (1,000 ohm-meters) with a Pipe (0.01 ohm-meter) at the Surface. 6-2

LIST OF TABLES

2-1. Liquid Waste Disposal Facilities and Discharge Volumes near WMA TX-TY 2-6
2-2. Liquid Waste Disposal Facility Operable Unit Assignments 2-17
4-1. Simulation Details and Statistics of 3D Model Domain TXTY-STS1iii 4-8
4-2. Simulation Details and Statistics of 3D Model Domain TXTY-STS5ii 4-22
4-3. Simulation Details and Statistics of 3D Model Domain TXTY-STS2ii 4-32
4-4. Simulation Details and Statistics of 3D Model Domain TXTY-STS6 4-44
4-5. Simulation Details and Statistics of 3D Model Domain TXTY-STS7ii 4-50
4-6. Simulation Details and Statistics of 3D Model Domain TXTY-STS8i 4-55
4-7. Simulation Details and Statistics of 3D Model Domain TXTY-WTW1i 4-63
4-8. Simulation Details and Statistics of 3D Model Domain TXTY-WTW6 4-65
4-9. Simulation Details and Statistics of 3D Model Domain TXTY-WTW8 4-67
4-10. Simulation Details and Statistics of 3D Model Domain TXTY-STS3i 4-72

ABBREVIATIONS AND ACRONYMS

3D	three-dimensional
bgs	below ground surface
CH2M HILL	CH2M HILL Hanford Group, Inc.
Columbia Energy	Columbia Energy & Environmental Services, Inc.
DOE	U.S. Department of Energy
EM	electromagnetic induction
GPR	ground penetrating radar
GPS	Global Positioning System
MAG	magnetometry
OU	Operable Unit
RAM	Random Access Memory
RCRA	Resource Conservation and Recovery Act of 1976
SGE	surface geophysical exploration
SST	single-shell tank
STS	surface-to-surface
WMA	waste management area
WTW	well-to-well

This page is intentionally left blank.

1.0 INTRODUCTION

This report documents geophysical exploration activities completed at the TX and TY tank farms and surrounding areas (referred to as the TX-TY Complex) at the U.S. Department of Energy (DOE) site in Washington State in fiscal year 2008. hydroGEOPHYSICS, Inc. and Columbia Energy & Environmental Services, Inc. (Columbia Energy), with support from technical staff of CH2M HILL Hanford Group, Inc. (CH2M HILL), conducted a geophysical survey of the subsurface of the TX-TY Complex, located in the 200 West Area of the Hanford Site. Data collection and analysis were performed in accordance with RPP-PLAN-35244, *Work Plan for Surface Geophysical Exploration of the TX and TY Tank Farm and Surrounding Areas*. This work was performed as an integrated effort between CH2M HILL and Fluor Hanford (FH) to investigate both the tank farms and the surrounding areas. The survey integrated several geophysical methods including magnetic gradiometry (also referred to as magnetometry) (MAG), electromagnetic induction (EM), ground penetrating radar (GPR), and electrical resistivity. High-resolution electrical resistivity data were collected using both point-source (located on the surface) and line-source electrodes (steel-cased wells).

The collection of geophysical methods used at the TX-TY Complex is generally termed surface geophysical exploration (SGE). The results of the EM and MAG characterization can be found in *Surface Geophysical Exploration of TX, and TY Tank Farms at the Hanford Site: Results of Background Characterization with Magnetics and Electromagnetics* (RPP-RPT-36893). The results of the GPR characterization can be found in *Surface Geophysical Exploration of TX, and TY Tank Farms at the Hanford Site: Results of Background Characterization with Ground Penetrating Radar* (RPP-RPT-38104). This report will focus only on the results of the electrical resistivity characterization effort.

1.1 SCOPE

The scope of this electrical resistivity characterization survey included data acquisition on both point electrodes and wells, data processing that included the use of methods and controls to ensure quality in the processing and reduction of data collected, data visualization that included development of two-dimensional (2D) contouring of data collected from individual resistivity lines, and compilations of three-dimensional (3D) resistivity cross sections.

Overall characterization activities in the TX-TY Complex study were divided among key areas and methodologies for the site as follows.

The 216-T-21 through T-25 trench area to the west of the TX tank farm was characterized with surface-to-surface (STS) electrical resistivity measurements. These trenches were the focus of a targeted survey to understand the distribution of resistivity beneath these waste sites. The study included both a series of 2D inversions of data collected at electrodes spaced approximately 20 feet (6 meters) along each resistivity transect. The study also included a 3D inversion of all STS data collected in this area.

The 216-T-19 crib and tile field and the 216-Z-7 crib to the south; the 216-T-13 trench, 216-T-36 crib area, 216-T-18 crib area to the north; and the TY cribs (216-T-26 through 216-T-28); and

the 216-T-31 French drain to the east were also characterized with STS electrical resistivity measurements. These cribs and trenches analyzed to map low-resistivity regions using a series of 2D inversions of data collected at electrodes spaced 20 feet (6 meters) apart along each resistivity transect. This survey also included three separate 3D inversion analyses of the STS resistivity within each of the three areas.

The TX and TY farms and surrounding areas were characterized with well-to-well (WTW) and STS electrical resistivity measurements. Analysis of this farm area used an inversion of data collected with both WTW and STS.

STS and WTW resistivity measurements collected across the TX-TY Complex, including areas inside and outside the farm fence boundary, were modeled separately in 3D inversion models that made use of a new, multi-processor inversion routine developed specifically for SGE projects, called EarthImager3DCL®. For a site the size of TX-TY Complex, the previous SGE resistivity inversion modeling software would have required that data be subdivided into smaller areas in order to accommodate the software memory and hardware limitations. With an upgraded version of the resistivity inversion software, the model domain size is controlled by the total amount of physical random access memory (RAM) residing in the computer. For a given model domain, the processing time is limited by the RAM speed, the number of available processors and the processor speed.

The final stage of this overall geophysical investigation involved analyzing and presenting the data to identify potential subsurface contamination from each of the areas investigated.

1.2 OBJECTIVES

The main objective for this geophysical investigation was to collect and analyze electrical resistivity data to identify and locate low resistivity regions in and around the TX-TY Complex. Low resistivity is indicative of increased moisture or increased concentration of electrolytes compared to background conditions

1.3 REPORT LAYOUT

This overall scope and content of this report is divided into several main sections as follows:

- **Section 1.0, Introduction** – Describes the scope and objectives of the investigation.
- **Section 2.0, Background** – Describes the geologic and hydrologic setting and information regarding the disposal activities in and around of TX-TY Complex.
- **Section 3.0, Quality Assurance** – Presents general methods and controls used to ensure the quality and control of data collection, reduction, and processing and configuration control of software and database changes used in this study.
- **Section 4.0, Results and Interpretations** – Presents the results from the electrical resistivity surveying effort and an interpretation of the resistivity measurements including the results of the inversion analysis.

® EarthImager3DCL is a registered trademark of Advanced Geosciences, Inc.

- **Section 5.0, Conclusions** – Provides a summary and conclusions drawn from the results and interpretations.
- **Section 6.0, Limitations** – Discusses the limitation of using geophysical methods in the TX-TY Complex area. Limitations are presented in a framework relative to data acquisition, data processing, and data presentation/visualization.
- **Section 7.0, Lessons Learned and Recommendations** – Presents lessons learned and recommendations for streamlining future SGE efforts in other areas of the Hanford Site.
- **Section 8.0, References** – Provides a listing of references cited in the report.
- **Appendix A, Resistivity Acquisition Methodology** – Presents the detailed logistics of collecting resistivity data at TX-TY Complex, including the STS and WTW measurements.
- **Appendix B, Data Reduction and Processing** – Presents the methodology used to reduce and process the resistivity data collected.
- **Appendix C, Data Archival** - Describes the process used to archive and store the raw resistivity data.
- **Appendix D, Background Geophysical Properties** – Presents summaries of background geophysical properties contained in the selected EM, MAG, and GPR reports that were used in and provided the basis for the resistivity inversion modeling and interpretation.
- **Appendix E, 2D Inversions** – Provides plots of all 2D inversion results for each STS survey line collected as a part of the TX-TY Complex investigation.

This page intentionally left blank.

2.0 BACKGROUND

2.1 SITE DESCRIPTION

The TX and TY tank farms are two of 12 single-shell tank (SST) farms on the Hanford Site that form waste management area (WMA) TX-TY. The SGE investigation extended beyond the WMA TX-TY boundary; therefore, the TX and TY tank farms and surrounding areas are herein referred to as the TX-TY Complex. The TX-TY Complex is located in the northern portion of the 200 West Area as shown in Figure 2-1, and includes a number of past-practice liquid discharge facilities (i.e., cribs and trenches) located mainly to the west, southeast, and northeast of the TX and TY tank farms (Figure 2-2). The TX-TY Complex facilities received a variety of waste streams generated primarily during bismuth phosphate plutonium separations operations at T Plant and uranium recovery operations a U Plant (*Historical Vadose Zone Contamination from T, TX, and TY Tank Farm Operations* [RPP-5957]).

CH2M HILL has responsibility for vadose zone characterization at the tank farms under the direction of the DOE, Office of River Protection. The Hanford Site Groundwater Remediation Project has responsibility for characterization of the cribs and trenches outside the tank farm and for all groundwater monitoring at the tank farms characterization activities are integrated through the direction of the DOE, Richland Operations Office.

The TX-TY Complex contains the following tank farm facilities:

- TX tank farm—18 100-series SSTs with 758,000-gallon capacity
- TY tank farm—6 100-series SSTs with 758,000-gallon capacity
- Leak detection systems
- Tank ancillary equipment.

The 100-series SSTs are 75 feet (23 meters) in diameter and approximately 37 feet (11 meters) tall from base to dome. The general configuration of tanks in the TX and TY tank farms is shown in Figure 2-3. As noted in Figure 2-2, 13 of the 24 SSTs in the TX-TY Complex are currently designated as tanks that have been confirmed or assumed to have leaked in *Waste Tank Summary for the Month Ending October 31, 2006* (HNF-EP-0182).

The TX-TY Complex contains the following past-practice liquid waste disposal facilities (Figure 2-3):

- Five TX trenches (216-T-21 through 216-T-25) west of the TX tank farm. Open excavations 10 feet wide by 10 feet deep. The 241-T-21 through 241-T-24 trenches are 240 feet long. The 216-T-25 trench is 180 feet long.
- 216-T-19 crib and tile field southeast of the TX tank farm. A 12 foot long by 12 foot wide crib and an 85 foot wide by 390 foot long tile field. The tile field contains a distribution system of perforated piping placed 23 feet below the ground surface.
- 216-T-31 French drain east of the TX tank farm. An underground injection well.

- Three TY cribs (216-T-26 through 216-T-28) east of the TY tank farm. Excavations 30 feet long by 30 feet wide by 15 feet deep containing a distribution system of piping placed within a layer of gravel backfill.
- 216-T-18 test crib northeast of the TY tank farm. A 30 foot long by 30 foot wide by 15 foot deep excavation containing perforated piping within a gravel layer to distribute liquid waste.
- 216-T-13 trench north of the TY tank farm. A 20 foot wide by 20 foot deep by 80 foot long open excavation.
- 216-T-36 crib northwest of the TY tank farm. A 160 foot long by 10 foot wide by 15 foot deep excavation containing a perforate pipe buried 11 feet deep to distribute liquid waste.
- 242-T evaporator on the border between the TX and TY tank farms. Used primarily in association with the 216-T-19 crib and tile field to reduce waste volumes and conserve tank space.

Supporting background information on the TX and TY tank farm facilities can be found in the following documents:

- RPP-5957, *Historical Vadose Zone Contamination from T, TX, and TY Tank Farm Operations*. Summarizes construction, operations, and liquid discharge history for the TX and TY tank farms and adjacent cribs and trenches.
- RPP-7123, *Subsurface Conditions Description of the T and TX-TY Waste Management Area*. Describes tank release events, contaminant occurrences, and environmental conditions in the TX and TY tank farms.
- RPP-23752, *Field Investigation Report for Waste Management Areas T and TX-TY*. Provides findings from characterization activities conducted in 2003 and 2004 at the TX and TY tank farms.

Supporting background information on the adjacent cribs and trenches can be found in the following documents:

- DOE/RL-2003-64, *Feasibility Study for the 200-TW-1 Scavenged Waste Group, the 200-TW-2 Tank Waste Group, and the 200-PW-5 Fission-Product Rich Waste Group Operable Units*. Summarizes findings from characterization activities conducted in 2001 at the 216-T-26 crib (representative site for 216-T-18 crib in 200-TW-1 Operable Unit [OU]) and 216-B-38 trench (representative site for TX trenches in 200-TW-2 OU).
- DOE/RL-2006-51, *Remedial Investigation Report for the Plutonium/Organic-Rich Process Condensate/Process Waste Group Operable Unit: Includes the 200-PW-1, 200-PW-3, and 200-PW-6 Operable Units*. Summarizes findings from characterization activities conducted in 2006 at the 216-Z-9 trench (representative site for 216-T-19 crib in 200-PW-1 OU).
- DOE/RL-2005-61, *Remedial Investigation Report for the 200-LW-1 (300 Area Chemical Laboratory Waste Group) and 200-LW-2 (200 Area Chemical Laboratory Waste Group)*

Operable Units. Summarizes findings from characterization activities conducted in 2004 and 2005 at the 216-T-28 crib (representative site for 216-T-27 crib in 200-LW-1 OU).

- DOE/RL-2004-24, *Feasibility Study for the 200-CW-5 (U Pond/Z Ditches Cooling Water Waste Group), 200-CW-2 (S Pond and Ditches Cooling Water Waste Group), 200-CW-4 (T Pond and Ditches Cooling Water Waste Group), and 200-SC-1 (Steam Condensate Waste Group) Operable Units*. Summarizes findings from characterization activities conducted in 2001 at the 216-T-26 crib (representative site for 216-T-36 crib in 200-SC-1 OU).

Figure 2-1. Location of TX and TY Tank Farms in the 200 West Area.

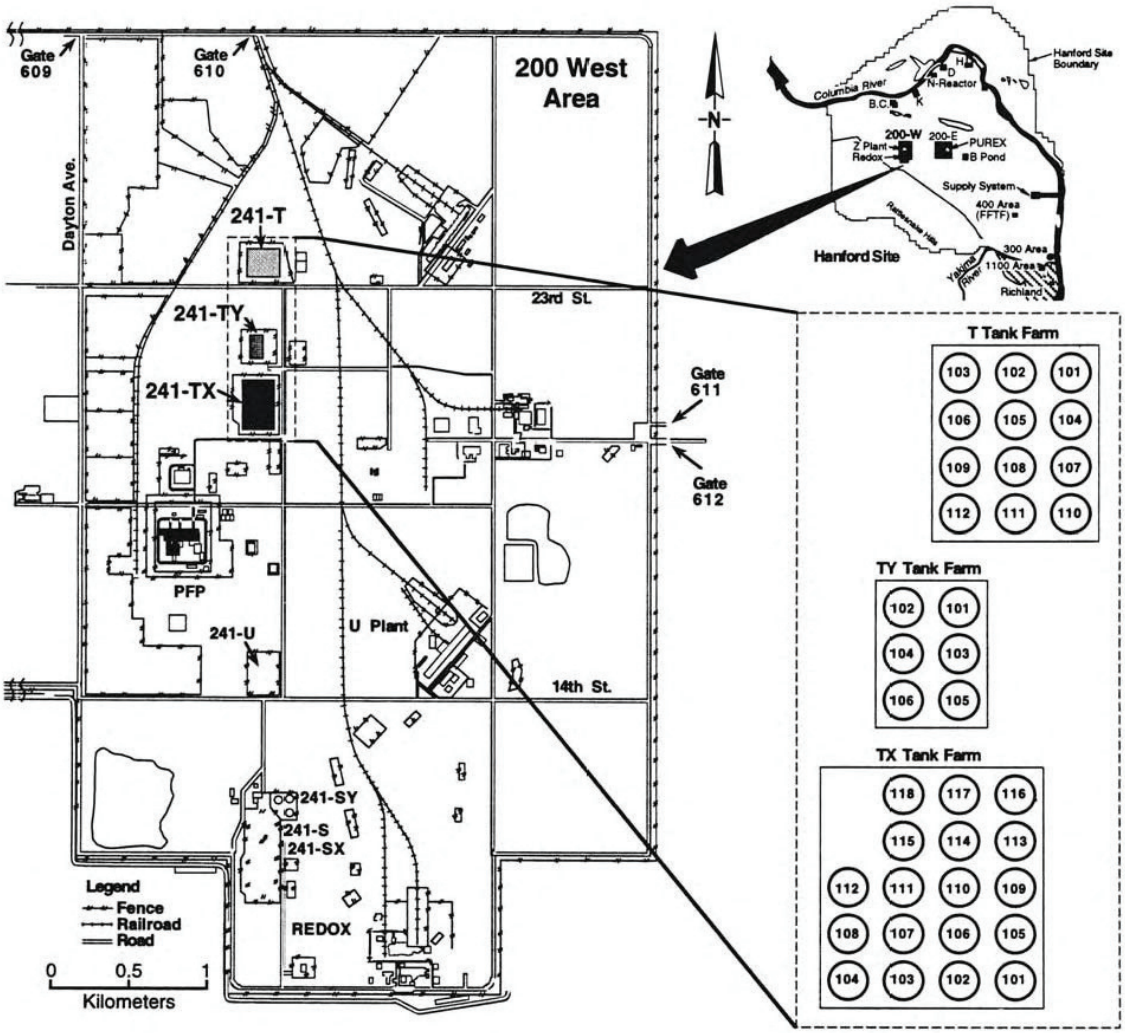

Source: RPP-23752, 2005, *Field Investigation Report for Waste Management Areas T and TX-TY*, Rev. 0-A, CH2M HILL Hanford Group, Inc., Richland, Washington.

Figure 2-2. TX and TY Tank Farms and Surrounding Facilities.

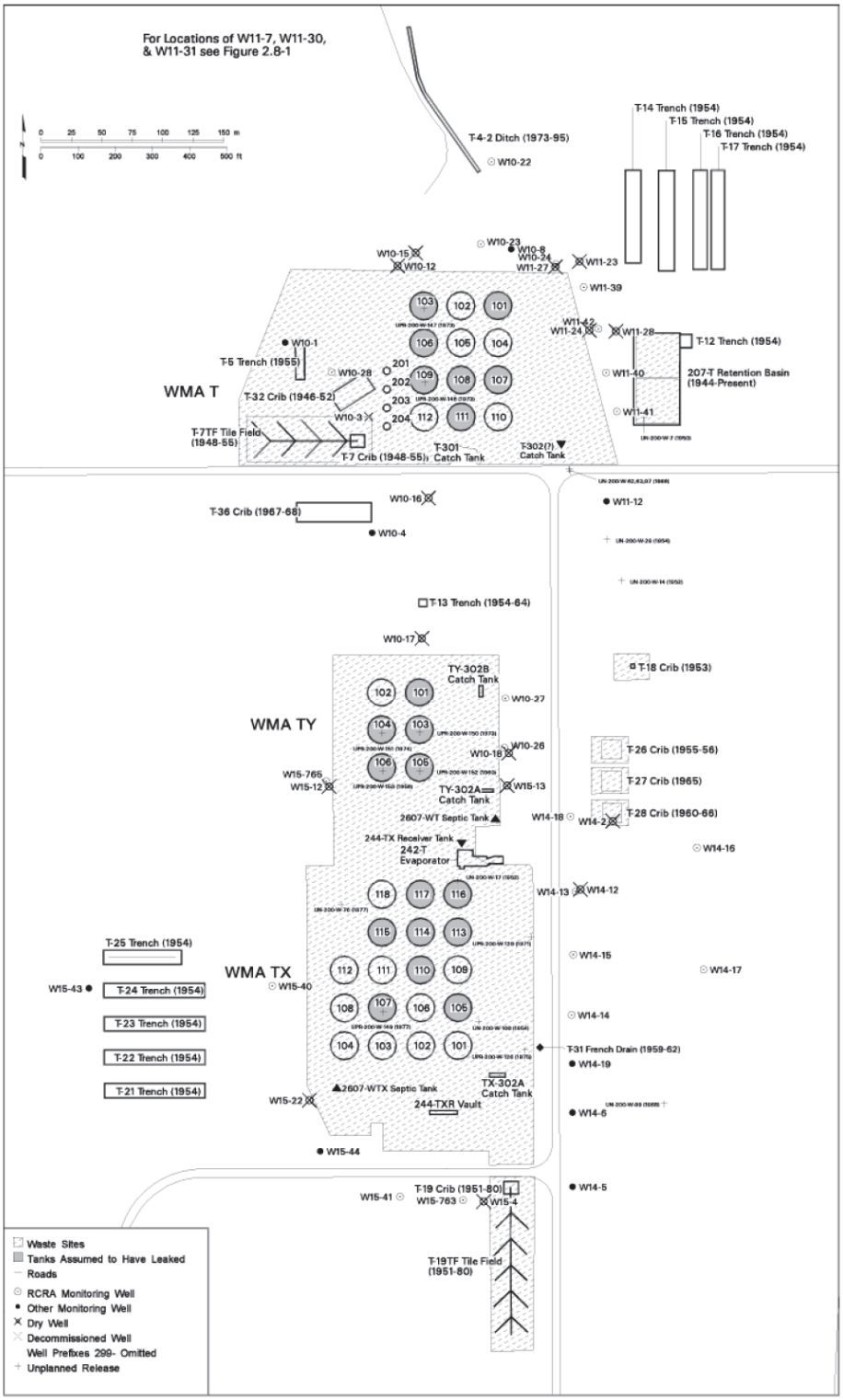

Source: RPP-23752, 2005, *Field Investigation Report for Waste Management Areas T and TX-TY*, Rev. 0-A, CH2M HILL Hanford Group, Inc., Richland, Washington.

Figure 2-3. General Configuration of Tank Construction in Waste Management Area TX-TY.

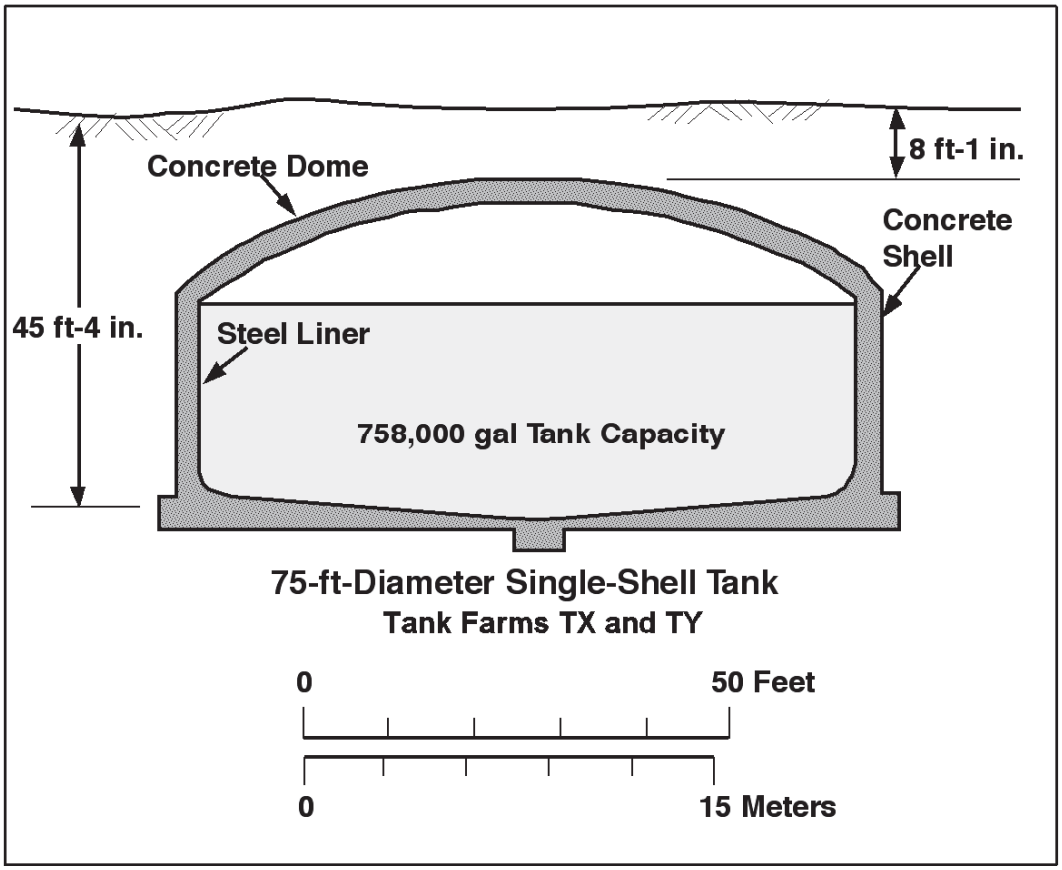

Source: DOE/ORP-2005-01, 2006, *Initial Single-Shell Tank System Performance Assessment for the Hanford Site*, Rev. 0, CH2M HILL Hanford Group, Inc., Richland, Washington.

2.2 OPERATIONAL HISTORY

The TX tank farm was constructed between 1947 and 1949 and began receiving waste in 1949. It was originally built to provide tank space for bismuth phosphate waste from T Plant and later was used a part of the uranium recovery process (RPP-7123). The TY tank farm was constructed between 1951 and 1952 and began receiving waste in 1953. It was built to provide tank space for the uranium recovery process (RPP-7123). Due to limited tank space, the 242-T Evaporator was built in 1951 to reduce waste volumes and the 216-T-19 crib and tile field was constructed to receive condensate from the evaporator. Through the 1950s and into the 1960s, generated waste volumes continued to exceed the available tank space, forcing the intentional discharge of relatively high waste volumes into the vadose zone. Additional cribs and trenches were constructed to receive the liquid discharges. Planned waste management activities continued up until the early 1980s.

2.2.1 Liquid Waste Releases at TX-TY Complex

Over their operating history, facilities in and around the TX-TY Complex have intentionally and unintentionally released liquid wastes to the vadose zone. The adjacent waste management facilities intentionally discharged liquid wastes, while 13 of the 24 SSTs, along with some of their associated ancillary equipment, are known or suspected to have unintentionally released waste. These discharges have led to substantial contaminant plumes distributed in the vadose zone, in some cases to the water table, within and around the tank farm.

During waste management operations, substantial volumes of liquid wastes were discharged to the TX-TY Complex cribs and trenches as shown in Table 2-1. These discharges occurred during four large-scale operation periods (RPP-5957).

- Postwar bismuth phosphate processing (1946 to 1956). Discharges of multiple bismuth phosphate waste streams began early in the TX-TY Complex operating history and continued until the shutdown of plutonium separation operations at T Plant in 1956.

- Uranium recovery operations (1952 to 1958). Scavenged waste and process condensate were discharged during this period.

- Central decontamination operations (1958 to 1969). Following the conversion of T Plant into a central decontamination facility in 1958, decontamination waste and liquid waste from the 300 Area were discharged at the TX-TY Complex.

- In-Tank Solidification operations (1965 to 1974). Steam condensate and process condensate were discharged during this period. The In-Tank Solidification program was discontinued as a method of liquid waste removal in 1974 and replaced by saltwell pumping.

Removal of pumpable liquids has been completed at all TX-TY Complex SSTs and the tanks are all listed as interim stabilized in HNF-EP-0182.

Table 2-1. Liquid Waste Disposal Facilities and Discharge Volumes near WMA TX-TY.[a] (2 Sheets)

Facility/ Component	Liquid Waste Discharge Volume (gallons)	Operational Period
216-T-13 trench	2.6E+04	1954-1964
216-T-18 crib	2.6E+05	1953
216-T-19 crib and tile field	1.2E+08	1951-1976
216-T-21 trench [b]	1.2E+05	1954
216-T-22 trench [b]	4.0E+05	1954
216-T-23 trench [b]	4.0E+05	1954
216-T-24 trench [b]	4.1E+05	1954
216-T-25 trench [b]	7.9E+05	1954
216-T-26 crib	3.2E+06	1955-1956

Table 2-1. Liquid Waste Disposal Facilities and Discharge Volumes near WMA TX-TY.[a] (2 Sheets)

Facility/ Component	Liquid Waste Discharge Volume (gallons)	Operational Period
216-T-27 crib	1.9E+06	1965
216-T-28 crib	1.1E+07	1960-1966
216-T-31 French drain	Large Volume	1954-1962
216-T-36 crib	1.3E+05	1967-1969

[a] Modified from Table 3-28 of RPP-23752, 2005, *Field Investigation Report for Waste Management Areas T and TX-TY*, Rev. 0-A, CH2M HILL Hanford Group, Inc., Richland, Washington.

[b] Specific-retention trenches 216-T-21 through 216-T-25 received limited short-term discharge volumes to prevent contaminant breakthrough to the unconfined aquifer.

The volumetric distribution of discharged waste around the TX-TY Complex varies. Figure 2-5 shows the disposal volumes and tank leak volumes graphically, depicted as circles with diameters proportional to discharge volume. The volumes shown in the figure are based on data reported in RPP-23752 and HNF-EP-0182. The figure shows that over 140 million gallons of liquid have been discharged to the subsurface. Over 85 percent (120 million gallons) of the total volume was discharged to the 216-T-19 crib and tile field to the southeast. The TY cribs to the east and TX trenches to the west received 12 percent (16 million gallons) and 2 percent (2 million gallons) of the total volume, respectively. The SSTs discharged less than 120,000 gallons to the subsurface (based on leak volumes reported in HNF-EP-0182).

Of the past-practice facilities listed in Table 2-1, the most significant discharges occurred at the TX trenches, the 216-T-19 crib and tile field, and the TY cribs. The TX trenches (216-T-21 through 216-T-25) were operated as specific-retention trenches, which were used for discharge of more concentrated waste in volumes that were intentionally limited to prevent breakthrough of contaminants to the unconfined aquifer (RPP-7123). The five TX trenches collectively received over 2 million gallons of first-cycle bismuth phosphate waste (1C) in 1954. RPP-23752 indicates that the specific-retention strategy was generally successful, and much of the discharged contamination likely remains below the trenches in the vadose zone.

In contrast, much larger volumes of more dilute waste streams were discharged to the 216-T-19 crib and tile field and the TY cribs (in particular the 216-T-28 crib). Discharge volumes at these facilities were probably sufficient to drive mobile contaminants (e.g., nitrate, chromium, technetium-99) to the water table (RPP-23752). The 216-T-19 crib and tile field operated the longest (1951 to 1976) and received the largest discharge volume (over 120 million gallons) of all the TX-TY Complex facilities. The discharges were mainly 242-T Evaporator condensate with some bismuth phosphate waste (2C, 5-6, and 224 waste) (RPP-7123). The TY cribs (216-T-26 through 216-T-28) operated from the mid-1950s to the mid-1960s and received over 16 million gallons of waste, about 75 percent of which (12 million gallons) went to the 216-T-28 crib. The discharges included tributyl phosphate waste (TBP), scavenged 1C waste, T Plant decontamination waste, and 340 Building laboratory waste (RPP-7123).

Figures 2-4 through 2-7 show the distribution of electrolytes (anions and cations) and major radionuclides based on data reported in RPP-26774, *Hanford Soil Inventory Model*.

Figure 2-4. Liquid Waste Volumes Discharged Around Waste Management Area TX-TY.

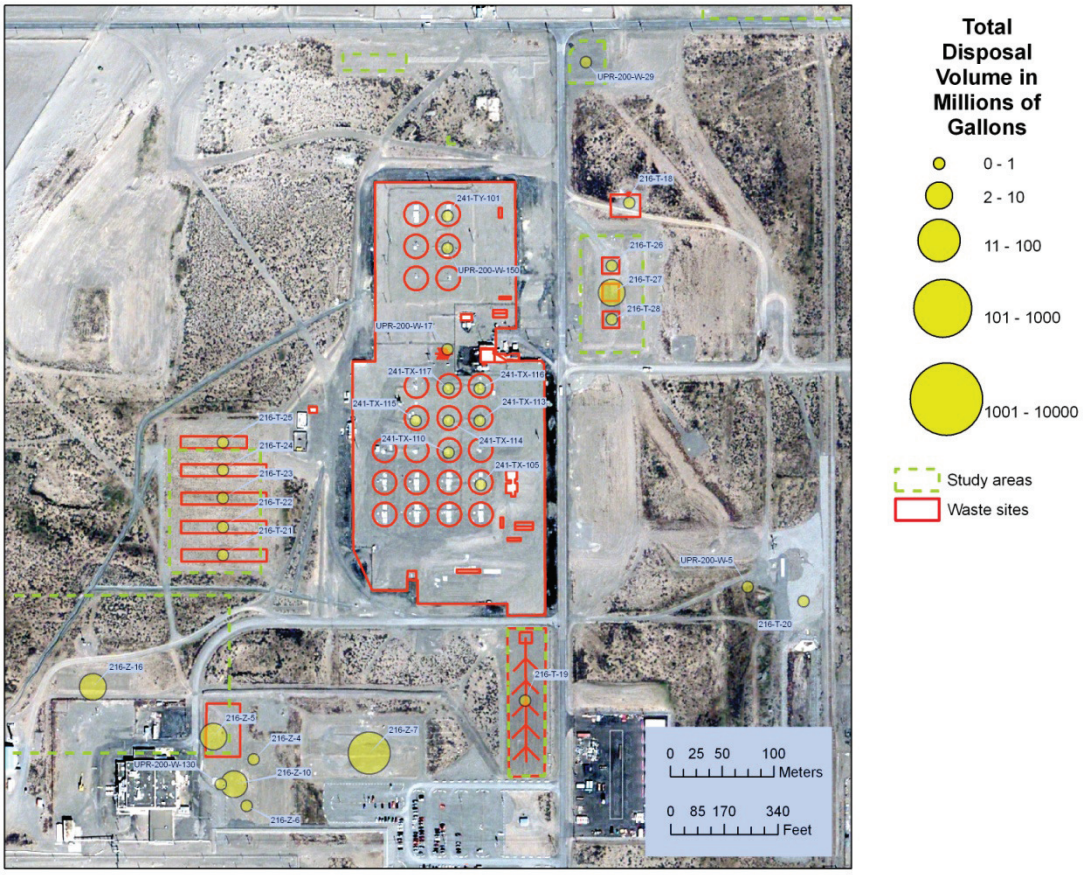

Figure 2-5. Major Anions Discharged Around Waste Management Area TX-TY.

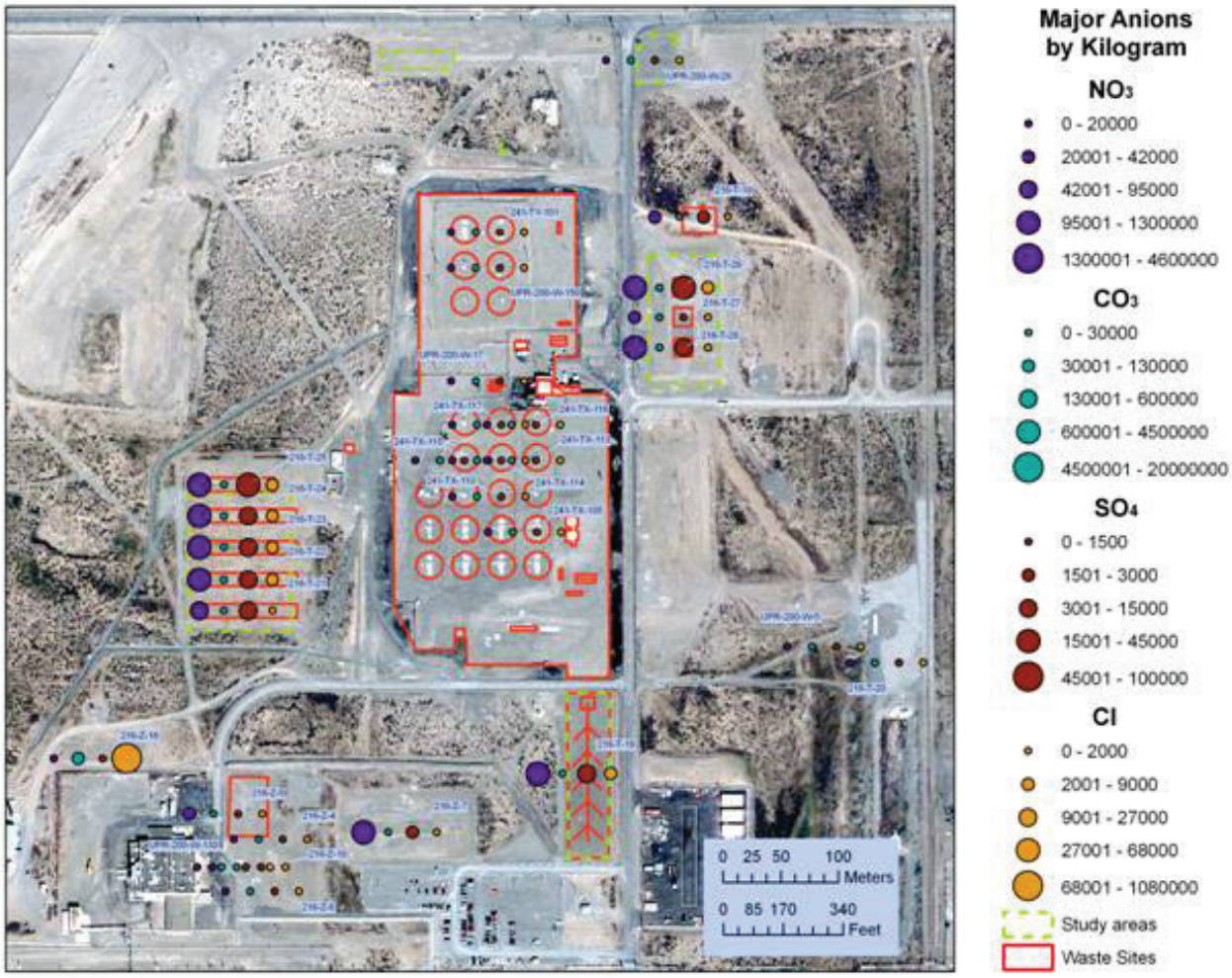

Figure 2-6. Major Cations Discharged Around Waste Management Area TX-TY.

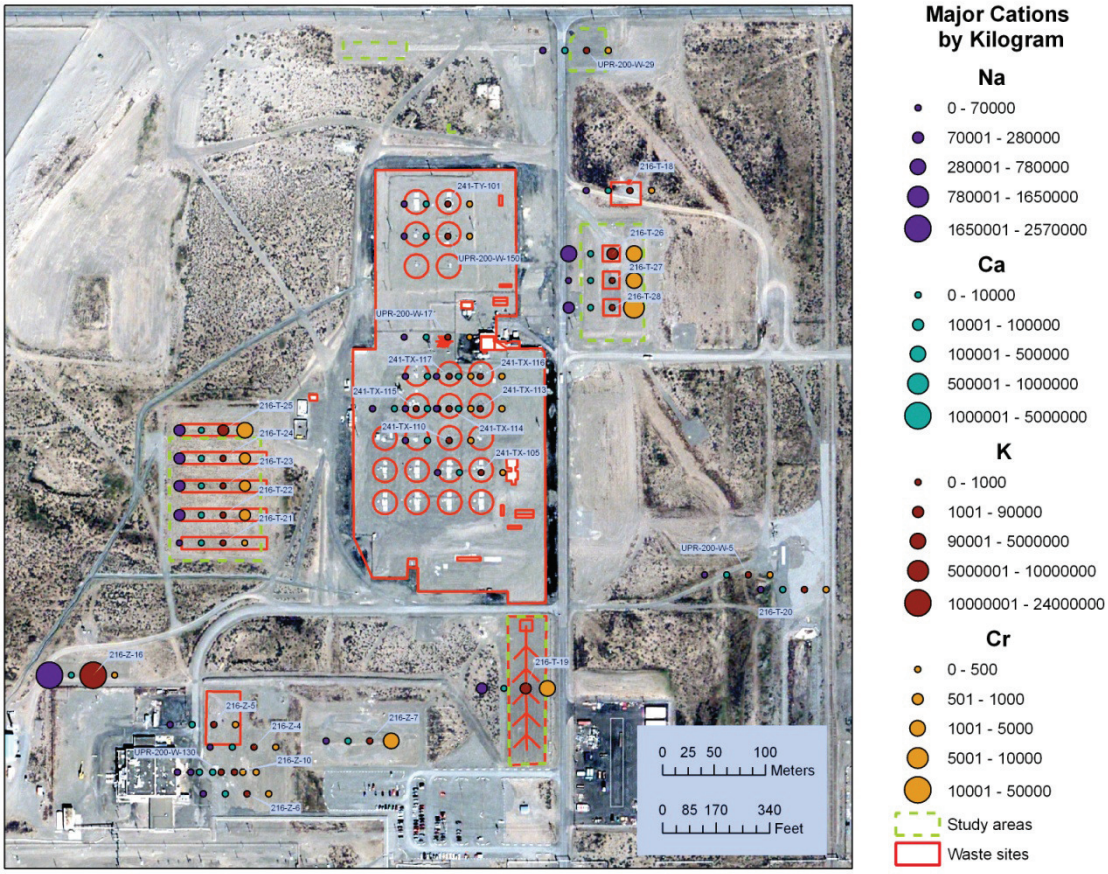

The 13 TX-TY Complex SSTs identified as confirmed or assumed to have leaked are as follows (HNF-EP-0182):

- TX tank farm—TX-105, TX-107, TX-110, TX-113, TX-114, TX-115, TX-116, and TX-117
- TY tank farm—TY-101, TY-103, TY-104, TY-105, and TY-106.

Reported leak volumes range from 35,000 gallons (tank TY-105) to <1,000 gallons (tank TY-101). Some of the waste loss events were well documented, while others had little data available to support a leak volume estimate. All TX tank farm leakers (except TX-107) have a leak volume estimate of 8,000 gallons in HNF-EP-0182. This is a non-tank specific value averaged over 19 tanks located in several tank farms that are considered to have leaked a total of about 150,000 gallons. Tank TX-107 is assigned a leak volume of 2,500 gallons based on liquid level drops and elevated borehole gamma readings.

HNF-EP-0182 assigns tanks TY-101, TY-103, and TY-104 leak volumes of 3,000 gallons or less based primarily on small drops in liquid level. Tanks TY-105 and TY-106 are assigned leak

volumes of 35,000 gallons and 20,000 gallons, respectively, based on borehole gamma activity, liquid level observations, and waste transfer records indicating an apparent waste loss.

The leak volume estimates reported in HNF-EP-0182 have not been updated for many years and the quality of the evidence supporting the estimates varies considerably. *Tank Farm Vadose Zone Contamination Volume Estimates* (RPP-23405) provided updated leak volume estimates to support the development of leak inventories for *Initial Single-Shell Tank System Performance Assessment for the Hanford Site* (DOE/ORP-2005-01). Of the 13 designated leakers in the TX and TY tank farms, RPP-23405 provided estimated leak volumes for 6 tanks (TX-107, TY-101, TY-103, TY-104, TY-105, and TY-106). The remaining 7 tanks were noted as lacking sufficient information to develop an estimate. The RPP-23405 leak volumes agree with the HNF-EP-0182 volumes with the exception of tank TX-107, which increased in volume from 2,500 to 8,000 gallons.

In addition to past-practice releases and tank leaks, a number of unplanned releases (UPR) from near-surface ancillary equipment have been reported for WMA TX-TY, spanning the entire operational period (RPP-23752). These releases are not tracked in the HNF-EP-0182 report but are addressed in RPP-23405. The RPP-23405 reassessment provided leak volume estimates for two unplanned releases in the TX-TY Complex (both in the TX tank farm), consisting of a 5-gallon leak from a riser leak south of the 242-T Evaporator (UPR-200-W-12) and a 2,500-gallon leak from a TX-105 to TX-118 line leak (UPR-200-W-100).

2.2.2 Infrastructure and Waste Delivery to TX-TY Complex

In addition to the intentional liquid waste discharges to the cribs and unplanned waste releases, leaks from water distribution lines in and around the tank farm and known meteorological events may have contributed to waste migration in the vadose zone (RPP-23752). Figure 2-8 shows a compilation of the infrastructure, including pipes, tanks, and diversion boxes used to transfer waste and supply the tank farm with water. This figure was generated from multiple site infrastructure drawings.

Figure 2-7. Major Radionuclides Discharged Around Waste Management Area TX-TY.

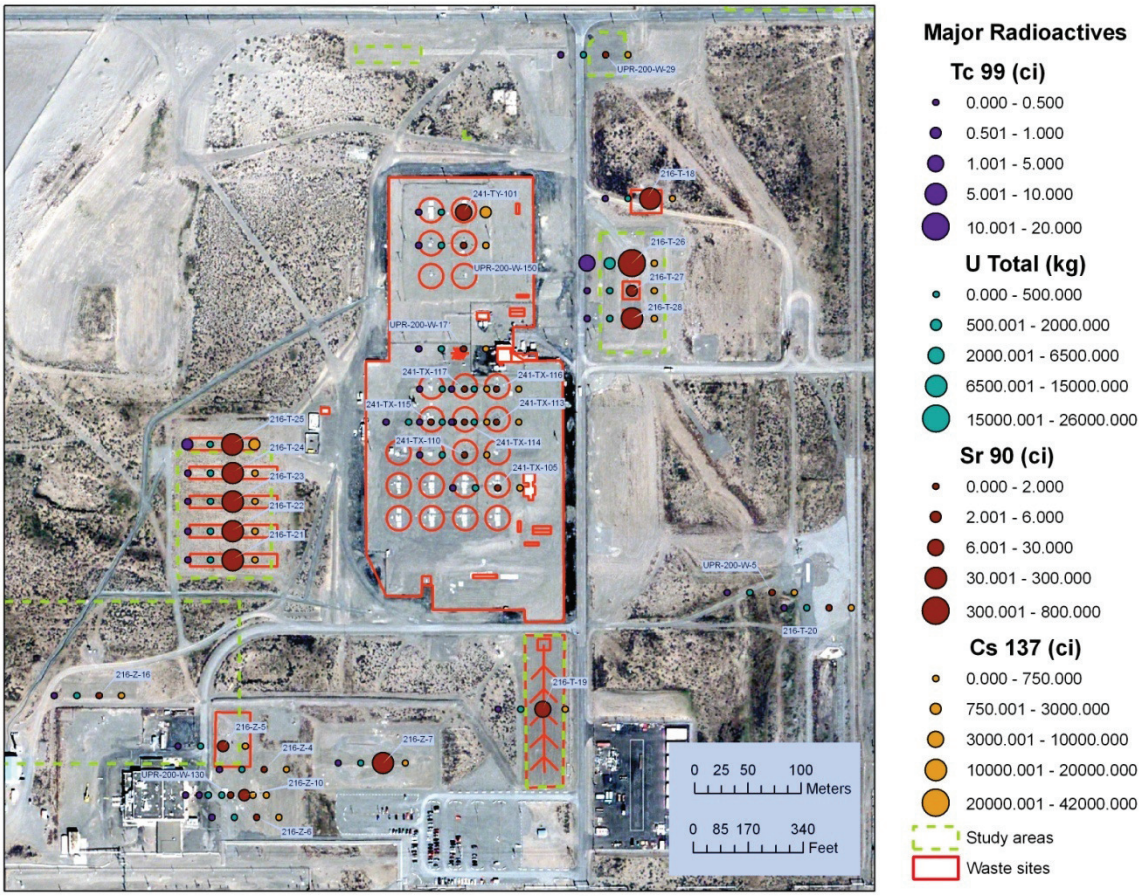

Figure 2-8. Infrastructure Map for TX and TY Tank Farms.

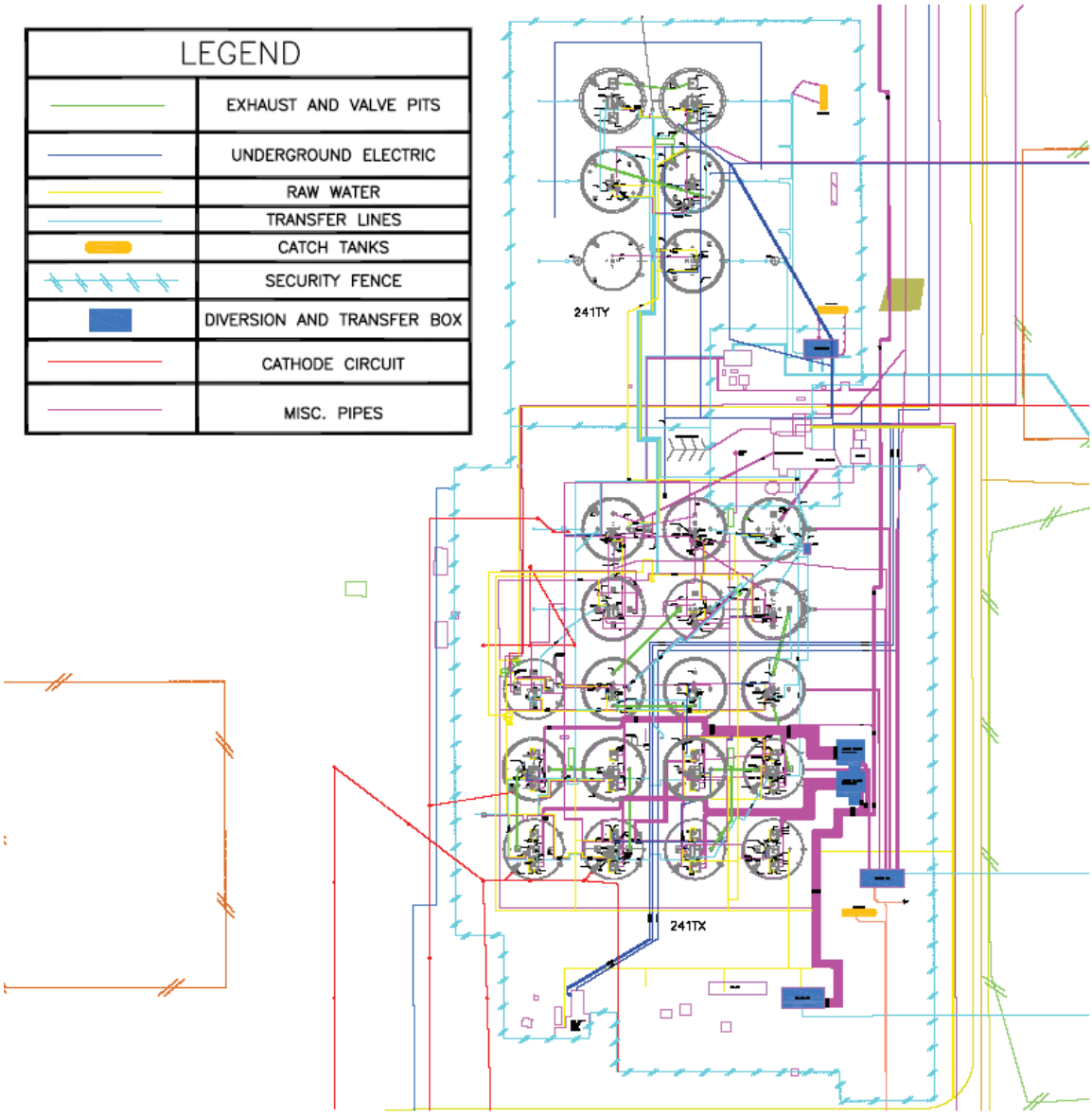

Adapted from existing site infrastructure drawings.

2.3 ENVIRONMENTAL SETTING

The geology of the TX-TY Complex and immediate vicinity is well understood as a result of several decades of site characterization activities. Sedimentary and stratigraphic conditions have been described in numerous reports, including the following publications:

- *Field Investigation Report for Waste Management Ares T and TX-TY* (RPP-23752)
- *Subsurface Conditions Description of the T and TX-TY Waste Management Areas* (RPP-7123)
- *Geology of the Separations Areas, Hanford Site, South Central Washington* (RHO-ST-23)
- *Geology Data Package for the Single Shell Tank Waste Management Areas at the Hanford Site* (PNNL-15955)
- *Geology, Hydrogeology, Geochemistry, and Mineralogy Data Package for the Single-Shell Tank Waste Management Areas at the Hanford Site* (RPP-23748).

Four major stratigraphic units underlie the TX-TY Complex. In ascending order these are the Miocene-age igneous Columbia River Basalt Group overlain by three sedimentary units consisting of the Miocene- to Pliocene-age Ringold Formation (including the member of Taylor Flats [R_{tf}] and member of Wooded Island [R_{wi}]), the Cold Creek unit (including subunits CCU_u and CCU_l), and the Pleistocene-age Hanford formation (including subunits H1 and H2). Also, backfill materials consisting of poorly sorted cobbles, pebbles, and coarse to medium sand derived from the Hanford H1 unit are distributed around the tanks and tank infrastructure.

The backfill, Hanford formation, Cold Creek unit, and the upper portion of the Ringold Formation make up the vadose zone, which is approximately 230 feet thick in this area. The unconfined aquifer is contained within the lower portion of the Ringold Formation. The water table lies approximately 200 feet below the bottom of the tank farm excavations within the Ringold formation unit E. The Hanford formation is between 75 and 100 feet thick and thickens towards the south and west. The Cold Creek unit is a calcite-rich paleosol that is between 20 and 35 feet thick. The overall thickness of the Ringold Formation is about 375 feet.

The geologic features that have had the most significant influence on contaminant migration and distribution in the vadose zone are the highly-cemented CCU_l layer and the slight dip of all layers toward the south (RPP-23752). The CCU_l appears to have largely prevented vertical migration of contaminants below the subunit and enhanced lateral migration. The stratigraphic dip to the south appears to have influenced the migration of some of the contaminants in that direction.

2.4 HISTORICAL CHARACTERIZATION EFFORTS

The SSTs are regulated under various DOE orders and policies in addition to the *Resource Conservation and Recovery Act of 1976* (RCRA) and the Washington State *Hazardous Waste Management Act* (RCW 70.105) and its implementing requirements in *Washington Administrative Code* 173-303, "Dangerous Waste Regulations." The SSTs are operating under interim status permit pending closure. The SST farms are grouped into WMAs for the purpose of groundwater monitoring and vadose zone corrective actions. Investigations to support WMA corrective action decisions are being implemented through the RCRA corrective action process

as described in the Hanford Federal Facility Agreement and Consent Order (Ecology et al. 1989) Change Request M-45-98-03 (Ecology et al. 1991).

Each 100-series tank in the TX-TY Complex is surrounded by a group of monitoring boreholes (drywells) in which radiometric instruments were used to detect changes in activity levels in the sediments surrounding the borehole. The TX tank farm has 96 drywells, installed from 1947 to 1977. The TY tank farm has 22 drywells, installed from 1951 and 1977. The maximum logged depth in most drywells is between 75 and 150 feet (23 and 46 meters) below ground surface (ft bgs) (RPP-7123).

During active waste management operations, the drywells served as both primary and secondary leak detection devices. Gross gamma logging of the drywells took place over several decades allowing evaluation of the time-dependent behavior of the gamma-emitting radionuclides. From 1997 to 1999 high-resolution spectral gamma logging of the TX-TY Complex drywells was conducted as part of the baseline vadose zone characterization for the TX-TY Complex. Results are documented in tank farm summary reports issued by the DOE Grand Junction (Colorado) Office (*Hanford Tank Farms Vadose Zone: TX Tank Farm Report* [GJO-97-13-TAR]; *Hanford Tank Farms Vadose Zone: TY Tank Farm Report* [GJO-97-30-TAR]).

From 2003 to 2004, field characterization activities were conducted at WMA TX-TY in support of RCRA corrective action process requirements. The major investigative activities included vertical borehole installation, soil sampling, and analysis at locations southwest of tank TX-105, southwest of tank TX-107, and southeast of tank TX-104. Investigation results are documented in RPP-23752. Most recently, vadose zone contamination was investigated in the TY tank farm using direct push technology at five locations near tanks TY-105 and TY-106. Investigation results are presented in *Characterization of Direct Push Vadose Zone Sediments from the T and TY Waste Management Areas* (PNNL-16649).

Investigations to support remedial action decisions at the TX-TY Complex cribs and trenches are being implemented through the remedial investigation/feasibility study process under the *Comprehensive Environmental Response, Compensation, and Liability Act of 1980* (CERCLA). The facilities have been assigned to operable units (OU) as shown in Table 2-2 for the purpose of conducting the remedial investigation/feasiblity work. An analogous site approach is being used to streamline the characterization process. Findings from site investigations at "representative" sites are applied to other "analogous" sites that were not sampled. Representative/analogous sites for the TX-TY Complex cribs and trenches are indicated in Table 2-2. From 2001 to 2006, characterization activities including borehole installation and soil sampling and analysis were conducted at representative sites for all of the OUs shown in Table 2-2.

Since 1991, chemicals and radionuclides have been tracked under RCRA in unconfined aquifer samples collected from monitoring wells in and around WMA TX-TY (RPP-23752). Waste Management Area TX-TY was placed in assessment groundwater monitoring in 1993 due to elevated specific conductance (a measure of electrical conductivity of water) in down gradient monitoring wells. PNNL-16005 (*RCRA Assessment Plan for Single-Shell Tank Waste Management Area TX-TY*) provides the most recent update to the groundwater quality assessment plan for WMA TX-TY. Tank waste contaminants historically detected in groundwater beneath the TX-TY Complex at concentrations exceeding limits specified in Title

40 *Code of Federal Regulations*, Part 141, "National Primary Drinking Water Regulations" (40 CFR 141) include technetium 99, iodine-129, tritium, chromium, and nitrate (PNNL-16005).

Table 2-2. Liquid Waste Disposal Facility Operable Unit Assignments.

Facility/Component	Operable Unit	Representative/Analogous Site
216-T-13 trench	200-MG-2*	N/A
216-T-18 crib	200-TW-1	Analogous site to 216-T-26 crib
216-T-19 crib and tile field	200-PW-1	Analogous site to 216-Z-9 trench
216-T-21 trench	200-TW-2	Analogous site to 216-B-38 trench
216-T-22 trench	200-TW-2	Analogous site to 216-B-38 trench
216-T-23 trench	200-TW-2	Analogous site to 216-B-38 trench
216-T-24 trench	200-TW-2	Analogous site to 216-B-38 trench
216-T-25 trench	200-TW-2	Analogous site to 216-B-38 trench
216-T-26 crib	200-TW-1	Representative site for 216-T-18 crib and 216-T-36 crib
216-T-27 crib	200-LW-1	Analogous site to 216-T-28 crib
216-T-28 crib	200-LW-1	Representative site for 216-T-27 crib
216-T-31 French drain	200-MG-2[a]	N/A
216-T-36 crib	200-SC-1	Analogous site to 216-T-26 crib

NA = not applicable.

*200-MG-2 is one of several newer operable units established during recent operable unit scope modifications as described in Change Order M-15-06-02 to the *Hanford Federal Facility Agreement and Consent Order* (Ecology et al. 2006). It contains simple waste sites for which current information is considered sufficient for decision making.

2.4.1 Vadose Zone

Drywell logging data indicate that the major gamma-emitting contaminants in the TX and TY tank farms vadose zone are cesium-137, cobalt-60, ruthenium-106, antimony-125, uranium-235, and uranium-238 (RPP-7123). The primary areas of elevated gamma readings occur adjacent to the 13 tanks identified as confirmed or assumed leakers. The data also indicate that generalized near-surface contamination at lower concentrations is widespread inside the tank farms. The evaluation of time-dependent behavior indicates that in certain areas the more mobile radionuclides such as cobalt-60 and ruthenium-106 have migrated downward from their locations of emplacement (RPP-7123).

In the TX tank farm, gamma logging data from drywells near tank TX-107 show elevated concentrations of cobalt-60 and europium-154 from 45 to 70 ft bgs that indicate the presence of a substantial leak plume (RPP-23405). RPP-23405 increased the leak volume estimate for tank TX-107 from 2,500 to 8,000 gallons based on plume size estimates. Evaluation of the historic data for this tank indicates migration of cobalt-60 contamination from northeast to southwest between 1977 and 1992 (RPP-7123).

Gamma data indicate that two distinct zones of uranium-bearing contamination are present in the TX tank farm near tanks TX-104 and TX-105. Although tank TX-104 is not listed as a "confirmed or assumed" leaker in HNF-EP-0182, the gamma data provide evidence of an unreported high-uranium waste loss event near this tank as well as tank TX-105. Drywells on the south sides of both tanks contain elevated uranium-235 and uranium-238 from 45 to 100

ft bgs. In both cases, a line drawn around the drywells outlines a rough oval with the long axis running northeast to southwest, suggesting the plumes have migrated laterally to the south and west as well as vertically in the vadose zone (RPP-7123).

Drywells associated with postulated leaks from tanks TX-110, TX-114, and TX-113 contain slightly elevated cesium-137 readings at the tank bottom depth. Tank TX-114 is believed to be the most likely to have leaked (RPP-7123). The source of the gamma contamination near the other tanks is ambiguous (RPP-7123).

Three boreholes, positioned to probe three separate contamination areas, were installed in the TX tank farm during 2003 and 2004 field characterization activities. The targeted areas consisted of the waste lost from tank TX-107 (borehole C3831) and the uranium-bearing waste lost from tanks TX-104 and TX-105 (boreholes C3832 and C3830, respectively) (RPP-23752). In the tank TX-105 borehole (C3830), elevated concentrations of technetium-99, nitrate, and uranium were measured in borehole sediment samples primarily between 59 and 100 ft bgs (RPP-23752). In the tank TX-107 borehole (C3831), technetium-99, cobalt-60, nitrate, and sodium were found from 60 ft bgs to the bottom of the borehole at 115 ft bgs (RPP-23752). Maximum technetium-99 and sodium concentrations occurred at about 60 ft bgs and maximum nitrate concentrations occurred at 86 ft bgs. In the tank TX-104 borehole (C3832), elevated technetium-99 and nitrate concentrations began at about 76 ft bgs and generally increased with depth in the borehole (RPP-23752). Maximum technetium-99 and nitrate concentrations occurred between 105 and 115 ft bgs. Uranium was elevated in the lower portion of the borehole between about 62 and 110 ft bgs. Elevated sodium occurred from 63 to 115 ft bgs with a maximum at 76 ft bgs (RPP-23752).

In the TY tank farm, drywell gamma logging data near tank TY-105 show elevated cesium-137 and cobalt-60 concentrations indicative of a tank leak from 50 to 150 ft bgs (RPP-7123). Although the tank TY-105 reported leak volume is large (34,000 gallons), it is not clearly substantiated in the operations record (RPP-7123). Waste transfer records supporting the assumed 20,000 gallon leak from tank TY-106 are ambiguous and not well supported by gamma data from nearby drywells (RPP-23405). A 2006 direct push characterization campaign at tanks TY-105 and TY-106 provided evidence that sediment at tank bottom depth near these tanks has unquestionably been contaminated by tank waste (PNNL-16649). Drywells near tank TY-103 contain elevated cesium-137 readings near the tank bottom depth from 45 to 50 ft bgs and elevated cobalt-60 concentrations deeper in the vadose zone (RPP-7123). Slightly elevated gamma activity has been observed in drywells near tanks TY-101 and TY-104.

At the 216-T-26 crib (representative site for the 216-T-18 and 216-T-36 cribs), soil data from a borehole drilled and sampled in 2001 during 200-TW-1 OU remedial investigation activities indicate the main zone of contamination extends from 18 to 36.5 ft bgs and is associated with the effluent release point at the crib bottom (DOE/RL-2003-64). Cesium-137 is the dominant contaminant in this zone (maximum concentration 47,900 pCi/g). Significant reduction in contamination levels is associated with the top of the sand-dominated Hanford H2 unit (at approximately 36.5 ft bgs) and the top of the CCU (at approximately 94.5 ft bgs). Contaminants detected in soil samples from 36.5 to 94.5 ft bgs include technetium-99, cobalt-60, uranium isotopes, and nitrate. Only technetium-99, tritium, nitrate, and phosphate were detected below 94.5 ft bgs. The effluent volume discharged to the 216-T-26 crib was greater than the associated

soil column pore volume by a factor of about 18, suggesting the effluent volume was sufficient to reach the aquifer during operations. Contamination extends laterally beyond the 216-T-26 crib boundary to the south and may intersect contamination associated with the 216-T-27 crib. The contaminant profile suggests little contamination is spreading to the north (DOE/RL-2003-64). Contaminant distribution for the analogous 216-T-18 crib is expected to be similar to that for the representative site (216-T-26 crib), with the zone of highest contamination extending to about 31 ft bgs. However, contamination levels are expected to be lower because contaminant loads were lower and effluent volume was only about a factor of 1.5 greater than pore volume (DOE/RL-2003-64). Contaminant distribution for the analogous 216-T-36 crib is expected to be significantly lower than that for the representative site (216-T-26 crib) because volume discharged was 4 percent of the representative site volume and did not exceed pore volume (DOE/RL-2004-24).

At the 216-B-38 trench (representative site for the 216-T-21 through -25 trenches), soil data from a borehole drilled and sampled in 2001 during 200-TW-2 OU remedial investigation activities indicate the major zone of contamination is associated with the point of release at about 15 ft bgs and extends to a depth of about 40 ft bgs (DOE/RL-2003-64). Cesium-137 is the dominant contaminant in this zone (maximum concentration 226,000 pCi/g). Radionuclide concentrations from 40 to 200 ft bgs were mostly less than 2.0 pCi/g. Contaminants detected from 40 to 200 ft bgs include technetium-99, tritium, nitrate, nitrite, and phosphate. Nitrate and nitrite were distributed deep in the vadose zone to a maximum depth of 200 ft bgs (DOE/RL-2003-64). The effluent volume discharged to the 216-B-38 trench was less than a third of the associated soil column pore volume, suggesting the effluent volume was not sufficient to reach the aquifer during operations. In addition to the one borehole, five direct-push holes were installed along the center axis of the 216-B-38 trench. The direct-push data indicate that cesium-137 contamination extends more than 125 ft from the east end of the trench (i.e., along half the length of the trench) and 20 to 25 ft on either side of the trench. Contaminant distribution for the analogous TX trenches is expected to be similar to that for the representative site (216-B-38 trench). The effluent volumes discharged to the TX trenches were generally less than half of the available pore volume, except for the 216-T-25 trench where the discharged volume was approximately equal to the pore volume (DOE/RL-2003-64).

At the 216-Z-9 trench (representative site for the 216-T-19 crib), soil data were obtained from two boreholes drilled and sampled during in 2006 during 200-PW-1 OU remedial investigation activities (DOE/RL-2006-51). Borehole 299-W15-46 was a vertical borehole installed south of the trench. Borehole 299-W15-48 was a slant borehole installed beneath the trench. The primary focus of the sampling was to characterize the CCU for the presence of DNAPL carbon tetrachloride; however, samples were also analyzed for radiological and chemical contaminants. Contaminants were detected to depths of about 140 ft bgs beneath the trench and 185 ft bgs to the south of the trench 140 ft bgs. The dominant contaminants were americium-241 (maximum concentration 309,000 pCi/g at 112 ft bgs) and plutonium-239/240 (maximum concentration 115,000 pCi/g at 66 ft bgs). The maximum nitrate concentration beneath the trench was 5,910 mg/kg at 112 ft bgs. The effluent volume discharged to the 216-Z-9 trench was about 1.5 times the estimated pore volume beneath the trench, suggesting the effluent volume was sufficient to reach the aquifer during operations. DOE/RL-2006-51 defers evaluation of analogous sites (such as the 216-T-19 crib) to the feasibility study, which is not yet available.

However, the effluent volume discharged to the 216-T-19 crib was about 36 times the available pore volume.

At the 216-T-28 crib (representative site for the 216-T-27 crib), soil data from a borehole drilled and sampled in 2005 during 200-LW-1 OU remedial investigation activities indicate the major zone of contamination is associated with the point of release at about 15 ft bgs and extends to a depth of about 30 ft bgs (DOE/RL-2005-61). Cesium-137 is the dominant contaminant in this zone (maximum concentration 3,100,000 pCi/g). Contaminant concentrations generally decrease with depth. Contaminants detected from 30 to 200 ft bgs include technetium-99, cobalt-60, hexavalent chromium, and nitrate. The maximum technetium-99 concentration was 1.6 pCi/g at 200 ft bgs. The effluent volume discharged to the 216-T-28 crib trench was greater than the associated soil column pore volume by a factor of over 60, suggesting the effluent volume was sufficient to reach the aquifer during operations (DOE/RL-2005-61). Contaminant distribution for the analogous 216-T-27 crib is expected to be lower than for the representative site (216-T-28 crib) because the effluent discharge volume was only about a factor of 4 greater than the pore volume.

Vertical distribution of moisture in the subsurface for selected boreholes in TX tank farm, taken from PNNL-14594, is shown in Figure 2-9. The moisture content shown was taken from direct measurements of soil samples using a thermogravimetric method and converted to volumetric moisture using a constant bulk density of 1.6 grams/cm^3 or from neutron moisture logs in three different boreholes. Vertical distribution of sulfate and nitrate from recent sampling and analysis efforts in the same boreholes, also taken from PNNL 14594, are summarized in Figure 2-10. These figures are provided in this document to show potential electrolytic targets in the vadose zone to indirectly compare to the resistivity results presented in Section 4 in the TX farm area.

The moisture data of Figure 2-9 in general shows moisture contents ranging from less than 5 percent by volume to greater than 15 percent by volume. A few fine-grained layers do appear in the lithology conincident with the higher moisture contents. Moisture data from borehole C3832 for example, shows eight separate layers with relatively high moisture (i.e., greater than 10 percent). The moisture data itself does not show an indication of a subsurface plume resulting from historical liquid waste disposal. The limited geochemical data on sulfate and nitrate given in the same selected boreholes in TX tank shows some high values of both nitrate and sulfate in the range of 60 to 90 feet (20 to 30 meters) bgs. In boreholes B3831 and B3832, nitrate levels remain relatively high down below the 90-foot (30-meter) depth to the bottom of the borehole

2.4.2 Unconfined Aquifer

Contaminants currently detected in groundwater at WMA TX-TY along with potential contamination sources are discussed in PNNL-16005 and *Hanford Site Groundwater Monitoring for Fiscal Year 2006* (PNNL-16346). In FY 2006, a network of 16 monitoring wells, sampled quarterly, was used to monitor the groundwater at WMA TX-TY (PNNL-16346). Monitoring is conducted under the requirements of RCRA and the *Atomic Energy Act*. All upgradient wells for this WMA were converted to extraction wells for the 200-ZP-1 pump-and-treat system in July 2005.

In FY 2006, dangerous waste constituents found beneath WMA TX-TY were chromium and nitrate. Other constituents found beneath the WMA included carbon tetrachloride,

trichloroethene, tritium, technetium-99, and iodine-129. The carbon tetrachloride and trichloroethene are attributed to Plutonium Finishing Plant (PFP) operations (PNNL-16346).

Nitrate concentrations exceeded the drinking water standard (45 mg/L) in all wells in the WMA in FY 2006. Figure 2-11 shows a plume map for nitrate in the area. The nitrate in groundwater beneath the WMA is part of a regional plume that underlies much of the north 200 West Area. The highest average nitrate concentration during FY 2006 was 468 mg/L in well 299-W14-13. This value was a slight increase from 430 mg/L during the previous fiscal year. Much of the nitrate contamination beneath the WMA is attributed to PFP operations as well as past-practice disposal to cribs and trenches in the area. Some nitrate contamination also may be from the WMA, although distinguishing the different sources is extremely difficult (PNNL-16346).

Chromium was detected above the drinking water standard (100 ug/L) in two wells at WMA TX-TY during FY 2006. The highest average concentration was 740 ug/L in well 299-W14-13. The most likely source for the chromium contamination is assumed to be the WMA because no alternative sources have been identified (PNNL-16346).

A small tritium plume exists along the east side of the WMA. Tritium exceeded the drinking water standard (20,000 pCi/L) in three wells in the area. The highest average concentration was 1.7 million pCi/L in well 299-W14-13 during FY 2006, which was up slightly from 1.57 million pCi/L during the previous fiscal year. The source for the tritium could be the WMA or the adjacent liquid discharge facilities or a combination of these potential sources (PNNL-16346).

Technetium-99 exceeded the interim drinking water standard (900 pCi/L) in several wells on the east side of the WMA. The highest average technetium-99 concentration during FY 2006 was 7,600 pCi/L in well 299-W14-13. The source for the technetium-99 in these wells could be the WMA and/or one of the liquid discharge facilities or both (PNNL-16346). Technetium-99 is also found at levels above the drinking water standard in wells south and west of the WMA (Figure 2-12). Technetium-99 in these wells is thought to be drawn to the wells from beneath the TX and TY tank farms by extraction from the 200-ZP-1 pump-and-treat. Wells 299-W15-44 and 299-W15-765 were put into service as extraction wells in 2005 and the technetium concentration began to increase in these wells shortly thereafter (PNNL-16346).

Iodine-129 was detected in two wells at WMA TX-TY during FY 2006. The highest iodine-129 concentration measured during this period was 42.7 pCi/L in well 299-W14-13; the average concentration in this well was 33 pCi/L. Iodine-129 was also detected in well 299-W14-15 with a concentration of 3.49 pCi/L.

Groundwater flow direction varies beneath WMA TX-TY due to influences from the pump-and-treat operation. In the north part of the area, groundwater flow is changing from eastward to westward due to the recently converted extraction wells. South of the WMA, groundwater flow direction is toward the extraction wells located south or southwest of the WMA (PNNL-16346).

Figure 2-9. Vertical Distribution of Moisture in Selected Boreholes within the TX Tank Farm.

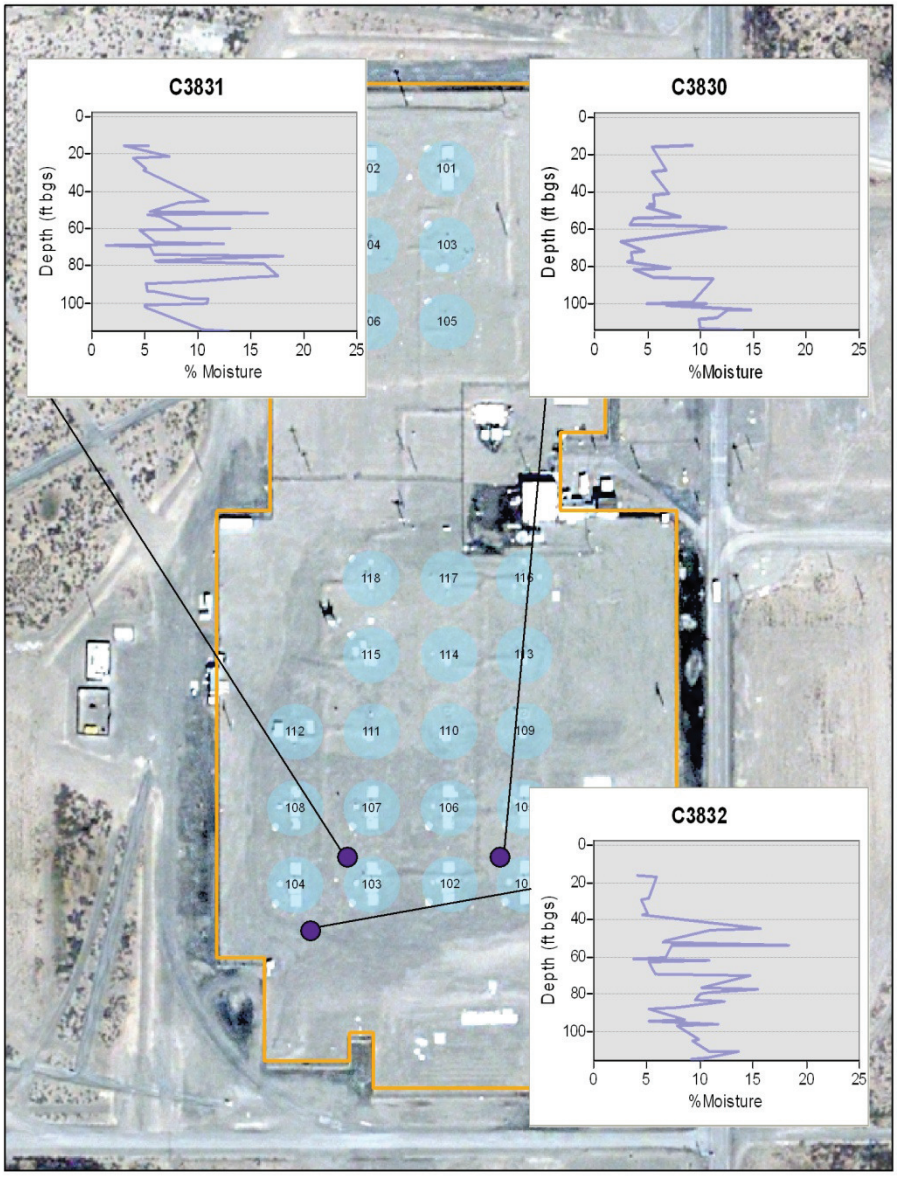

Source: PNNL-14594, 2004, *Characterization of Vadose Zone Sediments Below the TX Tank Farm: Boreholes C3830, C3831, C3832 and RCRA Borehole 299-W10-27*, Pacific Northwest National Laboratory, Richland, Washington.

Figure 2-10. Vertical Distribution of Nitrate and Sulfate from Selected Boreholes within the TX Tank Farm.

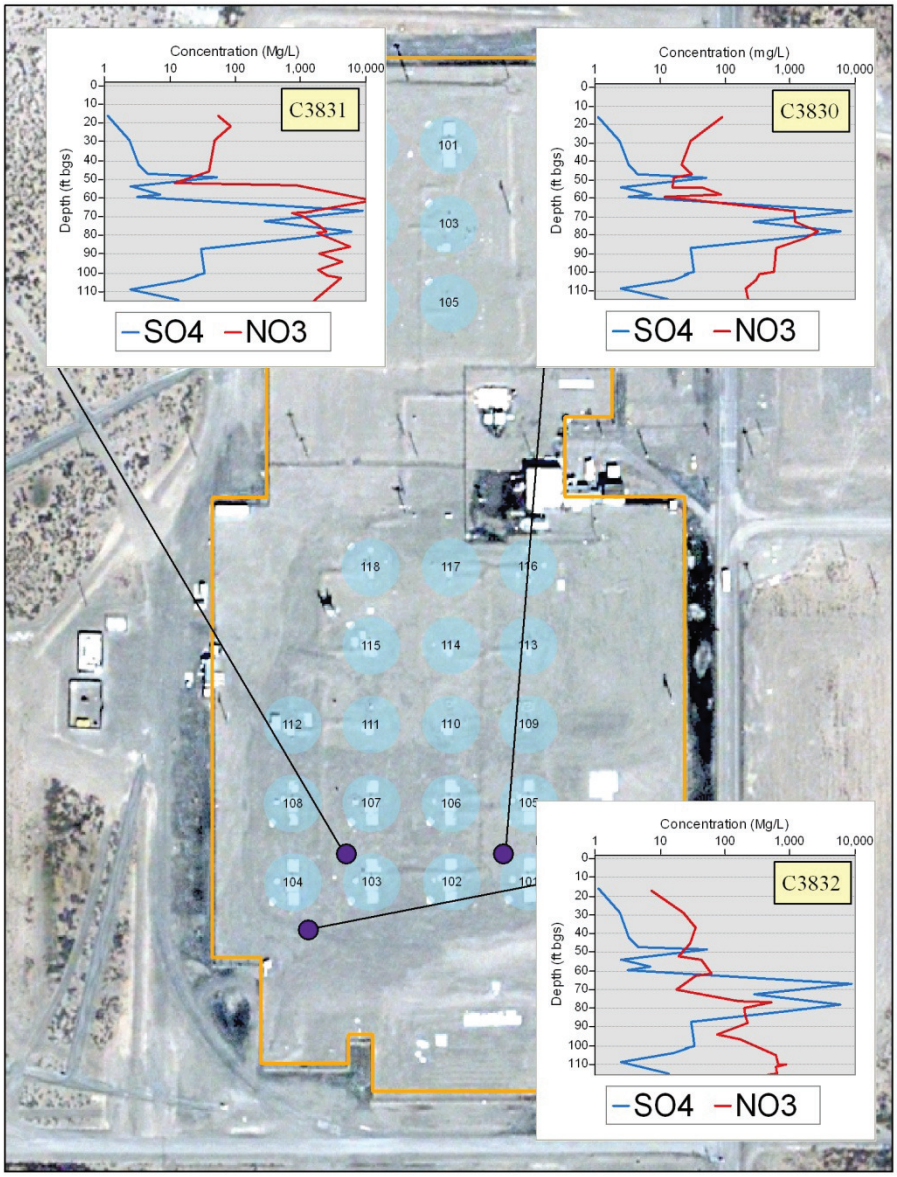

Source: PNNL-14594, 2004, *Characterization of Vadose Zone Sediments Below the TX Tank Farm: Boreholes C3830, C3831, C3832 and RCRA Borehole 299-W10-27*, Pacific Northwest National Laboratory, Richland, Washington.

Figure 2-11. Average Nitrate Concentrations in Central and North 200 West Area, Upper Part of Unconfined Aquifer.

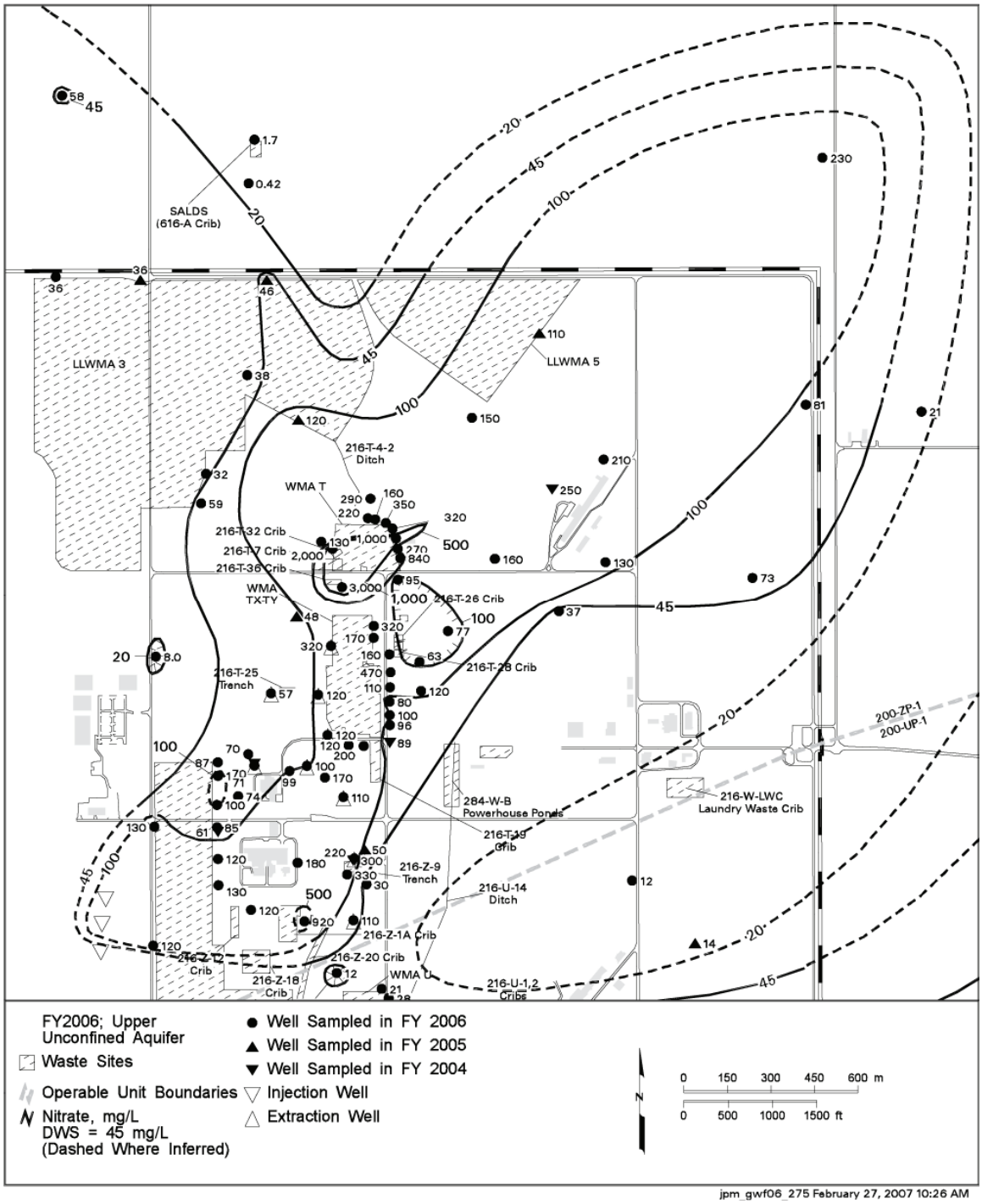

Source: PNNL-16346, 2007, *Hanford Site Groundwater Monitoring for Fiscal Year 2006*, Pacific Northwest National Laboratory, Richland, Washington.

Figure 2-12. Average Technetium-99 Concentrations in North 200 West Area, Upper Part of Unconfined Aquifer.

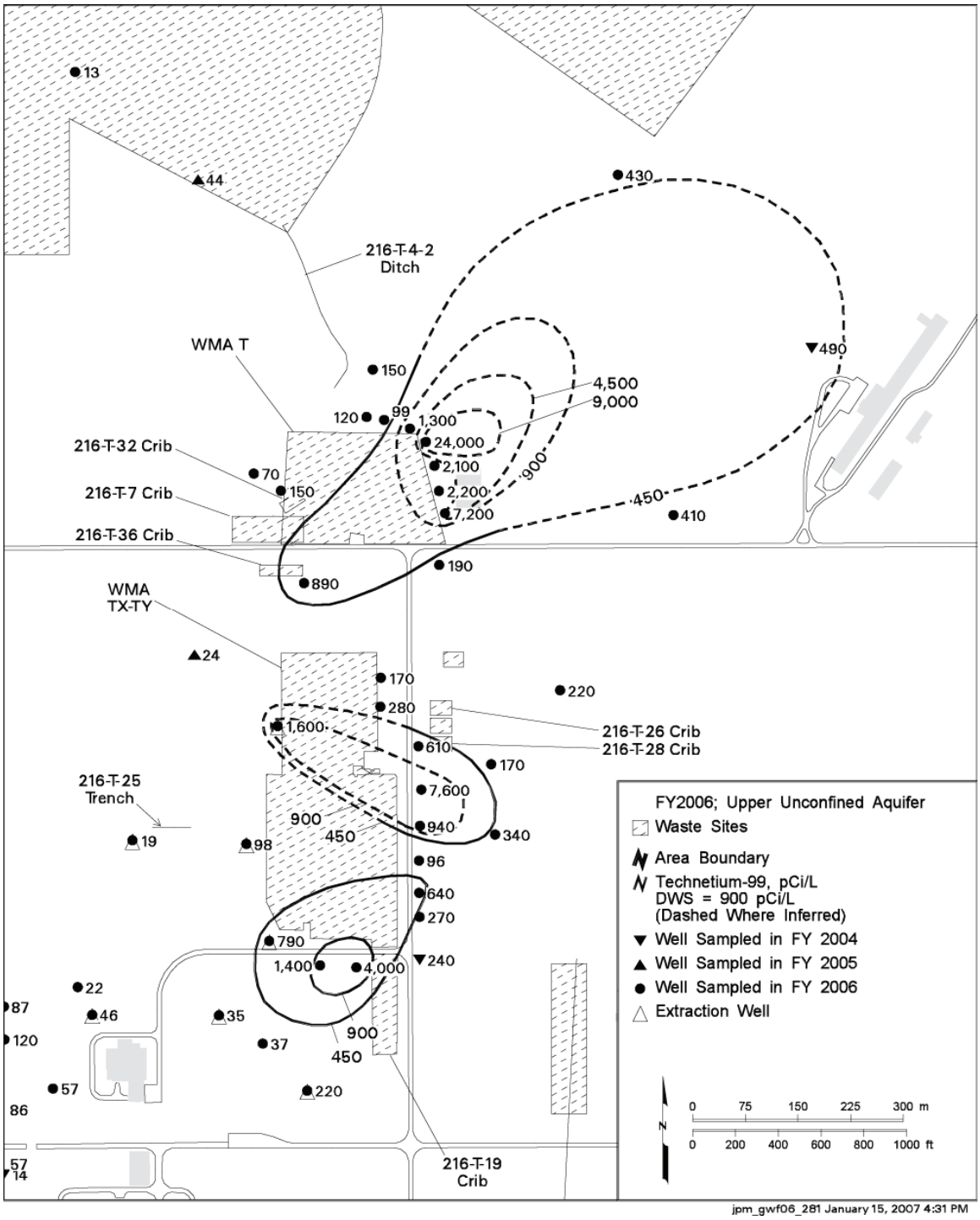

Source: PNNL-16346, 2007, *Hanford Site Groundwater Monitoring for Fiscal Year 2006*, Pacific Northwest National Laboratory, Richland, Washington.

This page intentionally left blank.

3.0 QUALITY ASSURANCE

Collection and analysis of SGE data are performed under a project-specific quality assurance plan using a graded approach that conforms to applicable requirements from Columbia Energy quality assurance procedures (*Quality Assurance Plan for Surface Geophysical Exploration Projects* [CEES-0333]). These procedures implement the requirements of *Quality Assurance Requirements for Nuclear Facility Applications* (ASME NQA-1) and *Quality Assurance* (DOE O 414.1C). Work not covered in the quality assurance plan will conform to accepted industry standards for SGE and sound engineering principles.

The quality assurance plan implements the criteria of DOE O 414.1C and the following requirements from ASME NQA-1:

- Organization (Requirement 1)
- Quality Assurance Program (Requirement 2)
- Instructions, Procedures, and Drawings (Requirement 5)
- Document Control (Requirement 6)
- Corrective Action (Requirement 16)
- Quality Assurance Records (Requirement 17).

Columbia Energy and hydroGEOPHYSICS, Inc. collect data using designed systems or off-the-shelf commercially available hardware. Designed systems conform to applicable requirements in approved procedures that address design, design analysis, design verification, and engineering drawing.

A project specific software management plan, *Software Management Plan for Surface Geophysical Exploration Projects* (CEES-0338), was prepared to implement a graded approach to software management in accordance with the following requirements documents:

- "Quality Assurance Requirements for Computer Software for Nuclear Facility Applications" (ASME NQA-1, Subpart 2.7)
- CEES-0333
- *Software Engineering* (CE-ES-3.5)
- *High Resolution Resistivity Characterization of Single Shell Tank Farm Waste Management Areas* (Contract 28090)
- DOE O 414.1C.

3.1 DATA COLLECTION

The setup, operation, and maintenance of the SGE equipment used in collecting and analyzing resistivity data is described in *Surface Geophysical Exploration System Design Description* (CEES-0360). This document identifies the requirements for the hardware and software used for data collection and analysis and provides a rationale for the hardware and software selected for use.

Calibration requirements are described for hardware used to collect geophysical data. As an example, the manufacturer (Advanced Geosciences, Inc.) of the resistivity data acquisition instrument (SuperSting R8®) recommends a yearly calibration of internal calibration resistors. The calibration is performed at the manufacturer's facility and a certificate of calibration is provided. A copy of the calibration documentation, serial numbers, and expiration dates are maintained in project files.

In addition, daily inspection of the receiver calibration is performed onsite using the manufacturer-supplied calibration resistor test box. The supplied test box is connected to the SuperSting R8 before commencing the daily survey. A specific calibration test firmware is provided within the SuperSting and provides the operator with a pass/fail indication for each of the eight receiver channels. If any of the channels fail, a recalibration or repair is required.

3.2 DATA PROCESSING

Data processing is performed using a number of software packages. The requirements and responsibilities for the identification, evaluation, development, testing, and maintenance of quality-affecting software acquired, developed, or modified in support of the SGE efforts are defined in the CEES-0338.

® SuperSting R8 is a registered trademark of Advanced Geosciences, Inc.

4.0 RESULTS AND INTERPRETATIONS

This section presents the results and interpretations of analysis performed on resistivity data collected at the TX-TY Complex. The primary objective of this investigation was to map areas or regions of low resistivity in and around the TX-TY Complex (TX and TY tank farms and surrounding areas) using electrical resistivity methods.

The details of the SGE resistivity method and theoretical basis applied to this evaluation of the subsurface in the TX-TY Complex is provided in Appendix A of the RPP-34690 (*Surface Geophysical Exploration of the B, BX, and BY Tank Farms at the Hanford Site*).

The detailed logistics of collecting resistivity data at the TX-TY Complex, including the STS, WTS and WTW surveys, are presented in Appendix A. The methodologies used to process and export resistivity data are presented in Appendix B. The general process used for database archival and retrieval of raw resistivity data is provided in Appendix C. Appendix D provides a summary of the background geophysical properties contained in the selected EM, MAG, and GPR reports for the TX-TY Complex that were used to provide a basis for the interpretation of resistivity inversion models in close proximity to buried infrastructure.

This section presents analysis results and interpretation of resistivity data for the four wastes site areas outside the TX and TY tank farms in Sections 4.1 through 4.4 Discussion relevant to the areas inside the tank farm areas follow in Section 4.5. The results and interpretations for these subsections begin with discussion of the 2D resistivity modeling results and then are followed by discussion of 3D modeling results. Discussion of modeling analyses of the STS resistivity data collected for the overall TX-TY Complex follow in Section 4.6.

The Res2DINV (Geotomo, Ltd.) inversion modeling software was selected for processing of all individual resistivity STS survey lines collected within the TX-TY Complex area. Res2DINV was chosen over EarthImager2D (Advanced Geosciences, Inc.) in order to make use of the least squares deconvolution method (Loke, 1995). This method improves inversion model resolution by reducing distortions related to highly conductive materials buried near electrodes, such as metallic pipelines or other infrastructure. A discussion of the inversion parameters and optimization routines in this software are given in Section B.3.2 of Appendix B. Appendix E show plots of all 2D inversion results for each STS survey line collected as part of the TX-TY survey. In addition to the plots shown in Appendix E, color-contoured HRR (raw apparent resistivity) sections are plotted and used for quality control and as an aid in the interpretation of the results.

Advanced Geosciences, Inc. EarthImager3DCL was selected for all 3D resistivity inversion models. EarthImager 3DCL was first developed during the B Complex SGE effort in order to effectively process very large and complex 3D resistivity inversion models which were not previously possible using commercial software (RPP-34690, *Surface Geophysical Exploration of the B, BX, and BY Tank Farms at the Hanford Site*).

A resistivity color scale was optimized for the TX-TY Complex inversion model results in order to maximize the viewer's differentiation of color and associated resistivity values. The color

scale consists of a spectrum that is similar to a rainbow with colder shades (blue) representing low resistivity values that trend to hotter colors (red) to represent higher resistivity values. The method used to optimize the TX-TY Complex resistivity color scale is described in APPENDIX B.

Based on the results presented in this section, the primary objective was met through a combination of 2D and 3D inversion models that utilize STS, WTW and WTS electrode types and geometries. The results from the EM-MAG infrastructure interpretations, GPR mapping and GIS infrastructure mapping efforts were used to interpret and isolate the effects of infrastructure on the resistivity inversion model results.

4.1 TX TRENCHES (216-T-21 THROUGH 216-T-25) AREA

The area surrounding the TX trenches (216-T-21 through 216-T-25) was the first focus for STS 2D and 3D resistivity inversion analysis. The TX trench area is covered by STS survey lines 1E through 6E and portions of 7E through 9E and 5N through 17N (APPENDIX C) as well as the 3D STS inversion model domain referred to as TXTY-STS1iii (See Figure 4-1.). In general, no significant buried infrastructure exists in this area as interpreted from the EM and Mag Report (RPP-36893) and maps of known infrastructure (Figure 2-7).

Figure 4-1. STS Survey Lines and Model Domain Associated with TX Trench Area.

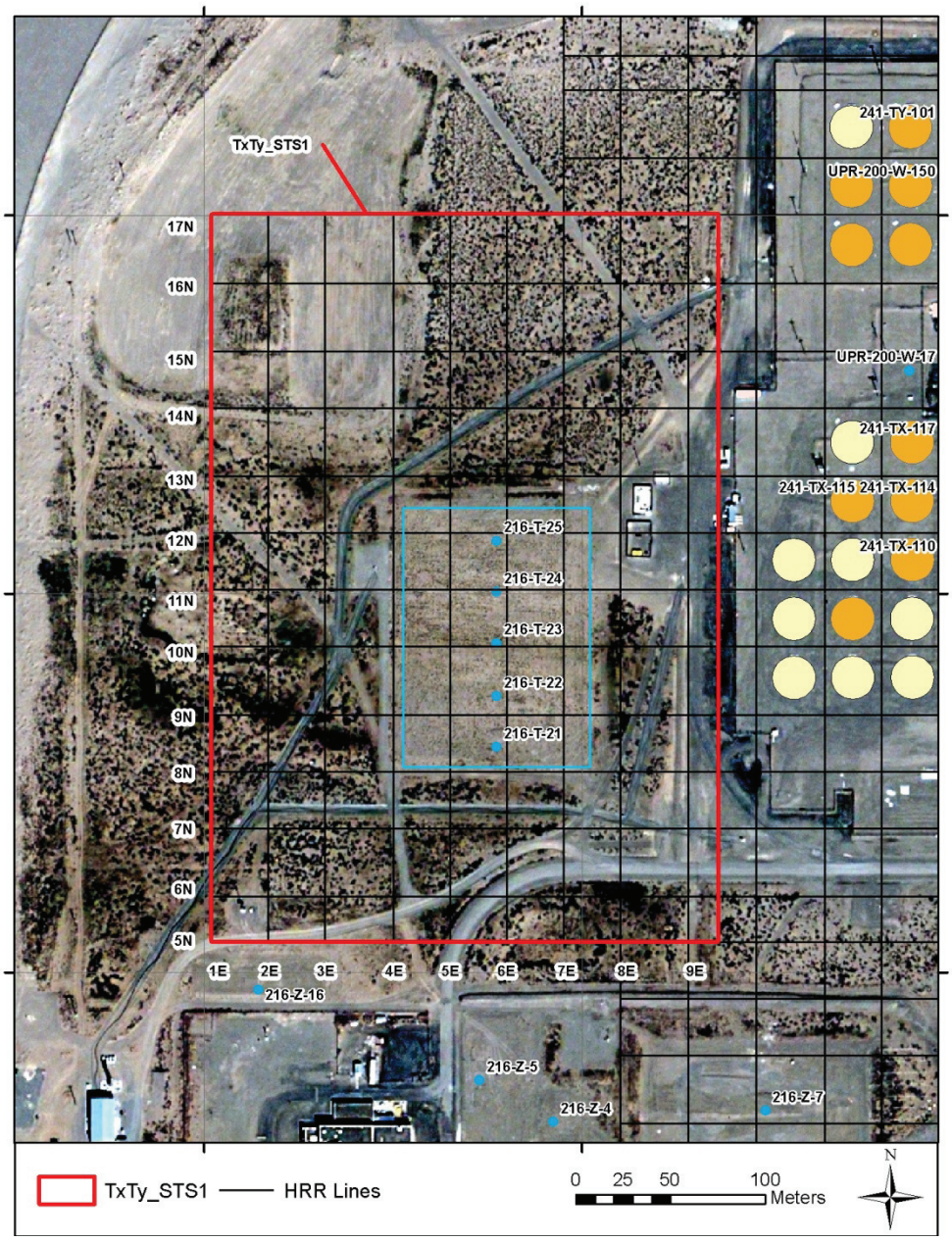

4.1.1 2D Inversion Model Results

Review of resistivity estimated with 2D inversion models of STS survey lines in the TX trench area show a uniformly resistive upper 15m model layer that ranges in value from 300 to 5,000 ohm-m. This range of resistivity is consistent with background resistivity values measured at other SGE sites (RPP-34690, *Surface Geophysical Exploration of the B, BX, and BY Tank Farms at the Hanford Site and* RPP-RPT-28955, *Surface Geophysical Exploration of T Tank Farm*). The upper model layer values fall off relatively smoothly with depth towards the local water table at approximately 260 feet (80 meters).

The primary resistivity target in this region is a low (1-30 ohm-m) resistivity region that lies directly below the 216-T-21 to 216-T-25 trenches. Results for 2D resistivity models of survey lines 5E, 6E, 11N and 10N provide examples that define the depth and extent of this target by bisecting the center at right angles. The north-south extent of this target is defined by the blue contours(1-35 ohm-m) at Station Meters 85 to 215 in Line 5E (Figure 4-2) and Station Meters 95-230 in Line 6E (Figure 4-3). The east-west extent is defined by the blue contours (1 to 35 ohm-m) at Station Meters 140-195 in Line 10N (Figure 4-4) and Station Meters 120-180 in Line 11N (Figure 4-5). No significant buried infrastructure is annotated at the locations of the 216-T-21 to 25 trenches in these figures.

Figure 4-2. 2D Inversion Model Results - Line 5E.

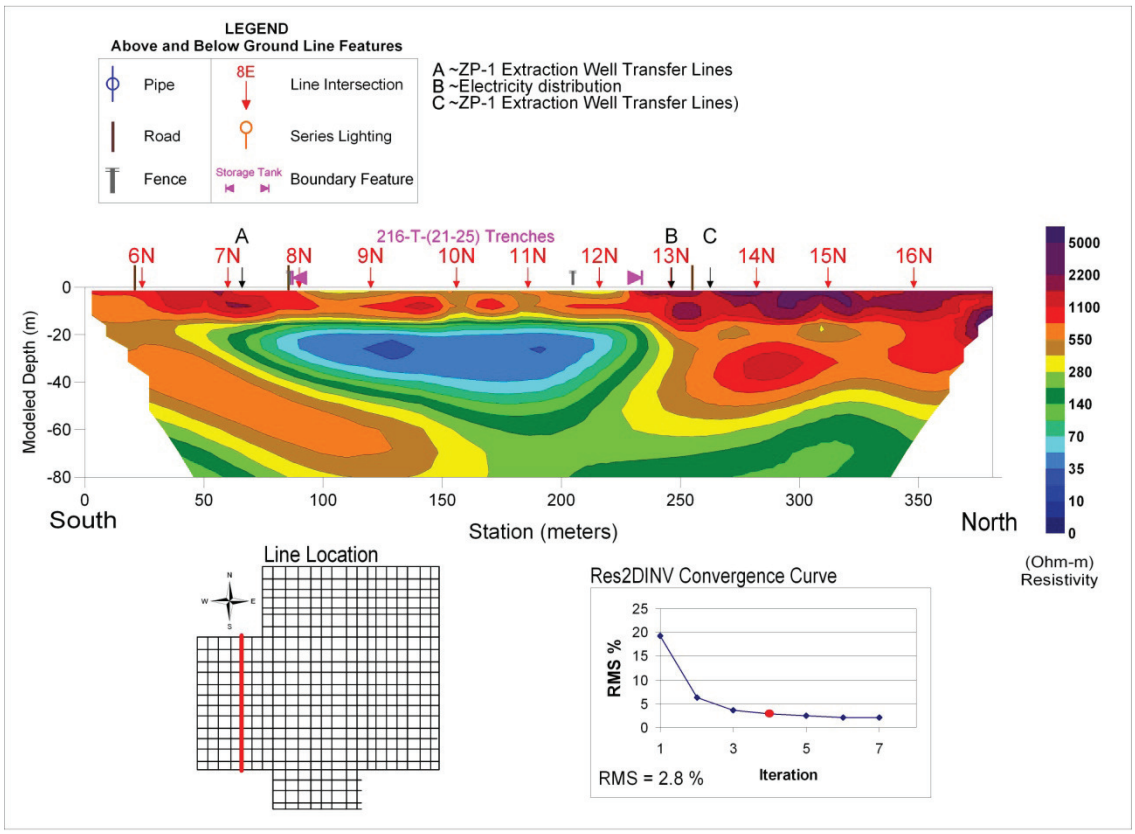

Figure 4-3. 2D Inversion Model Results - Line 6E.

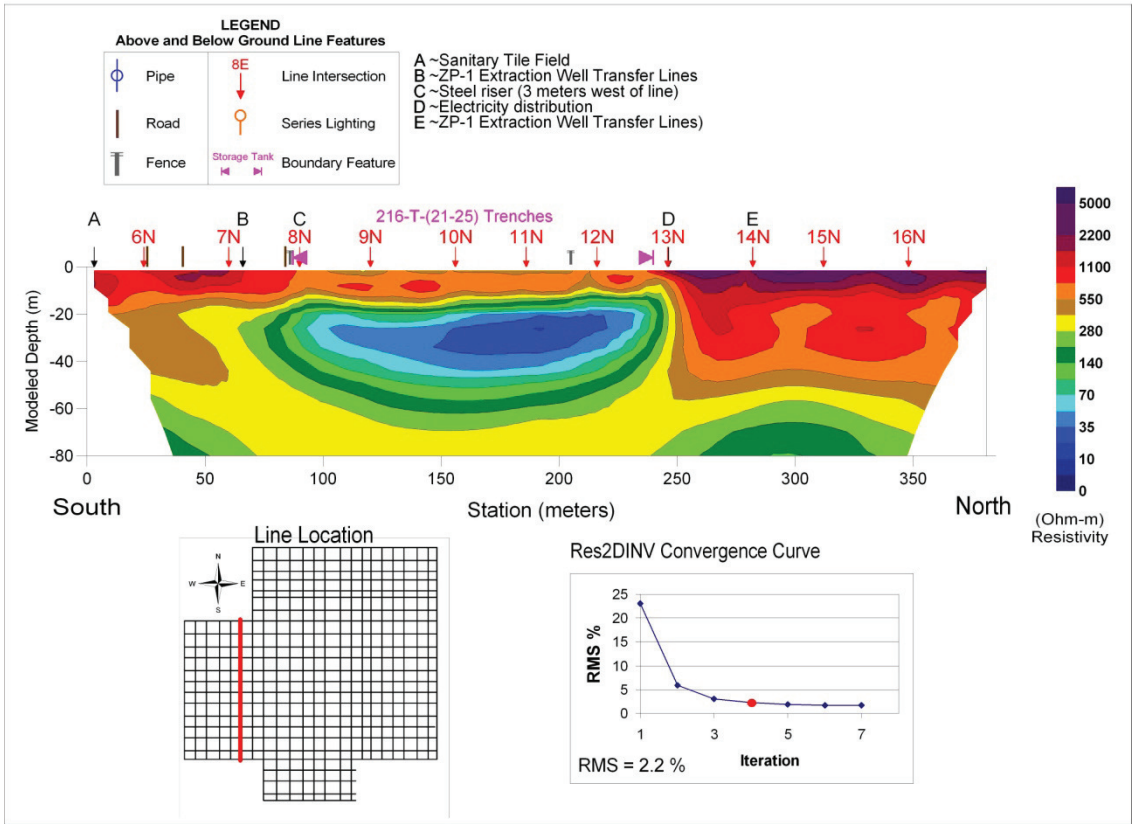

Figure 4-4. 2D Inversion Model Results - Line 10N.

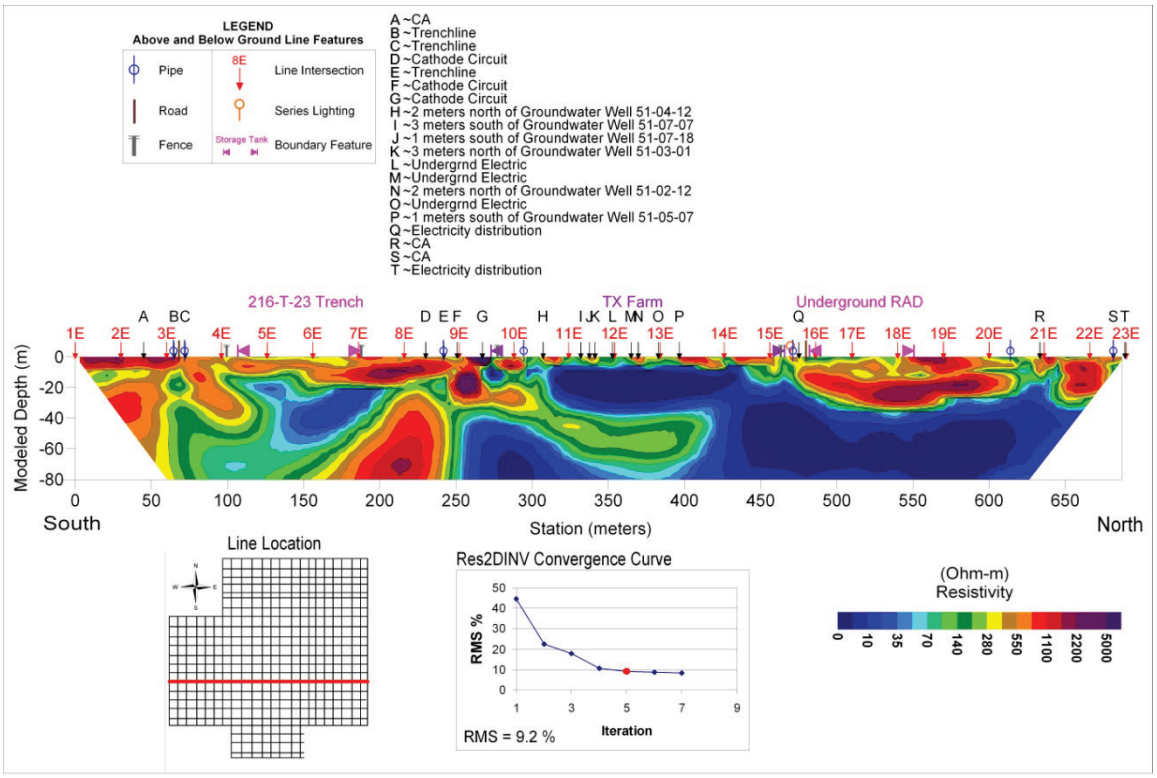

Figure 4-5. 2D Inversion Model Results - Line 11N.

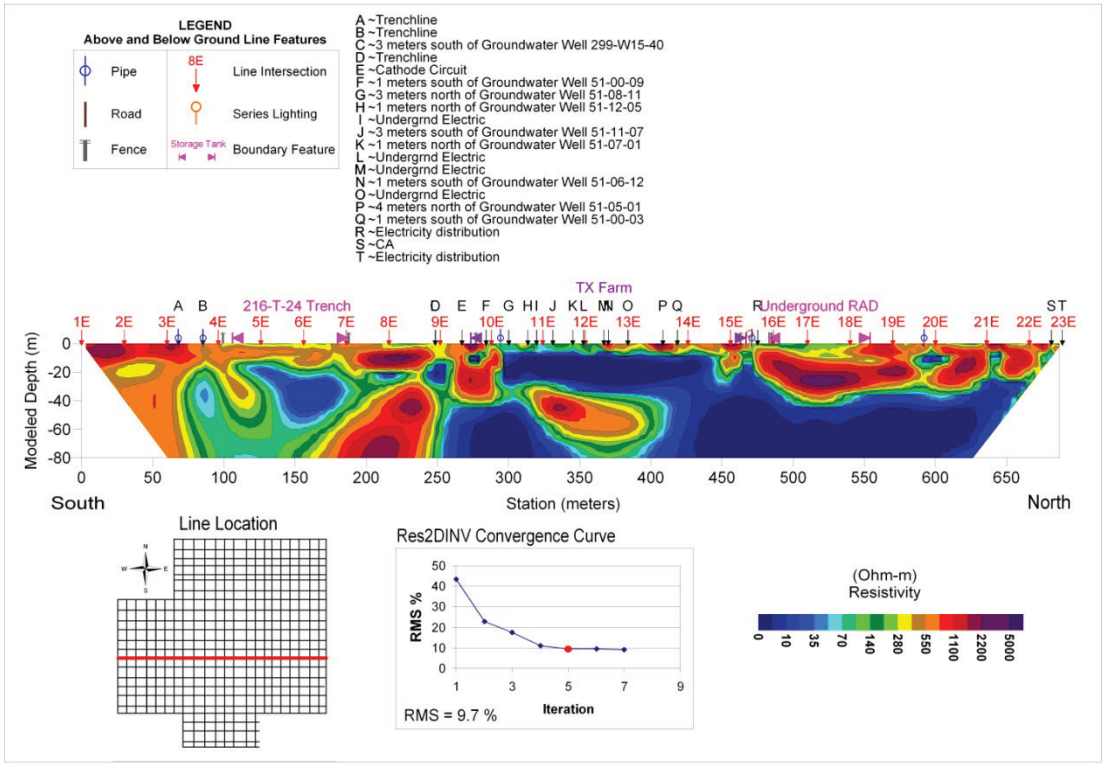

4.1.2 3D Inversion Model Results

This section describes the results of the 3D inversion model analysis of resistivity data collected over the TX trenches area at the TX-TY Complex.

A compilation of all orthogonal resistivity lines within the red polygon model domain in Figure 4-1 was used for a 3D STS inversion model called TxTy_STS1iii. The resistivity data for this model were collected at 6 meters electrode spacing and 30 meter orthogonal line separations and inverted using EarthImager3DCL v1.1.3. The model runtimes, domain description and convergence statistics are shown in Table 4-1. A plot of model convergence is provided in Figure 4-6.

A review of modeling results indicates that the location and aerial extent of the primary low resistivity target is centered at the 216-T-21 to 216-T-25 trenches (Figures 4-7 through 4-10). The primary low resistivity target falls within the range of 1-40 ohm-m and is displayed as an iso-volume in semi-transparent red, with a secondary target of 40-75 ohm-m in semi-transparent green. This target lies directly below the 216-T-21 to 216-T-25 trenches at 20 meter depth and extends to approximately 60 meter depth. The shape and position of this target is consistent with the 2D inversion model results for this area. Figure 4-11 shows 6 orthogonal slices through the 3D inversion model domain. Both the shape and position of the primary target as well as the background values that surround the target are visible in this view.

Table 4-1. Simulation Details and Statistics of 3D Model Domain TXTY-STS1iii.

Input File	TXTY-STS1iii
Inversion start date	00:55:35 2008-03-10
Inversion end date	10:09:13 2008-03-10
Northing range (meter)	384
Easting range (meter)	276
Easting minimum	566,404
Northing minimum	136,016
Easting maximum	566,680
Northing maximum	136,400
Software version	EarthImager3DCL v1.1.3
Number of electrodes	1,020
Number of data points	22,287
Domain area (acres)	26.2
Number of domain nodes	382,470
Number of iterations	6
Root mean square of final iteration	4.66

Figure 4-6. TXTY-STS1iii Inversion Model Convergence Curve.

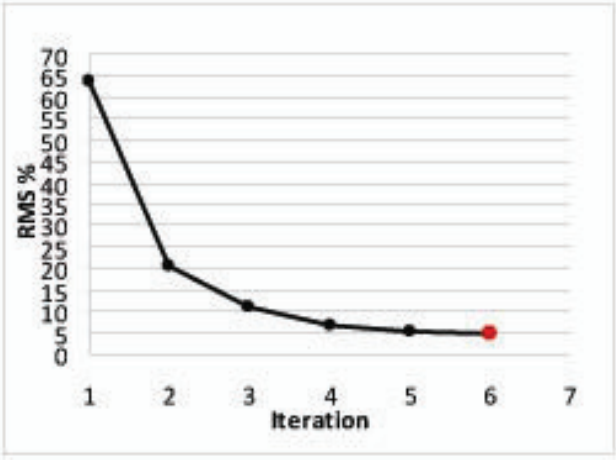

Figure 4-7. TxTy-TS1iii Inversion Model Results Showing 3D Plan View of Selected Resistivity Levels – TX Trench Area.

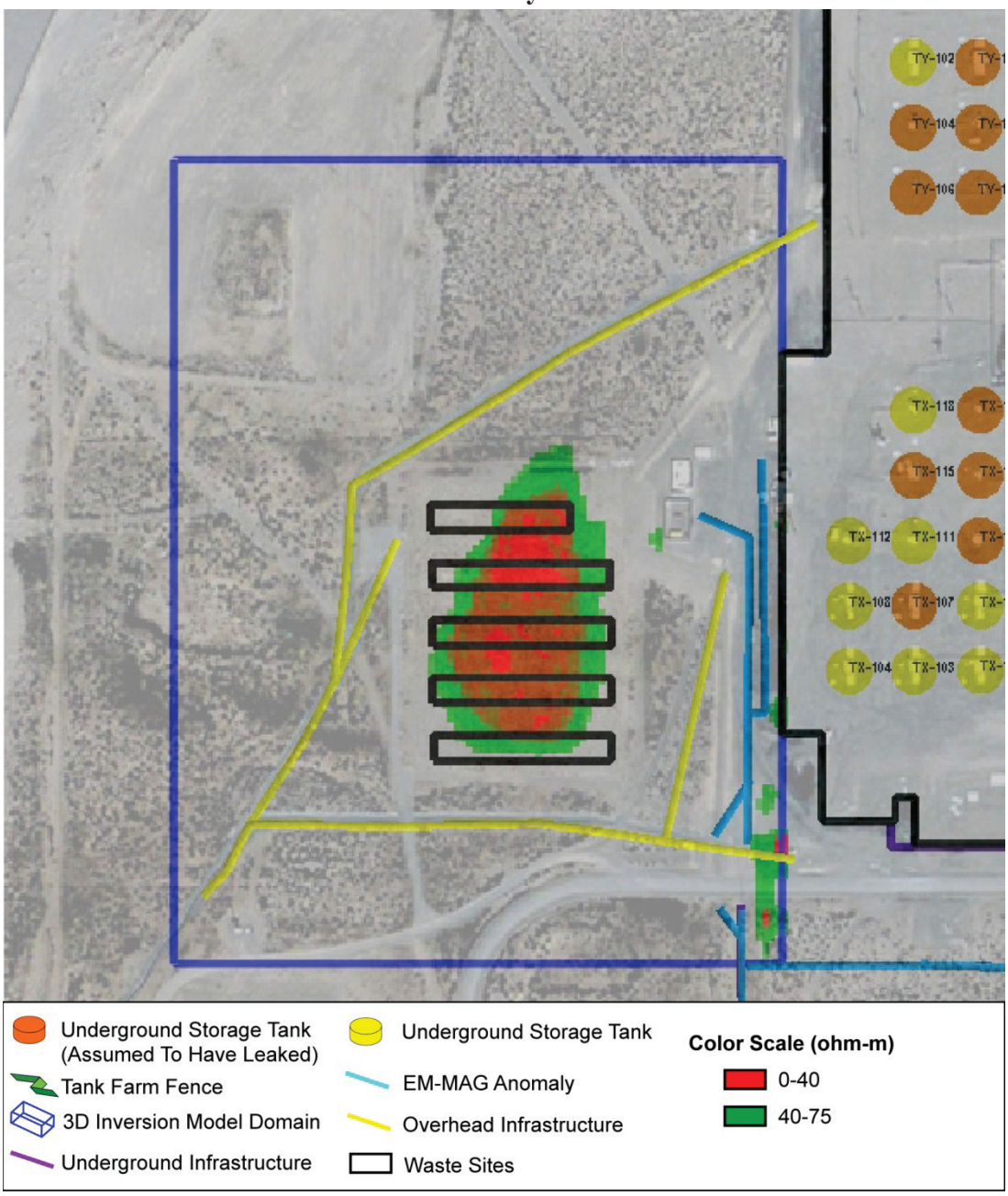

Figure 4-8. TXTY-STS1iii Inversion Model Results Showing 3D View from Southwest of Selected Resistivity Levels – TX Trench Area.

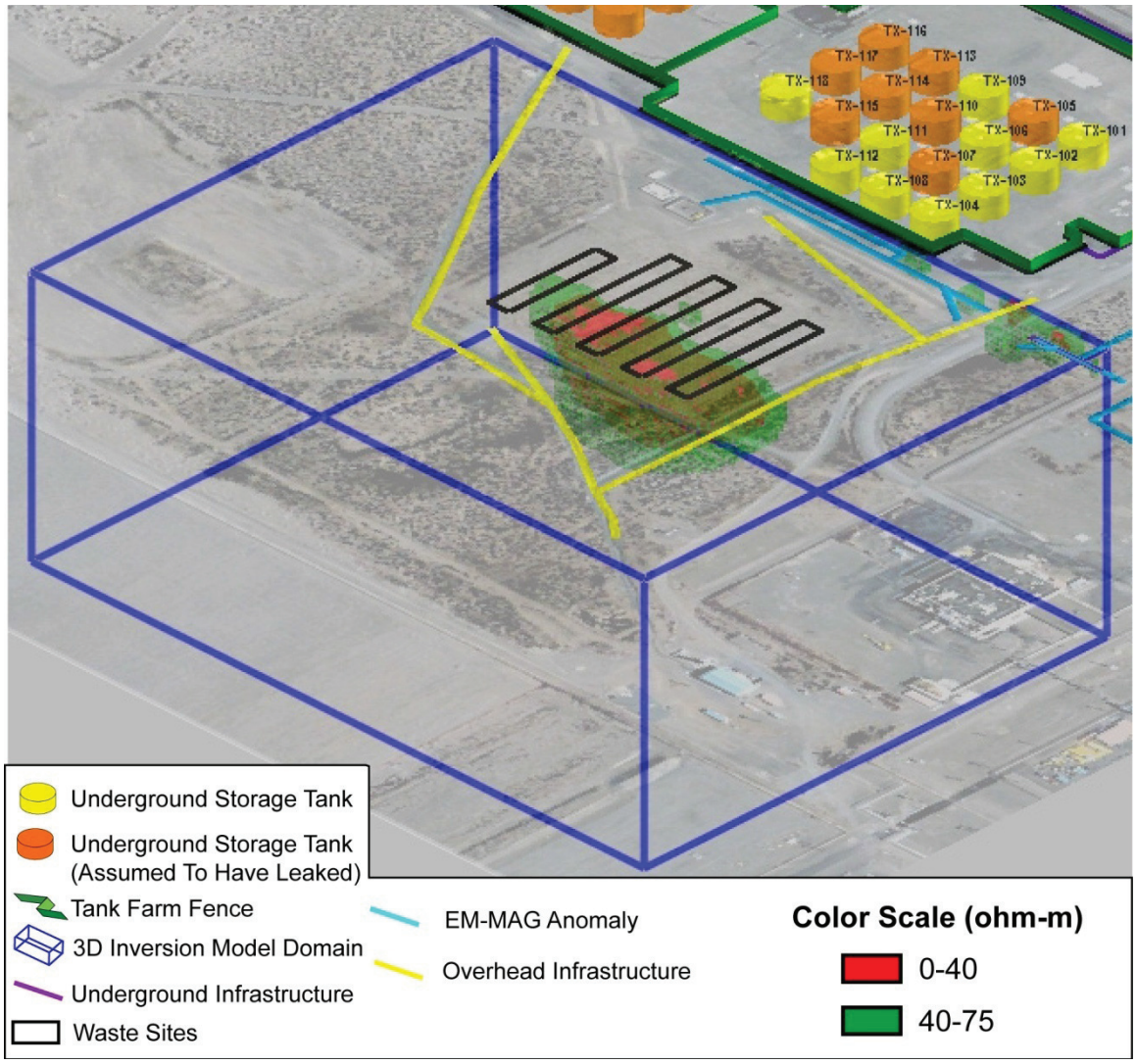

Figure 4-9. TXTY-STS1iii Inversion Model Results Showing 3D View from the Southeast of Selected Resistivity Levels – TX Trench Area.

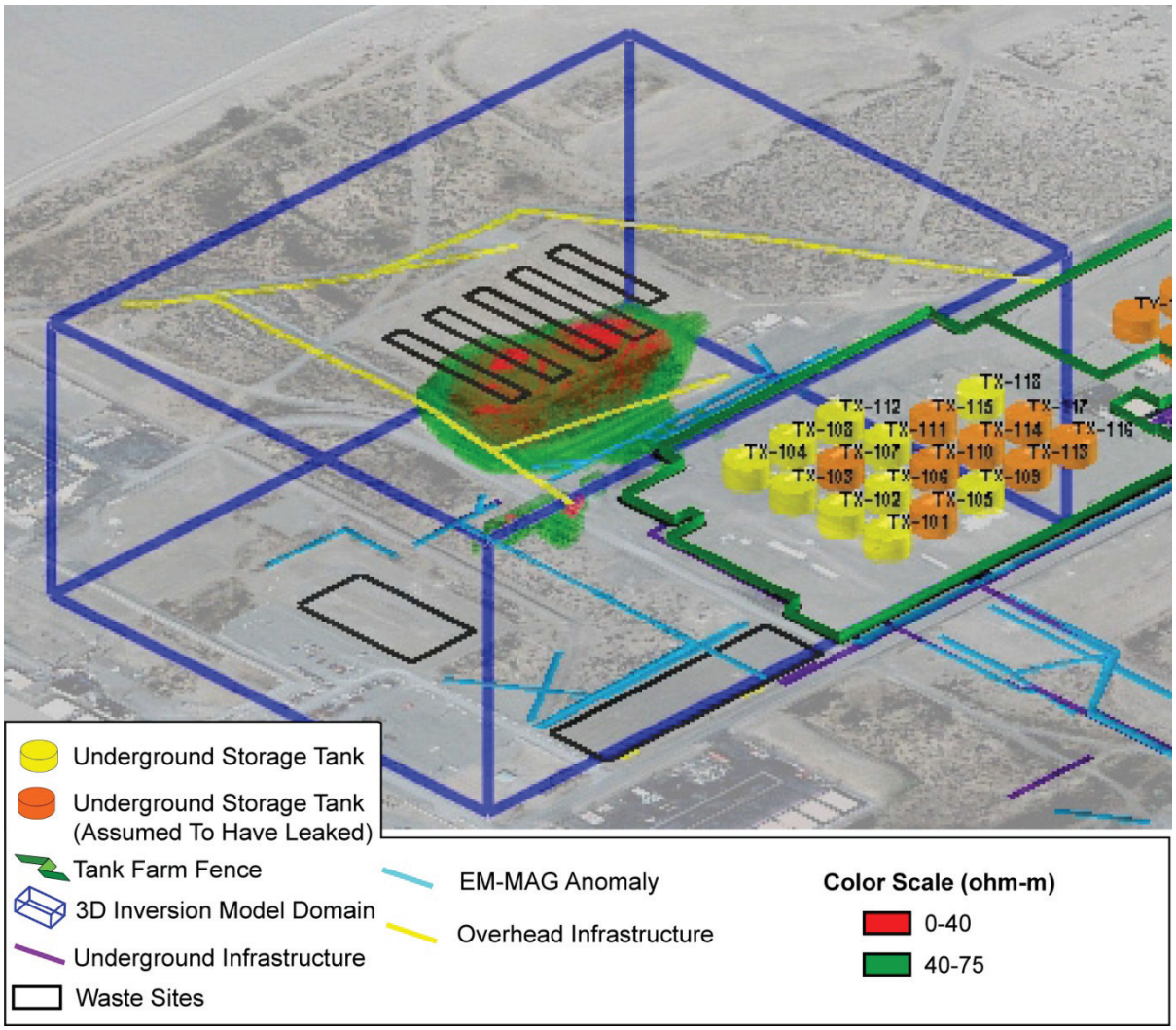

Figure 4-10. TXTY-STS1iii Inversion Model Results Showing 3D View from East of Selected Resistivity Levels – TX Trench Area.

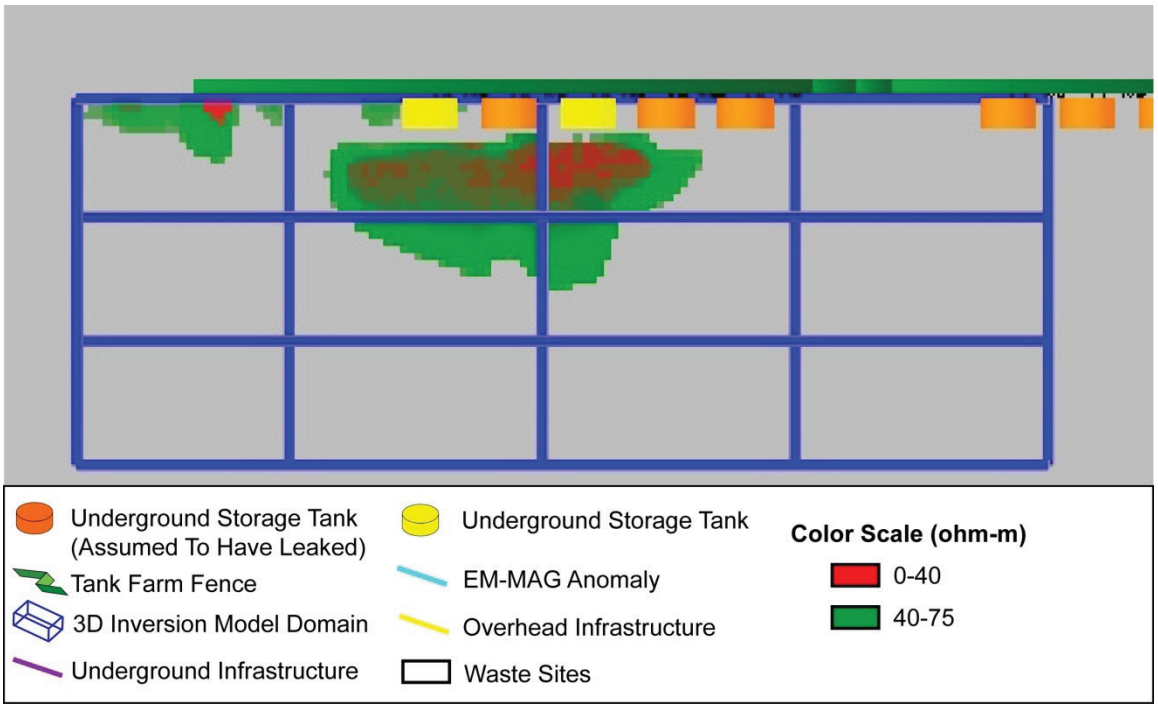

Figure 4-11. TXTY-STS1iii Inversion Model Results Showing 3D View from Above and South West of 2D Slices Through the Primary Target and Background Levels - TX Trench Area.

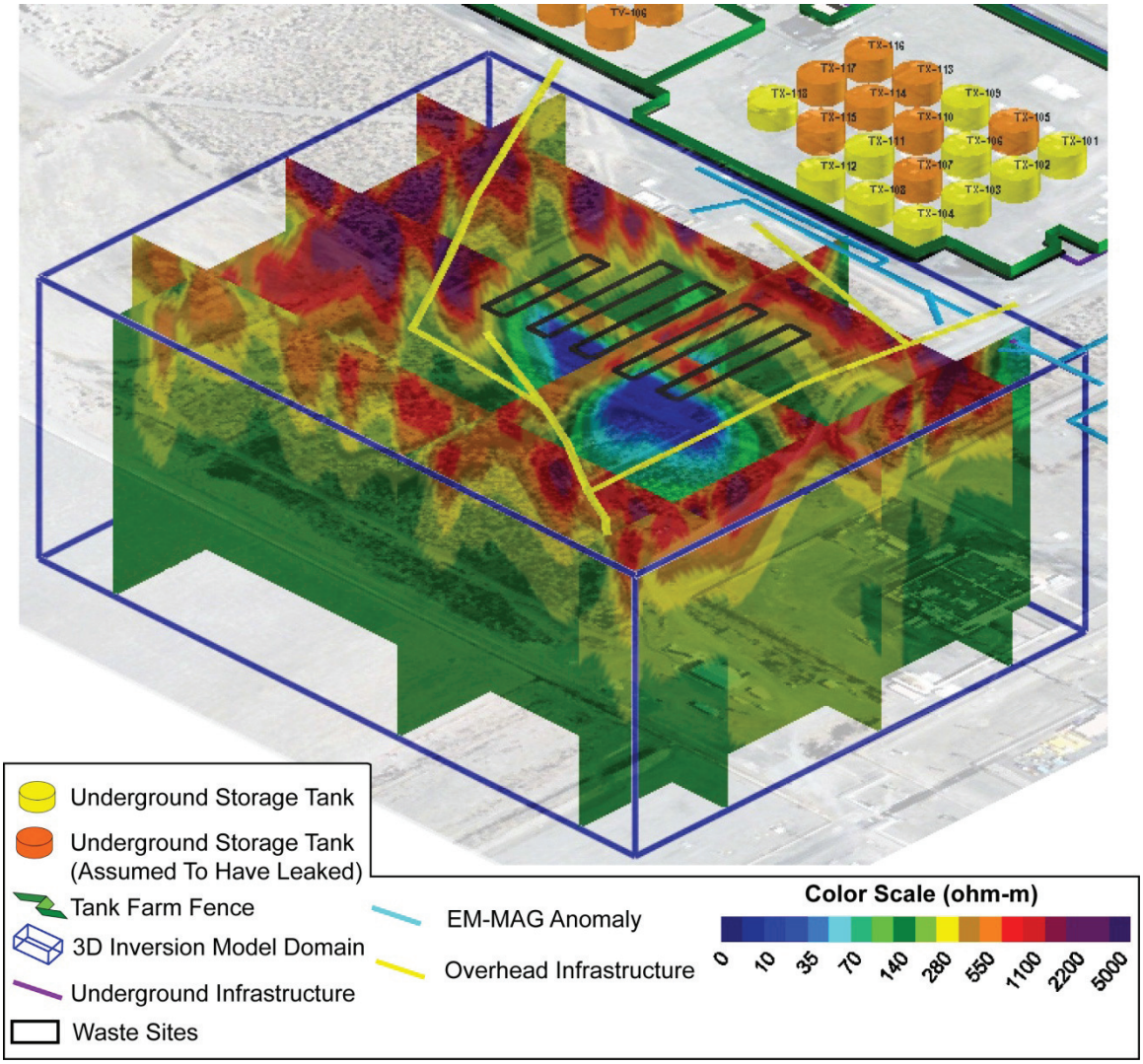

4.2 216-T-19 CRIB AND TILE FIELD AREA

The 216-T-19 crib and tile field and 216-Z-7 crib shown in Figure 4-12 is covered by STS survey lines 1N through 6N and portions of 8E through 15E (Appendix C) as well as the 3D STS inversion model domain referred to as TXTY-STS5 (see Figure 4-12). This area contains significant buried infrastructure as interpreted from the EM and Mag Report (RPP-36893) and maps of known infrastructure (Figure 2-8). The following interpretations of 2D resistivity inversion models were assisted by annotations of the position and type of buried infrastructure present for each model domain.

4.2.1 2D Inversion Model Results

A review of 2D STS resistivity inversion models surrounding the 216-T-19 trench and 216-Z-7 crib area reveals a surficial background resistivity layer in areas that are not in close proximity to buried metallic infrastructure. In areas free of infrastructure, these models show a uniformly resistive background layer in the upper 20m that ranges in value from 300 to 5000 ohm-m. Background values are well defined at station meters 100-250 in Line 2N (Figure 4-13) and 0-300 in Line 3N (Figure 4-14). The range of resistivity in the background layer is consistent with background resistivity values measured over the TX trenches (216-T-21 through 216-T-25) as well as other SGE sites (RPP-34690, *Surface Geophysical Exploration of the B, BX, and BY Tank Farms at the Hanford Site* and RPP-RPT-28955, *Surface Geophysical Exploration of T Tank Farm*).

Deeper model layers surrounding 216-T-19 trench and 216-Z-7 crib area reveal targets that are dominated by buried surface infrastructure, such as pipelines and groundwater wells that are in close proximity to the surface electrodes. These resistivity targets dominate the lower model layers and obscure the expected gradual lowering of resistivity as depths approach the local water table at approximately 80m. Even though buried infrastructure dominates the low resistivity targets in these models, several targets located directly beneath waste sites cannot be accounted for by known infrastructure alone.

4.2.1.1 216-T-19 Tile Field Area. A review of the 2D resistivity inversion models which cross the 216-T-19 tile field area reveals a primary low resistivity target that runs for much of the length of the 216-T-19 tile field in the north-south direction. This low resistivity target and the surrounding background values are well defined in Line 14E (Figure 4-15). Background high resistivity values (300-5000 ohm-m) are shown in Line 14E between station 0 and 50 m in the upper 20m model layers before the primary low resistivity (1-70 ohm-m) target starts between station 50 to 170 m and from 0 to 20m model depth (Figure 4-15). Line 15E shows two low resistivity targets as blue (1-70 ohm-m) discrete targets beneath the 216-T-19 tile field area between station 36 and 50 m and a depth of 30 m and again between station 95 and 125 m at a model depth of 35m. The target between station 36 and 50m in Line 15E has a similar shape and position to the primary low resistivity target in Line 14E. Infrastructure, which may influence this target, is not annotated in this portion of Line 15E. The second target between station 95 and 125 m in Line 15E has a much higher gradient and a lower over all resistivity value when compared to the target between station 36 and 50 m. The close proximity of groundwater well 299-W14-51 may influence the shape and lower resistivity of this second target.

Background values are indicated in Lines 2N and 3N between station 210 and 240 m in the upper 20-m model layers and directly below the tile field (Figures 4-13 and 4-14). Three additional low resistivity targets are indicated by the east-west trending Lines 2N and 3N which cross over 3 pipelines and the tile field (Figure 4-12). The low resistivity target in Line 3N is shown as a blue discrete volume (1-70 ohm-m) between station 158 and 205 m and 35 m model depth. It is unclear to what degree the low resistivity target in Line 2N between stations 30 and 200 m at a 25-m model depth is influenced by buried pipelines or other infrastructure (Figure 4-13) or the 216-T-19 crib and the 216-Z-7 crib.

4.2.1.2 216-Z-7 Crib Area. A review of 2D STS resistivity inversion models surrounding the 216-Z-7 crib area reveals a low resistivity target of 1-70 ohm-m centered beneath the crib

area. Results from Line 3N show this target between station 70 and 125 m and at a depth of 20 to 35 m (Figure 4-14). The size, shape and gradient of the resistivity values in this target are consistent with previous SGE low resistivity targets beneath liquid waste disposal sites where minimal infrastructure was present (RPP- RPP-34690 at B Complex; RPP-RPT-28955 at T Farm).

A review of previous SGE raw data showing low resistivity targets beneath liquid waste disposal sites with minimal infrastructure suggests that interference from the cathotic protection circuit and groundwater well L3875 annotated in Figure 4-14 is minimal for this particular line. Results from Line 2N show a similar low resistivity target (1-70 ohm-m) between station 60 and 80 m and between depths of 12-60 m (Figure 4-13). However, the low resistivity target in Line 2N has much sharper gradients and lower values than the target in Line 3N. The significantly lower resistivity values, sharper gradients and vertical shape of the target in Line 2N is most likely due to interference from the close proximity of steel-cased groundwater wells 299-W15-7 and 299-W15-64 (Figure 4-13).

Both Lines 9E and 10E run north-south across the 216-Z-7 crib area at the southern edge of the model domain (see Figures 4-17 and 4-18). Both of these models show only the upper background resistivity layers in detail because the electrode geometry at the line edges is too limited to allow for full exploration depth.

Figure 4-12. Model Domain of 216-T-19 Crib and Tile Field and 216-Z-7 Crib Area.

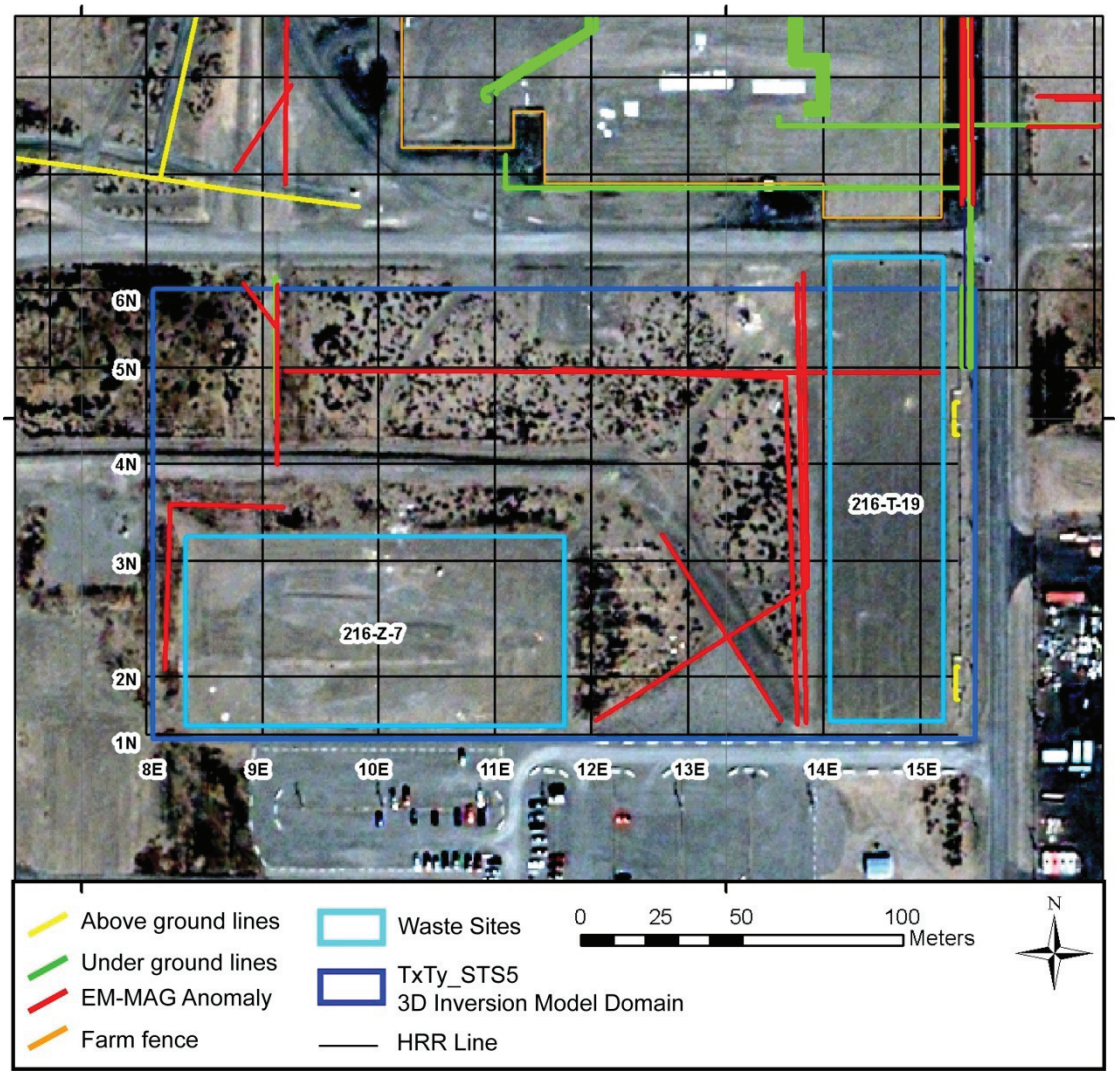

Figure 4-13. Model Results for 2D Inverse Model Domain of Resistivity Survey Line 2N.

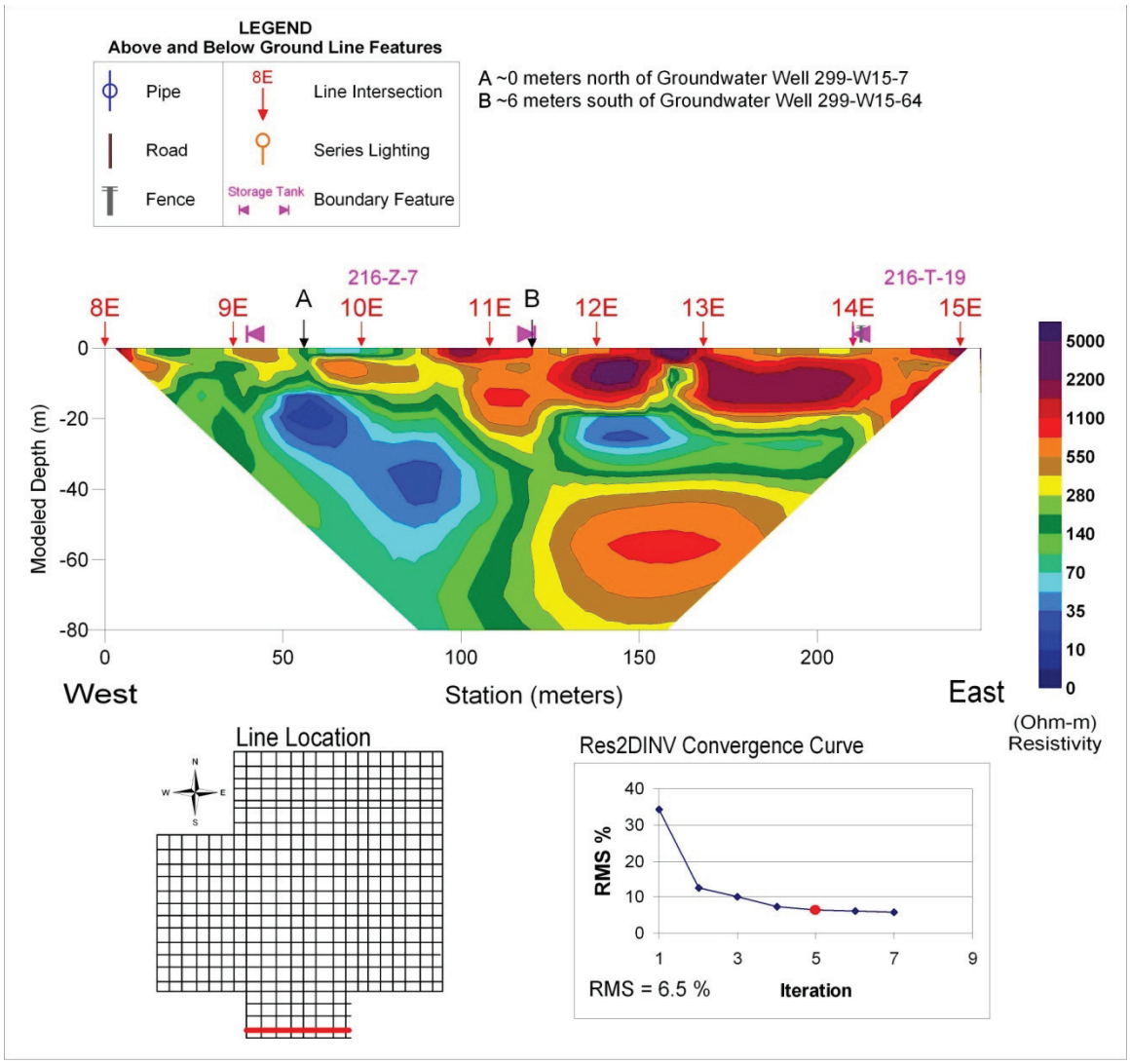

Figure 4-14. Model Results for 2D Inverse Model Domain of Resistivity Survey Line 3N.

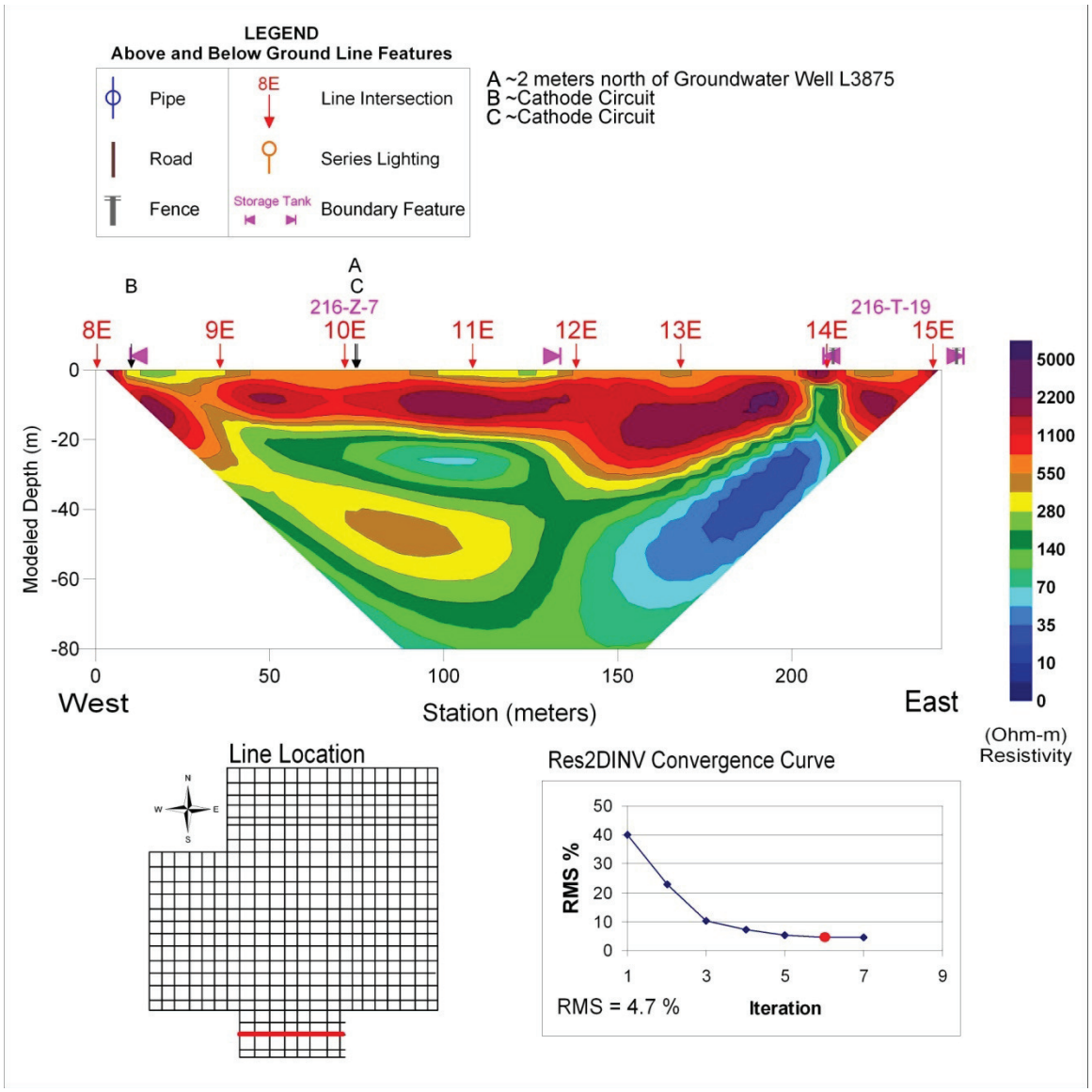

Figure 4-15. Model Results for 2D Inverse Model Domain of Resistivity Survey Line 14E.

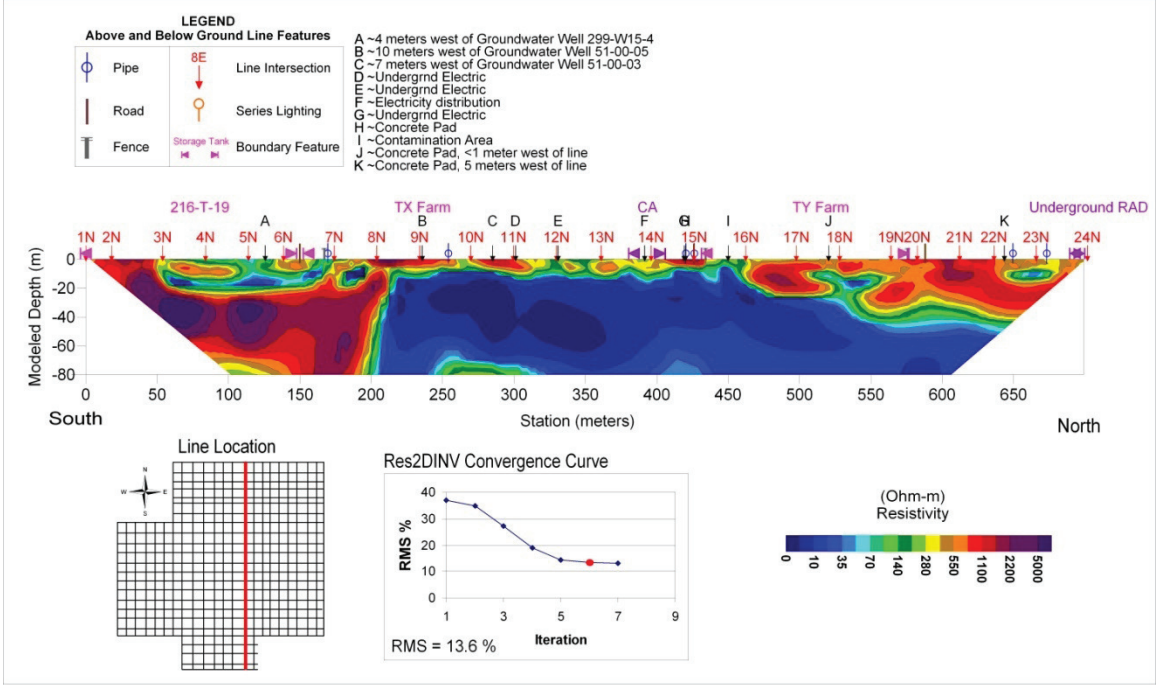

Figure 4-16. Model Results for 2D Inverse Model Domain of Resistivity Survey Line 15E.

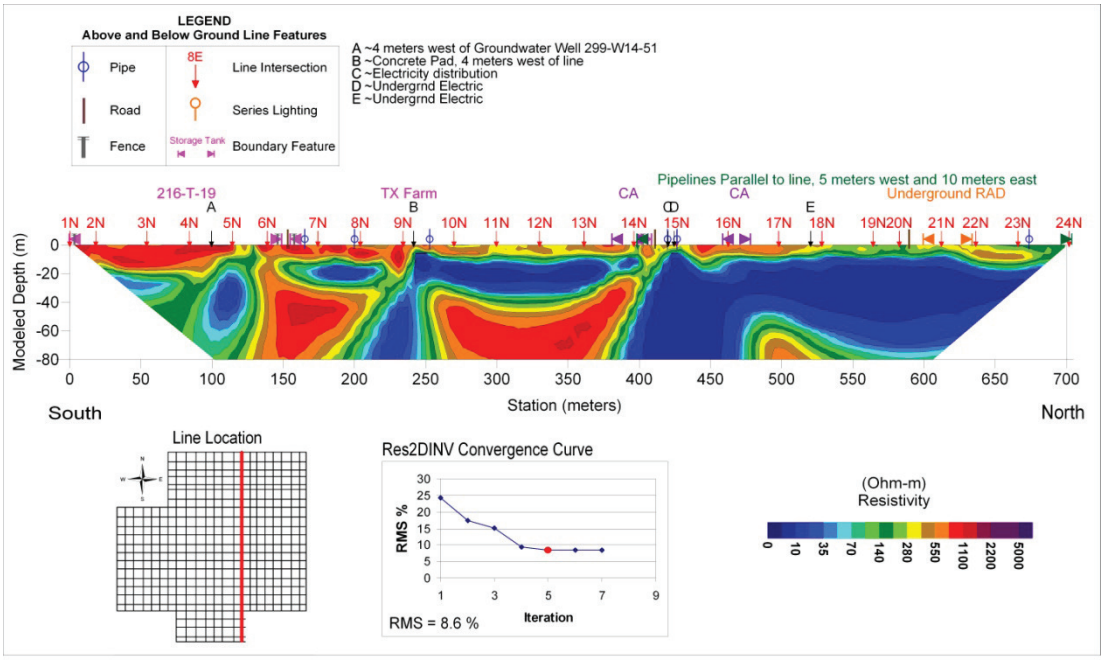

Figure 4-17. Model Results for 2D Inverse Model Domain of Resistivity Survey Line 9E.

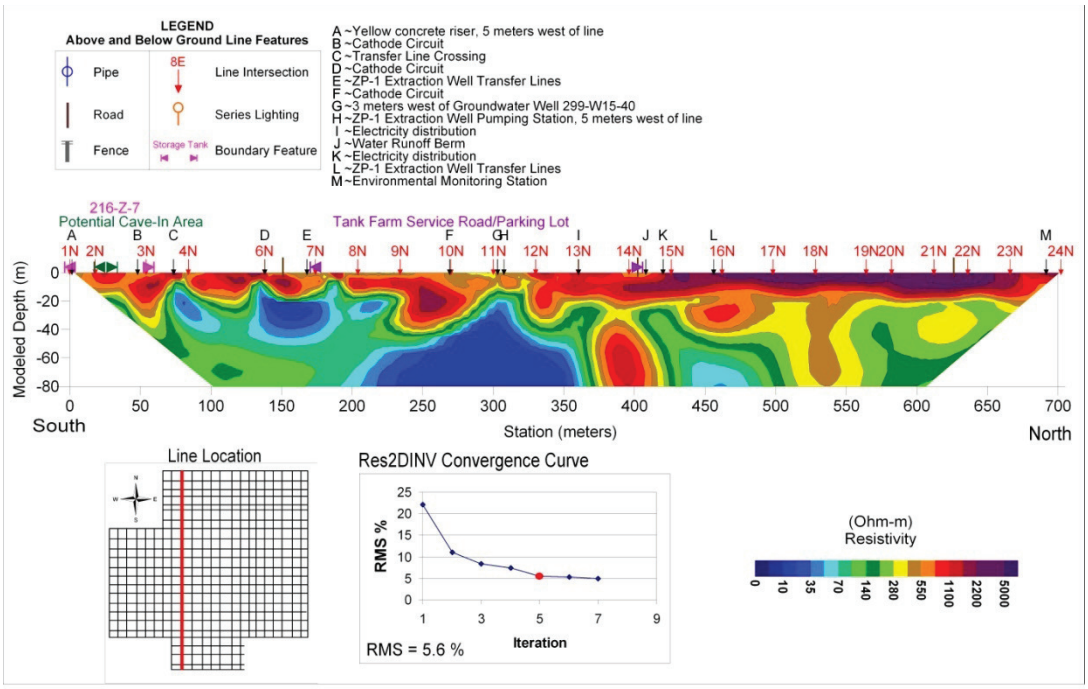

Figure 4-18. Model Results for 2D Inverse Model Domain of Resistivity Survey Line 10E.

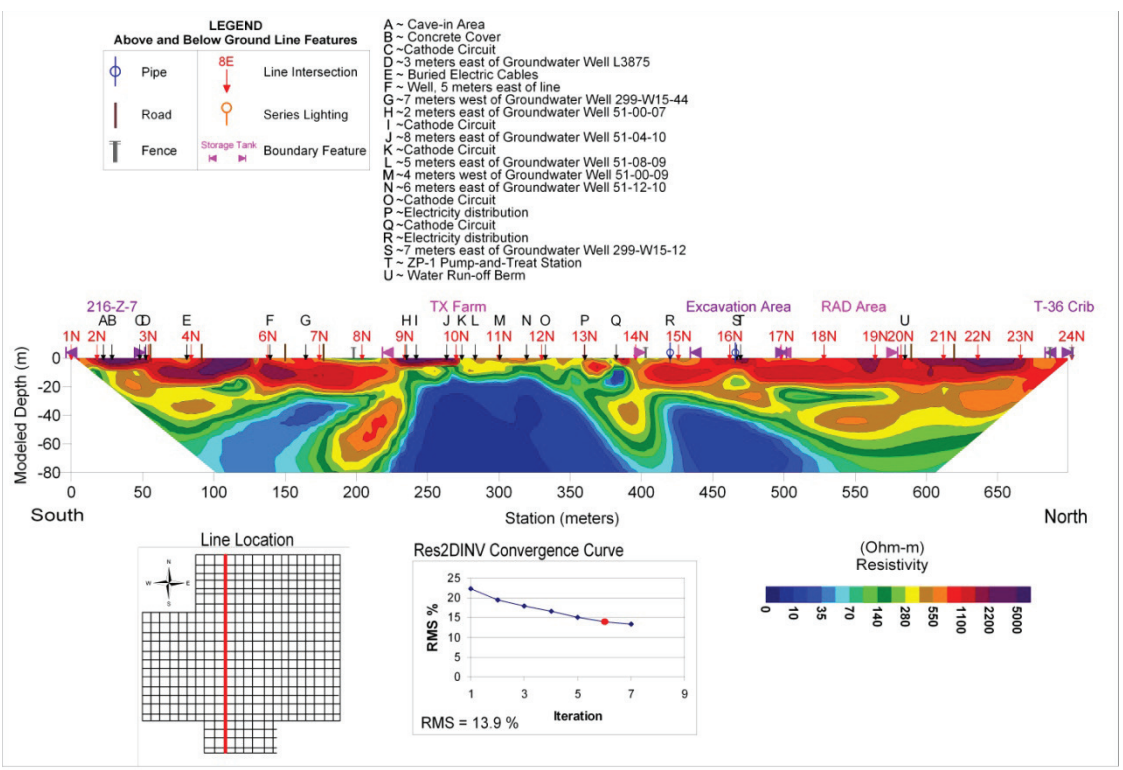

4.2.2 3D Inversion Model Results

This section describes the results of the 3D inversion model analysis of STS resistivity data collected over the 216-T-19 crib and tile field and 216-Z-7 area. A compilation of all orthogonal resistivity lines within the blue polygon model domain, in Figure 4-12, was used for a 3D STS model called TXTY-STS5ii. The resistivity data for this model was collected at 6m electrode spacing and 30m orthogonal line separations and inverted using EarthImager3DCL v1.1.3. The model runtimes, domain description and convergence statistics are shown in Table 4-2. A plot of model convergence is provided in Figure 4-19.

A review of modeling results and infrastructure locations indicates that the location and aerial extent of all primary low resistivity targets can be associated with some influence of buried metallic infrastructure (Figure 4-8). The primary low resistivity targets in this model domain fall within the range of 1-115 ohm-m and are displayed as an iso-volume in semi-transparent red, with a secondary target of 115-130 ohm-m in semi-transparent green. In Figure 4-20, it is difficult to disassociate the influence of the pipeline intersections in the northern end of the 216-T-19 crib from the primary low resistivity target (red volume). The shape and position of the red volume is consistent with the 2D inversion model results for Line 15E in this area. A low resistivity target in Line 15E between station 95 and125 m is in close proximity to groundwater well 299-W14-51. This steel-cased well may influence the shape and the lower resistivity of the primary low resistivity target in both the 2D and 3D model domains beneath the tile field as they are based on the same raw data (Figure 4-16).

A low resistivity target (red volume) at the western portion of the 216-T-19 crib area appears to be heavily influenced by pipelines (Figure 4-20, 4-21, 4-22, and 4-23). Figure 4-22 shows a side view from the south of a discrete secondary (green) target at approximately 50-m depth beneath the eastern portion of the 216-T-19 crib which appears to have minimal influence from known infrastructure. Figure 4-21 indicates how the remaining primary (red) and secondary (green) targets closely follow pipelines plotted in this area.

Table 4-2. Simulation Details and Statistics of 3D Model Domain TXTY-STS5ii.

Input File	TXTY-STS-5ii
Inversion start date	23:04:32 2008-07-03
Inversion end date	23:47:24 2008-07-03
Northing range (meter)	135.5
Easting range (meter)	252.5
Easting minimum	566622.5
Northing minimum	135905
Easting maximum	566875
Northing maximum	136040.5
Software version	AGI EarthImager3DCL
Number of electrodes	393
Number of data points	4795
Domain area (acres)	8.5
Number of domain nodes	136500
Number of iterations	6
Root mean square of final iteration	9.13

Figure 4-19. Model Convergence Chart Showing RMS % and Iteration Number for the 3D Inversion Model of the TXTY-STS5ii Domain.

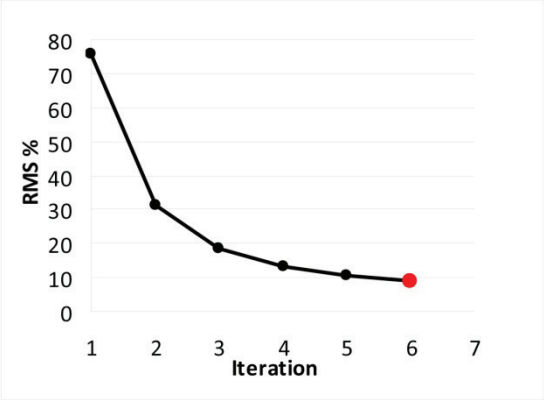

Red dot = selected model iteration

Figure 4-20. 3D Resistivity Inversion Model for the TXTY-STS5ii Domain - View is from above and South-East.

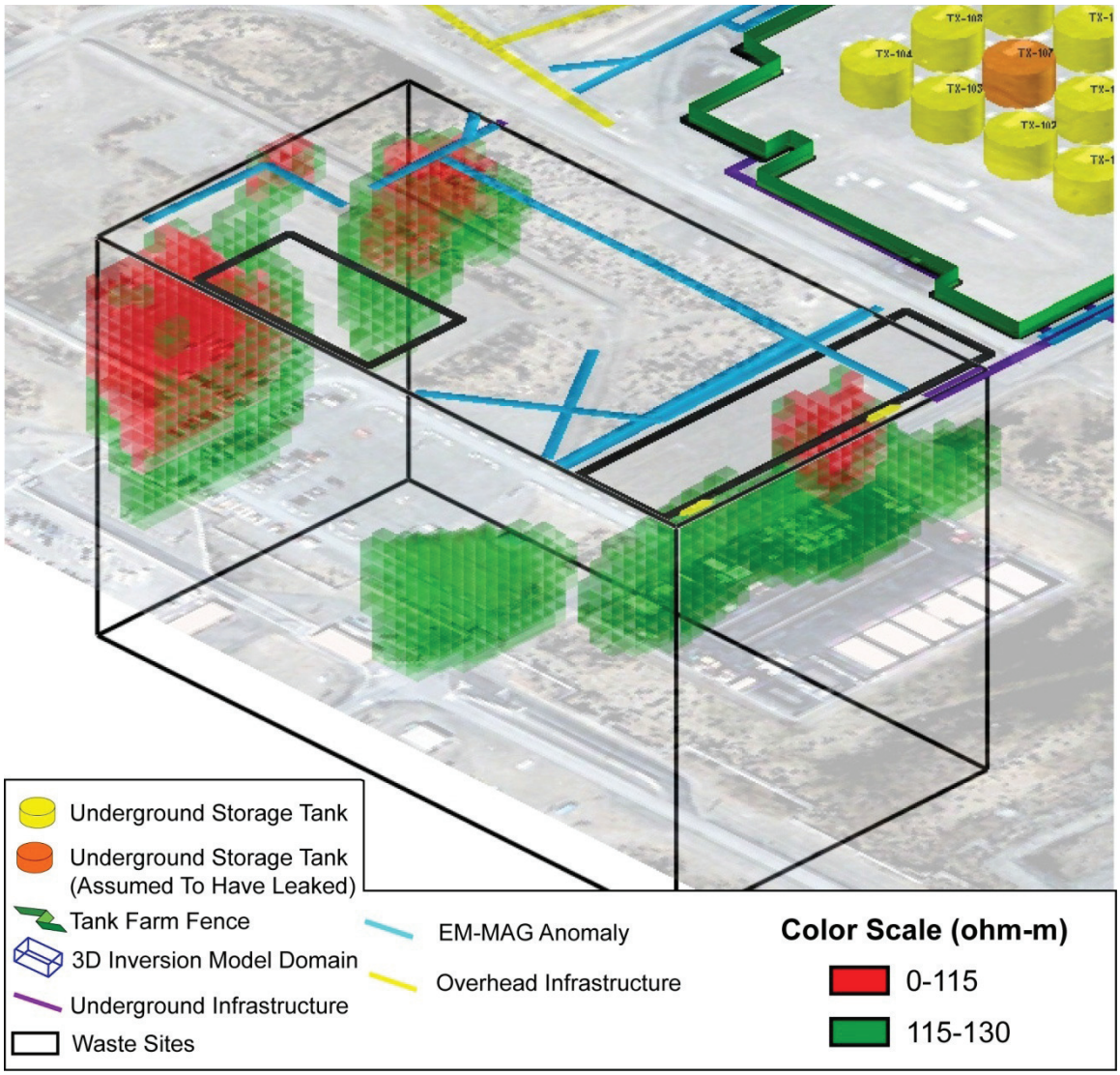

Figure 4-21. 3D Resistivity Inversion Model for the TXTY-STS5ii – View is From Above and Southwest Direction.

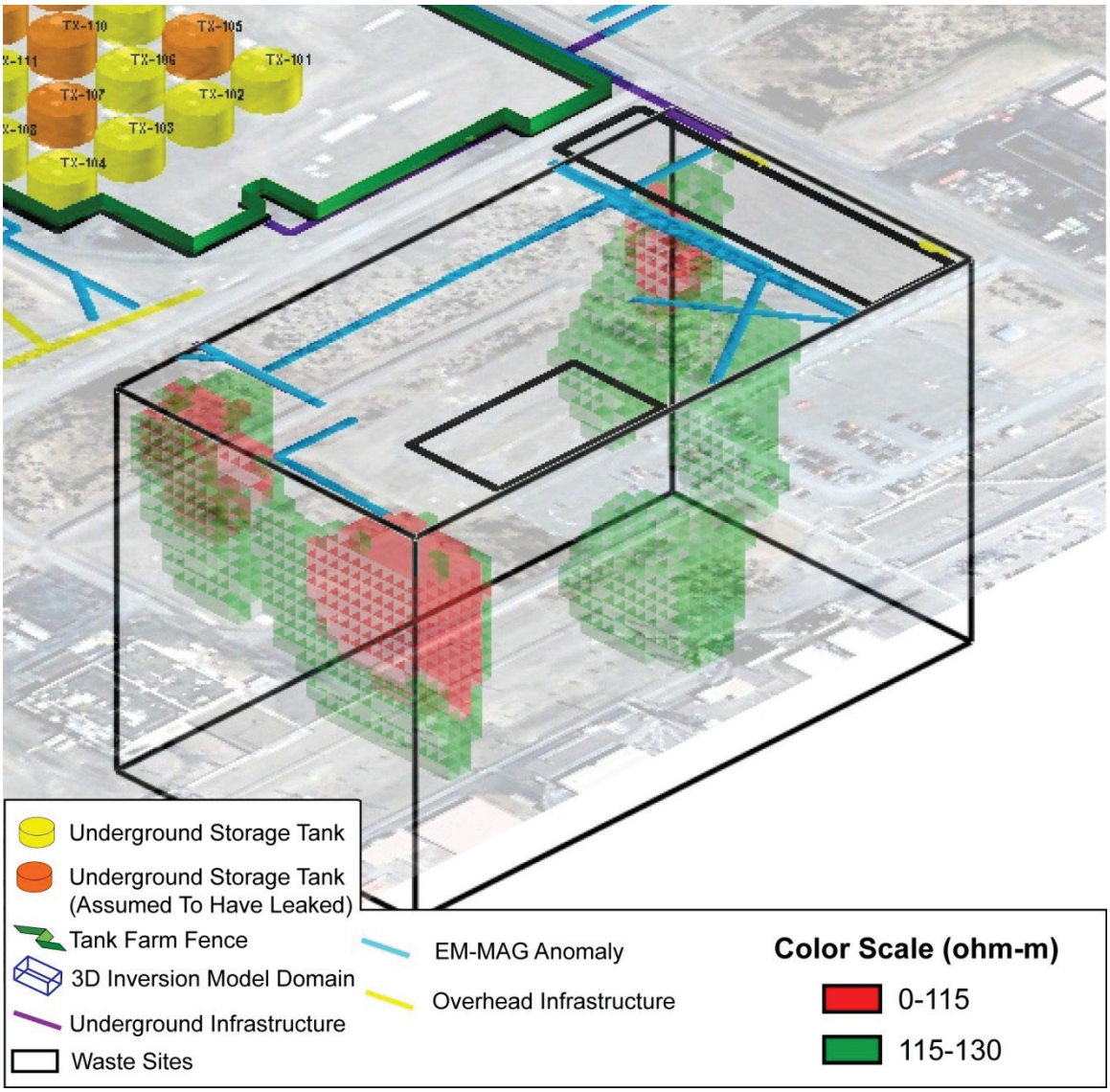

Figure 4-22. Plan View of Model Results for 3D TXTY-STS5ii Inverse Model Domain.

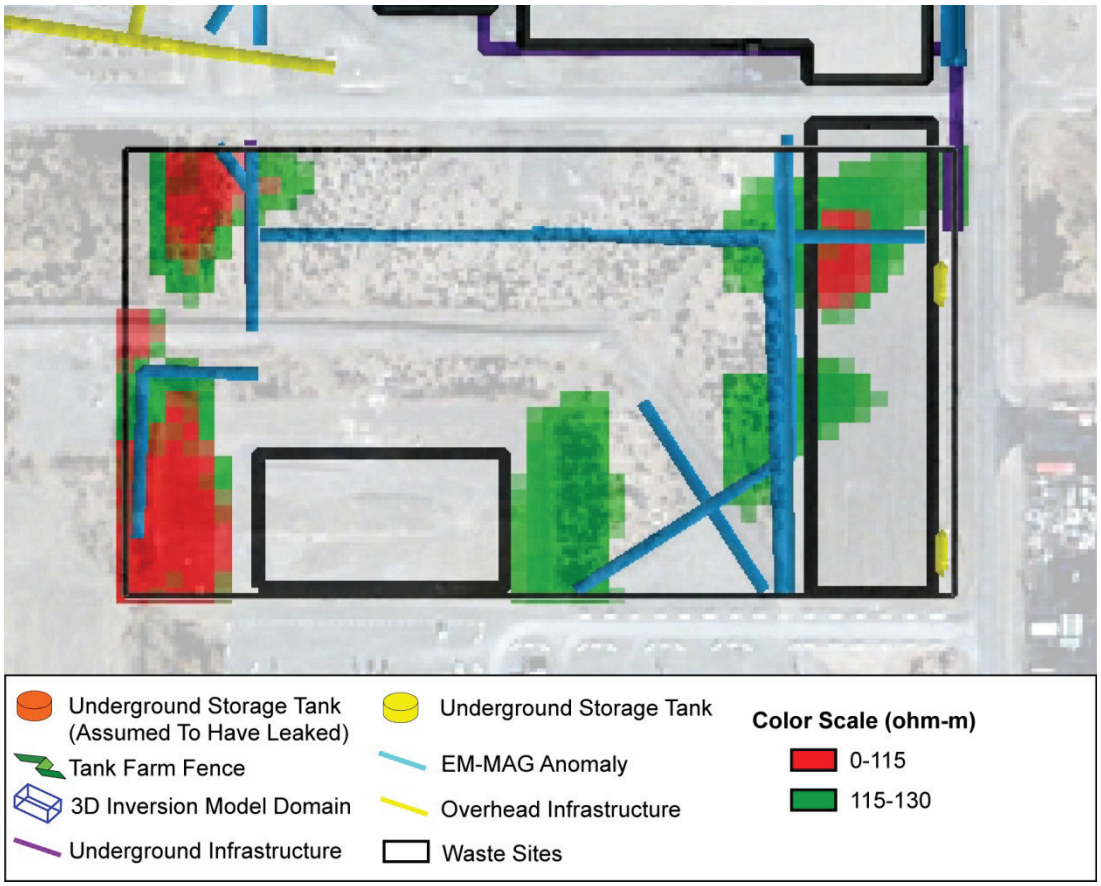

Figure 4-23. Cross-sectional View of Model Results from South Direction for 3D TXTY-STS5ii Inverse Model Domain.

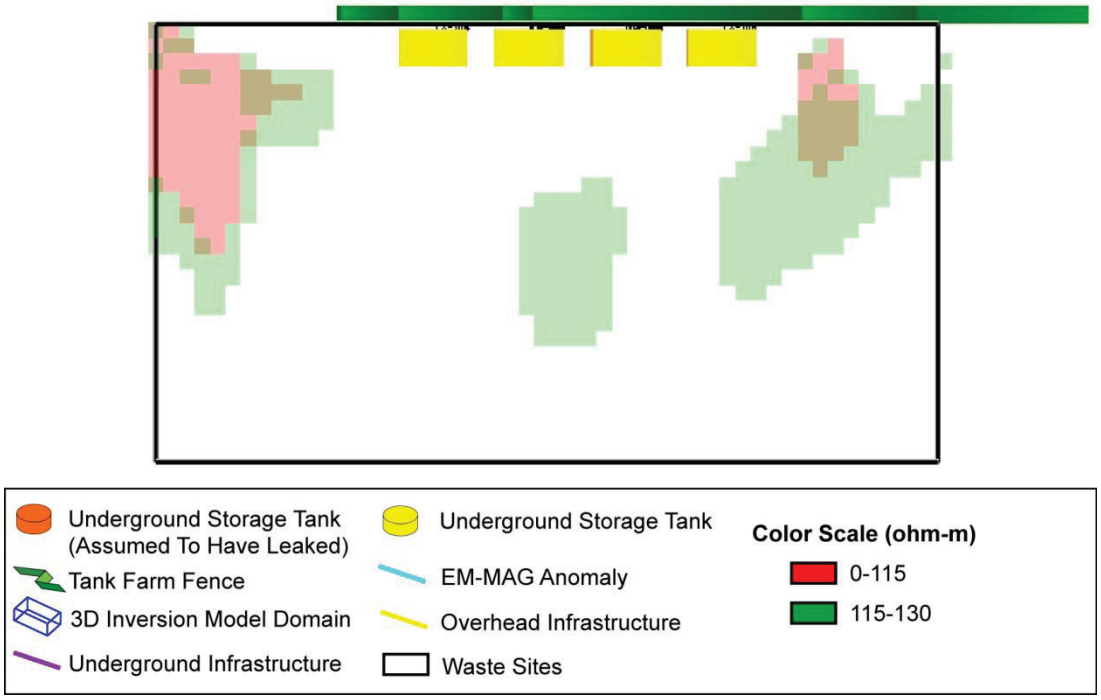

4.3 TY CRIB (216-T-26 THROUGH 216-T-28) AND 216-T-31 FRENCH DRAIN AREA

An area containing the TY cribs (216-T-26 through 216-T-28 cribs) and the 216-T-31 French drain area east of the TX and TY tank farms was analyzed using both 2D and 3D model domains as shown in Figure 4-24. The extent of the 3D model used in the analyses of this specific area is given as model TXTY-STS2.

4.3.1 2D Inversion Model Results

For the specific area of the TY cribs (216-T-26 through 216-T-28), 2D inversions were performed using RES2DINV with STS resistivity data collected along east-west lines 15N through 17N and along north-south lines 16E through 19E.

For the specific area of the 216-T-31 French drain, 2D inversions were performed using Res2DINV with STS resistivity data collected along east-west lines 9N and 10N and north-south lines 14E and 15E.

Analysis of the HRR raw data, maps of infrastructure, and inversion models for this area show a profound impact from pipes and other buried infrastructure. The infrastructure, shown in Figure 2-7, is provided as a point of reference for review of the inversion results for the TY cribs area and the 216 French drain area. Key features of the infrastructure are provided in the plots of model inversion results as symbols at the surface.

Nearly all east-west and north-south survey lines that cross the TY cribs area are impacted by the presence of buried infrastructure and surface features (steel risers, underground electric lines, and groundwater wells). Model results from Line 16N, provide an example of the effects of these infrastructure features (Figure 4-25). A review of inversion results along survey Line18E (see Figure 4-25), which crosses perpendicular through the middle of the TY cribs, shows the difficulty in identifying discrete low-resistivity targets associated with the waste disposal at TY cribs in the presence of nearby buried and surface infrastructure.

A review of 2D resistivity inversion models surrounding the TY cribs and 216-T-31 French drain area reveals a surficial background resistivity layer in areas that are not in close proximity to buried metallic infrastructure. In areas free of infrastructure, these models show a uniformly resistive background layer in the upper 20m that ranges in value from 300 to 5000 ohm-m. Some examples of well-defined background values are shown between station 0-300 m in Line 16N (Figure 4-25); between stations 0-300 m and 470 to 520 m in Line 18E (Figure 4-26), between stations 0-70 m and 180-250 m in Line 10N (Figure 4-27), and between stations 0-50 m and 200-230 m in Line 14E (Figure 4-28). The range of resistivity in the background layer is consistent with background resistivity values measured over the TX trenches (216-T-21 through 216-T-25) as well as other SGE sites (RPP-34690 and RPP-RPT-28955).

As in the area south of TX farm, described in Section 4.2, deeper model layers over large areas within Lines 16N, 18E, 10N, and 14E reveal targets that are dominated by buried and surface infrastructure, such as pipelines and groundwater wells that are in close proximity to the surface electrodes. These resistivity targets dominate the lower model layers and obscure the expected gradual lowering of resistivity as model depths approach the local water table at approximately 80m.

Results of Line 18E show the effects of these local infrastructure features on resistivity inversion results for the same area (Figure 4-26). A low resistivity feature may be apparent at shallow depths in the area around the cribs. These shallow model layers are based on narrow spaced electrodes, which are less affected by infrastructure in close proximity but not directly beneath the electrode line (3D infrastructure). Groupings of pipelines, such as along Camden Road, will have an increasing effect on wider spaced electrode data used in the deeper model layers. At depth below the cribs, the effect of nearby 3D infrastructure obscures any resolution of discrete targets which may be associated with waste disposal at the cribs.

Figure 4-24. STS Survey Lines and Model Domain Associated with TY Cribs and 216-T-31 French Drain Area.

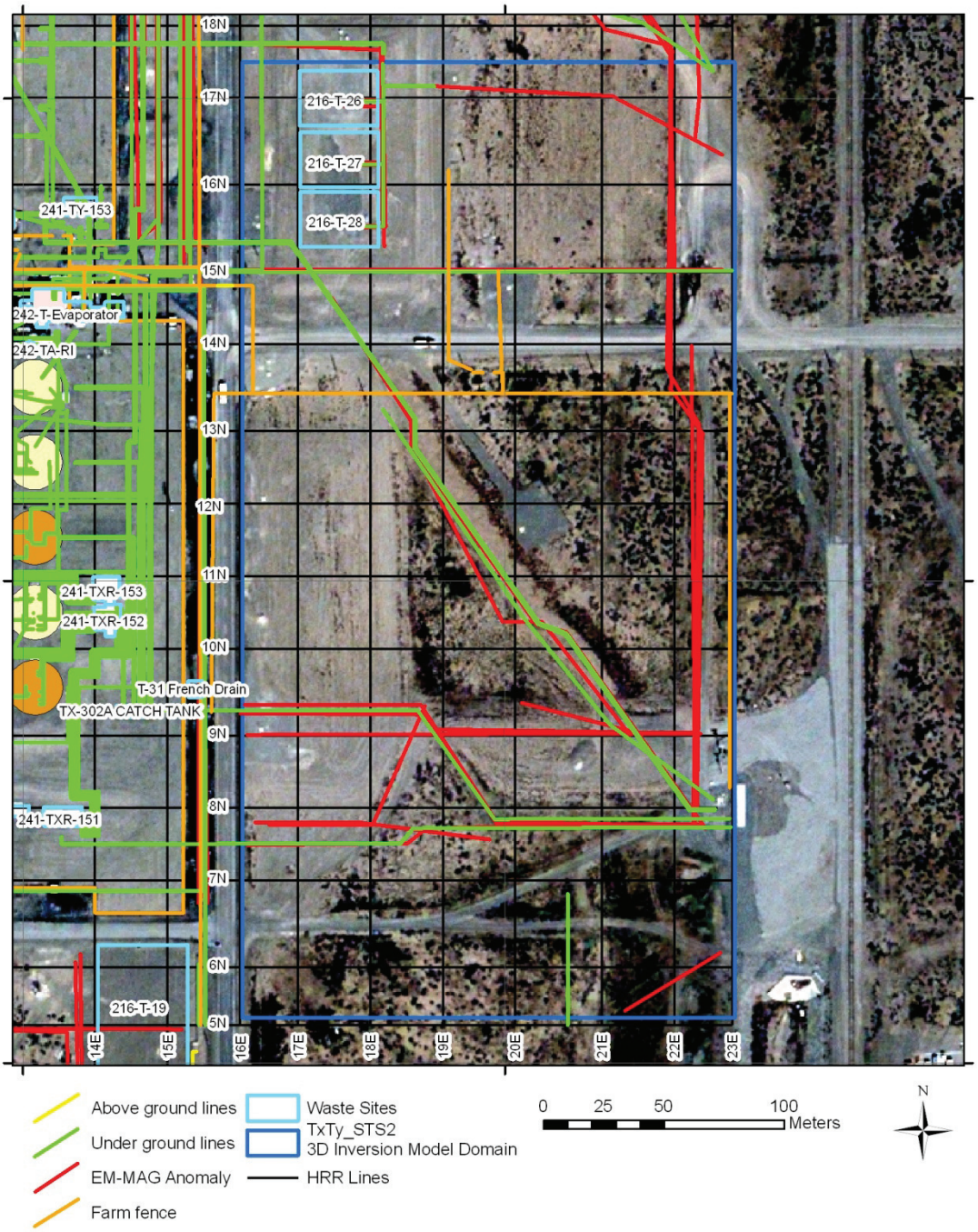

Figure 4-25. Model Results for 2D Inverse Model Domain of Resistivity Survey Line 16N.

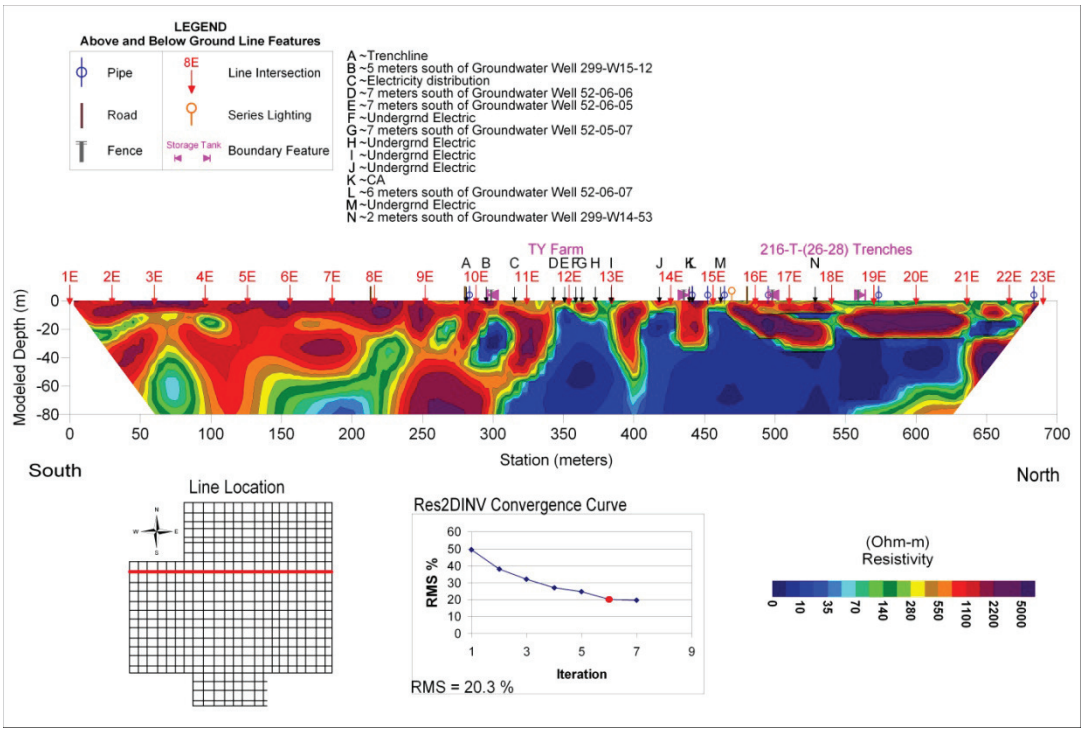

Figure 4-26. Model Results for 2D Inverse Model Domain of Resistivity Survey Line 18E.

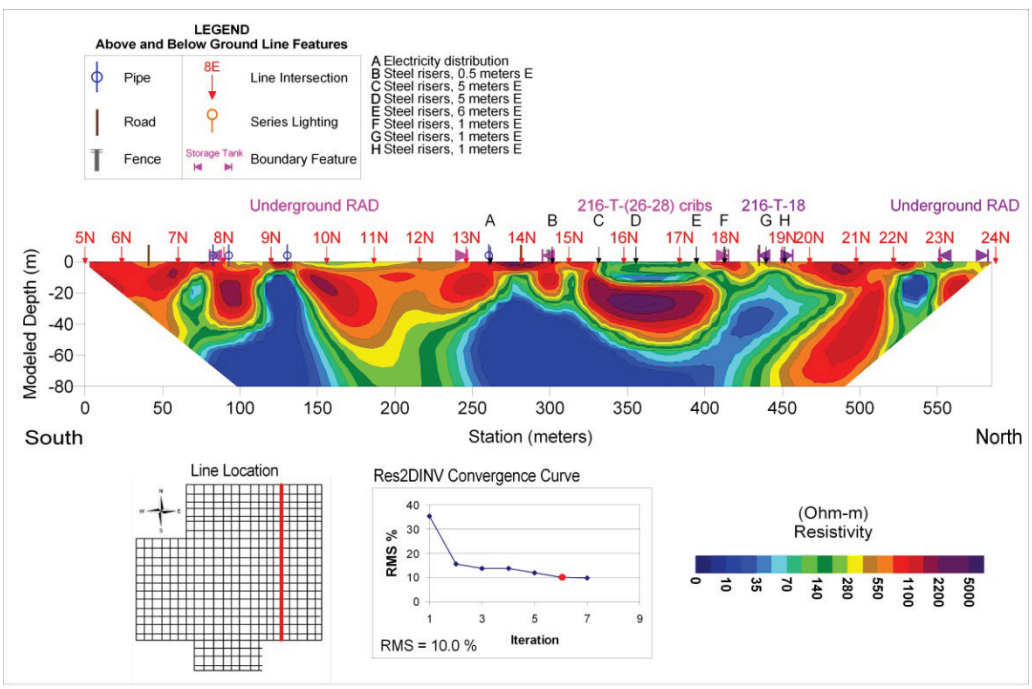

The east-west and north-south survey lines that cross the 216-T-31 French drain area are also impacted by the presence of buried infrastructure and surface fences. Results of Line 10N, given in Figure 4-27, provide a representative east-west example of the effects of infrastructure on resistivity inversion results. The combination of surface pipes, groundwater wells, and underground electric utilities along this specific survey line dominate the major resistivity features shown in the model plot at station distance 450 m.

The results of Line 14E, given in Figure 4-28, show a north-south example through the same area. These survey lines, the effects of the underground electric utilities, wells and surface pipes also dominate the key resistivity features in vicinity of the 216-T-31 French drain shown in the model plot near the intersection of the survey line 10N at about Station distance 270 m.

Figure 4-27. Model Results for 2D Inverse Model Domain of Resistivity Survey Line 10N.

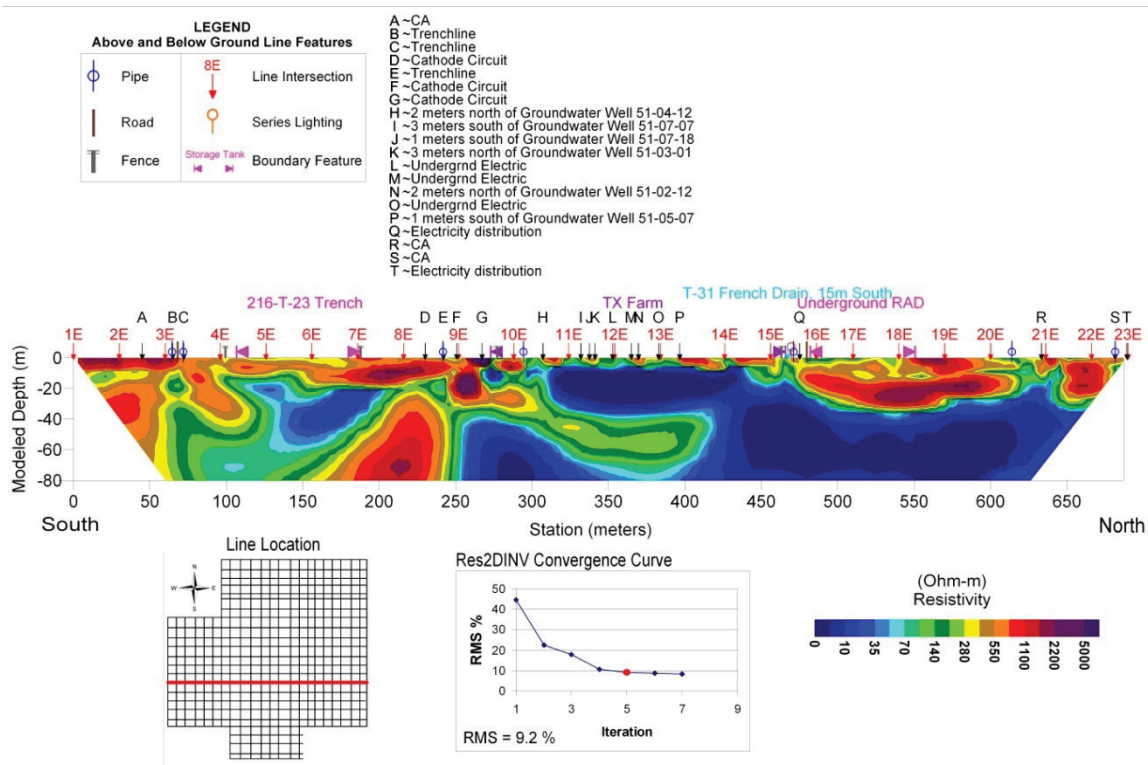

Figure 4-28. Model Results for 2D Inverse Model Domain of Resistivity Survey Line 14E.

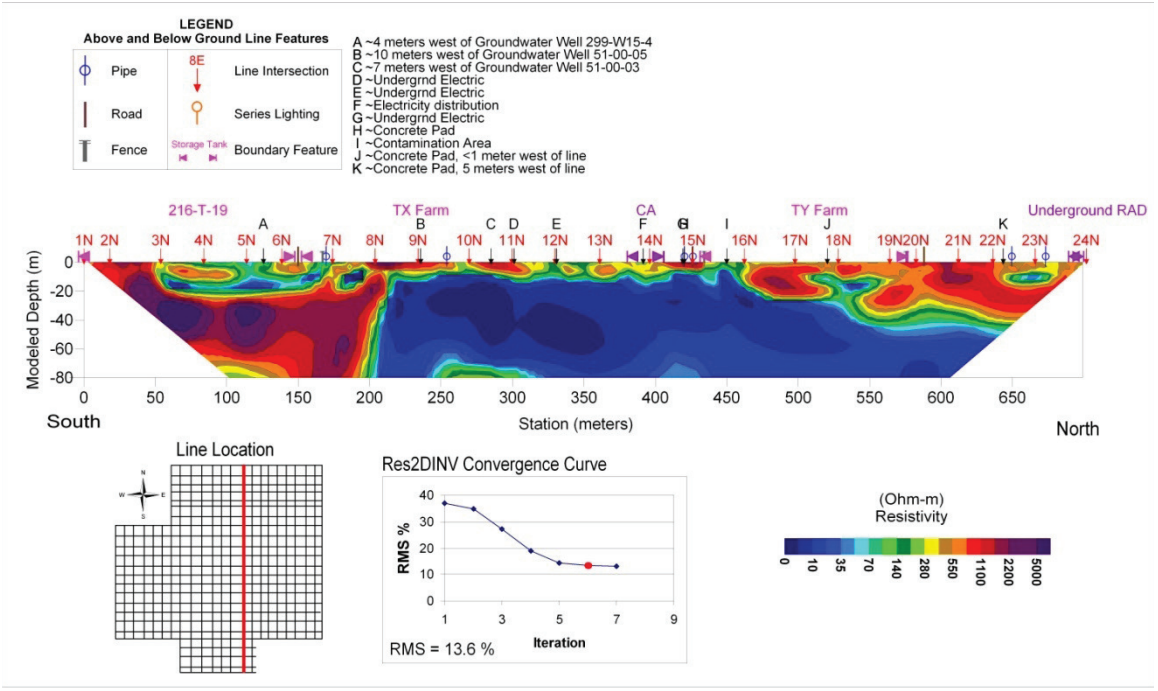

2D inversion results of all other STS resistivity survey lines in the general area of the TY cribs and 216-T-31 French drain are provided in Appendix E.

4.3.2 3D Inversion Model Results

STS resistivity data collected along the east-west and north-south survey lines in the TY cribs and 216-T-31 French drain area were also evaluated in a 3D resistivity inversion model, referred to as TXTY-STS2iii. The lateral extent of this domain is provided in Figure 4-24.

3D resistivity inversion modeling of the TY cribs and 218-T-31 French drain area was accomplished with EarthImager3DCL v1.0.1. Specific details and inversion statistics for this model domain is provided in Table 4-3. Iteration 21 is used to depict modeling results.

Table 4-3. Simulation Details and Statistics of 3D Model Domain TXTY-STS2ii.

Input File	TXTY-STS-2iii
Inversion start date	3/18/2008 12:48:16 AM
Inversion end date	07:50:59 2008-03-19
Northing range (meter)	396
Easting range (meter)	204
Easting minimum	566891
Northing minimum	136019
Easting maximum	567095
Northing maximum	136415
Software version	AGI EarthImager3DCL v1.1.1
Number of electrodes	894
Number of data points	21342
Domain area (acres)	19.9
Number of domain nodes	330336
Number of iterations	21
Root mean square of final iteration	7.64

Figure 4-29. TXTY-STS2iii Inversion Model Convergence Curve.

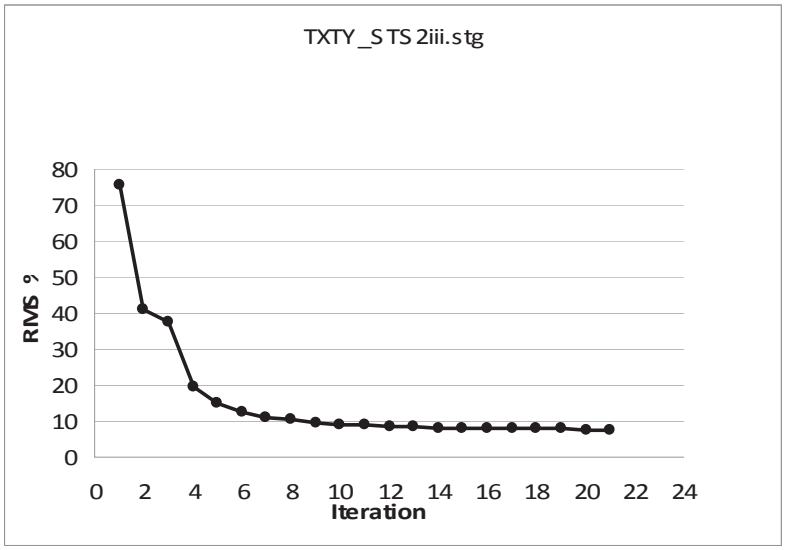

Figures 4-30 and 4-31 present the results for the 3D TXTY-STS2ii inverse model from above and the southeast and southwest directions, respectively. The black box in these figures defines the extent of the inversion domain. The model was inverted with all resistivity data at the 20-foot (6-meter) electrode spacing. The figure highlights two discrete resistivity target levels at 25 and 50 ohm-m respectively. The 0-25 ohm-m value is represented in semi-transparent red and the 25 - 50 ohm-m level is represented as semi-transparent transparent green.

A selected plan profile is given in Figure 4-32. A review of this image and previous plots in Figures 4-30 and 4-31 suggests that the main low-resistivity targets are associated with linear trends along buried infrastructure. However, the size and depth of these main targets appears to be too large to be associated entirely with surface and buried infrastructure in the vicinity of the electrodes.

Figure 4-30. View of Model Result from Southeast Direction for 3D TXTY-STS2ii Inverse Model Domain.

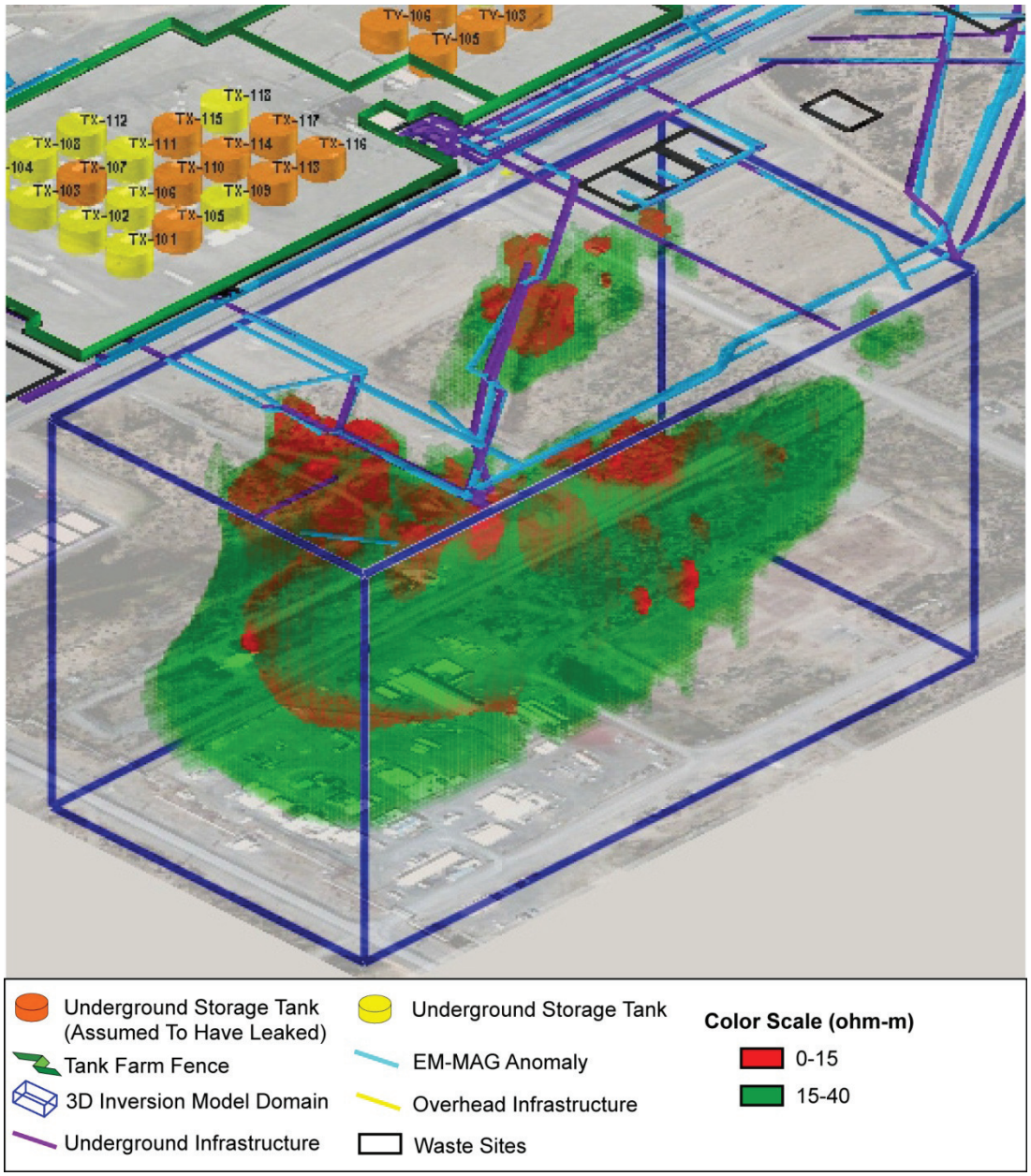

Figure 4-31. View of Model Results from Southwest Direction for 3D TXTY-STS2ii Inverse Model Domain.

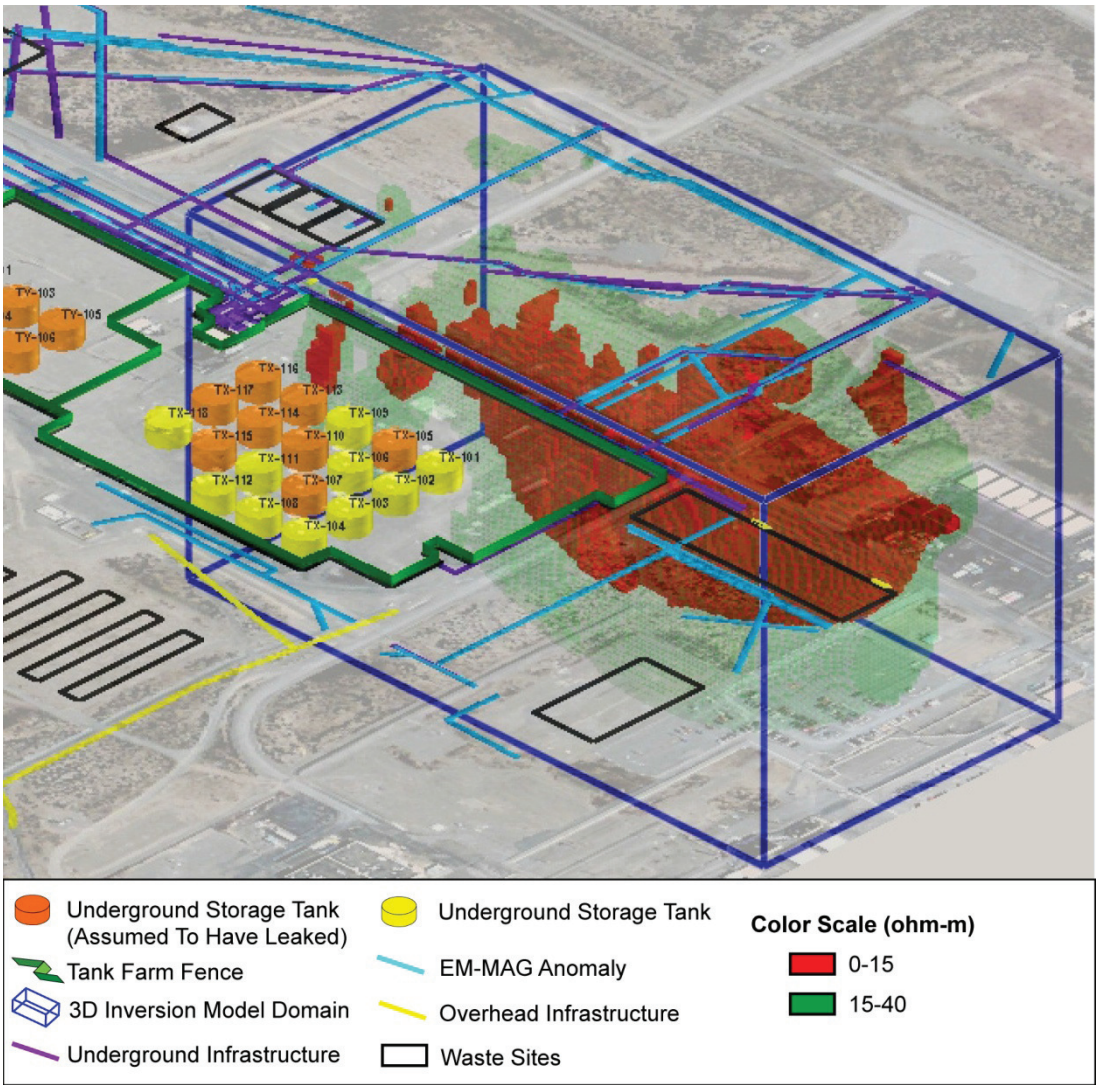

Figure 4-32. Plan View of Model Results for 3D TXTY-STS2iii Inverse Model Domain.

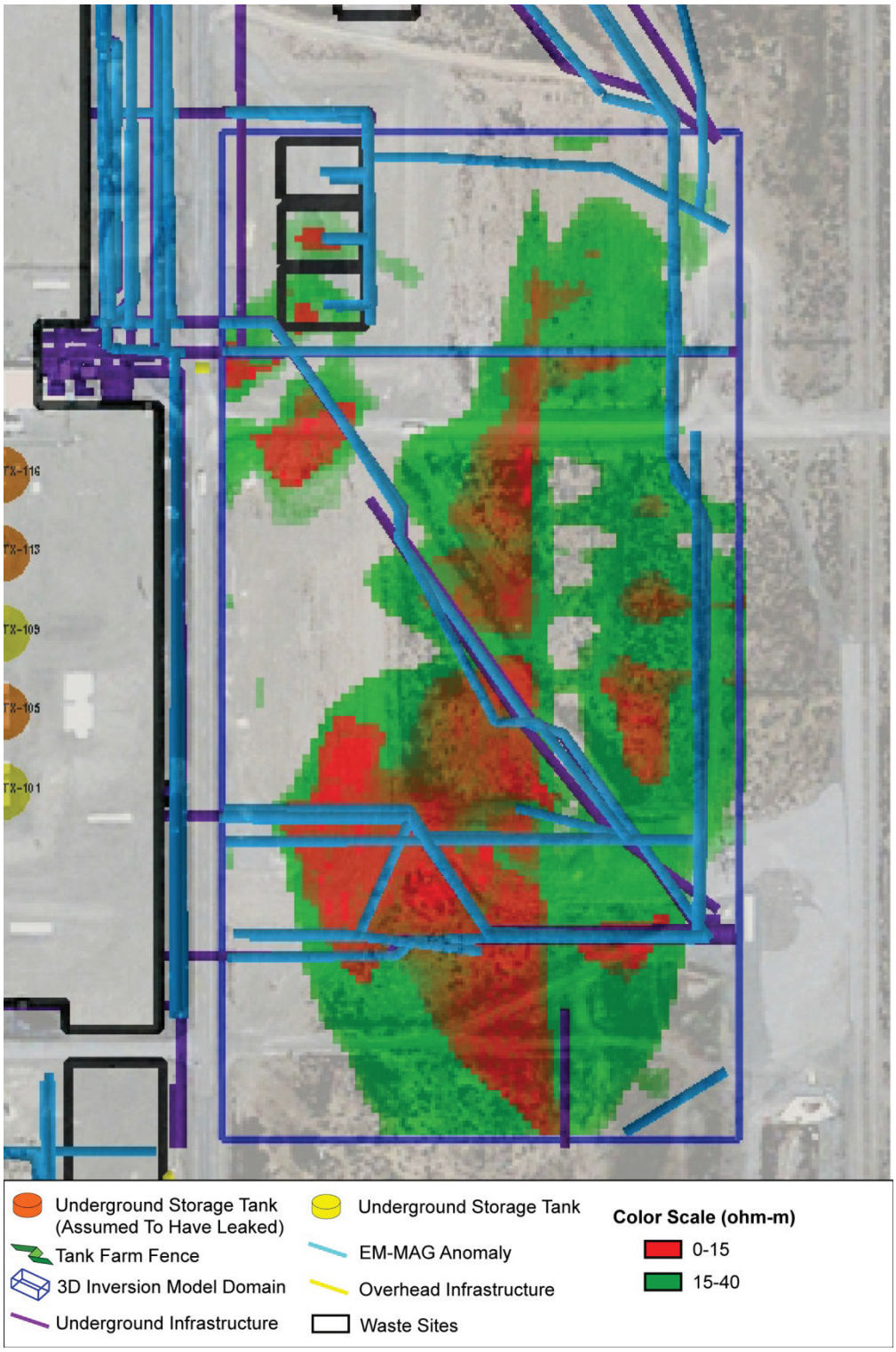

4.4 NORTHERN WASTE SITE AREA CONTAINING 216-T-36 CRIB, 216-T-13 TRENCH, AND 216-T-18 TEST CRIB AREA

The 216-T-36 crib, 216-T-13 trench and 216-T-18 Test crib area is the next area where resistivity was evaluated with the 2D and 3D inversion modeling process. Modeling efforts were largely focused on 2D inversion models along STS survey lines shown in Figure 4-33. STS resistivity data collected along 2D survey lines in the northern waste site area was also evaluated by combining multiple orthogonal lines into 3D model domains referred to as TXTY-STS6 (entire Northern Waste Site Area), TXTY-STS7ii (Eastern part of the waste area), and TXTY-STS8i (Western part of the waste area). The lateral extent of the domains is shown in Figure 4-34. The results of these inversion models are included in this section.

Figure 4-33. STS Survey Lines and 3D TXTY-STS6 Model Domain Associated with Northern Waste Site Area – TX-TY Complex.

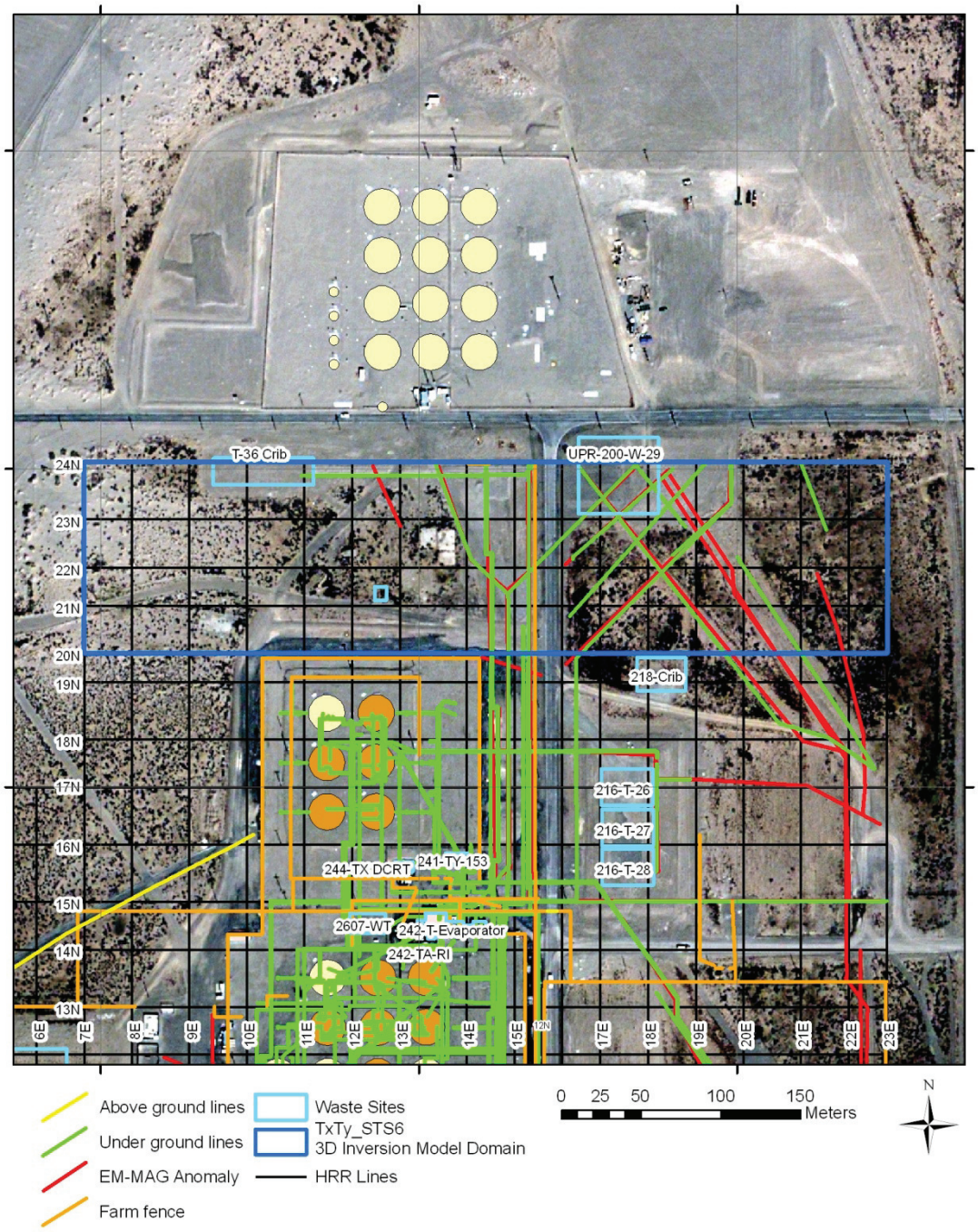

4.4.1 2D Inversion Modeling Results

Line 24N crosses the 216-T-36 crib area as well as several metal surface fences and known locations of buried infrastructure. The 2D inversion results of Line 24N (Figure 4-34) provide an example of the effects of buried near surface infrastructure on both surficial and deeper resistivity inversion model layers at this waste site area.

A review of 2D resistivity inversion models surrounding the waste sites in the area north of TY farm reveals a surficial background resistivity layer in areas that are not in close proximity to buried metallic infrastructure. In areas free of infrastructure, these models show a uniformly resistive background layer in the upper 20 m that ranges in value from 300 to 5000 ohm-m. Some examples of well-defined background values are shown between station 0-170 m and 420-470 m in Line 24N (Figure 4-34); between station 0-200 m in Line 22N (Figure 4-35), between station 0-110 m and 590-680 m in Line 12E (Figure 4-36), between station 0-80 m and 460-520 m in Line 18E (Figure 4-37), between station 0-110 m in Line 19N (Figure 4-38). The range of resistivity in the background layer is consistent with background resistivity values measured over the TX trenches (216-T-21 through 216-T-25) as well as other SGE sites (RPP-34690 and RPP-RPT-28955).

As in other areas at TX-TY Complex that are outside the farms, deeper model layers over large areas within the Lines 24N, 22N, 12E, 18E, and 19N reveal targets that are dominated by buried near surface infrastructure, such as pipelines and deeper infrastructure, such as groundwater wells, that are in close proximity to the surface electrodes. These resistivity targets dominate the lower model layers and obscure the expected gradual decrease in resistivity as depths approach the local water table at approximately 80 m.

4.4.1.1 216-T-36 Crib. 2D Inversion modeling results along survey Line 24N (Figure 4-34) at the 216-T-36 crib site show the depth and extent of a low resistivity target defined by blue contours (10-35 ohm-m, between station 90 and 140 m). This target is below the waste site between depths of 35 and 55 m. The physical waste site location along the survey line is approximately between station 65 and 165 m. Although buried infrastructure is present in areas of this survey line east of the T-36 crib, no known significant buried infrastructure is located at the 216-T-36 crib, with the exception of a pipe leading into the crib from the east.

Figure 4-34. 2D Inversion Model Results - Line 24N.

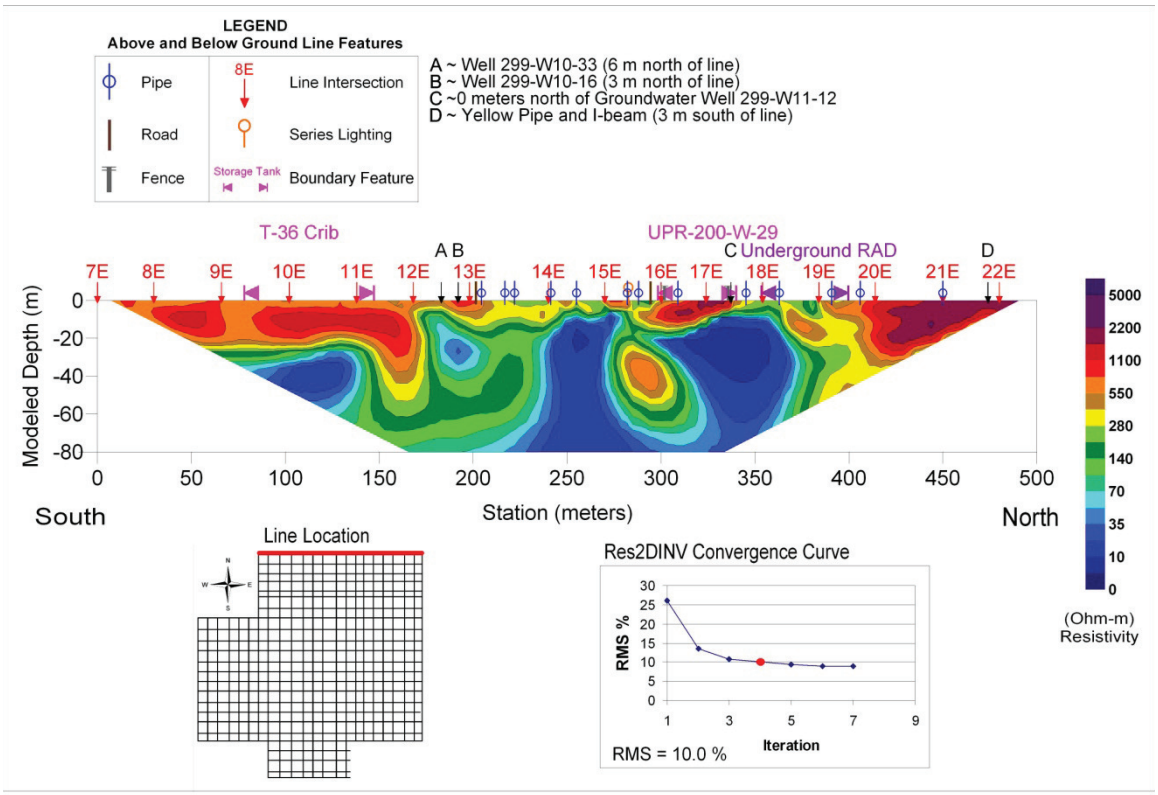

4.4.1.2 216-T-13 Trench. The 216-T-13 trench 2D resistivity inversions were performed with STS resistivity data collected along east-west lines 21N and 22N and north-south lines 11E through 12E. The results of Line 22N (Figure 4-35) and Line 12E (Figure 4-36) contain targets associated with the 216-T-13 trench.

2D inversion modeling results along Line 22N (Figure 4-35) at the 216-T-13 crib site (approximately between station 150 and 190 m) shows a low resistivity target defined by the blue contours (1-35 ohm-m). The target is located below the waste site at a depth between approximately 25 and 50 m. The depth of this low resistivity target is consistent with the low resistivity target inferred from inversion model results for survey Line 12E between station 600 and 680 m. This target is found beneath the approximate location of 216-T-13 at about the same depth as depicted in Line 22N.

As in the case of results for survey Line 24N, buried infrastructure that may affect the inversion results in other areas of the survey line are present, but no known significant buried infrastructure exist at the specific location of the 216-T-13 trench.

Figure 4-35. 2D Inversion Model Results - Line 22N.

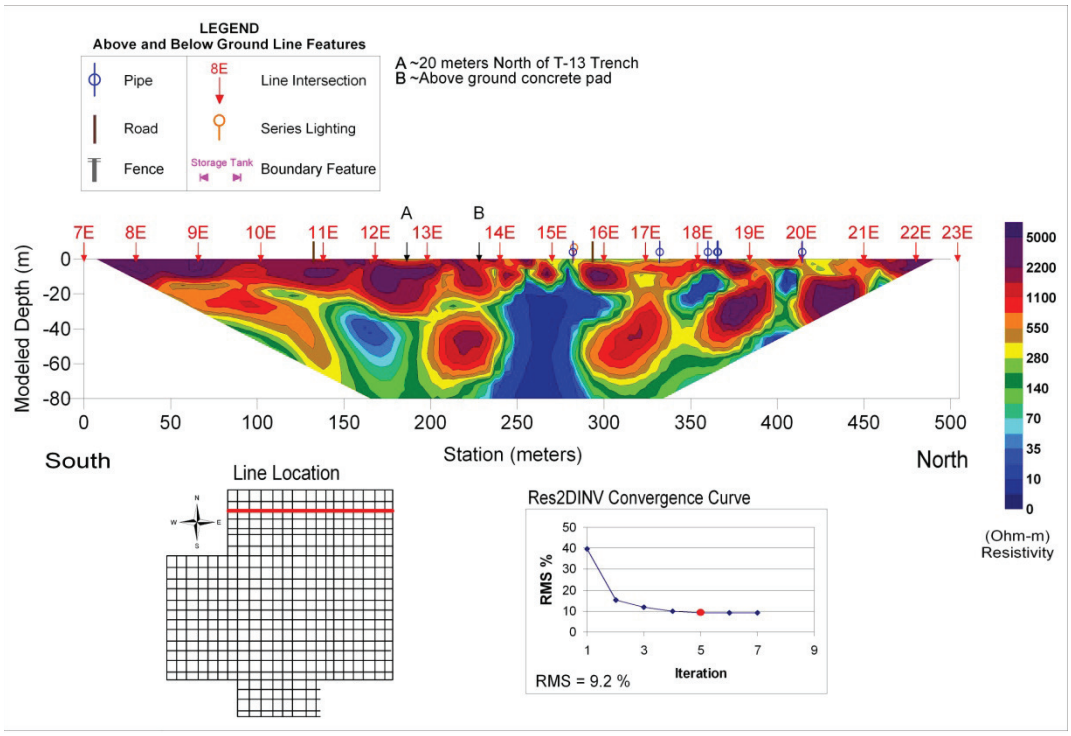

Figure 4-36. 2D Inversion Model Results - Line 12E.

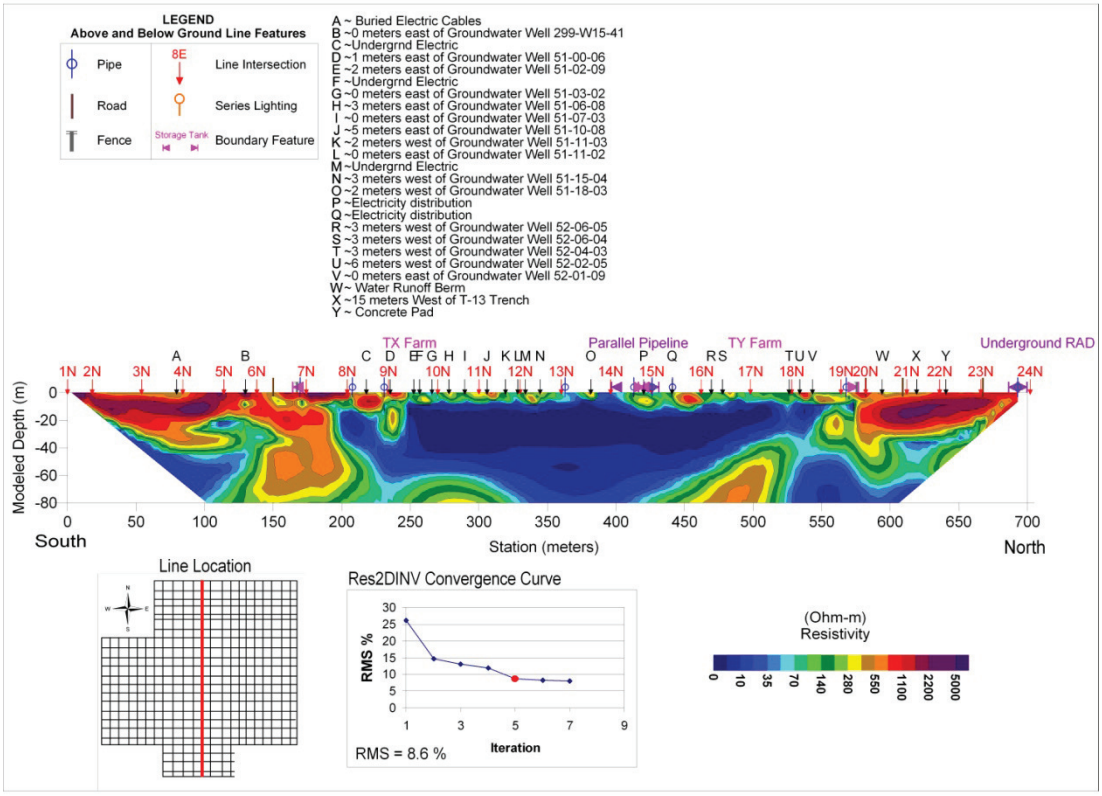

4.4.1.3 216-T-18 Test Crib. For the specific area of the 216-T-18 Test crib, 2D inversions were performed with STS resistivity data collected along north-south Lines 18E through 19E and east-west Lines 19N and 20N. The impact created by the presence of buried infrastructure and surface fences is shown along multiple segments within each of these lines. The results of Line 18E (Figure 4-38) provides an example of the effects of local features on resistivity inversion results and the specific results for this waste site area along a north-south section. The results of Line 19N (Figure 4-39) provide a good example of the effects of these local features on resistivity inversion results and the specific results for this waste site area along an east-west section.

A review of results along survey Line 18E suggests a potential low resistivity target (less than 35 ohm-m) located between station 430 and 440 m, at a depth of approximately 35 to 50 meters. However, the existence of nearby surface and buried infrastructure in the general area may affect these data.

2D inversion results along survey Line 19N also show a low resistivity target of similar magnitude (less than 35 ohm-m) located beneath the waste site (between station 350 and 360 m). This target is located at a shallower depth than seen on Line 18E; between depths of 10 and 20 m. Nearby buried infrastructure may have an effect on the magnitude and depth of both targets identified in Lines 18E and 19N.

Figure 4-37. 2D Inversion Model Results - Line 18E.

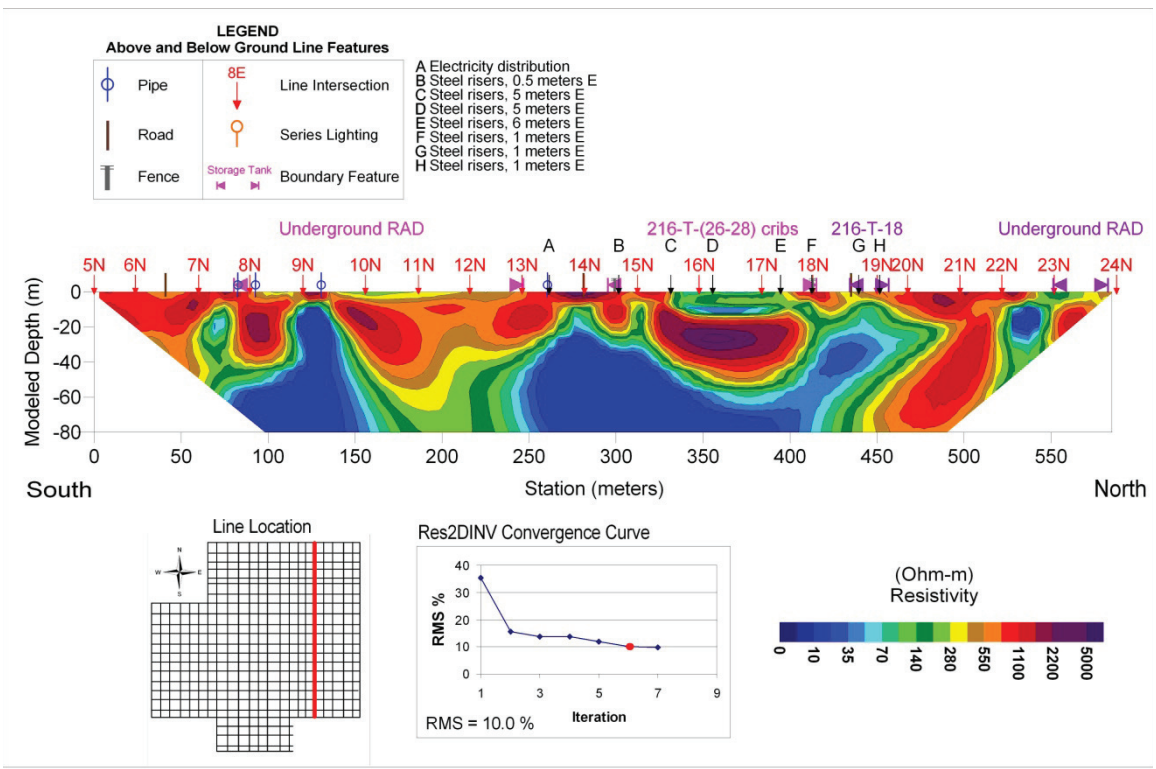

Figure 4-38. 2D Inversion Model Results - Line 19N.

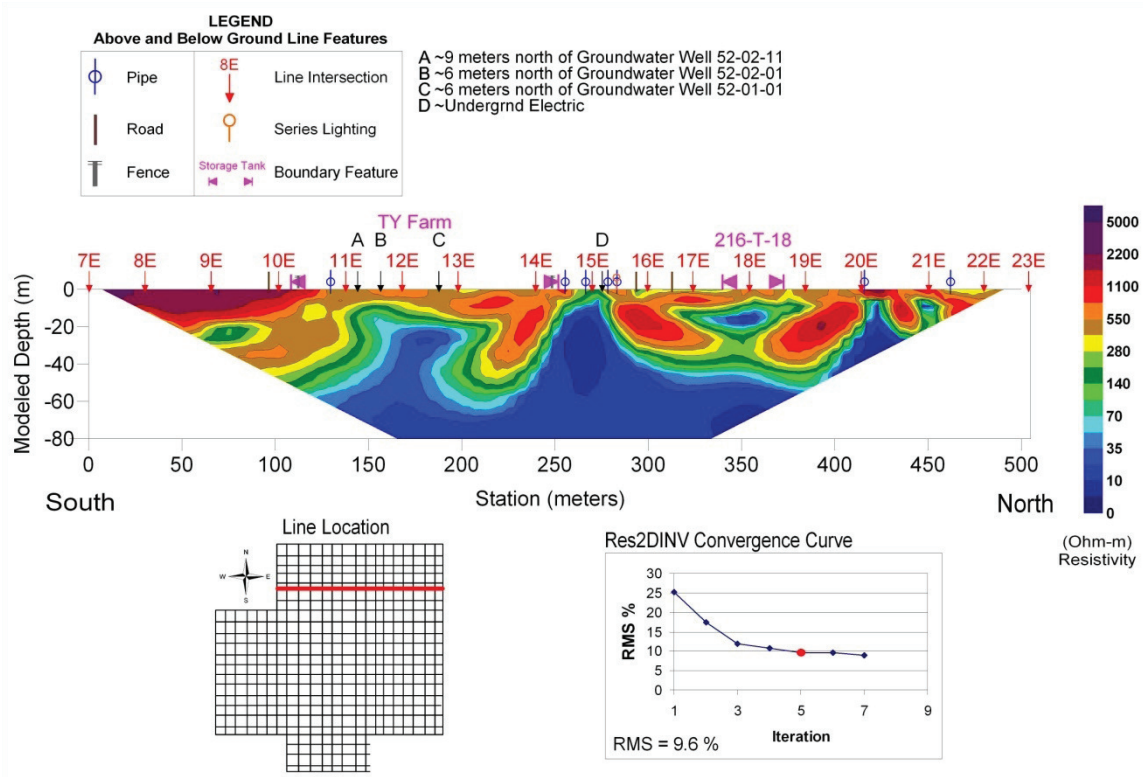

4.4.2 3D Inversion Model Results

This section describes the results of the 3D inversion model analysis of STS resistivity data collected over the northern waste site area. A compilation of all orthogonal resistivity lines within this domain was used for three 3D STS inversion models; TXTY-STS6, TXTY-STS7ii and TXTY-STS8i. The resistivity data for these models was collected at a 6 m electrode spacing along lines with 30 m orthogonal separation and was inverted using EarthImager3DCL v1.1.3.

4.4.2.1 3D Inversion Model Results - TXTY-STS6. The TXTY-STS6 inversion model domain contains a compilation of all orthogonal resistivity lines over the northern area of the TX-TY Complex within the specific domain area shown in Figure 4-34. Model runtimes, domain description and convergence statistics are shown in Table 4-1. A plot of model convergence is provided in Figure 4-39.

A review of modeling results and infrastructure locations indicates that the location and aerial extent of all primary low resistivity targets in the TXTY-STS6 model domain can be associated with some influence of buried metallic infrastructure (Figures 2-7 and 4-34). The primary low resistivity targets in this model domain fall within the range of 0-40 ohm-m and are displayed as an iso-volume in semi-transparent red, with a secondary target of 40-55 ohm-m in semi-transparent green.

A low resistivity target (red volume) at the central part of model domain appears to be heavily influenced by pipelines (Figure 4-40, 4-41, 4-42, and 4-43). No other targets that could be associated with the wastes sites in this area are evident in these results.

Analysis of the TXTY-STS6 model results with regards to convergence statistics, target acquisition, and sensitivity, led to the processing of two new model domains: the TXTY-STS7ii model that focuses on the eastern part of the northern waste site area and the TXTY-STS8i model that focuses on the western part of the same area. The results of these models are discussed in the following two sections.

Table 4-4. Simulation Details and Statistics of 3D Model Domain TXTY-STS6.

Input File	TXTY-STS-6
Inversion start date	09:04:03 2008-07-23
Inversion end date	10:01:01 2008-07-23
Northing range (meter)	114
Easting range (meter)	498
Easting minimum	566593
Northing minimum	136487
Easting maximum	567091
Northing maximum	136601
Software version	AGI EarthImager3DCL
Number of electrodes	659
Number of data points	12953
Domain area (acres)	14.0
Number of domain nodes	196980
Number of iterations	6
Root mean square of final iteration	11.85

Figure 4-39. Convergence Curve for 3D TXTY-STS6 Inversion Model.

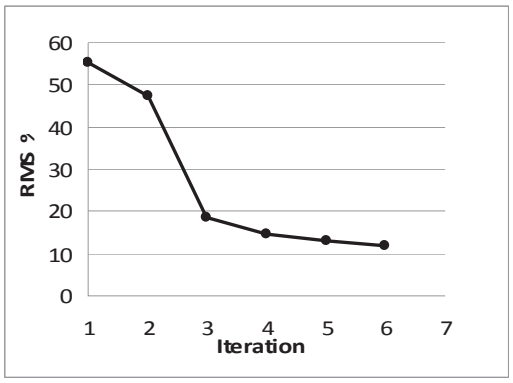

Figure 4-40. View of Model Results from Southeast Direction for 3D TXTY-STS6 Inverse Model Domain.

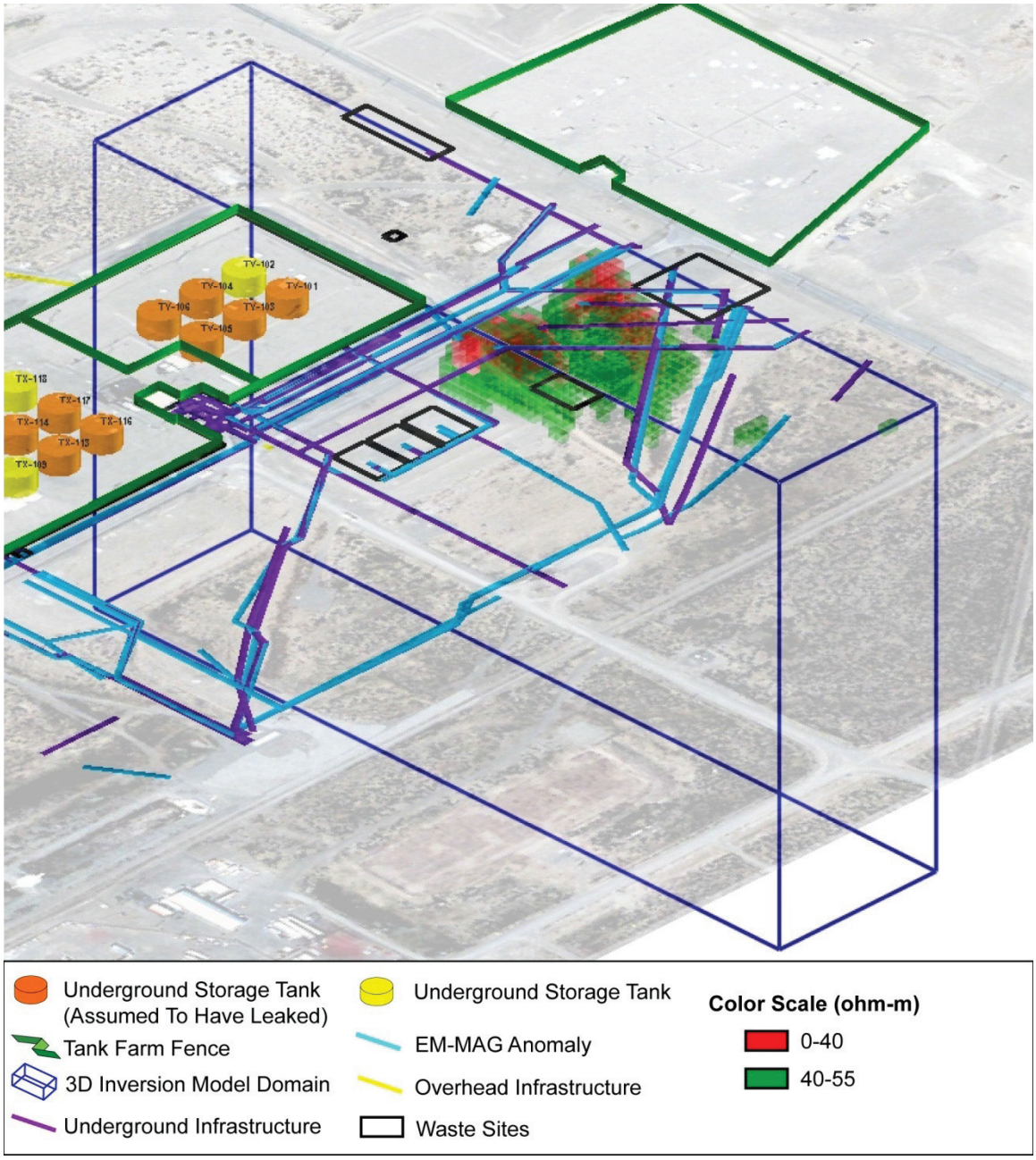

Figure 4-41. View of Model Results from Southwest Direction for 3D TXTY-STS6 Inverse Model Domain.

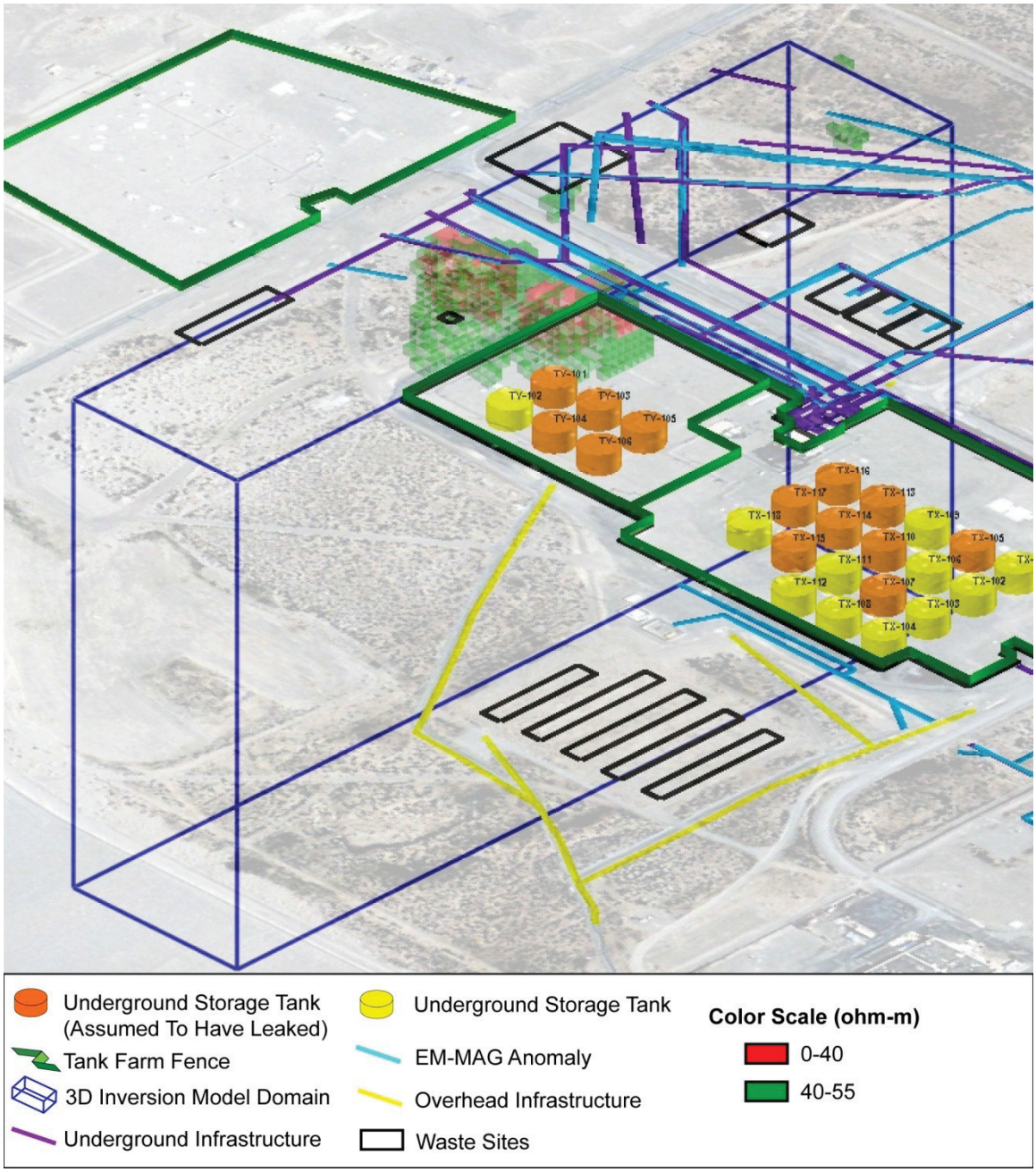

Figure 4-42. Plan View of Model Results for 3D TXTY-STS6 Inverse Model Domain.

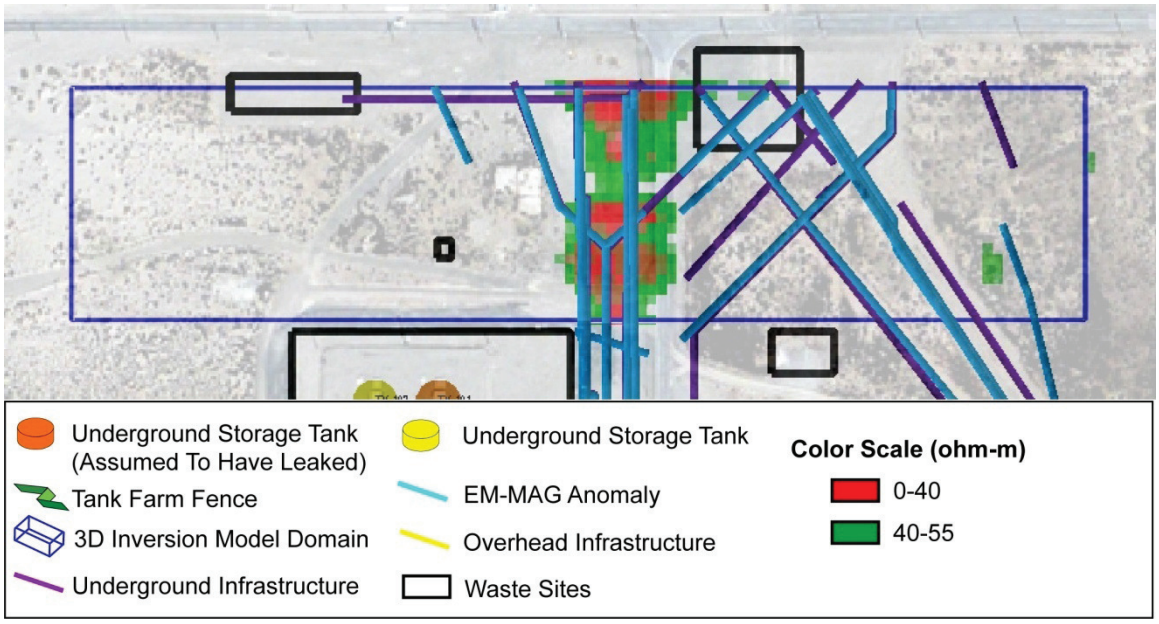

Figure 4-43. View of Model Results from Southwest Direction for 3D TXTY-STS6 Inverse Model Domain.

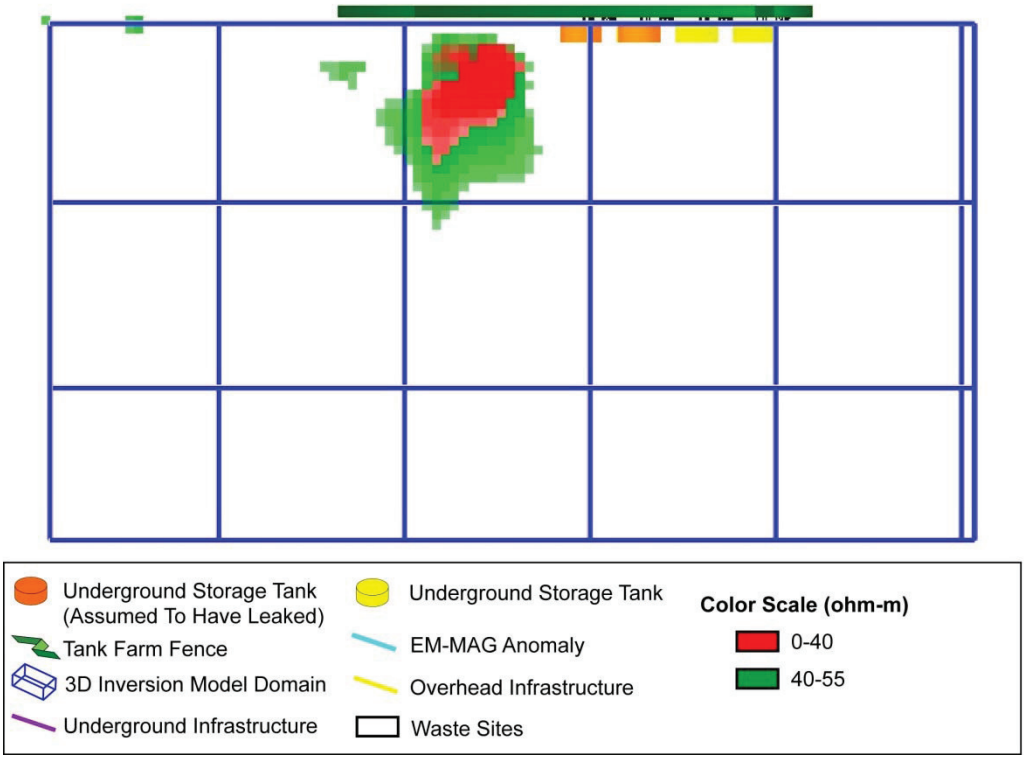

4.4.2.2 3D Inversion Model Results - TXTY-STS7. The TXTY-STS7ii inversion model focuses on the eastern part of the northern waste site area (see Figure 4-44). Model runtimes, domain description and convergence statistics for the TXTY-STS7ii model are shown in Table 4-5. A plot of model convergence is provided in Figure 4-45.

A review of modeling results and infrastructure locations indicates that the location and aerial extent of all primary low resistivity targets can be associated with some influence of buried metallic infrastructure (Figure 2-7 and 4-44). The primary low resistivity targets in this model domain fall within the range of 0-40 ohm-m and are displayed as an iso-volume in semi-transparent red, with a secondary target of 40-55 ohm-m in semi-transparent green.

A low resistivity target (red volume) at the central part of model domain appears to be heavily influenced by pipelines (Figures 4-46, 4-47, and 4-48).

However, a target is found in the general location of the 216-T-18 Test crib just north of the TY cribs. This feature is generally consistent with the shape and size of the target noted in the 2D inversion results along Lines 18E and 19N, discussed in Section 4.4.1.3.

Figure 4-44. STS Survey Lines and 3D TXTY-STS7ii Associated with Northern Waste Site Area – TX-TY Complex.

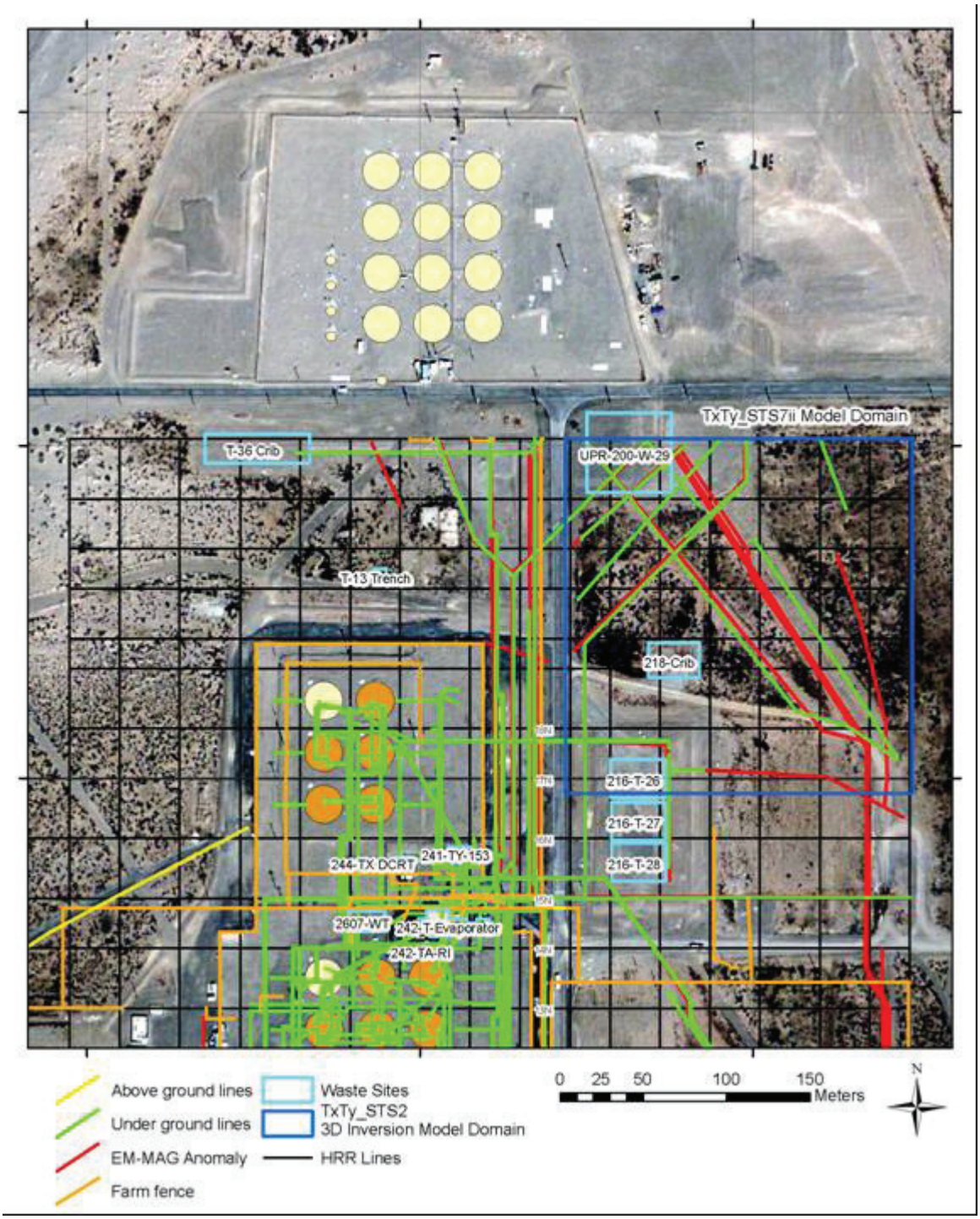

Table 4-5. Simulation Details and Statistics of 3D Model Domain TXTY-STS7ii.

Input File	TXTY-STS-7ii
Inversion start date	15:16:54 2008-07-23
Inversion end date	15:37:45 2008-07-23
Northing range (meter)	198
Easting range (meter)	198
Easting minimum	566893
Northing minimum	136403
Easting maximum	567091
Northing maximum	136601
Software version	AGI EarthImager3DCL
Number of electrodes	484
Number of data points	5909
Domain area (acres)	9.7
Number of domain nodes	112752
Number of iterations	7
Root mean square of final iteration	9.53

Figure 4-45. Convergence Curve for 3D TXTY-STS7ii Inversion Model.

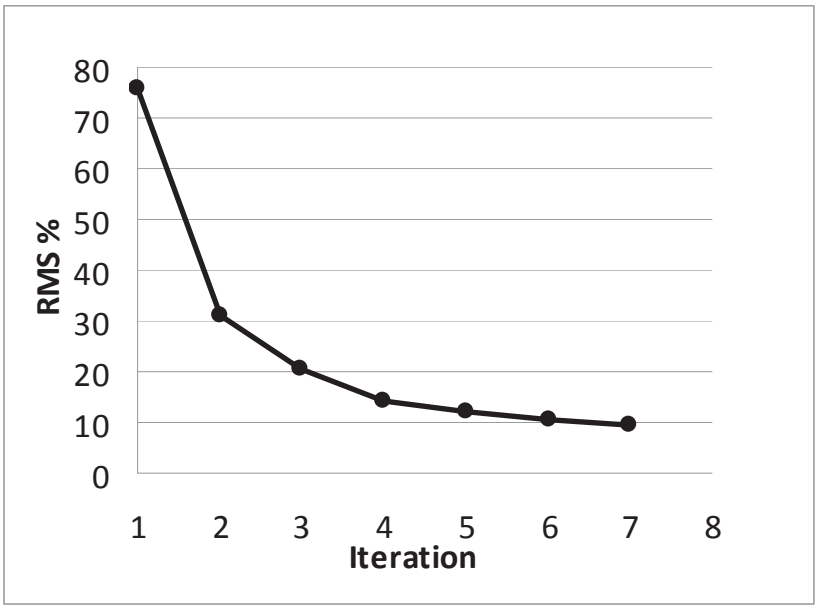

Figure 4-46. View of Model Results from Southeast Direction for 3D TXTY-STS7ii Inverse Model Domain.

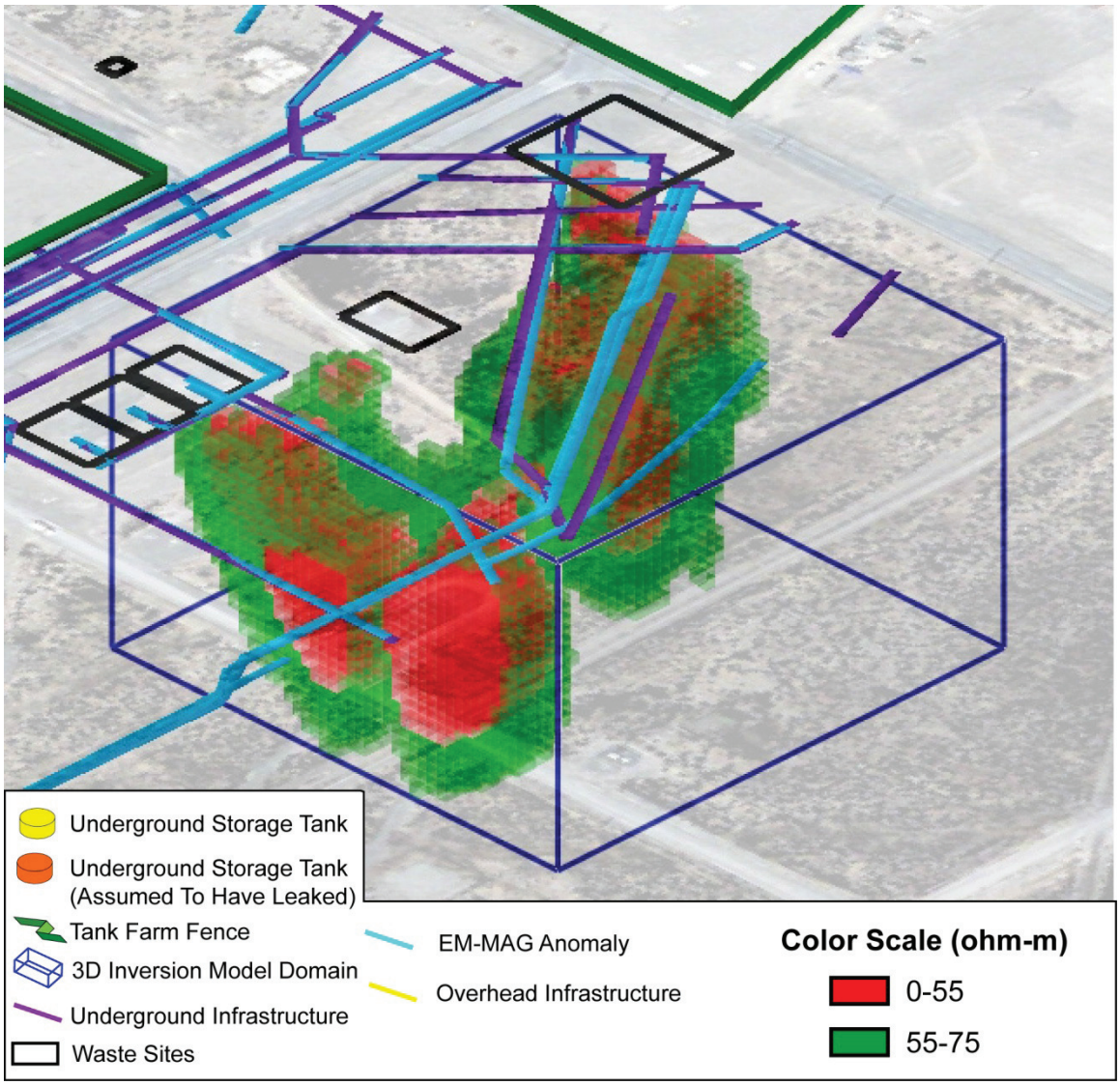

Figure 4-47. Plan View Model Results for 3D TXTY-STS7ii Inverse Model Domain.

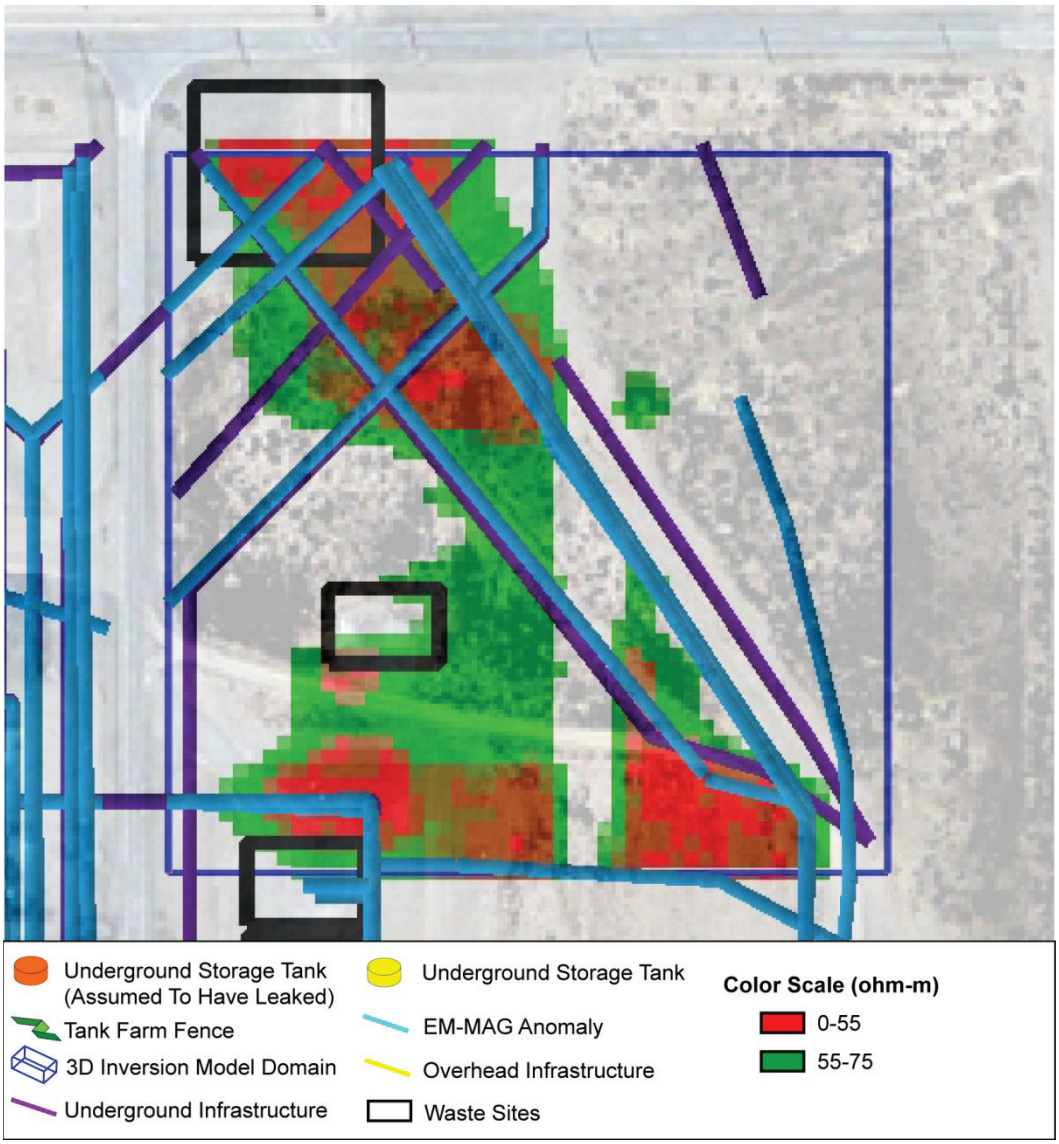

Figure 4-48. Cross-sectional View of Model Results from East Direction for 3D TXTY-STS7ii Inverse Model Domain.

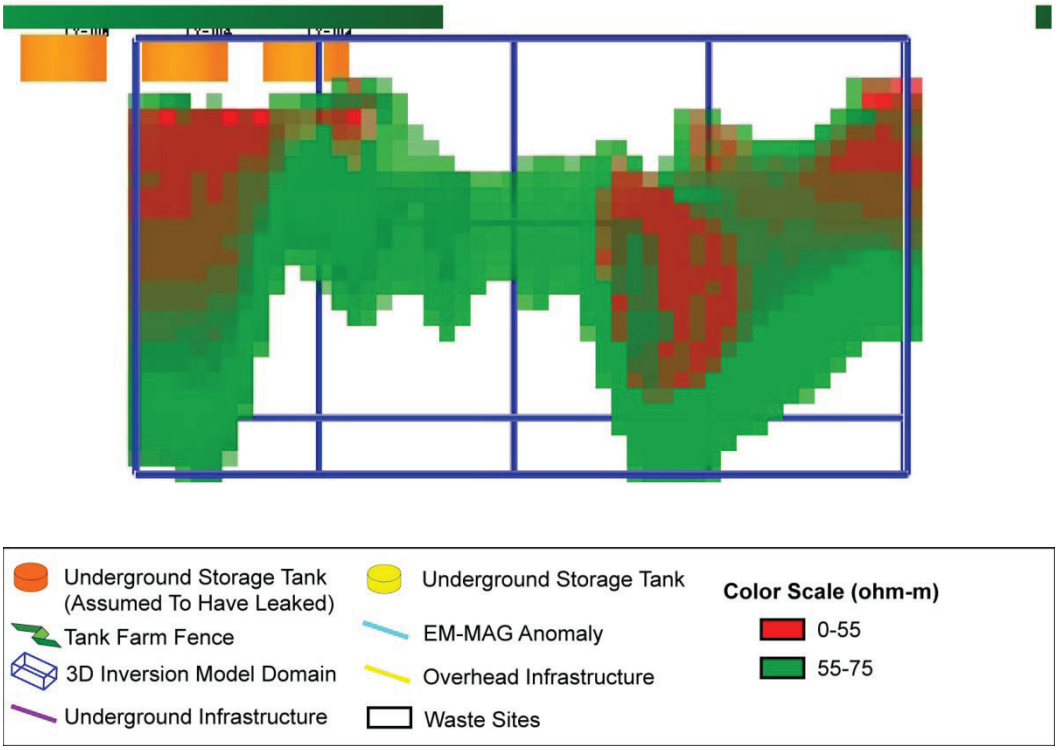

4.4.2.3 3D Inversion Model Results - TXTY-STS8. The TXTY-STS8i inversion model focuses on the western part of the northern waste site area where the amount of buried infrastructure is limited (see Figure 4-49). Model runtimes, domain description and convergence statistics for the TXTY-STS8i model are shown in Table 4-6. A plot of model convergence for this specific model is provided in Figure 4-50.

A review of modeling results and the small number of infrastructure locations show some association of a low resistivity target with buried infrastructure found just east of the 216-T-36 crib (Figures 2-7 and 4-49). The primary low resistivity targets in this model domain fall within the range of 0-40 ohm-m and are displayed as an iso-volume in semi-transparent red, with a secondary target of 40-55 ohm-m in semi-transparent green.

The most prominent low resistivity target (red volume) found along the north central part of the model domain is associated with the 216-T-36 crib (Figures 4-51, 4-52, 4-53, and 4-54). A pipe leading into the crib from the east does have some associated impact with the eastern edge of these targets. However, the target associated with the crib area itself is notable and expands into a hydrologically plausible shape beneath the crib area. This feature is generally consistent with the shape and size of the target noted in the 2D inversion results along Line 24N (discussed in Section 4.4.1.1).

No targets that could be associated with the 216-T-13 wastes site are evident in the model results.

Figure 4-49. STS Survey Lines and 3D TXTY-STS6 and TXTY-STS8i Model Domains Associated with Northern Waste Site Area – TX-TY Complex.

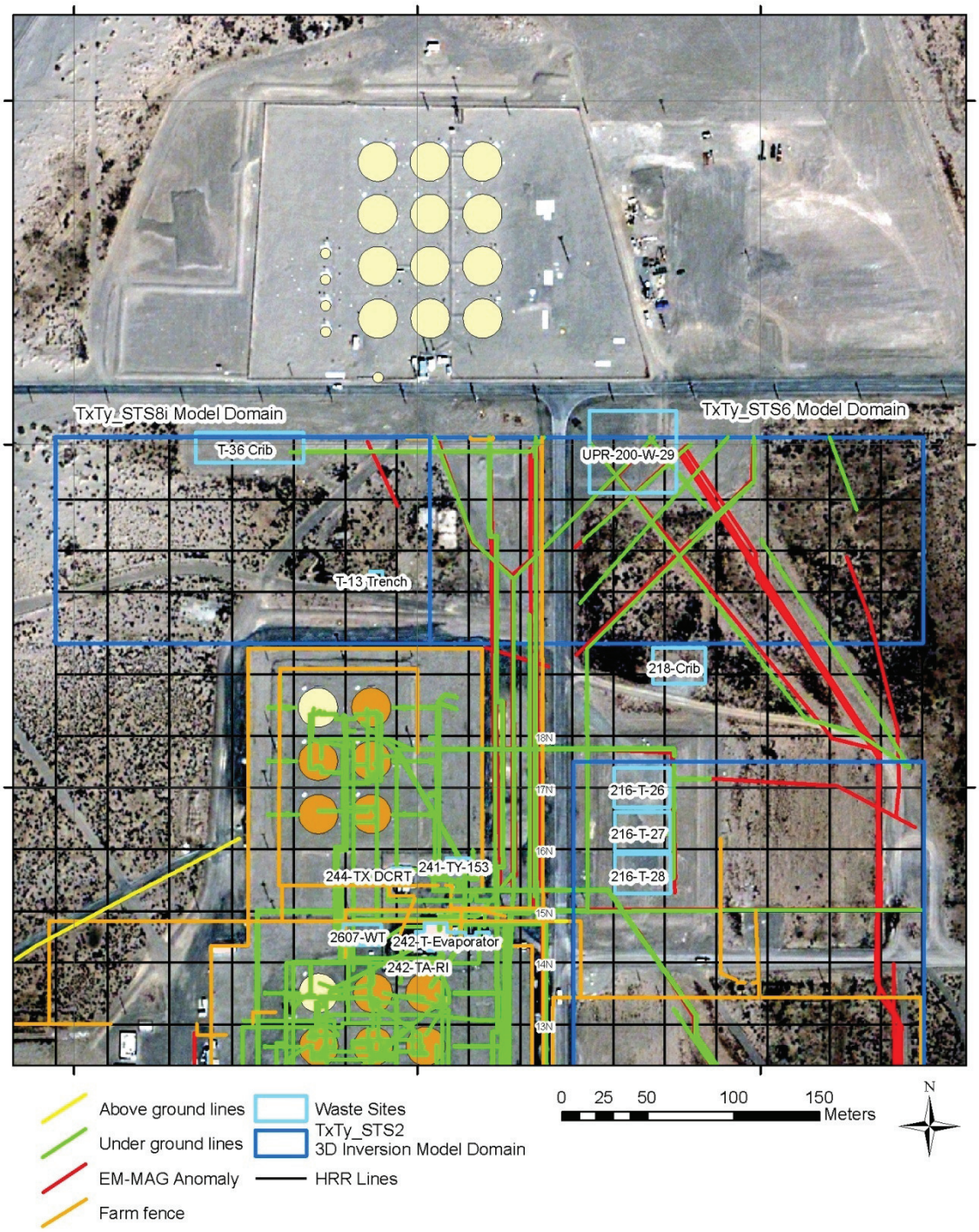

Table 4-6. Simulation Details and Statistics of 3D Model Domain TXTY-STS8i.

Input File	TXTY-STS8i
Inversion start date	10:50:52 2008-07-24
Inversion end date	10:52:50 2008-07-24
Northing range (meter)	114
Easting range (meter)	210
Easting minimum	566593
Northing minimum	136487
Easting maximum	566803
Northing maximum	136601
Software version	AGI EarthImager3DCL
Number of electrodes	287
Number of data points	3365
Domain area (acres)	5.9
Number of domain nodes	53040
Number of iterations	5
Root mean square of final iteration	6.16

Figure 4-50. Convergence Curve for TXTY-STS8i Inversion Model Convergence Curve.

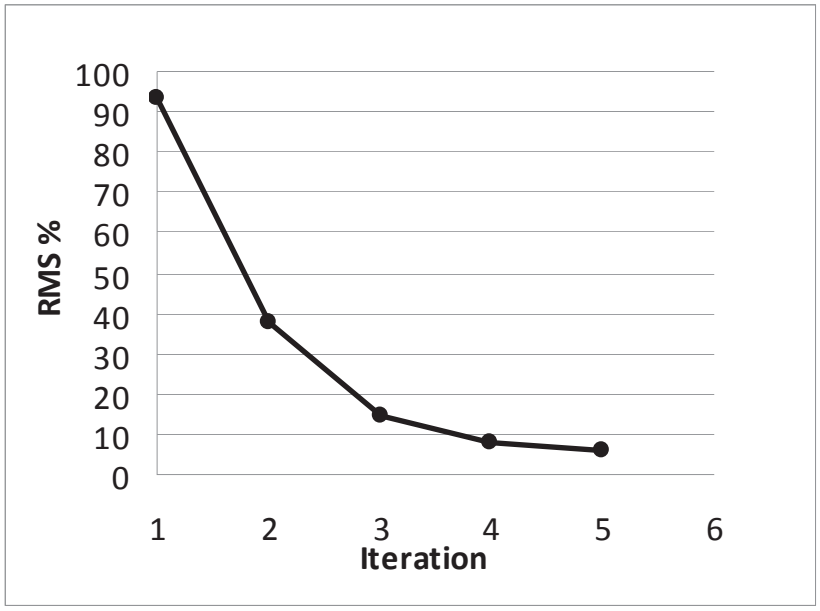

Figure 4-51. View of Model Results from Southeast Direction for 3D TXTY-STS8i Inverse Model Domain.

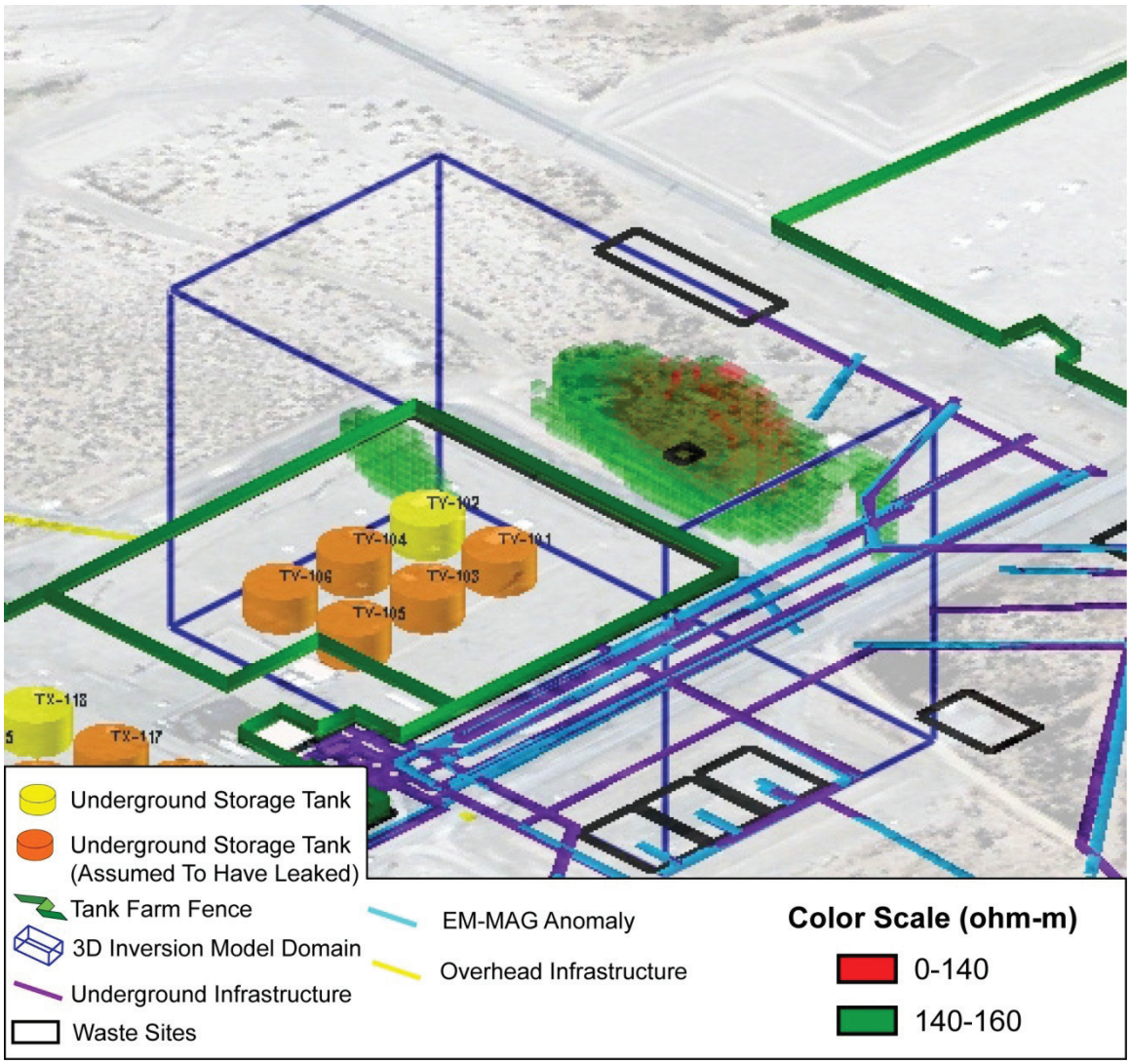

Figure 4-52. View of Model Results from Southwest Direction for 3D TXTY-STS8i Inverse Model Domain.

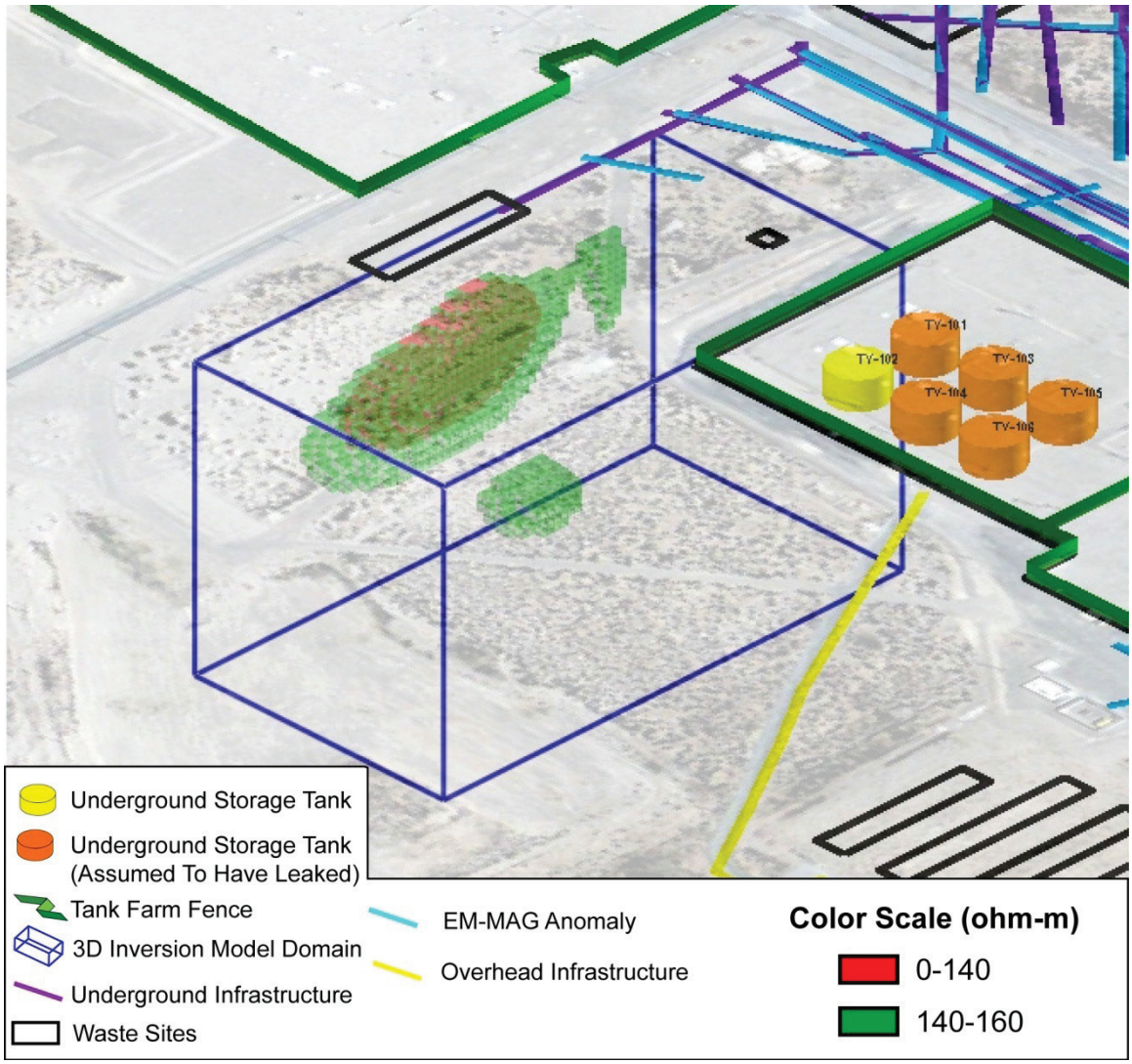

Figure 4-53. Plan View Model Results for 3D TXTY-STS8i Inverse Model Domain.

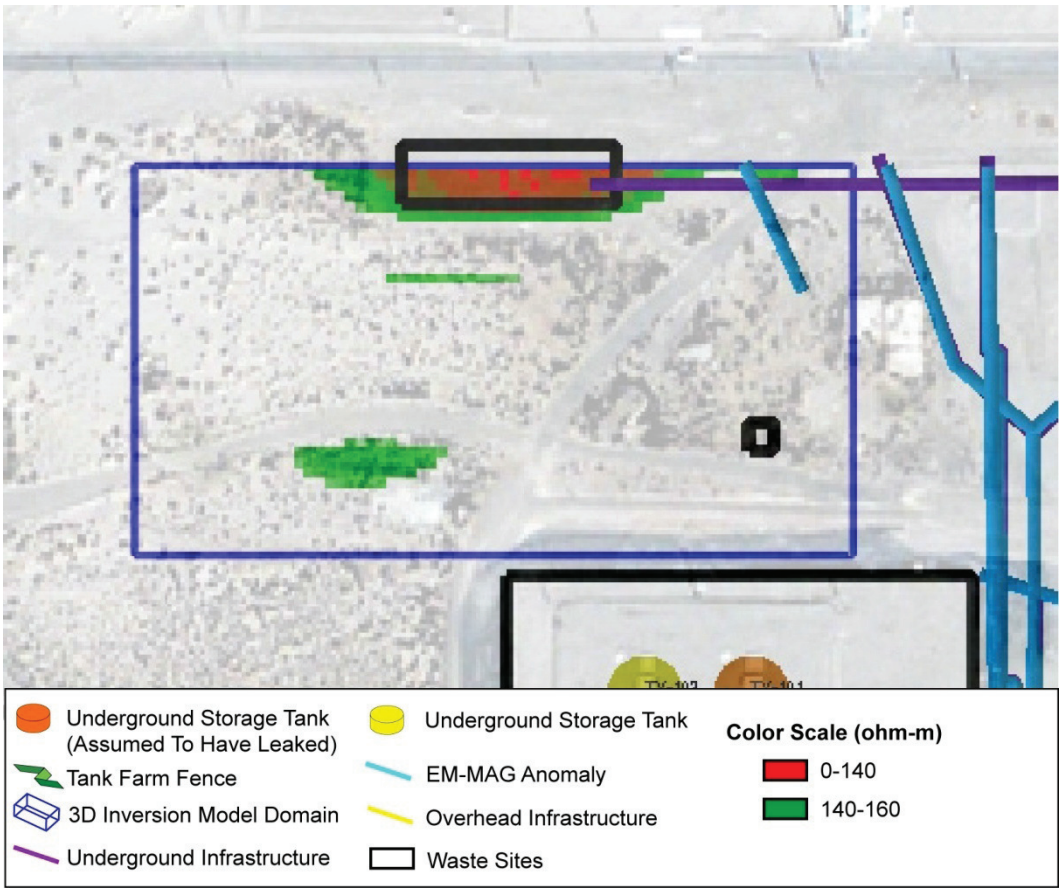

Figure 4-54. Cross-sectional View of Model Results from the North Direction for 3D TXTY-STS8i Inverse Model Domain.

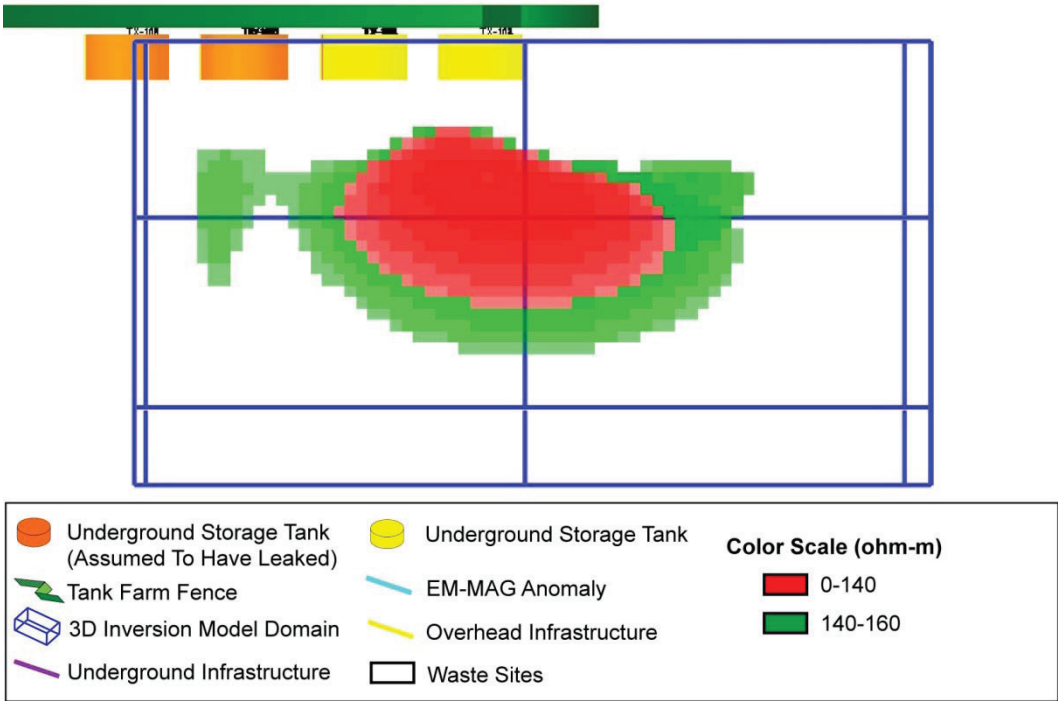

4.5 TX AND TY TANK FARM AREAS

Interpretation of WTW data was performed with the EarthImager3DCL v1.1.3 long electrode resistivity inversion modeling software. This software incorporates the resistivity data measured from long electrodes as well as accounting for the 3D position, diameter, length , and electrical conductivity of the steel well casings that comprise the long electrodes in the WTW model domains. Visualizations of the model results are shown in plan view as discrete low resistivity primary targets (red) and secondary targets (green). A small amount of depth information is available from these plots based on the color of the semi-transparent targets. For example, a deeper shade of red indicates that more of the primary target is present at depth when compared to lighter shades of red. This plotting scheme accounts for the lack of vertical control when locating 3D resistivity targets using steel well casings as long electrodes. A detailed discussion of the theory of long electrode resistivity measurements (WTW measurements), data quality control, resistivity inversion modeling and data visualization is given in Appendix B.

WTW data analysis using resistivity inversion models was performed in the following order:

- TX-TY Complex Models that considered all available electrode types including vadose zone wells, groundwater wells and point source electrodes which were added in an attempt to improve resolution in areas where wells were sparse, (TXTY-WTW1i inversion model)

- TX and TY Tank Farm models that considered smaller and more focused domains using various combinations of electrode types in order to improve results and answer questions that arose from modeling of the entire site.

The following presents the results and interpretation of these inversion model analyses.

4.5.1 WTW Data Analysis of TX-TY Complex area

The first focus of resistivity inversion model analysis considered all WTW data collected at vadose zone wells, groundwater wells, and point source electrodes within the entire TX-TY Complex. This model domain includes point source electrodes in areas of sparse well coverage in an attempt to expand the required rectilinear model domain to include areas outside the TX and TY farm fences where well distribution is sparse. The theoretical benefits of adding point source electrodes to expand the effective amount of data within the domain was inferred using synthetic forward modeling analyses detailed in the TX-TY Complex work plan (RPP-35244).

The TX-TY Complex model domain, referred to as the TXTY-WTW1i resistivity inversion model, is illustrated in Figure 4-55. The details of domain coverage and model parameters are provided in Table 4-7. The convergence chart for this model can be viewed in Figure 4-56.

Results for the TXTY-WTW1i inversion model are shown in Figure 4-57 as a primary low resistivity target of 0.1 to 5 ohm-m (semi-transparent red) and a secondary resistivity target of 5 to 10 ohm-m (semi- transparent green). A review of these results suggests that the use of WTW data collected at point source electrodes as a means of expanding data coverage in outlying areas and improving model resolution was not effective. A review of these model results produced no identifiable features related to specific tanks within the farms or waste sites outside the farms regardless of the primary and secondary target level selected.

Differences in the benefits of including point source measurements inferred in the pre-survey design analysis and the lack of effectiveness of including point source electrode measurements in field measured WTW data analysis suggest that other factors may be affecting the modeling results. A significant complication in measuring these data has to do with the large differences in contact resistance between the point source electrodes and the long electrodes. The difference in contact resistance between the two types of electrodes (shallow 11-inch point source electrodes and the much longer and firmly connected 230-260 foot groundwater wells) was found to have a 1-2 orders of magnitude difference at TX-TY Complex. The variability of the quality of the electrical contact with the local soils at TX-TY Complex for these two electrode types is not accounted for by the synthetic modeling methods commercially available at this time.

Modeling results within the TX trench area of the TXTY-WTW1i model, which rely almost exclusively on WTW data collected at point source electrodes, show the ineffectiveness of using these types of measurements in the WTW analysis. Results of the WTW analysis based on adding these types of measurements in this area show little resolution of the well-defined low resistivity target identified beneath these trenches in both the 2D and 3D analysis of the STS data provided in Section 4.1.

Based on the results of the TXTY-WTW1i inversion model, the next focus of WTW inversion models includes only wells as electrodes. However, based on the distribution of all available

wells at the TX-TY Complex, it is not possible to compile a rectilinear model domain which includes both vadose zone and ground water wells in an acceptable distribution. Based on the distribution of available groundwater wells and experience from previous SGE WTW efforts (references), subsequent WTW resistivity modeling efforts were focused on the higher quality data available from vadose zone wells inside the TX and TY tank farm fences.

The naming scheme for the WTW models is sequential and any gaps in model numbers between models included in this report chapter reflects models which were used for testing or models which did not achieve an appropriate convergence criteria and model results.

4.5.2 WTW Data Analysis of TY Tank farm area

The next focus of WTW resistivity inversion modeling was the local-scale area inside the TY farm. This model domain, referred to as the TXTY-WTW6 inversion model, considers only WTW data collected at wells completed in the vadose zone inside the TY tank farm fence (see Figure 4-55). Model runtimes, domain description, and convergence statistics for the TXTY-WTW6 model are given in Table 4-8. A plot of model convergence for this specific model is provided in Figure 4-58.

A review of results of the TXTY-WTW6 inversion model domain, provided in Figure 4-59, shows a primary low-resistivity target of 1-30 ohm-m (red) and 30-70 ohm-m (green). The distribution of the primary and secondary targets in this model suggests that a cluster of lower resistivity targets can be associated with underground tanks which are known to have leaked. This is particularly evident when comparing the general lack of low resistivity targets near Tank 102, which is not classified as a tank assumed to have leaked.

In addition to this possible correlation, the primary and secondary resistivity targets do not adhere strictly to a linear pattern along buried pipelines with regards to the buried infrastructure shown in Figure 4-59. The shape and position of the low resistivity targets in the TXTY-WTW6 model domain suggests that infrastructure alone does not fully explain the source of these targets.

4.5.3 WTW Data Analysis of TX Tank farm area

The next focus of WTW resistivity inversion modeling was the area inside the TX farm. This model domain, which is referred as the TXTY-WTW8 inversion model, considers WTW data collected from all wells completed in the vadose zone inside the TX tank farm fence (see Figure 4-55). Model runtimes, domain description, and convergence statistics for the TXTY-WTW8 model are given in Table 4-9. A plot of model convergence for this specific model is provided in Figure 4-60.

A review of results of the TXTY-WTW8 inversion model domain, provided in Figure 4-61, shows a primary low resistivity target of 0.1-5 ohm-m (red) and 5-10 ohm-m (green). The distribution of the primary and secondary targets in this model is more dispersed and irregular when compared to the TxTy_WTW6 domain. This target dispersion may be influenced by the significantly higher number of buried pipes and other infrastructure shown within the TX farm boundary (Figure 4-61) when compared with the TY farm area (Figure 4-59). The clustering of low resistivity targets around the 107, 108, 111 and 112 tanks and the more dispersed low

resistivity targets in other parts of the domain do not strictly follow the paths of known buried infrastructure, but they appear to be influenced by them to some degree in this area (Figure 4-61).

Figure 4-55. Model Domains of TX and TY Tank Farm Areas.

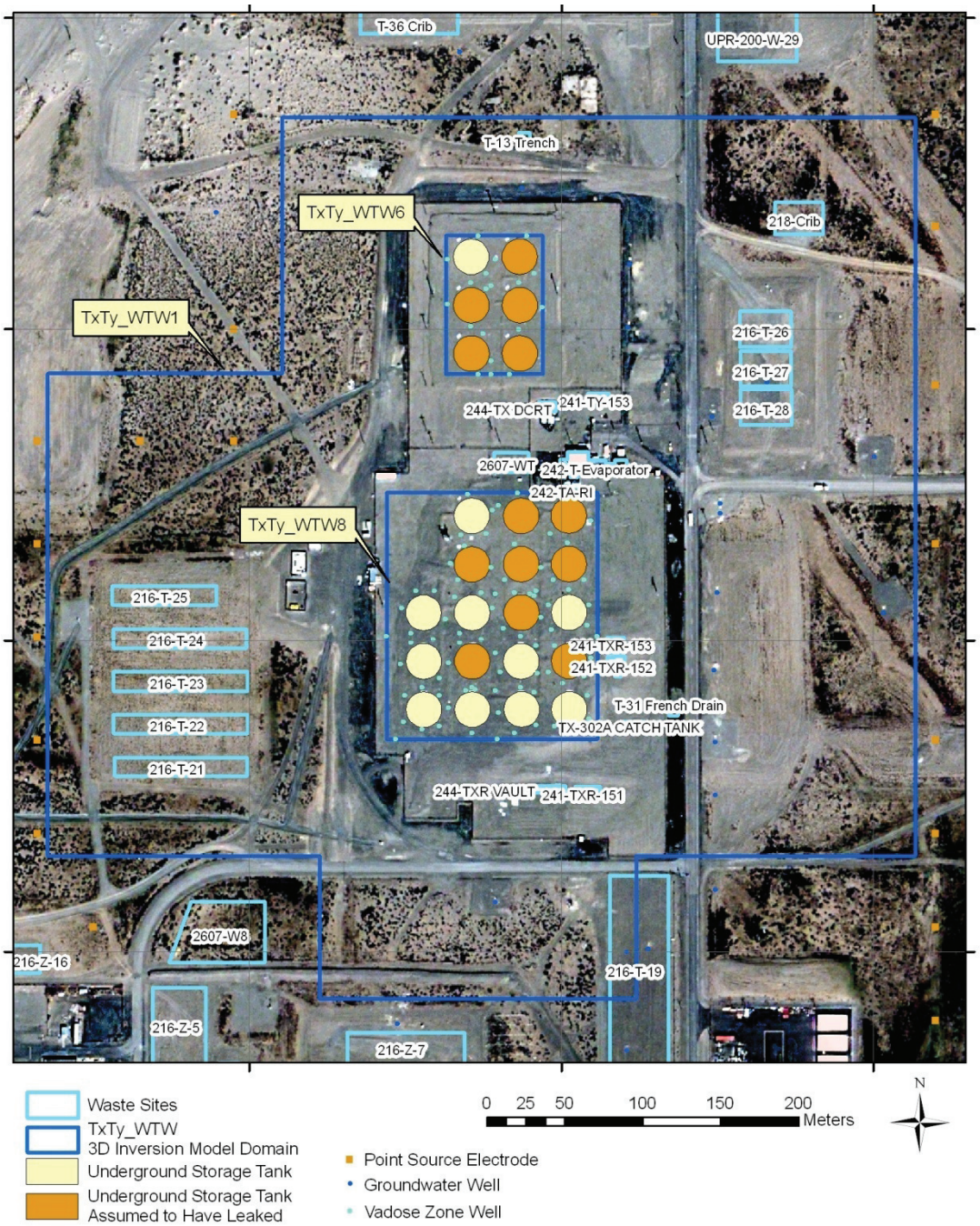

Table 4-7. Simulation Details and Statistics of 3D Model Domain TXTY-WTW1i.

Input File	TXTY-WTW1i
Start Date Time	11/27/07 15:54
End Date Time	12/12/07 13:01
Northing Range(m)	794
Easting Range(m)	693
Easting Min	566,409
Northing Min	135,825
Easting Max	567,102
Northing Max	136,619
Software Name	AGI EarthImager 3D CL v1.1.3
Electrode Type	Vadose Zone, Groundwater and Point Source
No. Electrodes	161
No. Data Points	10,965
Domain Area (acres)	136
No. Domain Nodes	10,303,236
Final RMS	5.68

Figure 4-56. Convergence Chart for WTW Inverse Model Domain TXTY-WTW1i.

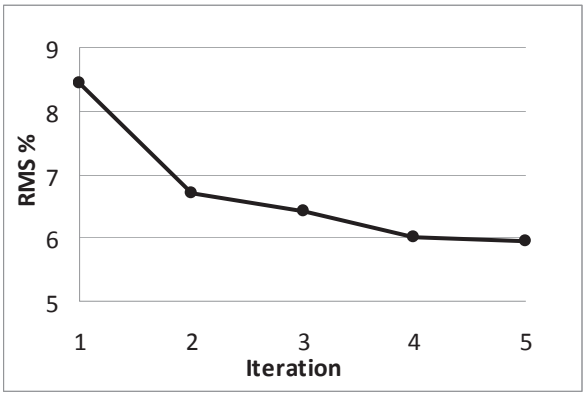

Figure 4-57. Results For 3D TXTY-WTW1i Inverse Model.

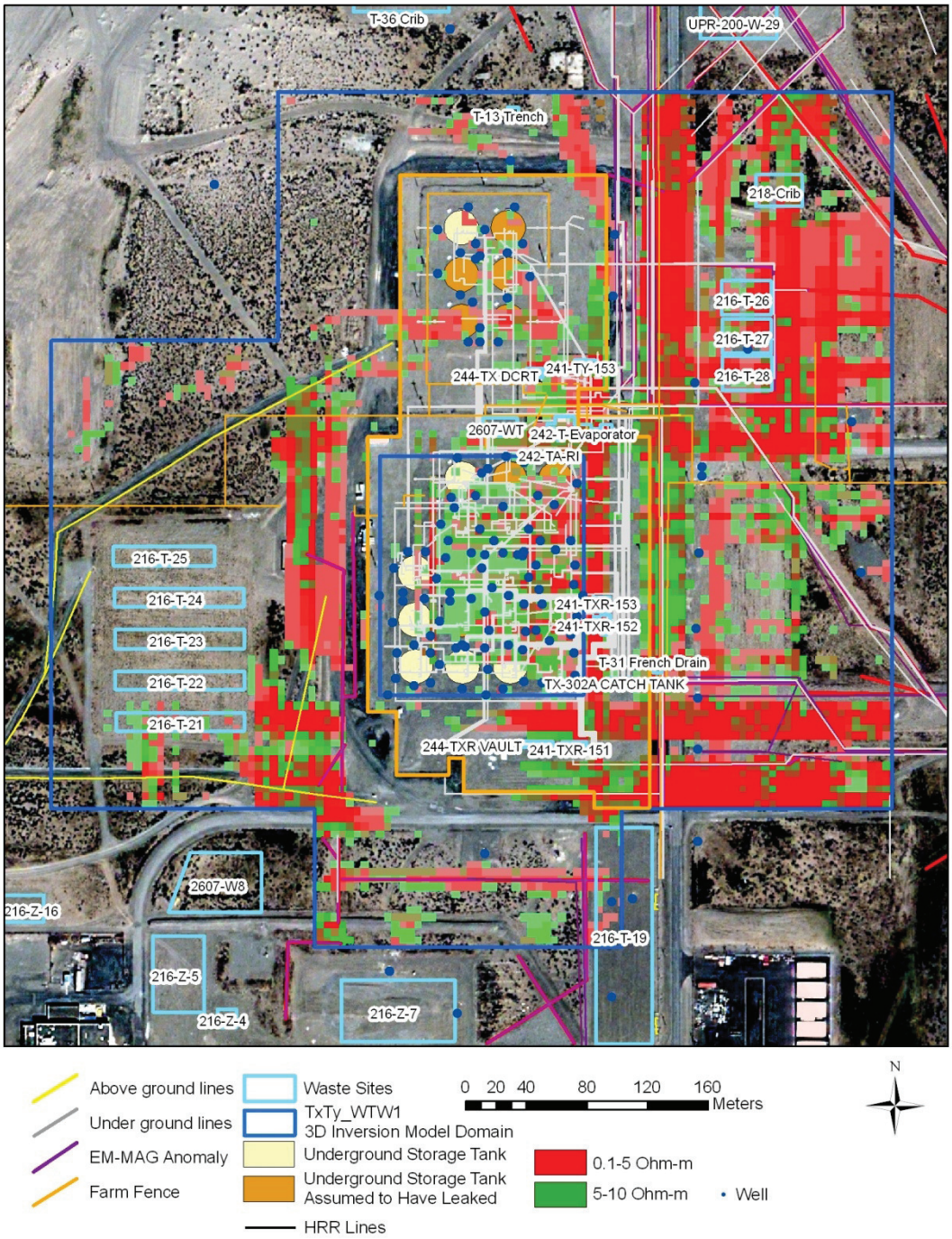

Table 4-8. Simulation Details and Statistics of 3D Model Domain TXTY-WTW6.

Input File	TXTY-WTW6
Start Date Time	1/25/08 19:21
End Date Time	1/25/08 19:42
Northing Range(m)	89
Easting Range(m)	61
Easting Min	566,727
Northing Min	136,371
Easting Max	566,788
Northing Max	136,460
Software Name	AGI EarthImager 3D CL 64-Bit
Electrode Type	VZ
No. Electrodes	21
No. Data Points	304
Domain Area (acres)	1
No. Domain Nodes	131,625
Root mean square of final iteration	9

Figure 4-58. Convergence Chart for WTW Inversion Model Domain TXTY-WTW6.

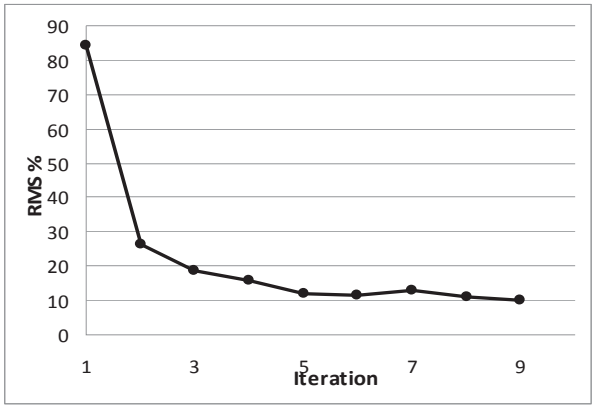

Figure 4-59. Model Results for 3D TXTY-WTW6 Inverse Model Domain.

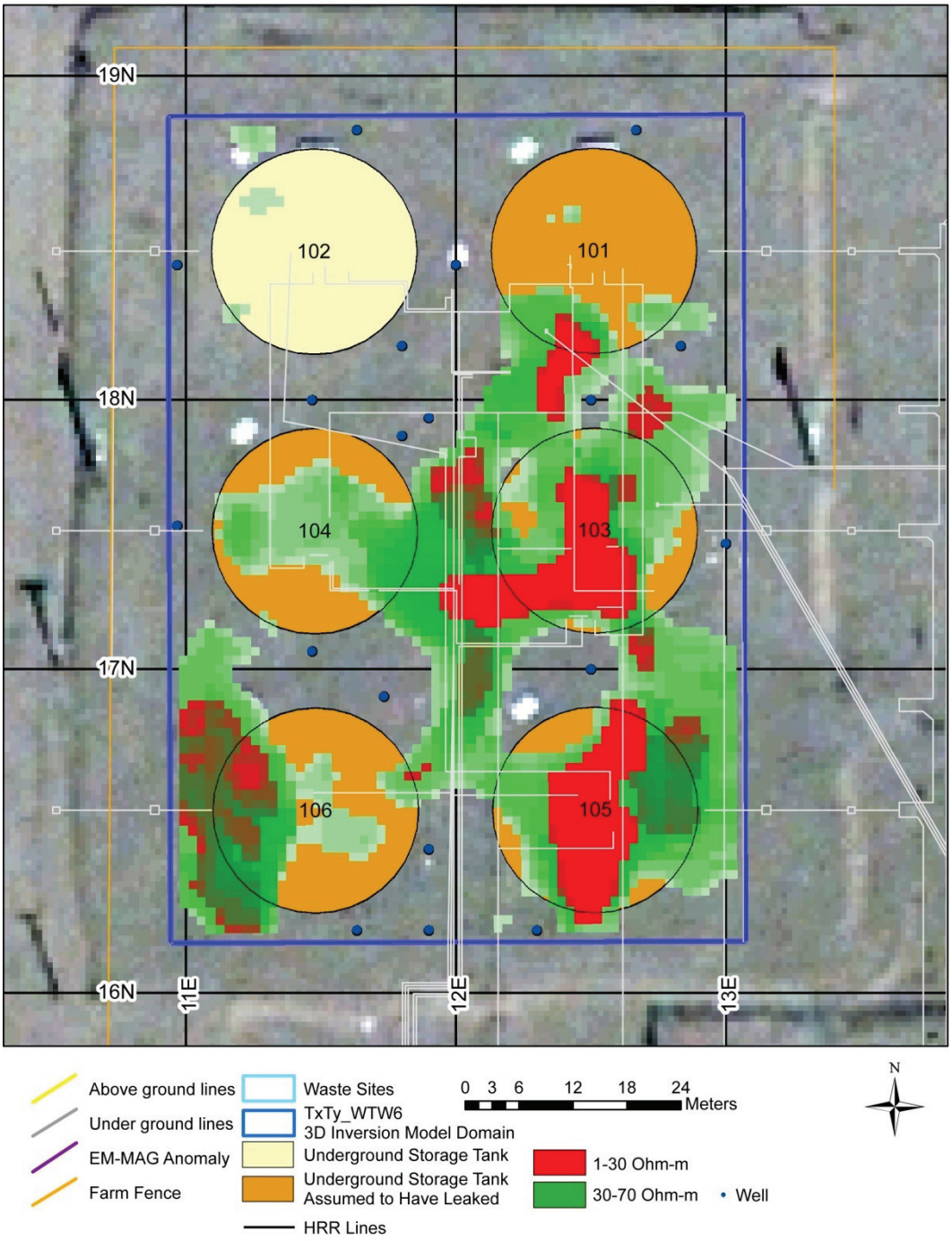

Table 4-9. Simulation Details and Statistics of 3D Model Domain TXTY-WTW8.

Input File	TXTY-WTW8
Inversion Operator	Jason Greenwood
Current Status	Converged
Start Date Time	1/30/08 19:14
End Date Time	1/31/08 10:47
Northing Range(m)	158
Easting Range(m)	135
Easting Min	566,688
Northing Min	136,137
Easting Max	566,823
Northing Max	136,295
Software Name	AGI EarthImager 3D CL 64-Bit
Software Version	v.1.1.3
Electrode Type	VZ
No. Electrodes	85
No. Data Points	6,586
Domain Area (acres)	5
No. Domain Nodes	957,145
Root mean square of final iteration	4.7

Figure 4-60. Convergence Chart for WTW Inversion Model Domain TXTY-WTW8.

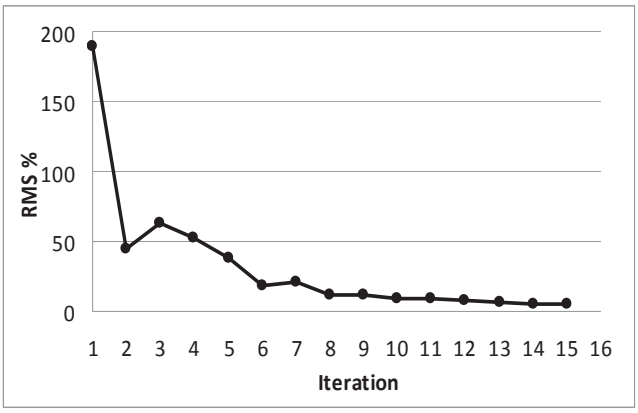

Figure 4-61. WTW Resistivity Inversion Model Results for the TXTY-WTW8 Domain.

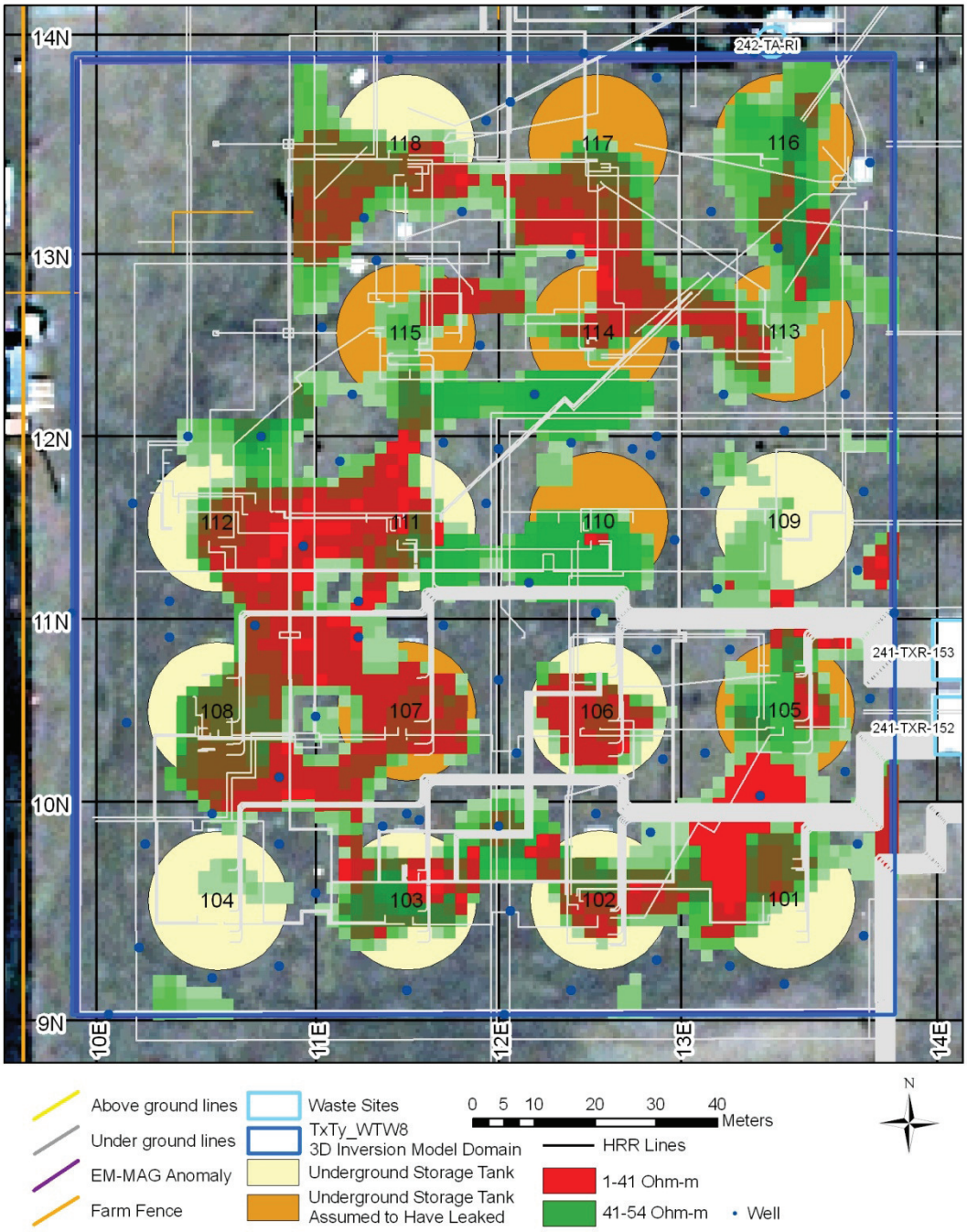

4.6 TX-TY COMPLEX AREA

The broader TX-TY Complex is the next area where resistivity was estimated with the inversion process. Analyses of this specific area were largely done with 3D inversion of STS resistivity data collected within the model domain shown in Figure 4-62.

4.6.1 3D STS Inversion Model Results

Resistivity data collected along the 23 east-west and 24 north-south STS survey lines in the TX-TY Complex area were evaluated in a 3D model of the area referred to as TXTY-STS3i. The lateral extent of this domain is given Figure 4-62.

3D inversion of the overall TX-TY Complex area was accomplished with EarthImager3DCL v1.13. Specific details and inversion statistics for this model domain are provided in Table 4-10. A plot of model convergence for this specific model is provided in Figure 4-63.

Figure 4-62. Model Domain of TX-TY Complex-Wide Model TXTY-STS3i.

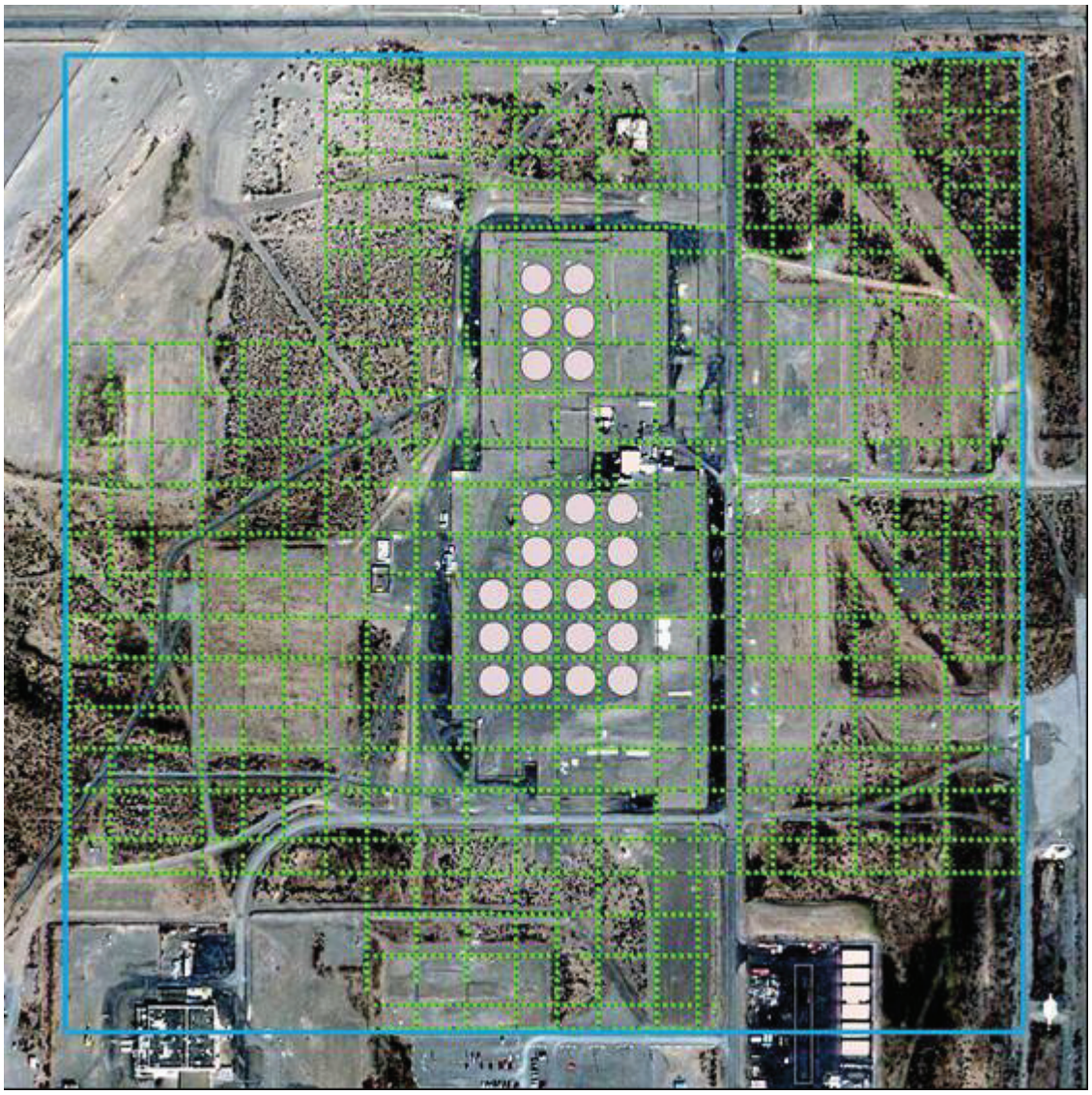

Figure 4-64 presents a view from above and the south-west direction of the results for the TXTY-STS3i model. The blue box in this figure defines the extent of the model domain. The model was inverted with all resistivity data at the 20-foot (6-meter) electrode spacing. The primary low resistivity target of 0 to 60 ohm-m is represented in semi-transparent red and the secondary resistivity target of 60 to 80 ohm-m is represented as semi-transparent green. Two aerial views, a plan view, and a side view of the the primary and secondary targets is given in Figures 4-64, 4-65, 4-66, and 4-67.

A review of modeling results shows that the location and aerial extent of the primary low resistivity targets can be associated with areas where buried metallic infrastructure are abundant (Figures 2-7 and 4-66). The most extensive areas of low resistivity are found beneath the TX and TY tank farms, the main road east of the tank farms, and areas to the east where subsurface infrastructure is pervasive. Other smaller areas of low-resistivity to the south and northeast contain linear low resistivity targets directly beneath pipelines or other buried infrastructure in the area.

Model results also suggest the occurrence of low-resistivity targets beneath the TX trench area west of the TX Tank farm. However, the aerial extent and depth of these targets is much more limited in size and shape than the low-resistivity targets identified beneath these waste sites in the local-scale 2D and 3D inversion modeling analysis of STS data presented in Section 4.1.

Additional targets identified beneath other wastes sites in the southern, eastern, and northern areas of the complex using local-scale 2D inversion models are not at all evident in the larger-scale inversion results for the TXTY-STS3i model. These results show that larger-scale STS inversion modeling in domains that include areas of significant buried infrastructure have clear limitations in identifying low resistivity targets at waste sites located both near areas with infrastructure and in outlying areas where infrastructure is not as prevalent.

Table 4-10. Simulation Details and Statistics of 3D Model Domain TXTY-STS3i.

Input File	TXTY-STS-3i
Inversion start date	16:32:55 2008-05-07
Inversion end date	05:05:08 2008-06-11
Northing range (meter)	702
Easting range (meter)	691
Easting minimum	566404
Northing minimum	135902
Easting maximum	567095
Northing maximum	136604
Software version	AGI EarthImager3DCL
Number of electrodes	3863
Number of data points	125574
Domain area (acres)	119.8659
Number of domain nodes	2478024
Number of iterations	12
Root mean square of final iteration	15.63

Figure 4-63. Model Convergence Showing RMS % and Iteration Number for the 3D Inversion Model of the TXTY-STS3i Domain.

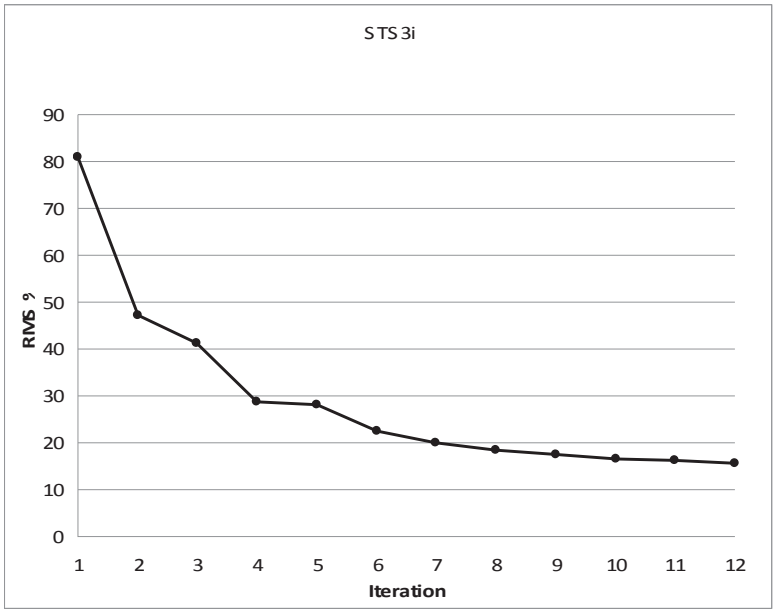

Figure 4-64. Isometric View of Model Results from Southwest Direction for 3D TXTY-STS3i Inverse Model Domain.

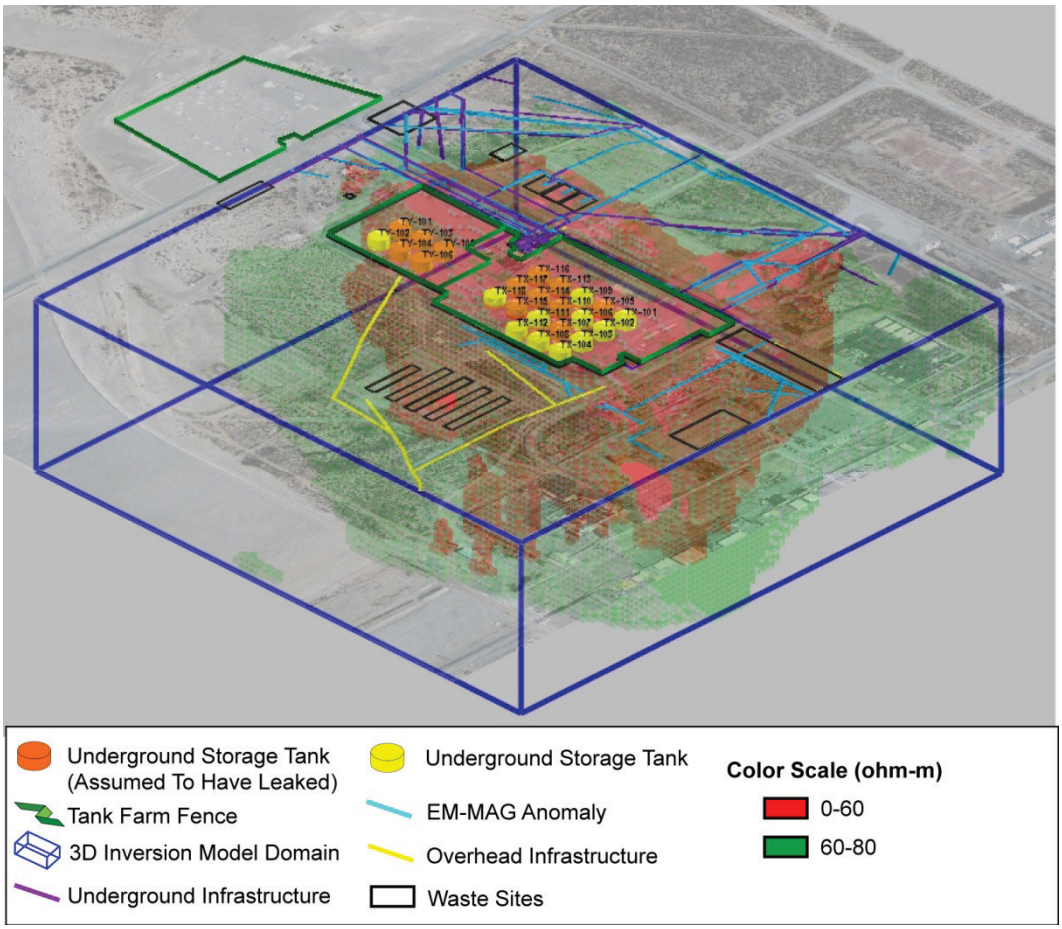

Figure 4-65. Isometric View of Model Results from Southeast Direction for 3D TXTY-STS3i Inverse Model Domain.

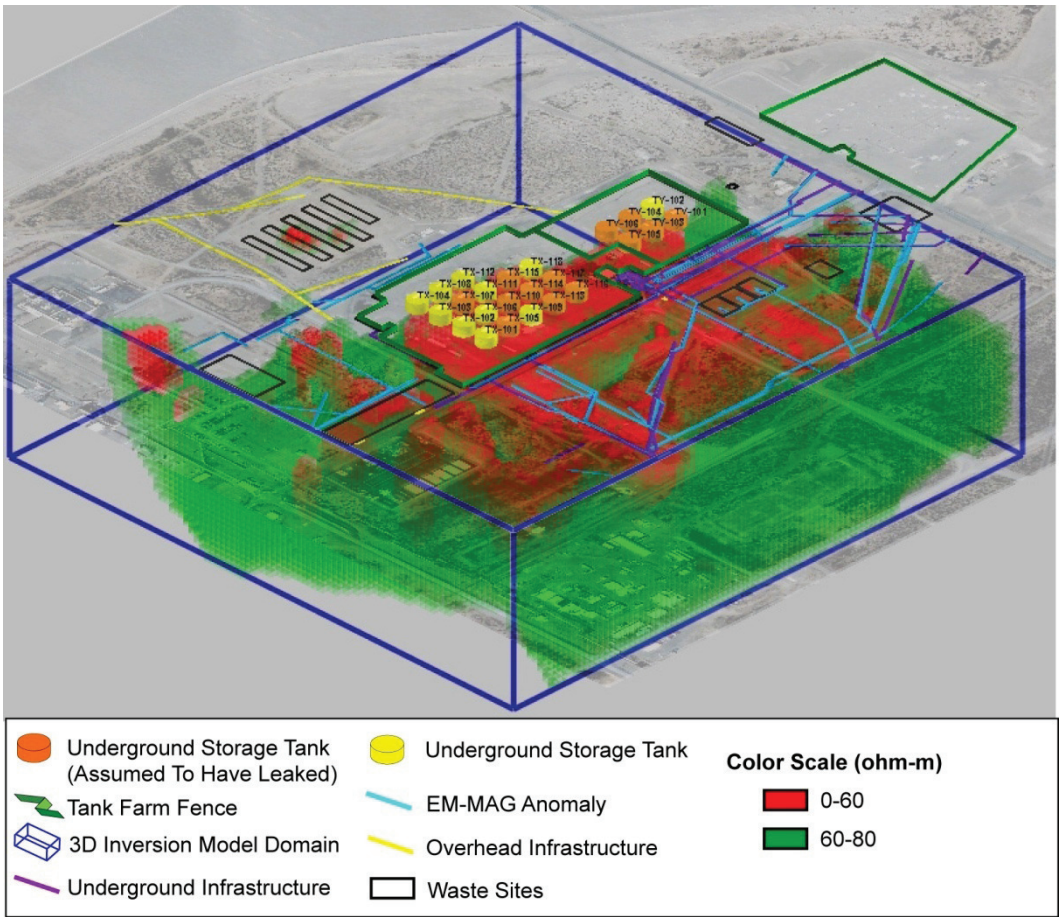

Figure 4-66. Plan View of Model Results For 3D TXTY-STS3i Inverse Model Domain.

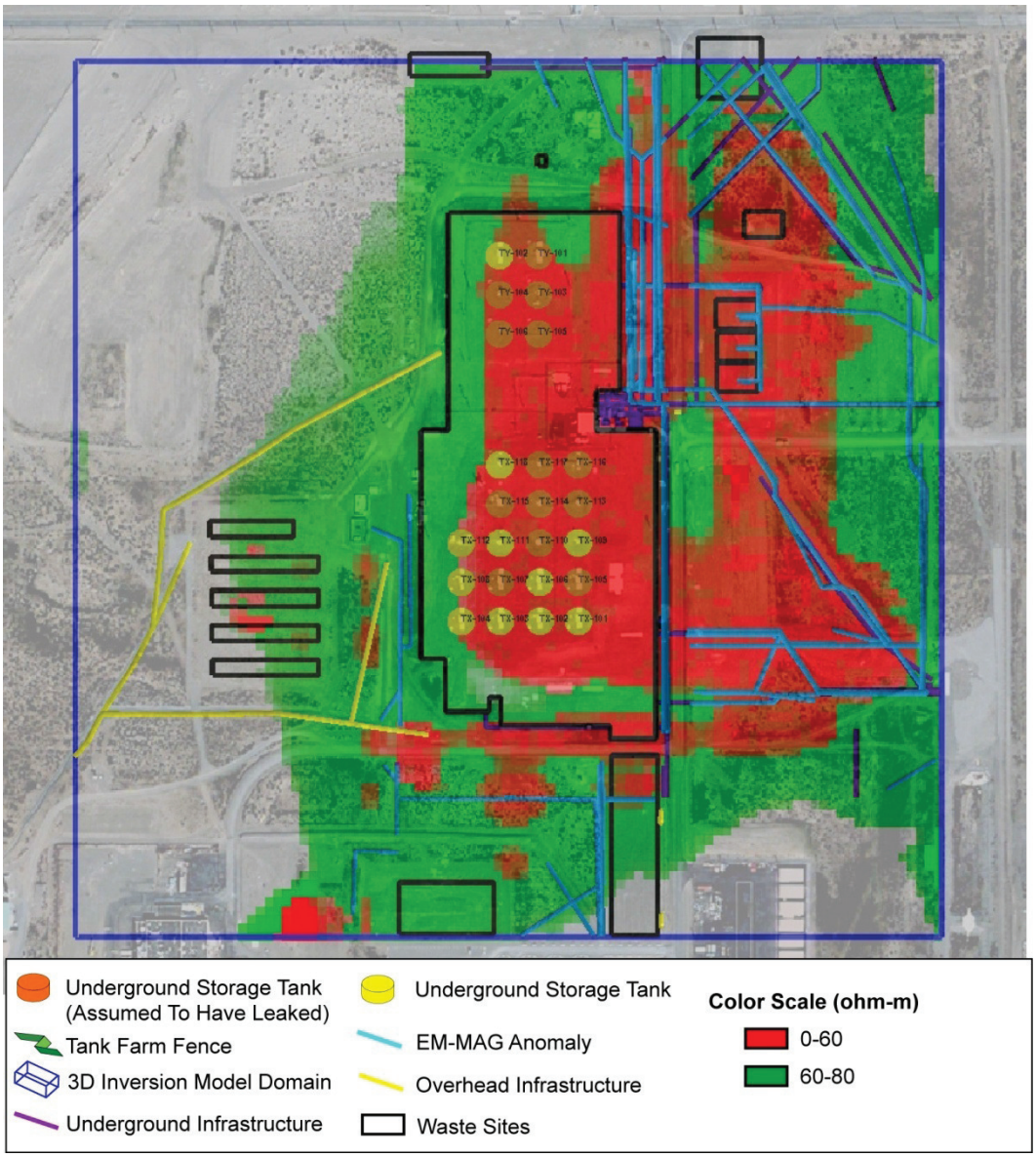

Figure 4-67. Cross-sectional View of Model Results from East Direction for 3D TXTY-STS3i Inverse Model Domain.

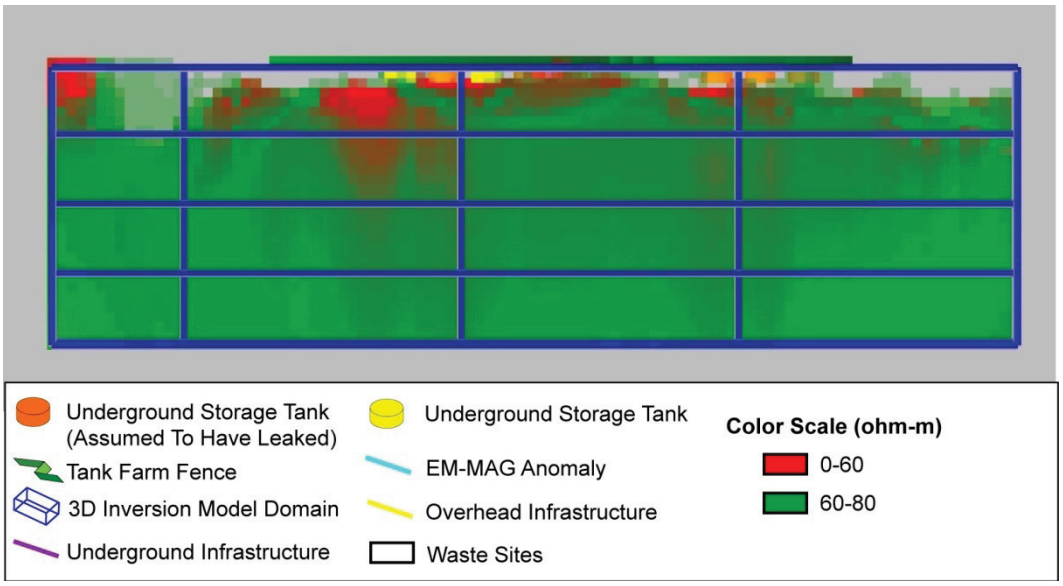

This page is intentionally left blank.

5.0 CONCLUSIONS

This section presents the conclusions drawn from the results and interpretations presented in Section 4.0. The primary objective of this investigation was to map areas or regions of low resistivity in and around the TX and TY Complex (TX and TY tank farms and surrounding areas) using electrical resistivity methods.

The TX-TY Complex area was characterized with both STS and WTW electrical resistivity methods. Both 2D and 3D were performed for all STS data collected both inside and outside the farm fence boundaries at the TX-TY Complex, including areas inside and outside the farm fence boundaries, was performed separately. The Res2DINV (Geotomo, Ltd.) inversion modeling software was selected for processing of all individual resistivity STS survey lines collected within the TX-TY Complex area. Res2DINV was chosen over EarthImager2D (Advanced Geosciences, Inc.) in order to make use of the least squares deconvolution method (Loke 1995). This method improves inversion model resolution by reducing distortions related to highly conductive materials buried near electrodes, such as metallic pipelines or other infrastructure.

3D inversion modeling of data collected for the TX-TY Complex, including areas inside and outside the farm fence boundaries, was performed separately with STS and WTW measurements. The EarthImager3DCL inversion software (Advanced Geosciences, Inc.) was selected for all 3D resistivity inversion models. EarthImager3DCL v1.1.3 resistivity was first developed during the B Complex SGE effort in order to effectively process very large and complex 3D resistivity inversion models that were previously not possible using commercially available software (RPP-34690, *Surface Geophysical Exploration of the B, BX, and BY Tank Farms at the Hanford Site*).

Following are the main conclusions from the results and interpretation of the WTW data analyses performed within the overall TX-TY Complex area and the TX and TY tank farm areas.

WTW Analysis of TX-TY Complex. A review of the TX-TY Complex-wide WTW results that considered all available electrode types including vadose zone wells, groundwater wells and point source electrodes, suggested that use of point source electrode data as a means of expanding data coverage in outlying areas and improving model resolution was not effective. These analysis results produced no identifiable features related to specific tanks within the farms or waste sites outside the farms regardless of the primary and secondary target level selected. Results within the TX trench area of this model domain, which rely almost exclusively on WTW data collected at point source electrodes, show the ineffectiveness of using these types of measurements in the WTW analysis. Results of the WTW analysis based on adding these types of measurements in this area show little resolution of the well-defined low resistivity target identified beneath these trenches in both the 2D and 3D analysis of the STS data.

WTW Analysis within the TY Tank Farm Area. A review of results of local-scale 3D inversion modeling in the TY Tank farm, that considered WTW data collected at only vadose zone wells in TY farm area, showed a primary low-resistivity target. These results suggested that a cluster of lower resistivity targets can be associated with underground tanks which are assumed to have leaked. This was particularly evident when comparing the general lack of low

resistivity targets near Tank 102, which is not known to have leaked. In addition to this possible correlation, the primary and secondary resistivity targets do not adhere strictly to a linear pattern along the locations of buried infrastructure. However, the shape and position of the low resistivity targets in this model domain suggested that infrastructure alone does not fully control the distribution of this target.

WTW Analysis within the TX Tank Farm Area. A review of similar 3D results of inversion modeling in the TX Tank farm, that also considered only vadose zone wells in TX farm area, showed primary low resistivity targets that were more dispersed and irregularly distributed when compared to the local-scale results for the TY Farm area. The dispersed nature of these results suggested some influence by the significantly higher number of buried pipes and other infrastructure shown within the TX farm boundary when compared with the TY farm area. The clustering of low resistivity targets around the 107, 108, 111 and 112 tanks and the more dispersed low resistivity targets in other parts of the domain did not strictly follow the paths of known buried infrastructure, but they appeared to be influenced by them to some degree.

Following is a brief discussion of the main conclusions of the results and interpretation of the STS data analyses performed for the entire TX-TY Complex and in selected waste site areas outside of the tank farms.

STS Data Analysis of the TX-TY Complex. Review of 3D inversion modeling of all STS resistivity data collected within this model domain showed that the location and aerial extent of the primary low resistivity targets can be associated with areas where buried metallic infrastructure are abundant. The most extensive areas of low resistivity were found beneath the two tank farms, the main road east of the tank farms, and areas to the east where subsurface infrastructure is pervasive. Other smaller areas of low-resistivity found to the south and northeast appeared to contain distinct features associated with major pipelines or buried infrastructure. These results showed that larger-scale domain STS resistivity inversion models which include areas of significant buried infrastructure have clear limitations in identifying low resistivity targets at waste sites located both near areas with infrastructure and in outlying areas where infrastructure is not as prevalent

3D model results for the broader domain also suggested the occurrence of low-resistivity targets beneath the TX trench area west of the TX Tank farm. However, the aerial extent and depth of these targets was much more limited than the size and shape of low-resistivity targets identified beneath these waste sites in the local-scale 2D and 3D inversion modeling analysis of STS data.

Targets that were identified beneath other wastes sites in the southern, eastern, and northern areas of the TX-TY Complex using local-scale 2D inversion models were not evident in the larger-scale inversion results. These results show that larger-scale domain STS resistivity inversion models which include areas of significant buried infrastructure have clear limitations in identifying low resistivity targets at waste sites located both near areas with infrastructure and in outlying areas where infrastructure is not as prevalent

STS Data Analysis of Waste Site Area outside the Tank Farms. The results from both 2D and 3D inversion of the resistivity data collected in the area of the TX trenches west of the tank farms showed a clear low-resistivity target relative to a background resistivity, directly below the trenches. The primary target in this region was a low (1-30 ohm-m) resistivity target located directly below the 216-T-21 to 216-T-25 trenches. The area of the low-resistivity target was

primarily contained within the footprint of the trenches. Analysis of the STS data in the 2D and 3D analysis suggest that the low-resistivity target is isolated from the expected water table depth.

Review of 2D and 3D analyses showed that nearly all east-west and north-south lines that cross the 216-T-19 crib and tile field and the 216-Z-7 areas south of TX tank farm were impacted by the presence of buried infrastructure and surface fences. However, review of selected 2D resistivity inversion models in the 216-T-19 crib and tile field area revealed a primary shallow low resistivity target that runs for much of the length of this waste site in the north-south direction. In addition, selected 2D model results near the 216-Z-7 crib area revealed a low resistivity target centered beneath the crib area.

Review of 2D results of nearly all east-west and north-south survey lines that cross the TY cribs area and 216-T-31 French drain areas east of the tank farms showed significant impacts from the presence of buried infrastructure and surface fences. These impacts made it difficult to identify any specific low-resistivity targets below these waste site areas. 3D modeling results of the area east of the tank farms that included these waste site areas showed primary low-resistivity targets that were linear and along areas of buried infrastructure. However, the size and depth of these targets appears to be too large to be caused by the impact of surface and buried infrastructure alone and may also show lower resistivity values due to potential leaks from pipelines.

Selected 2D analysis results of the area north of the TY tank farm identified low-resistivity targets generally located below the 216-T-36 crib, the 216-T-13 trench, and the 216-T-18 Test crib. However, only selected 3D analysis of STS data over the western and eastern part of the northern area yielded low resistivity targets beneath the 216-T-38 and 216-T-18 Test crib area that were consistent with the results of the 2D analysis at the same area. 3D analysis of STS data over the western half of the northern area was not able to confirm the results of the 2D analysis for the 216-T-13 trench area.

Areas with substantial infrastructure continue to present the most difficulties with regard to inversion modeling and associated interpretation of estimated resistivity distributions.

An overall review of both 2D and 3D inversion modeling results showed, in particular, that deeper model layers surrounding waste site areas, where infrastructure such as pipelines and groundwater wells are abundant near surface electrodes, showed apparent low-resistivity targets that are dominated by this infrastructure. The presence of these low resistivity targets can dominate the lower parts of model domains and obscure either changes in resistivity due to the effects of waste site discharges or to the expected gradual lowering of resistivity as one approaches the local water table at approximately 80 m. However, several targets located directly beneath some of the waste site areas cannot be accounted for by known infrastructure alone.

Target acquisition was improved in some areas of the Complex by focusing smaller model domains, when possible, between areas of known pipelines or other buried infrastructure. This was particularly evident by comparing the low resistivity target identified beneath the T-36 crib in the smaller and more focused model domain in the western part of the northern area of the complex and the complete lack of the same target in the much larger model domain which extended further to the east across a network of pipelines and infrastructure.

6.0 LIMITATIONS

The TX and TY farm area provides a challenging environment for surface geophysical characterization of subsurface soil conditions. This section describes impacts to the resistivity method caused by limitations in the electrodes (placement, dimensions, depth, and geometry), data collection equipment, deployment logistics, survey design, processing and visualization.

6.1 ELECTRODE GEOMETRY

Buried infrastructure has the greatest negative effect on acquisition of data, data interpretation, and data visualization. In addition, above-surface structures (e.g., pipelines, well heads, overhead power lines, tanks, metal buildings) prevent optimal placement of electrodes while also contributing to electrical and magnetic responses that mask changes caused by subsurface hydrogeologic changes. Data collection is limited by the quantity of available equipment, the logistics for deployment within an active work area, and project economics.

6.2 EQUIPMENT

The surface data were collected in a 2D arrangement, which was logistically easier and more cost effective due to the reduced equipment requirements relative to a fully 3D data acquisition effort.

The SuperSting R8 is limited to a 400-volt transmitter and the resolution of the data acquisition card is limited to a maximum of 30 nanovolts. The limited surface electrode grounding caused by limiting the permanent electrodes to less than 11 inches (28 centimeters), due to site safety restrictions, proved difficult in transmission with only a 400-volt system. Although this did not prevent data acquisition, it decreased the signal-to-noise ratio.

6.3 DEPLOYMENT LOGISTICS

Survey design and data collection efforts were constrained by existing above-grade infrastructure as well as the tank locations in the subsurface. Surface line location and spacing was limited to between tank rows. Previous experience covered in the survey design section of the work plan (RPP-PLAN-34594) indicates that attempting to collect a line of resistivity data over the top of a row of tanks would result in poor quality data. Above-grade infrastructure limits the placement of surface electrodes and ability to collect GPR data across the entire area of interest.

6.4 SUBSURFACE INFRASTRUCTURE

Infrastructure was mapped using a multi-method geophysical reconnaissance survey consisting of magnetic gradiometry, electromagnetic induction, and ground penetrating radar. The reconnaissance survey mapped the location and relative signal strength of underground pipelines and tanks. The end goal of inversion is to return a plume to original size, location, and electrical properties prior to infrastructure distortion. However, distortions due to infrastructure where large material property contrasts exist over short distances, prevent full reconstruction of plume shape and depth.

Additional constraints are necessary to increase the number of model equations to ensure the uniqueness in the solution. Figure 6-1 shows the results of inverting the apparent resistivity of a plume (10 ohm-meters) and near surface pipe at station 300 meters (0.01 ohm-meters) within a homogeneous background (1,000 ohm-meters) example. An a-priori model was used to attempt to correct for the pipeline influence. Potential field theory assumes that the total potential distribution has (nearly) the same value as the sum of each subsurface feature (i.e., background soil, plume, and pipe) modeled separately. Figure 6-1 inversion was completed using EarthImager2D with a smooth inversion scheme. The inversion reproduces the plume more accurately than an apparent resistivity pseudo-section but the bottom of the plume is still not well resolved, and the plume is highly pock-marked with the effects of pipe removal.

Figure 6-1. Electrical Resistivity Inversion of a Plume (10 ohm-meters) in a Homogeneous Background Sand (1,000 ohm-meters) with a Pipe (0.01 ohm-meter) at the Surface.

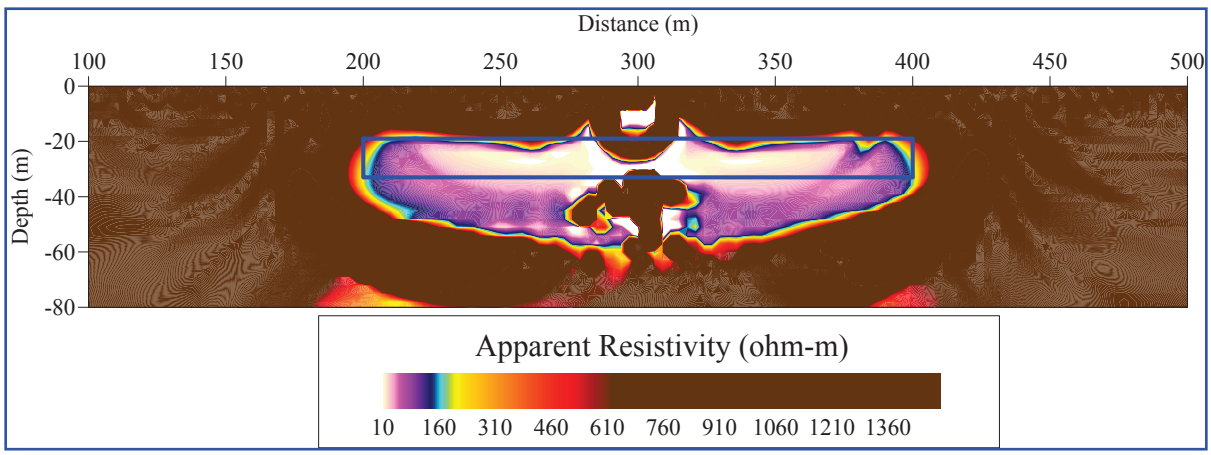

Note: The blue box represents original location of the plume during forward modeling with EarthImager2D.

The first attempts to accommodate the negative influence of infrastructure on resistivity data occurred during the T Farm SGE project (FY2005), where several models were inverted that contained varying degrees subsurface components, such as a tank or pipe. The simplest model illustrates a plume within a homogeneous unsaturated background soil. The plume has an electrical resistivity of 10 ohm meters, and the background soil has a resistivity of 1,000 ohm meters.

Resistivity inversion removes the “pants leg” resulting from pipe and tank effects. However, inversion does not adequately constrain the depth of the plume when data are collected from the surface only. Additionally, material property contrasts over short distances provide an additional level of difficulty for the inversion. Constraints are necessary to increase the number of model equations to ensure the uniqueness in the solution.

6.5 INVERSION

Processing system Random Access Memory (RAM) was the primary limitation for inversion model complexity. Previous SGE inversion models were severely limited by model domain size and required that data was batch processed into several smaller sub-domains. The development

of EarthImager3DCL has allowed very large model domains that contain the entire TX-TY Complex. Sub-domains in this effort were chosen based on specific data types and targets of interest (i.e., cribs and tile fields and electrode types). Nevertheless, it was possible to exceed the maximum RAM available for processing (128 GBytes with sixteen 3.0 GHz Pentium Quad Core processors) when running the most demanding model domains which contained the entire TX-TY Complex area and both 3 meter and 6 meter spaced STS data.

RAM requirements are minimized by proper cable layout which limits the number of unique rows and columns in the inversion model by placing electrodes along evenly spaced linear northing and easting lines. Memory requirements are further reduced when lines cross at the same electrode location. Line layout is complicated by infrastructure and the accurate placement of the lines using GPS by different operators at different times both inside and outside the farm boundaries.

6.6 VISUALIZATION

Visualization of TX-TY Complex datasets within a 3D space that contains infrastructure and aerial or satellite imagery is challenging. The extremely large size of the resistivity datasets required long computation times in order to render 3D volumes for plotting. These data were plotted using current releases of the commercially available software Rockworks, Golden Software Voxler® and Surfer®, ESRI® ArcMap 9.2, and MATLAB® 7.

The viewing angle, shading, lighting and optimal distribution of color values were chosen to allow the reader to see maximum details in the subsurface geophysical data while preserving key surface features, such as tanks and boundaries. Nevertheless, the number of concurrent volumes and colors in any given 3D volume was limited based on the viewing angle and mixing (transparency) of colors. Because of these limitations, some targets are better understood by viewing the 2D resistivity inversion plots or by viewing 2D slices of the 3D resistivity inversion volumes. The future addition of user selectable 3D digital models or motion graphics content may help solve these issues.

6.7 INTERPRETATION

6.7.1 Relating Resistivity Results to Contamination

SGE inversion results show low-resistivity targets that may be caused by an increase in soil moisture or inorganic salt concentrations. In the B-Complex analysis, laboratory resistivity measurements of soil samples representative of the Hanford, Cold Creek and Ringold formations were acquired to derive petrophysical relations (*Petrophysical Relationships of Electrical Resistivity for Hanford-Specific Soils* [RPP-33356]). It is hoped that the quantified relationships between electrical resistivity in response to increasing water content and soil contaminants (e.g., sodium nitrate or other inorganic salts) content will allow better calibration of observed

® Voxler and Surfer are registered trademarks of Golden Software, Inc.
® ESRI is a registered trademark of Environmental Systems Research Institute, Inc.
® MATLAB is a registered trademark of Mathworks, Inc. (Registrant).

SGE resistivity targets. The resulting data should provide a better understanding of what resistivity levels, in ohm-meters, best represent actual plume boundaries.

It is important to consider the confidence and reliability of the inversion results in order to avoid false positives and false negatives. To help establish confidence in evaluating areas of low resistivity, the following criteria should be confirmed.

- Do the results match hydrologic expectations correlating to waste disposal areas?
- Can the results be verified through core sampling data?
- Can the results be verified through a different geometric configuration of SGE?
- Are the low-resistivity areas continuous over broad areas?

6.7.2 Relating Resistivity Results to Other Characterization Methods

Direct comparisons should not be made to the other characterization methods employed at the tank farms, such as spectral gamma logging. This comparison is not endorsed on many levels. First, the scales of measurement between the two systems are highly disparate. The spectral gamma probe logs a drywell with a field of vision near the well. By contrast, SGE obtains large-scale volumetric averages covering areas the size of a tank farm. The scale increases for surface resistivity inversion with depth, and increases for WTW inversion at larger separations. Second, the contaminant of interest for each method (i.e., inorganic salts for SGE and gamma emitting radionuclides for spectral gamma) moves through the vadose zone under different mechanisms. Inorganic salts, especially nitrate, are transported primarily under advection or diffusion with little to no retardation. The nitrate plume will be relatively large. Most gamma-emitting radionuclides have large retardation coefficients under natural conditions and are transported more slowly. These radionuclide plumes associated with the gamma-emitting radionuclides are expected to be much smaller than the inorganic salt plumes.

7.0 LESSONS LEARNED AND RECOMMENDATIONS

Several lessons learned and recommendations for future deployments are suggested to improve the data acquisition, data quality, and data coverage of future SGE efforts at the Hanford Site tank farms.

7.1 LESSONS LEARNED

7.1.1 Data Collection/Field Work

A lessons-learned meeting was held following completion of data collection activities at the TX-TY Complex. The lessons-learned meeting was attended by personnel directly involved in the planning and executing the data collection. The primary lessons learned from the meeting included:

- The team of dedicated resources including electricians, operators and heath physics technicians that were used during data collection efforts at the TX-TY Complex, worked

very well together and should be maintained where at all possible for future SGE data collection.

- Support equipment, specifically the utility vehicles was invaluable for supporting field tasks such as spooling up the cables and watering electrodes.
- Installation of permanent surface electrodes was a labor and cost-saving benefit and it is recommended that permanent electrodes be installed at all future locations.
- Pre-staging material and equipment was effectively used to sustain data collection.
- Including tank farm support staff (operations, heath physics, etc.) in planning data collection activities was beneficial.
- Pre-Job Briefs were used to effectively communicate daily activities, ongoing issues, and information from other pre-job briefs was also shared.
- Increased communication and alternate means to enforce road blocks, helped minimize instances where site personnel did not adhere to road blocks and signage.
- Evaluating the need for spares and lead time for repair/replacement of equipment reduced down time during data collection.
- During WTW wire layouts and installations, site electricians assisted WTW data quality control efforts by measuring background voltages and contact resistance using manual volt-ohm meters before the surveys began.
- A cable tester was implemented during STS data collection activities. The cable tester was used in between cable deployments and provided a means to check for shorts between individual channels and improve data quality. Moisture in the cable connectors was discovered using the cable tester and the cable sections were returned to the manufacturer for repair.
- Developing a plan and strategy to iteratively develop sufficient confidence in the SGE results through confirmatory sampling, verification, and testing was helpful to support ongoing program needs to provide technically defensible estimates of contamination currently in the vadose zone along with ongoing monitoring.
- Use of the Leica 1200 real-time kinematic (RTK) GPS helped improve the accuracy of the physical location of the GPR data. All data were collected in real-time kinematic Mode, ensuring an improved accuracy of better than three centimeters.
- Use of Ag Leader Technology Heads-Up Display/GPS Lightbar to the GPS helped immensely in GPR navigation by projecting a virtual grid onto the survey area. The navigational display was set to alert the Smart Cart operator if accuracy is lost due to the operator steering more than 24 centimeters off the swath or real-time kinematic Mode being lost by the Leica 1200.
- No significant value to the WTS effort was realized with regards to resolution of low-resistivity targets when compared to WTW and STS readings alone. Results of the WTS readings did not resolve the low-resistivity target present beneath the western trenches or resolve any targets within the TX-TY farm fences.

7.1.2 Data Processing

Significant additional advances in data processing hardware and software were completed as part of the TX-TY Complex project. The primary findings after implementation of hardware and software upgrades are discussed below.

1. Inversion Hardware

    a. Random access memory specifications are critical to inversion algorithm speed. Speed tests with EarthImager3DCL revealed that front side bus speed (Mhz) and the associated RAM speed (Mhz) is more important than CPU speed for the fastest servers currently available.

    b. The current limitation on model domain size is the processing computers total RAM. A maximum system RAM of 128 GB allowed for about 5,000 STS electrodes and over 100,000 data points. A real-world example of this domain would be to simultaneously invert STS data from 100 acres in a full 3D model space using about 20-foot (6-meter) spaced surface electrodes.

    c. Analysis of EarthImager3DCL revealed that this software does not access the hard drive to the extent where a high revolutions per minute server type hard drive is required. A 7,000 revolutions per minute drive does not slow down inversion processing when compared to much higher cost 10,000 revolutions per minute hard drives, which are typically specified for high-end server systems by Dell.

2. Inversion Software

    a. EarthImager3DCL v1.1.3 was used for modeling the TX-TY data in this report. This version is fully multi-threaded and produces stable and repeatable results when tested with suites of controlled data during internal acceptance and testing procedures.

    b. The largest domain models in this report, such as the TXTY-STS3 domain, produced greater than 2 GB inversion output files. These very large files were too large to open in the available spreadsheet, visualization and ASCII viewing programs; therefore, parsing and filtering codes were written in MATLAB and Perl to handle these large files.

    c. Both total domain size and model processing speed are increased for a given total system RAM when perpendicular 2D resistivity lines cross at a common electrode location. Future line layouts should utilize as many common (tie line) points as possible. In addition, these lines should be orthogonal and equally spaced. These recommendations speed the processing and maximize the model domain by limiting the total number of cells that the EarthImager mesh generator is required to make in order to discretize the model using either the finite element or finite difference methods.

    d. The RES2DINV inversion modeling software was selected for analyses of all individual resistivity STS survey lines collected within the TX-TY Complex area. Res2DINV was chosen over EarthImager2D in order to make use of the least squares deconvolution method embodied in the software. This method improves

numerical resolution of inverted results when highly conductive objects, such as metallic pipelines, are present near surface electrodes (Loke 1995).

e. Target acquisition is improved by focusing smaller model domains, when possible, between areas of known pipelines or other buried infrastructure. This is particularly evident by comparing the low resistivity target beneath the T-36 crib in the smaller and more focused TXTY-STS8i model domain and the complete lack of the same target in the much larger TXTY-STS6 domain which extends further to the east across a network of pipelines.

7.2 RECOMMENDATIONS

Recommendations for potential improvements in data collection and/or analysis for future surface geophysical exploration deployments are presented in this section. The recommendations are broken into several categories including data acquisition, processing and modeling, verification, and review.

7.2.1 Data Acquisition

Some tank farms are known to be dynamic systems with possible transient plume movement both in the vadose zone and groundwater. For example, nitrate concentrations in groundwater around the T tank farm have shown significant increases within the last several years. To capture these dynamics, we recommend that the subsurface in vicinity of selected tank farms be evaluated with a successive time-series of resistivity data acquisition campaigns. Current practices of leaving permanent electrodes installed will provide for improved data quality for subsequent collection of time series data.

The WTW data proved to be invaluable to plume mapping within the tank farm when compared to STS methods. The disadvantage of the WTW data is that depth information is severely limited. In farm depth information could be improved, based on results from (B Complex reference), by including data measured from deep electrodes placed within and around a farm. Maximum benefit would be attained by distributing depth electrodes in an even distribution and in areas of low well density. Additionally, it is possible to install several deep electrodes in one single borehole in order to increase the local depth resolution.

Until new models and techniques are developed to effectively deal with buried infrastructure, a phased data collection and analysis process should be considered. The phased approach would investigate the site specific influence of infrastructure on resistivity data. A phased approach to data collection could include collection and analysis of GPR data on a relatively course grid followed by a well-to-well survey and limited surface-to-surface data collection. These results could then be used to define additional data collection.

The SuperSting R8 system has eight data acquisition card channels, meaning that only eight simultaneous measurements could be acquired at any time. A surface line of 1,640 feet (500 meters) requires almost 7 hours of data acquisition time. Increasing the number of available data acquisition card channels would be beneficial for future deployments and would yield acquisition of better quality data with a longer measurement time and a greater number of repeat measurement points.

7.2.2 Processing and Modeling

Areas with substantial infrastructure continues to present the most difficulties with regard to inversion modeling and associated interpretation of estimated resistivity distributions. It is recommended that new models be developed to more effectively deal with the effect of the infrastructure on inversion modeling results. The new models should make use different modeling methods, such as the analytic element method, filtering, or some other technique that would help to approximate the effects of infrastructure in inversion models.

All estimates of resistivity distributions resulting from inversion models need to be viewed and evaluated in terms of whether they are consistent hydrologically with site conditions. For tank conceptual models that are assumed to be leakers, the results of the inversion process should be validated against independent observations of vadose zone and/or groundwater contamination. However, the resistivity inversion process does not incorporate any aspect of hydrology. It is recommended that a joint inversion model be developed that would make use of both resistivity and unsaturated zone measurements

7.2.3 Verification of Results

The inversion modeling and interpretation of resulting resistivity distributions for tank farm suggested some targets that could be plume related. We recommend that results of these data analysis efforts can be used to help define locations for additional confirmational drilling and sampling.

Vertical resolution is difficult to attain with surface, WTW, and WTS resistivity methods and approaches. Borehole geophysical methods, such as electromagnetic induction, would provide vertically constrained electrical conductivity (reciprocal of resistivity) data from the formations surrounding the borehole given that the casing is made of non-electrically conductive materials such as polyvinyl chloride. This type of data is recommended to help verify and constrain the results obtained from resistivity inversion modeling of STS, WTS and WTW data.

This page intentionally left blank.

8.0 REFERENCES

40 CFR 141, "National Primary Drinking Water Regulations," *Code of Federal Regulations*, as amended.

ASME NQA-1, 2000, *Quality Assurance Requirements for Nuclear Facility Applications*, American Society of Mechanical Engineers. New York, New York.

Atomic Energy Act of 1954, 42 USC 2011 et seq., as amended.

CEES-0333, 2006, *Quality Assurance Plan for Surface Geophysical Exploration Projects*, Rev. 0, Columbia Energy & Environmental Services Inc., Richland, Washington.

CEES-0338, 2006, *Software Management Plan for Surface Geophysical Exploration Projects*, Rev. 0, Columbia Energy & Environmental Services, Inc., Richland, Washington.

CEES-0360, 2007, *Surface Geophysical Exploration System Design Description*, Rev. 0, Columbia Energy & Environmental Services, Inc., Richland, Washington.

CE-ES-3.5, 2006, *Software Engineering*, Rev. 0, Columbia Energy & Environmental Services, Inc., Richland, Washington.

DOE O 414.1C, 2005, *Quality Assurance*, U.S. Department of Energy, Washington, D.C.

DOE/ORP-2005-01, 2006, *Initial Single-Shell Tank System Performance Assessment for the Hanford Site*, U.S. Department of Energy, CH2M HILL Hanford Group, Inc., Richland, Washington.

DOE/RL-2003-64, 2004, *Feasibility Study for the 200-TW-1 Scavenged Waste Group, the 200-TW-2 Tank Waste Group, and the 200-PW-5 Fission-Product Rich Waste Group Operable Units,* Draft A, U.S. Department of Energy, Richland Operations Office, Richland, Washington.

DOE/RL-2004-24, 2004, *Feasibility Study for the 200-CW-5 (U Pond/Z Ditches Cooling Water Waste Group), 200-CW-2 (S Pond and Ditches Cooling Water Waste Group), 200-CW-4 (T Pond and Ditches Cooling Water Waste Group), and 200-SC-1 (Steam Condensate Waste Group) Operable Units*, Draft A, U.S. Department of Energy, Richland Operations Office, Richland, Washington.

DOE/RL-2005-61, 2006, *Remedial Investigation Report for the 200-LW-1 (300 Area Chemical Laboratory Waste Group) and 200-LW-2 (200 Area Chemical Laboratory Waste Group) Operable Units*, Draft A, U.S. Department of Energy, Richland Operations Office, Richland, Washington.

DOE/RL-2006-51, 2006, *Remedial Investigation Report for the Plutonium/Organic-Rich Process Condensate/Process Waste Group Operable Unit: Includes the 200-PW-1, 200-PW-3, and 200-PW-6 Operable Units*, U.S. Department of Energy, Richland Operations Office, Richland, Washington.

GJO-97-13-TAR, 1998, *Hanford Tank Farms Vadose Zone: TX Tank Farm Report*, U.S. Department of Energy Grand Junction Office, Grand Junction, Colorado.

GJO-97-30-TAR, 1998, *Hanford Tank Farms Vadose Zone: TY Tank Farm Report,* U.S. Department of Energy Grand Junction Office, Grand Junction, Colorado.

HNF-EP-0182, 2008, *Waste Tank Summary Report for Month Ending March 31, 2008,* CH2M HILL Hanford Group Inc., Richland, Washington.

M-45-98-03 (Ecology et al. 1989) Change Request (Ecology et al. 1991).

PNNL-15955, 2007, *Geology Data Package for the Single Shell Tank Waste Management Areas at the Hanford Site,* Rev. 1, Pacific Northwest National Laboratory, Richland, Washington.

PNNL-16005,2007, *RCRA Assessment Plan for Single-Shell Tank Waste Management Area TX-TY*, Rev. 0, Pacific Northwest National Laboratory, Richland, Washington.

PNNL-16649, 2007, *Characterization of Direct Push Vadose Zone Sediments from the T and TY Waste Management Area*, Rev. 0, Pacific Northwest National Laboratory, Richland, Washington.

RCW 70.105, *Hazardous Waste Management Act*, Revised Code of Washington, as amended.

RHO-ST-23, 1979, *Geology of the Separations Areas, Hanford Site, South Central Washington*, Rockwell Hanford Operations, Richland, Washington.

RPP-23405, 2008, *Tank Farm Vadose Zone Contamination Volume Estimates,* Rev. 3, CH2M HILL Hanford Group, Inc., Richland, Washington.

RPP-23748 , 2006, *Geology, Hydrogeology, Geochemistry, and Mineralogy Data Package for the Single-Shell Tank Waste Management Areas at the Hanford Site*, Rev. 0, CH2M HILL Hanford Group Inc., Richland, Washington.

RPP-23752, 2005, *Field Investigation Report for Waste Management Areas T and TX-TY*, Revision 0-A, CH2M HILL Hanford Group, Inc., Richland, Washington.

RPP-26744, 2005, *Hanford Soil Inventory Model*, Rev. 1, (PNNL-15367) Pacific Northwest National Laboratory, Richland, Washington.

RPP-34690, 2007, *Surface Geophysical Exploration of the B, BX, and BY Tank Farms at the Hanford Site,* Rev. 0, CH2M HILL Hanford Group, Inc., Richland, Washington.

RPP-34974, 2007, *Verification and Testing of the EarthImager Series of Electrical Resistivity Inversion Codes – A Benchmark Comparison*, Rev. 0, CH2M HILL Hanford Group, Inc., Richland, Washington.

RPP-5957, 2000, *Historical Vadose Zone Contamination from T, TX, and TY Tank Farm Operations*, Rev. 0, CH2M HILL Hanford Group, Inc., Richland, Washington.

RPP-7123, 2001, *Subsurface Conditions Description of the T and TX-TY Waste Management Area*, Rev. 0, CH2M HILL Hanford Group, Inc., Richland, Washington.

RPP-PLAN-35244, 2007, *Work Plan for Surface Geophysical Exploration of the TX and TY Tank Farm and Surrounding Areas*, Rev. 0, CH2M HILL Hanford Group, Inc., Richland, Washington.

RPP-RPT-28955, 2006, *Surface Geophysical Exploration of T Tank Farm*, Rev. 0, CH2M HILL Hanford Group, Inc., Richland, Washington.

RPP-RPT-30976, 2006, *Surface Geophysical Exploration of S Tank Farm at the Hanford Site*, Rev. 0, CH2M HILL Hanford Group, Inc., Richland, Washington.

RPP-RPT-31557, 2006, *Surface Geophysical Exploration of U Tank Farm at the Hanford Site*, Rev. 0, CH2M HILL Hanford Group, Inc., Richland, Washington.

RPP-RPT-31558, 2007, *Surface Geophysical Exploration of C Tank Farm at the Hanford Site*, Rev. 0, CH2M HILL Hanford Group, Inc., Richland, Washington.

RPP-RPT-34344, 2007, *Surface Geophysical Exploration of B, BX, and BY Tank Farms at the Hanford Site: Results of Background Characterization with Magnetics and Electromagnetics*, Rev. 0, CH2M HILL Hanford Group, Inc., Richland, Washington.

RPP-RPT-36893, 2008, *Surface Geophysical Exploration of TX, and TY Tank Farms at the Hanford Site: Results of Background Characterization with Magnetics and Electromagnetics*,Rev. 0, CH2M HILL Hanford Group, Inc., Richland, Washington.

RPP-RPT-38104, 2008, *Surface Geophysical Exploration of TX, and TY Tank Farms at the Hanford Site: Results of Background Characterization with Ground Penetrating Radar*, CH2M HILL Hanford Group, Inc., Richland, Washington.

WAC 173-303, "Dangerous Waste Regulation," *Washington Administrative Code,* as amended.

This page is intentionally left blank.

APPENDIX A

RESISTIVITY ACQUISITION METHODOLOGY

This page intentionally left blank.

TABLE OF CONTENTS

A1.0 INTRODUCTION A-1

A2.0 RESISTIVITY EQUIPMENT A-2
- A2.1 SUPERSTING R8 RESISTIVITY METER A-2
- A2.2 SWITCHBOX 56 ..... A-3
- A2.3 SURFACE RESISTIVITY ELECTRODES A-3
- A2.4 RESISTIVITY CABLES A-3
- A2.5 RESISTIVITY DISTRIBUTION PANEL A-5
- A2.6 ELECTRODE WATERING SYSTEM A-5

A3.0 DATA ACQUISITION—SURFACE-TO SURFACE SURVEY A-6

A4.0 DATA ACQUISITION—WELL-TO-WELL SURVEY A-20

A5.0 REFERENCES A-25

LIST OF FIGURES

A-1. HRR Survey Coverage Area, Showing Resistivity Line Locations-TX-TY Complex A-1

A-2. Remote Reference Electrode Installation A-2

A-3. Resistivity Equipment Showing Use of Lockout/Tagout Safety Equipment A-3

A-4. Permanent Installation Resistivity Electrode A-4

A-5. Deployment of Resistivity Cables A-4

A-6. Resistivity Distribution Panel for Connecting Individual Wires to Wells A-5

A-7. Watering Electrode Using Custom-Fabricated Mobile Watering System (Left) and In-Farm ATV with Watering System and Cable Deployment Reels (Right) A-6

A-8. Line 1E Repeatability Analysis Plot A-9

A-9. Line 1N Repeatability Analysis Plot A-10

A-10. Line 2E Repeatability Analysis Plot A-11

A-11. Line 3N Repeatability Analysis Plot A-12

A-12. Line 11E Repeatability Analysis Plot A-13

A-13. Line 1N Reciprocal Analysis Plot A-14

A-14. Line 3N Reciprocal Analysis Plot A-15

A-15. Line 4N Reciprocal Analysis Plot A-16

A-16. Line 3E Reciprocal Analysis Plot A-17

A-17. Line 4E Reciprocal Analysis Plot A-18

A-18. Line 5E Reciprocal Analysis Plot A-19

A-19. Deployment of Wire to Connect Monitoring Wells to Resistivity Data Acquisition System A-21

A-21. Deployment of Wire with All-Terrain Vehicle Outfitted with Wire Spooler A-22

A-22. Histogram Showing Results of Reciprocal Analysis for WTW Measurements A-23

A-23. Well Layout for WTW Resistivity Survey—TX-TY Complex Area A-24

LIST OF TABLES

A-1. Dates of Data Acquisition and Resistivity Survey Parameters for Lines Used in Surface-to Surface Survey—TX-TY-Complex Area A-7

A-2. Names of Vadose Zone Wells, Groundwater Wells, Point Source Electrodes Used in Well-to-Well Survey A-20

LIST OF TERMS

ATV	all-terrain vehicle
TX-TY Complex	TX and TY tank farm area
SGE	surface geophysical exploration
STS	surface-to-surface
WTW	well-to-well

This page is intentionally left blank.

A1.0 INTRODUCTION

Surface to surface resistivity data acquisition, which was initiated on October 16, 2007, was collected using near-surface electrodes laid out along an orthogonal grid of surface lines. The electrodes were spaced at 20 feet (6 meters) apart. By utilizing the steel casings as electrodes, data collection in and around the farm also made selective use of existing drywell and groundwater monitoring boreholes.

A summary of the surface resistivity survey coverage for TX and TY tank farm area (TX-TY Complex) can be viewed in Figure A-1. Resistivity lines are represented by red orthogonal lines.

Figure A-1. HRR Survey Coverage Area, Showing Resistivity Line Locations-TX-TY Complex.

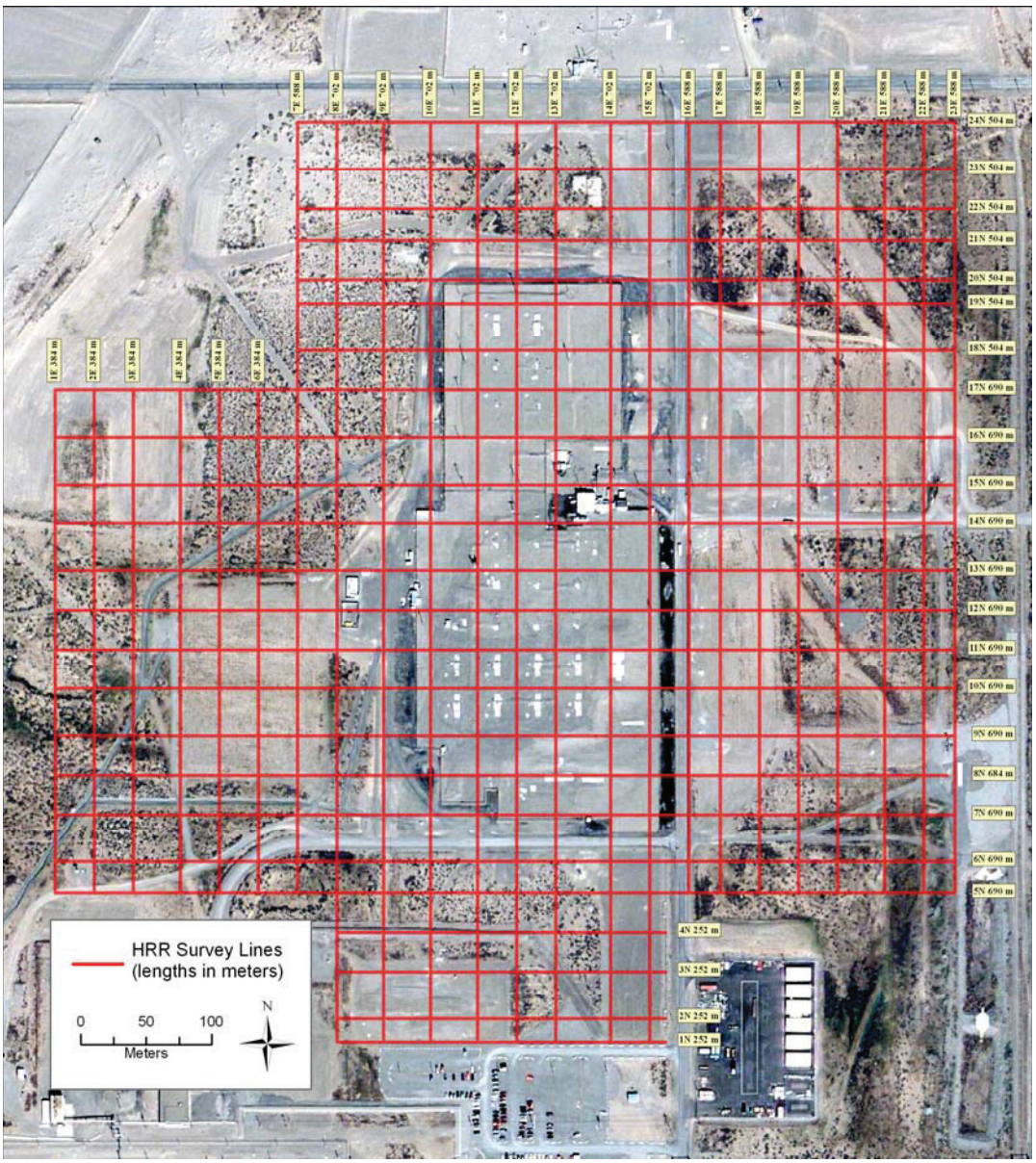

Previously installed remote reference electrodes used in the T Farm resistivity characterization survey were again utilized for the TX and TY Farm resistivity surveys (See RPP-RPT-28955). These reference electrodes were used for completing the four-pole measurements associated with the pole-pole resistivity array. A typical installation of remotes on the Hanford site is illustrated in Figure A-2.

Figure A-2. Remote Reference Electrode Installation.

A2.0 RESISTIVITY EQUIPMENT

A2.1 SUPERSTING R8 RESISTIVITY METER

The SuperSting R8/IP® resistivity data collection system was selected for collecting resistivity data in and around the tank farms. The SuperSting R8/IP is a state-of-the-art, multi-channel portable memory earth resistivity meter with memory storage of readings and user-defined measurement cycles.

The SuperSting R8 can be used with either active (automatic switching) or passive cables. Switchboxes can be used in combination with the passive cables to expand the number of electrodes used for data collection in a single layout

The setup for the SuperSting R8/IP meter with accessory parts and the use of lockout/tagout safety equipment shown in Figure A-3.

® SuperSting R8 and IP are registered trademarks of Advanced Geosciences, Inc.

Figure A-3. Resistivity Equipment Showing Use of Lockout/Tagout Safety Equipment.

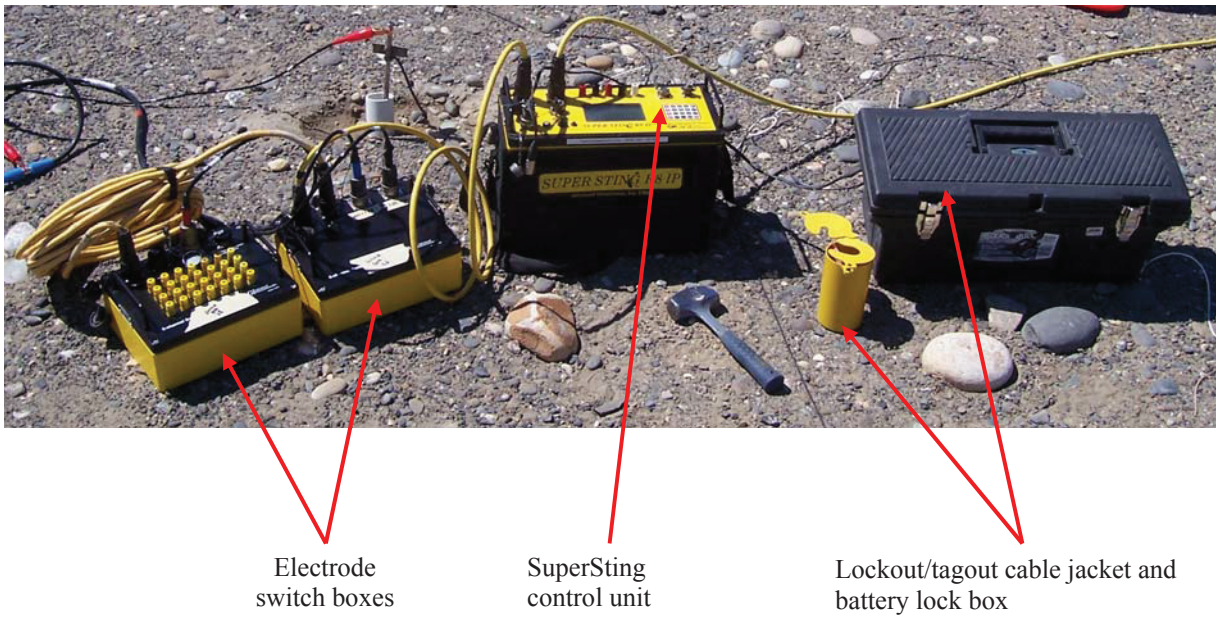

A2.2 SWITCHBOX 56

Switchboxes are used to direct or multiplex measurements through individual conductors of a passive electrode cable. The Advanced Geosciences, Inc. SwitchBox 56 resistivity multiplexer was selected for the project because it satisfied specific functional requirements for a minimum switching capacity of 162 electrode switching via any combination of multiplexer boxes. Three 56-electrode switchboxes were selected for use in this survey. Examples of two such switchboxes are illustrated in Figure A-3.

A2.3 SURFACE RESISTIVITY ELECTRODES

A custom stainless-steel surface electrode design, as shown in Figure A-4, was selected from a set of user-specific electrode designs that were tested as part of the T farm surface geophysical exploration project and was fabricated for use as permanent installation electrodes within the tank farm environment. This electrode design was adapted from standard resistivity electrodes used in previous surface geophysical exploration projects conducted at T farm and BC cribs in order to comply with tank farm safety concerns. The specific electrodes used in this project provide sufficient data quality while satisfying tank farm safety concerns.

A2.4 RESISTIVITY CABLES

A set of custom-fabricated passive cables with takeouts for up to 168-electrodes was used in conjunction with the SuperSting R8 resistivity system and the SwitchBox 56 multiplexer to transmit current to designated electrode locations. The cables were designed with electrode takeouts every 10 feet (3 meters) and 3-foot (1-meter) cable-to-electrode connectors were used to attach the cable to each surface electrode. The cables are divided into six sections in order to facilitate deployment logistics. The deployment of these resistivity cables as they were distributed and set out in and around the tank farms are illustrated in Figure A-5.

Figure A-4. Permanent Installation Resistivity Electrode.

Figure A-5. Deployment of Resistivity Cables.

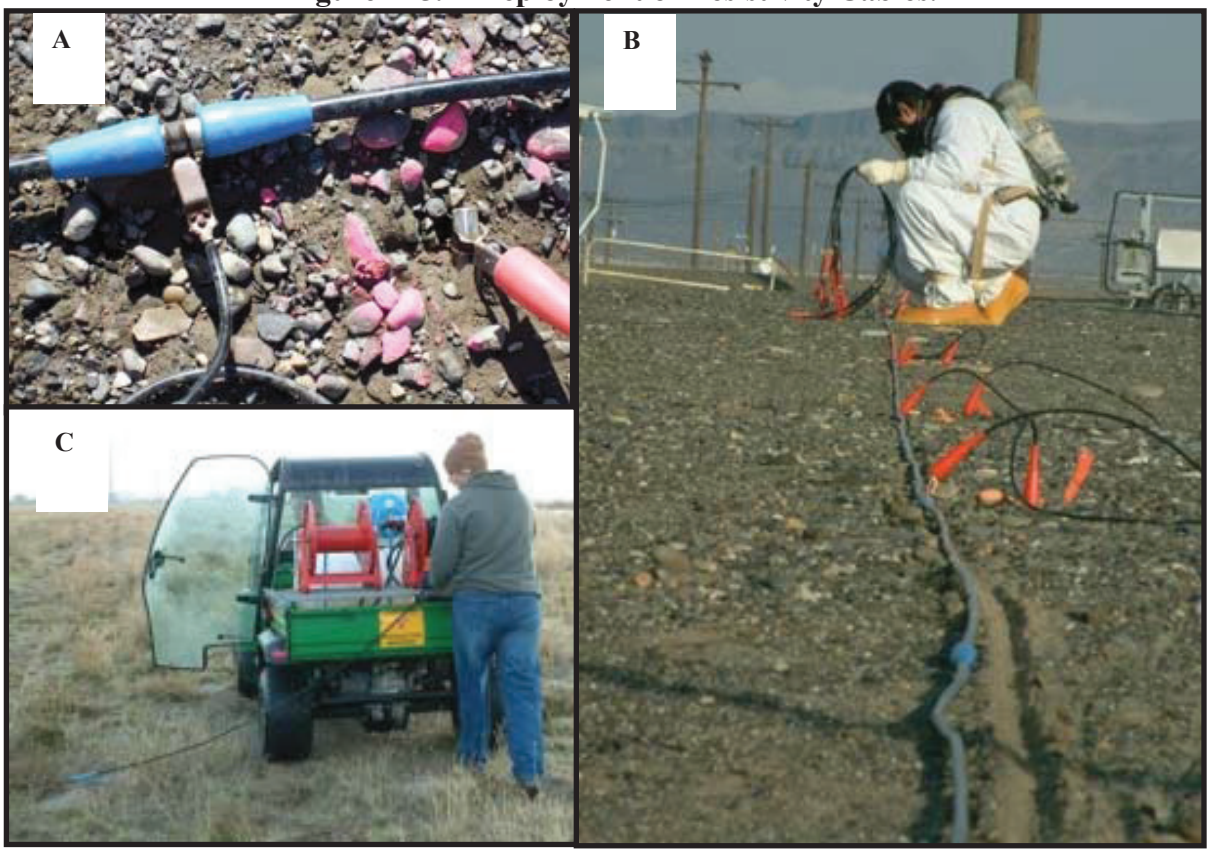

Notes: (A) Close-up of cable takeout with connector to electrode. (B) Cable being set-out within a tank farm. (C) Distribution of cable using an all-terrain vehicle (ATV) and a mounted cable reel.

A2.5 RESISTIVITY DISTRIBUTION PANEL

The custom-fabricated distribution panel was used to provide a means of connecting individual wires between the dry wells and groundwater wells and the Switchbox 56 multiplexer. The patch panel connects to the resistivity multiplexer using standard resistivity cables and can be used to verify continuity between individual sampling wells during field data collection. An example of a distribution panel used for connecting individual wires to dry wells or groundwater wells is shown in Figure A-6.

Figure A-6. Resistivity Distribution Panel for Connecting Individual Wires to Wells.

A2.6 ELECTRODE WATERING SYSTEM

To provide for improved operational efficiency, a mobile electrode watering system was assembled using a small chemical spray tank, a 12-volt pump, and a pressure tank. The watering system was placed into an ATV and driven along the surface lines to water the electrodes as shown in Figure A-7.

Figure A-7. Watering Electrode Using Custom-Fabricated Mobile Watering System (Left) and In-Farm ATV with Watering System and Cable Deployment Reels (Right).

A3.0 DATA ACQUISITION—SURFACE-TO SURFACE SURVEY

Two-dimensional (2D) resistivity data acquisition for the surface-to-surface (STS) survey was initiated on October 18, 2007, and completed on March 19, 2008. The STS survey collected resistivity data at surface electrodes laid out along orthogonal surface lines using a pole-pole array. The electrodes were spaced at 20 feet (6 meters) apart. Global positioning system data were collected at each electrode location to facilitate accurate geo-referencing of the resistivity data.

Data were collected along a total of 47 lines with 4,453 electrodes. The combined TX-TY Complex survey produced 26.7 line kilometers of coverage. Lines 1E through 23E were oriented in a south-north direction. Lines 1N through 24N were oriented in an east-west direction. North-south data collection began just west of the TX trenches, extended through and past the TX-TY tank farm, then across additional areas of interest to the east. East-west data collection began across the 216-Z-7 and 216-T-19 waste sites south of the TX tank farm boundary and progressed north of TY farm and through the 216-T-36 and T-13 cribs. A summary of dates of data acquisition and related survey parameters for each of these resistivity lines is provided in Table A-1.

Table A-1. Dates of Data Acquisition and Resistivity Survey Parameters for Lines Used in Surface-to Surface Survey—TX-TY-Complex Area. (2 Sheets)

Date of Acquisition	Line Number	Orientation	Length (meters)
1/15/2008	1E	North South	384
1/15/2008	2E	North South	384
1/15/2008	3E	North South	384
1/17/2008	4E	North South	384
1/18/2008	5E	North South	384
1/21/2008	6E	North South	384
1/23/2008 , 1/24/2008	7E	North South	588
1/30/2008, 1/31/2008	8E	North South	702
2/4/2008, 2/5/2008	9E	North South	702
3/13/2008, 3/14/2008	10E	North South	702
3/5/2008, 3/10/2008	11E	North South	702
3/5/2008, 3/11/2008	12E	North South	702
3/4/2008, 3/11/2008	13E	North South	702
2/29/2008, 3/12/2008	14E	North South	702
2/28/2008	15E	North South	702
2/6/2008	16E	North South	588
2/7/2008, 2/11/2008	17E	North South	588
2/11/2008, 2/12/2008	18E	North South	588
2/12/2008, 2/13/2008	19E	North South	588
2/20/2008, 2/21/2008	20E	North South	588
2/14/2008	21E	North South	588
2/19/2008	22E	North South	588
2/15/2008	23E	North South	588
10/18/2007	1N	East-West	252
10/22/2007	2N	East-West	252
10/18/2007	3N	East-West	252
10/22/2007	4N	East-West	252
10/22/2007, 10/23/2007	5N	East-West	690
10/24/2007	6N	East-West	690
10/25/2007	7N	East-West	690
10/31/2007	8N	East-West	690
10/30/2007	9N	East-West	690

Table A-1. Dates of Data Acquisition and Resistivity Survey Parameters for Lines Used in Surface-to Surface Survey—TX-TY-Complex Area. (2 Sheets)

Date of Acquisition	Line Number	Orientation	Length (meters)
11/6/2007, 11/7/2007	10N	East-West	690
11/13/2007, 11/14/2007	11N	East-West	690
11/15/2007, 11/19/2007	12N	East-West	690
11/20/2007, 11/21/2007	13N	East-West	690
11/27/2007, 11/28/2007	14N	East-West	690
12/3/2007, 12/4/2007	15N	East-West	690
12/17/2007, 12/18/2007	16N	East-West	690
12/19/2007, 3/17/2008	17N	East-West	690
3/18/2008	18N	East-West	504
3/19/2008	19N	East-West	504
1/7/2008	20N	East-West	504
1/8/2008	21N	East-West	504
1/9/2008	22N	East-West	504
1/10/2008	23N	East-West	504
1/14/2008	24N	East-West	504

STS DATA REPEATABILITY ANALYSIS

A total of four Ex-farm and one In-farm surface lines (1E, 1N, 2E, 3N, and 11E) were used to demonstrate repeatability between same configuration datasets. Two separate data collection events occurred on each of these lines, each at a different date but with identical configuration and survey parameters. Repeatability was assessed by computing the percent difference of the transfer resistance (or V/I) values between the two data collection periods along one survey line. Figures A-8 through A-12 show the graphical results of these analyses. The average percent difference for all repeat data points for all repeat lines is approximately 5 percent, with a low of 0% and a high of 100%. The analysis shows that the SuperSting R8 with the pole-pole array is capable of collecting repeat transfer resistance measurements at different periods in time.

Additionally, six Ex-farm reciprocal lines (1N, 3N, 4N, 3E, 4E, and 5E) were collected to analyze the repeatability of a reverse direction array compared to the original forward array data collection collected on the same surface line. The graphical results of these analyses are provided in Figures A-13 through A-18. The average percent difference for all reciprocal data points for all reciprocal lines is approximately 2 percent, with a low of 0% and a high of 79%. The analysis shows that the SuperSting R8 with the pole-pole array is capable of collecting reciprocal transfer resistance measurements on the same surface line and achieving like results.

Figure A-8. Line 1E Repeatability Analysis Plot.

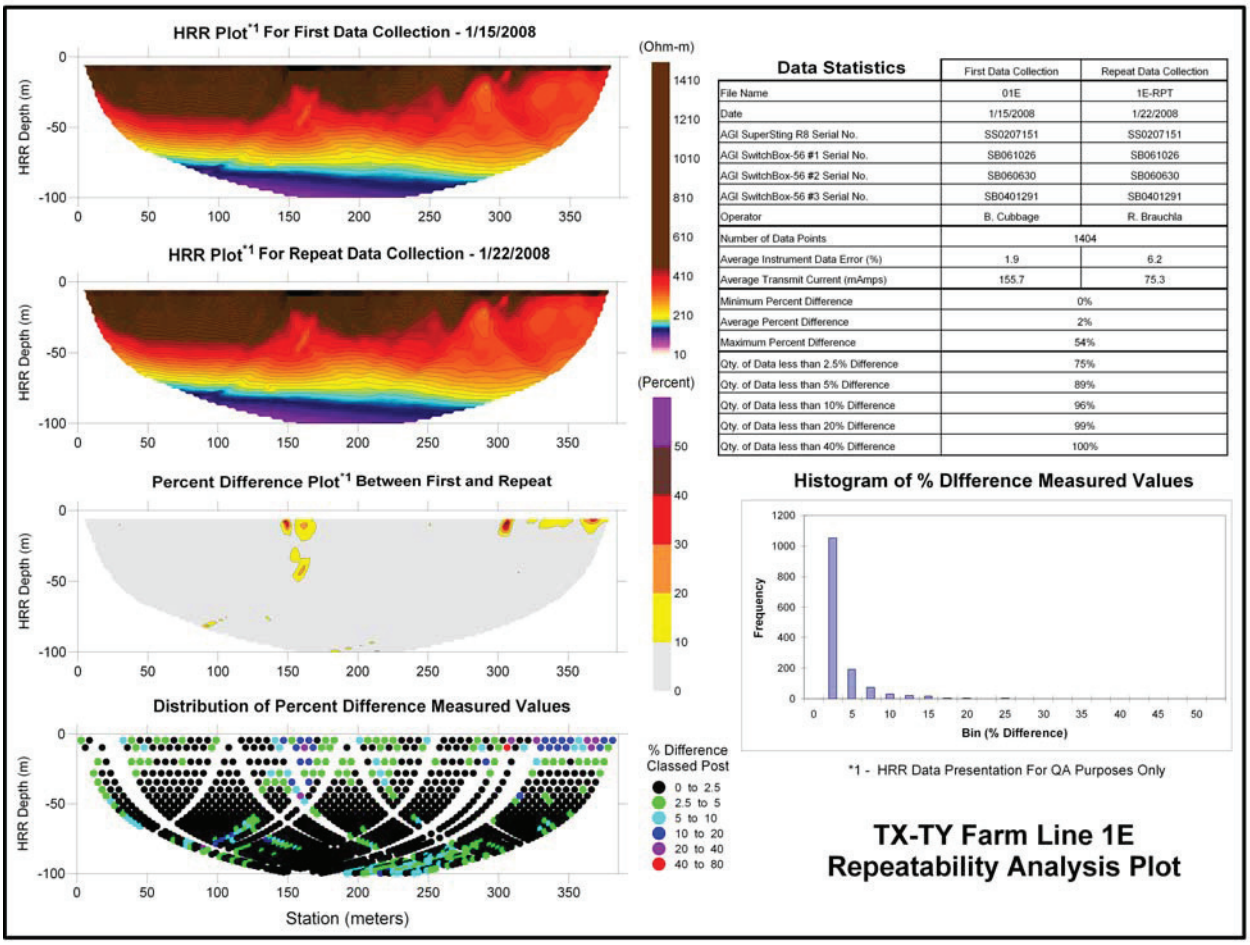

Data Statistics

	First Data Collection	Repeat Data Collection
File Name	01E	1E-RPT
Date	1/15/2008	1/22/2008
AGI SuperSting R8 Serial No.	SS0207151	SS0207151
AGI SwitchBox-56 #1 Serial No.	SB061026	SB061026
AGI SwitchBox-56 #2 Serial No.	SB060630	SB060630
AGI SwitchBox-56 #3 Serial No.	SB0401291	SB0401291
Operator	B. Cubbage	R. Brauchla
Number of Data Points	1404	
Average Instrument Data Error (%)	1.9	6.2
Average Transmit Current (mAmps)	155.7	75.3
Minimum Percent Difference	0%	
Average Percent Difference	2%	
Maximum Percent Difference	54%	
Qty. of Data less than 2.5% Difference	75%	
Qty. of Data less than 5% Difference	89%	
Qty. of Data less than 10% Difference	96%	
Qty. of Data less than 20% Difference	99%	
Qty. of Data less than 40% Difference	100%	

Figure A-9. Line 1N Repeatability Analysis Plot.

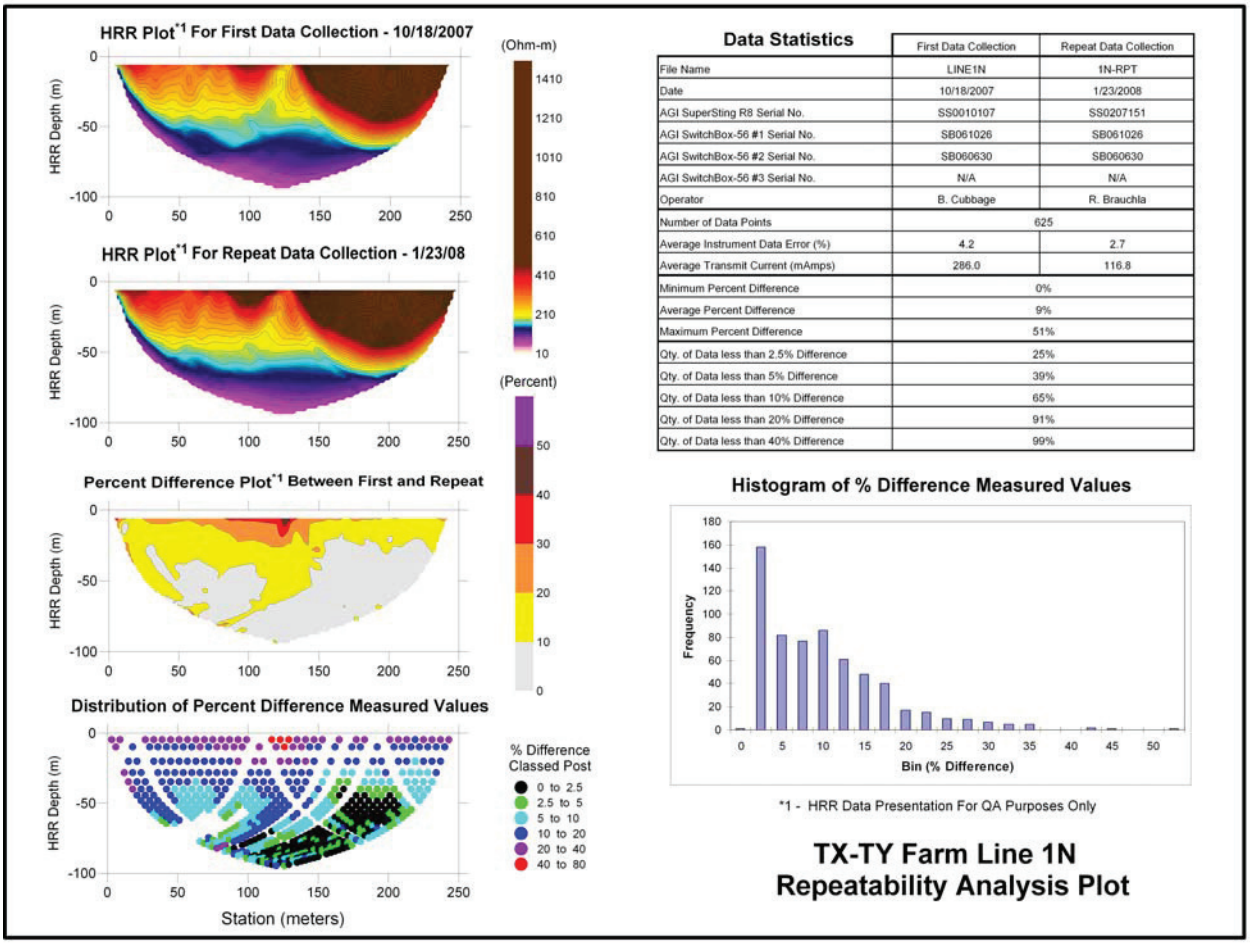

Data Statistics

	First Data Collection	Repeat Data Collection
File Name	LINE1N	1N-RPT
Date	10/18/2007	1/23/2008
AGI SuperSting R8 Serial No.	SS0010107	SS0207151
AGI SwitchBox-56 #1 Serial No.	SB061026	SB061026
AGI SwitchBox-56 #2 Serial No.	SB060630	SB060630
AGI SwitchBox-56 #3 Serial No.	N/A	N/A
Operator	B. Cubbage	R. Brauchla
Number of Data Points	625	
Average Instrument Data Error (%)	4.2	2.7
Average Transmit Current (mAmps)	286.0	116.8
Minimum Percent Difference	0%	
Average Percent Difference	9%	
Maximum Percent Difference	51%	
Qty. of Data less than 2.5% Difference	25%	
Qty. of Data less than 5% Difference	39%	
Qty. of Data less than 10% Difference	65%	
Qty. of Data less than 20% Difference	91%	
Qty. of Data less than 40% Difference	99%	

Figure A-10. Line 2E Repeatability Analysis Plot.

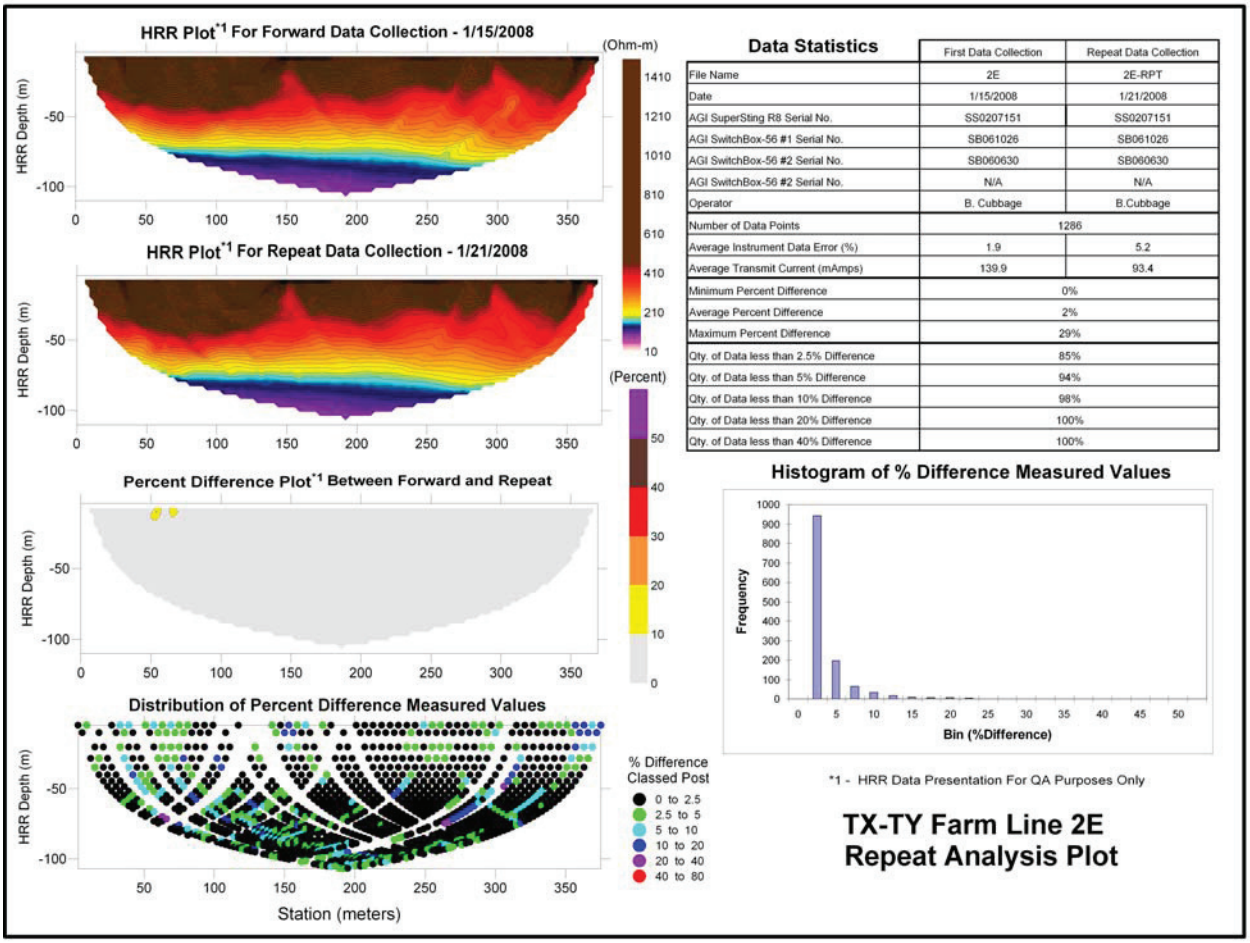

Data Statistics

	First Data Collection	Repeat Data Collection
File Name	2E	2E-RPT
Date	1/15/2008	1/21/2008
AGI SuperSting R8 Serial No.	SS0207151	SS0207151
AGI SwitchBox-56 #1 Serial No.	SB061026	SB061026
AGI SwitchBox-56 #2 Serial No.	SB060630	SB060630
AGI SwitchBox-56 #2 Serial No.	N/A	N/A
Operator	B. Cubbage	B.Cubbage
Number of Data Points	1286	
Average Instrument Data Error (%)	1.9	5.2
Average Transmit Current (mAmps)	139.9	93.4
Minimum Percent Difference	0%	
Average Percent Difference	2%	
Maximum Percent Difference	29%	
Qty. of Data less than 2.5% Difference	85%	
Qty. of Data less than 5% Difference	94%	
Qty. of Data less than 10% Difference	98%	
Qty. of Data less than 20% Difference	100%	
Qty. of Data less than 40% Difference	100%	

Figure A-11. Line 3N Repeatability Analysis Plot.

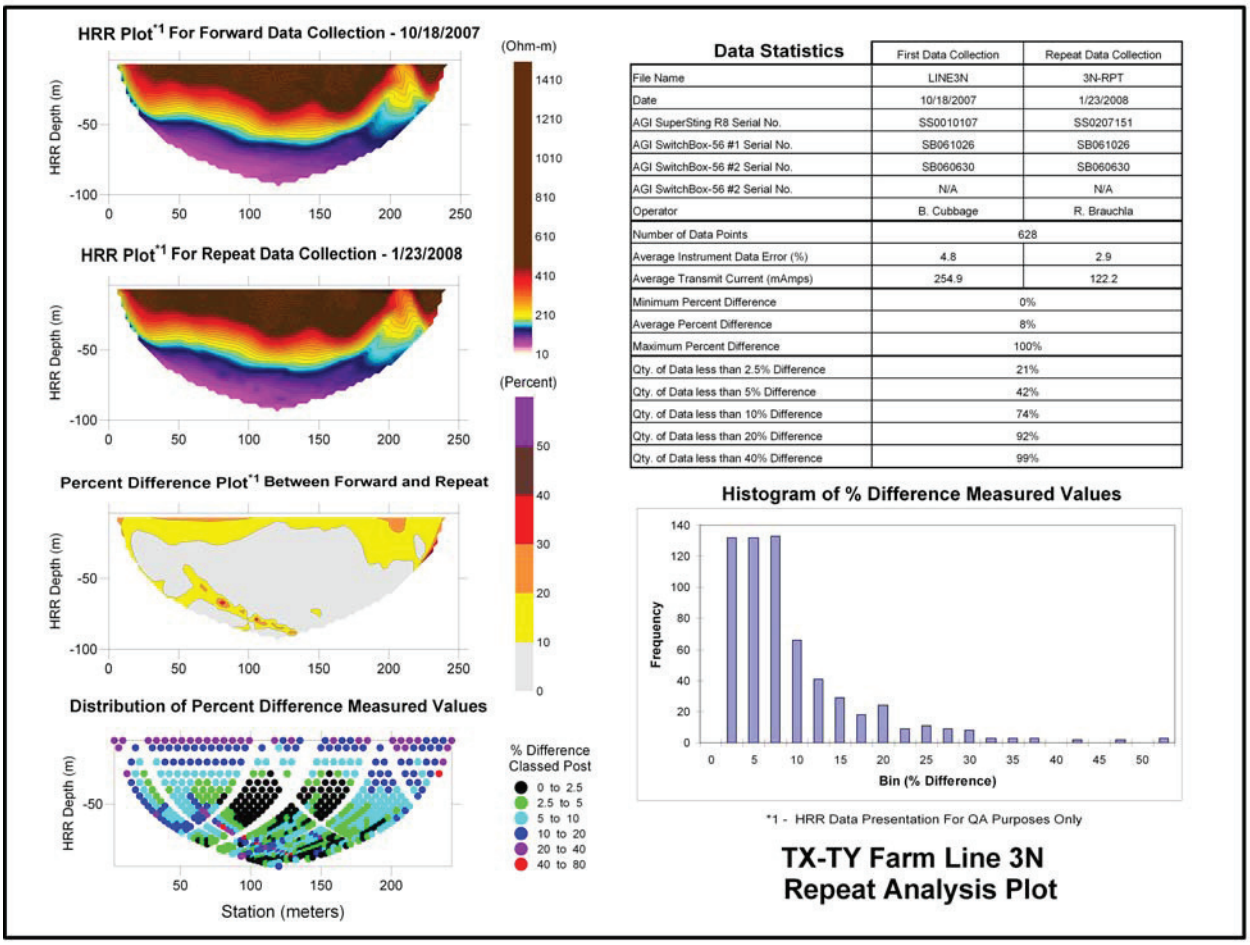

Data Statistics	First Data Collection	Repeat Data Collection
File Name	LINE3N	3N-RPT
Date	10/18/2007	1/23/2008
AGI SuperSting R8 Serial No.	SS0010107	SS0207151
AGI SwitchBox-56 #1 Serial No.	SB061026	SB061026
AGI SwitchBox-56 #2 Serial No.	SB060630	SB060630
AGI SwitchBox-56 #2 Serial No.	N/A	N/A
Operator	B. Cubbage	R. Brauchla
Number of Data Points	628	
Average Instrument Data Error (%)	4.8	2.9
Average Transmit Current (mAmps)	254.9	122.2
Minimum Percent Difference	0%	
Average Percent Difference	8%	
Maximum Percent Difference	100%	
Qty. of Data less than 2.5% Difference	21%	
Qty. of Data less than 5% Difference	42%	
Qty. of Data less than 10% Difference	74%	
Qty. of Data less than 20% Difference	92%	
Qty. of Data less than 40% Difference	99%	

Figure A-12. Line 11E Repeatability Analysis Plot.

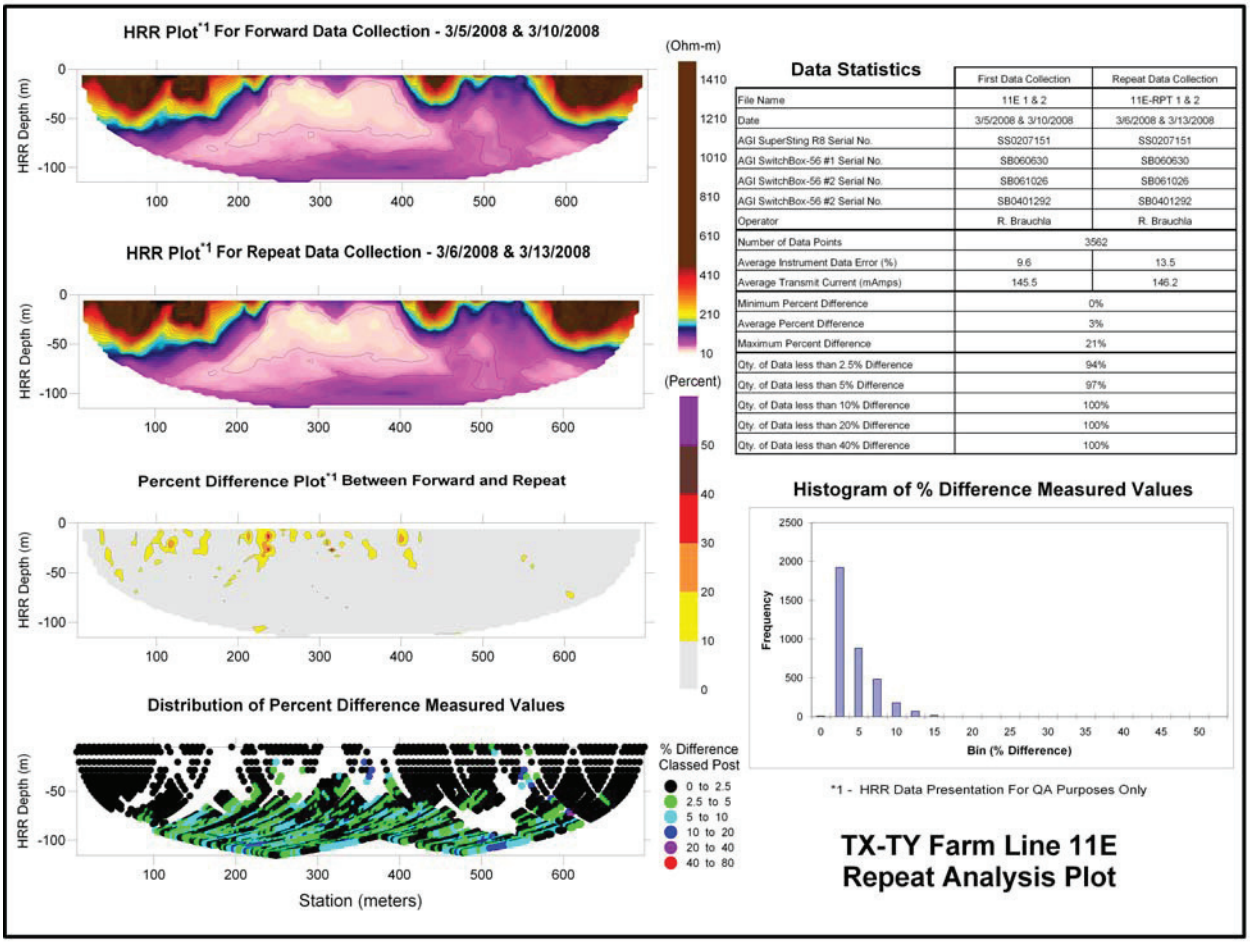

Data Statistics

	First Data Collection	Repeat Data Collection
File Name	11E 1 & 2	11E-RPT 1 & 2
Date	3/5/2008 & 3/10/2008	3/6/2008 & 3/13/2008
AGI SuperSting R8 Serial No.	SS0207151	SS0207151
AGI SwitchBox-56 #1 Serial No.	SB060630	SB060630
AGI SwitchBox-56 #2 Serial No.	SB061026	SB061026
AGI SwitchBox-56 #2 Serial No.	SB0401292	SB0401292
Operator	R. Brauchla	R. Brauchla
Number of Data Points	3562	
Average Instrument Data Error (%)	9.6	13.5
Average Transmit Current (mAmps)	145.5	146.2
Minimum Percent Difference	0%	
Average Percent Difference	3%	
Maximum Percent Difference	21%	
Qty. of Data less than 2.5% Difference	94%	
Qty. of Data less than 5% Difference	97%	
Qty. of Data less than 10% Difference	100%	
Qty. of Data less than 20% Difference	100%	
Qty. of Data less than 40% Difference	100%	

Figure A-13. Line 1N Reciprocal Analysis Plot.

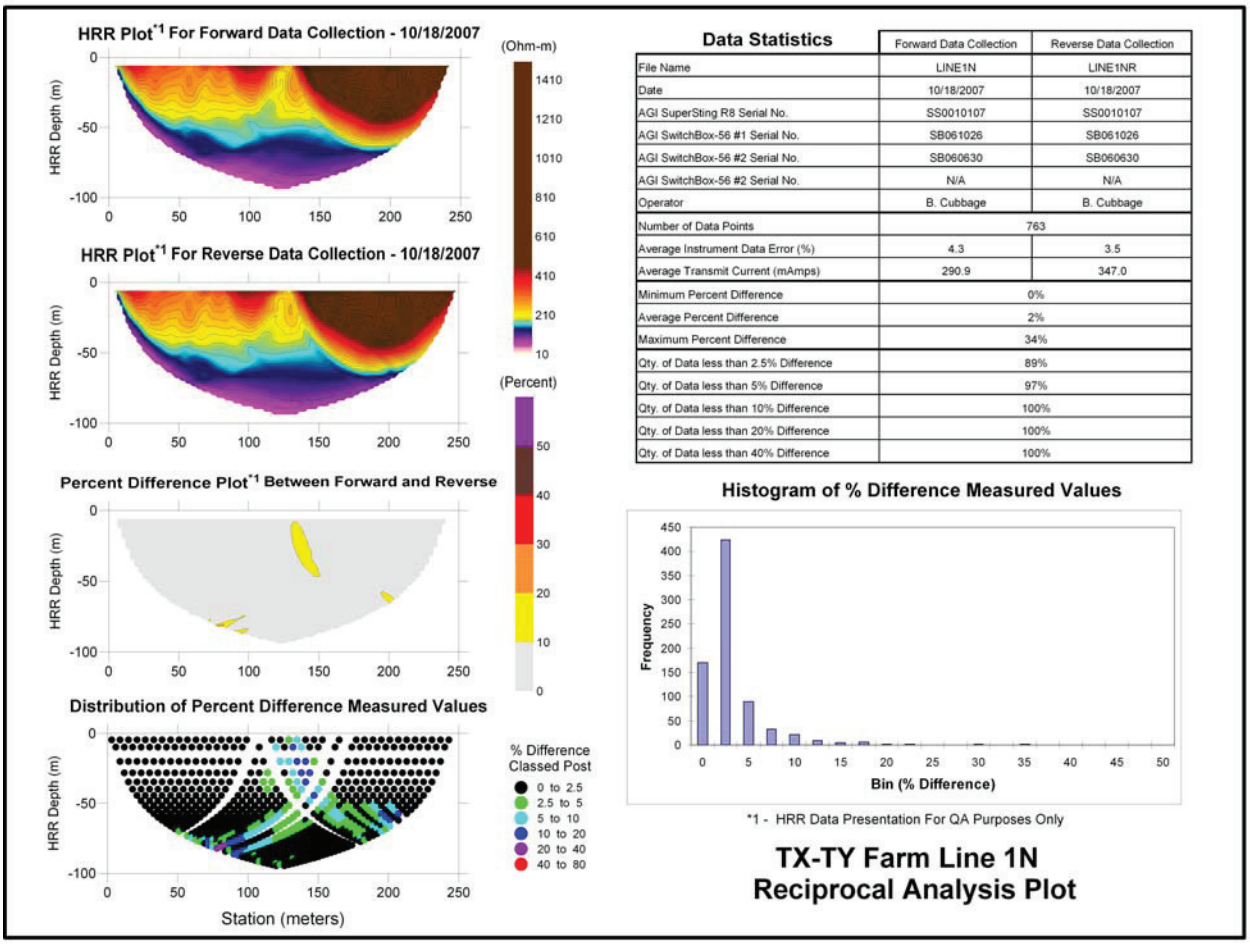

Data Statistics	Forward Data Collection	Reverse Data Collection
File Name	LINE1N	LINE1NR
Date	10/18/2007	10/18/2007
AGI SuperSting R8 Serial No.	SS0010107	SS0010107
AGI SwitchBox-56 #1 Serial No.	SB061026	SB061026
AGI SwitchBox-56 #2 Serial No.	SB060630	SB060630
AGI SwitchBox-56 #2 Serial No.	N/A	N/A
Operator	B. Cubbage	B. Cubbage
Number of Data Points	763	
Average Instrument Data Error (%)	4.3	3.5
Average Transmit Current (mAmps)	290.9	347.0
Minimum Percent Difference	0%	
Average Percent Difference	2%	
Maximum Percent Difference	34%	
Qty. of Data less than 2.5% Difference	89%	
Qty. of Data less than 5% Difference	97%	
Qty. of Data less than 10% Difference	100%	
Qty. of Data less than 20% Difference	100%	
Qty. of Data less than 40% Difference	100%	

Figure A-14. Line 3N Reciprocal Analysis Plot.

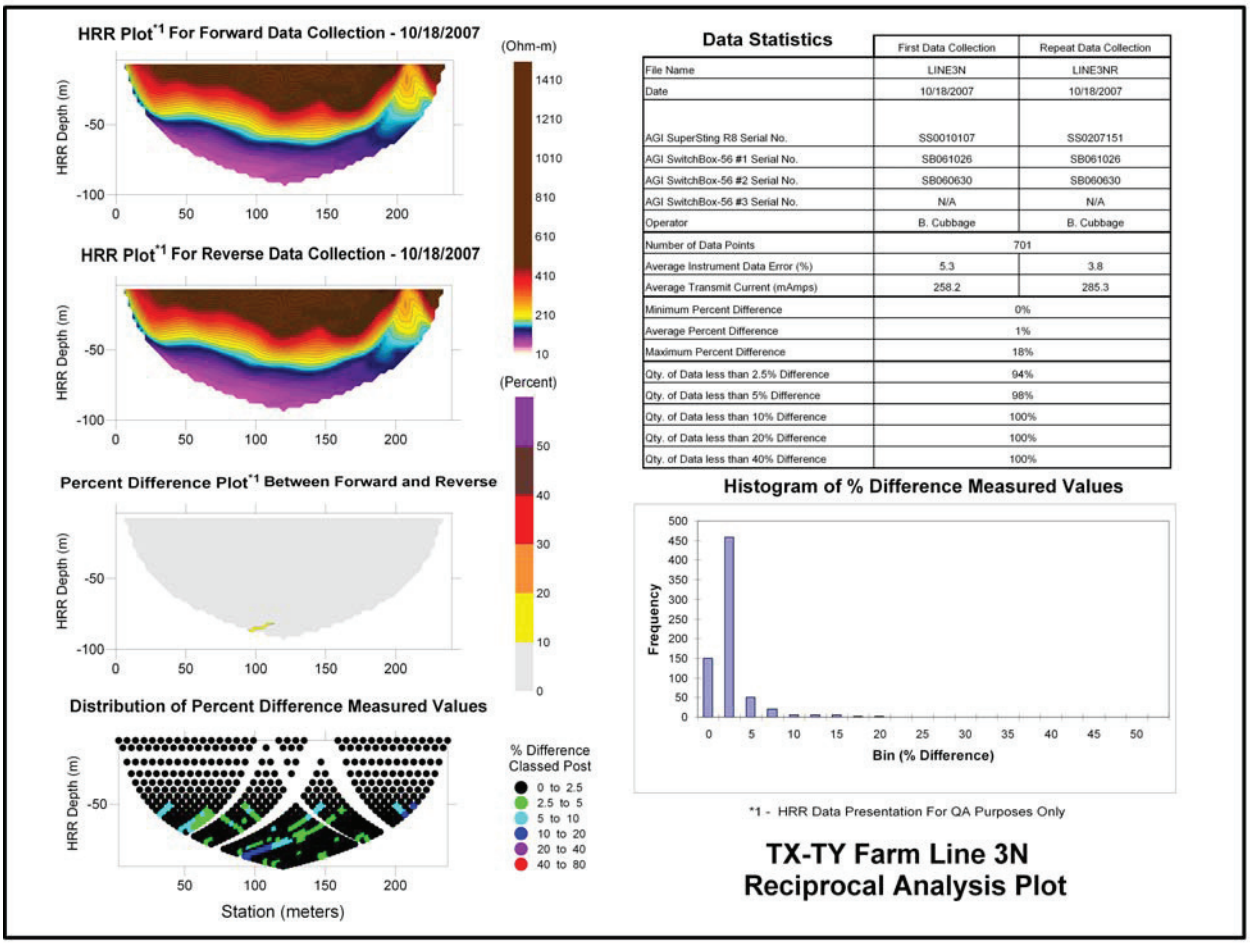

Data Statistics

	First Data Collection	Repeat Data Collection
File Name	LINE3N	LINE3NR
Date	10/18/2007	10/18/2007
AGI SuperSting R8 Serial No.	SS0010107	SS0207151
AGI SwitchBox-56 #1 Serial No.	SB061026	SB061026
AGI SwitchBox-56 #2 Serial No.	SB060630	SB060630
AGI SwitchBox-56 #3 Serial No.	N/A	N/A
Operator	B. Cubbage	B. Cubbage
Number of Data Points	701	
Average Instrument Data Error (%)	5.3	3.8
Average Transmit Current (mAmps)	258.2	285.3
Minimum Percent Difference	0%	
Average Percent Difference	1%	
Maximum Percent Difference	18%	
Qty. of Data less than 2.5% Difference	94%	
Qty. of Data less than 5% Difference	98%	
Qty. of Data less than 10% Difference	100%	
Qty. of Data less than 20% Difference	100%	
Qty. of Data less than 40% Difference	100%	

Figure A-15. Line 4N Reciprocal Analysis Plot.

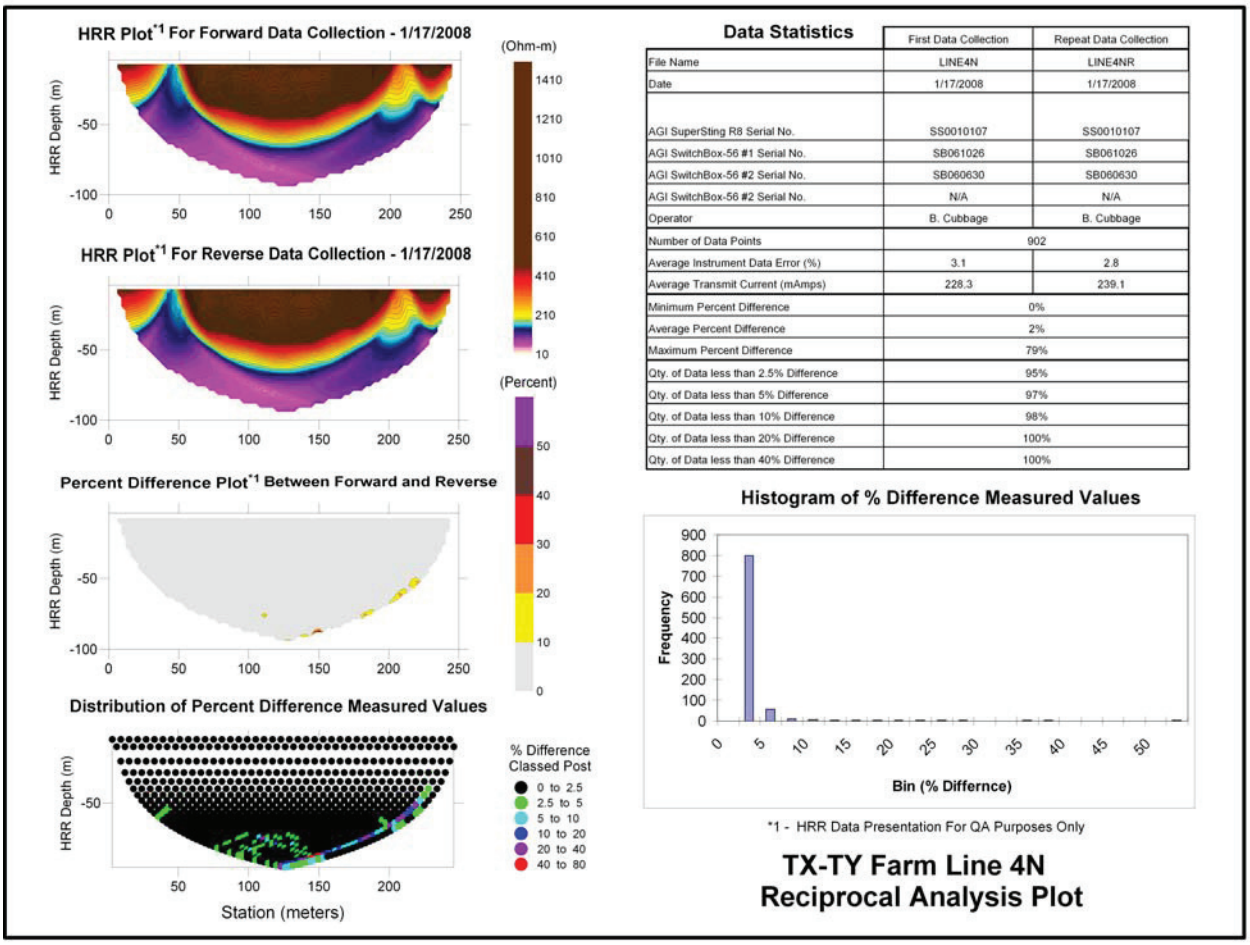

Data Statistics

	First Data Collection	Repeat Data Collection
File Name	LINE4N	LINE4NR
Date	1/17/2008	1/17/2008
AGI SuperSting R8 Serial No.	SS0010107	SS0010107
AGI SwitchBox-56 #1 Serial No.	SB061026	SB061026
AGI SwitchBox-56 #2 Serial No.	SB060630	SB060630
AGI SwitchBox-56 #2 Serial No.	N/A	N/A
Operator	B. Cubbage	B. Cubbage
Number of Data Points	902	
Average Instrument Data Error (%)	3.1	2.8
Average Transmit Current (mAmps)	228.3	239.1
Minimum Percent Difference	0%	
Average Percent Difference	2%	
Maximum Percent Difference	79%	
Qty. of Data less than 2.5% Difference	95%	
Qty. of Data less than 5% Difference	97%	
Qty. of Data less than 10% Difference	98%	
Qty. of Data less than 20% Difference	100%	
Qty. of Data less than 40% Difference	100%	

Figure A-16. Line 3E Reciprocal Analysis Plot.

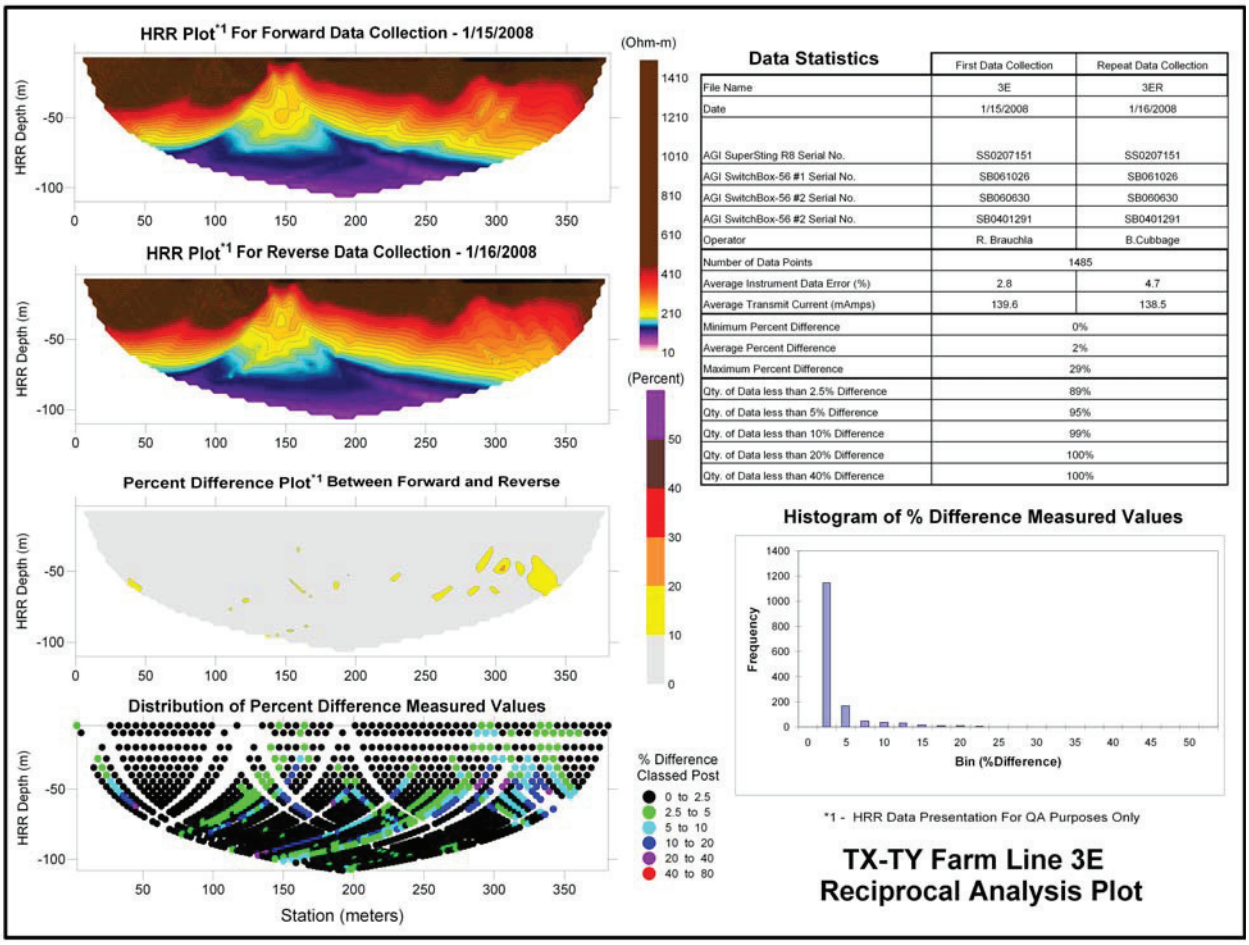

Data Statistics

	First Data Collection	Repeat Data Collection
File Name	3E	3ER
Date	1/15/2008	1/16/2008
AGI SuperSting R8 Serial No.	SS0207151	SS0207151
AGI SwitchBox-56 #1 Serial No.	SB061026	SB061026
AGI SwitchBox-56 #2 Serial No.	SB060630	SB060630
AGI SwitchBox-56 #2 Serial No.	SB0401291	SB0401291
Operator	R. Brauchla	B.Cubbage
Number of Data Points	1485	
Average Instrument Data Error (%)	2.8	4.7
Average Transmit Current (mAmps)	139.6	138.5
Minimum Percent Difference	0%	
Average Percent Difference	2%	
Maximum Percent Difference	29%	
Qty. of Data less than 2.5% Difference	89%	
Qty. of Data less than 5% Difference	95%	
Qty. of Data less than 10% Difference	99%	
Qty. of Data less than 20% Difference	100%	
Qty. of Data less than 40% Difference	100%	

Figure A-17. Line 4E Reciprocal Analysis Plot.

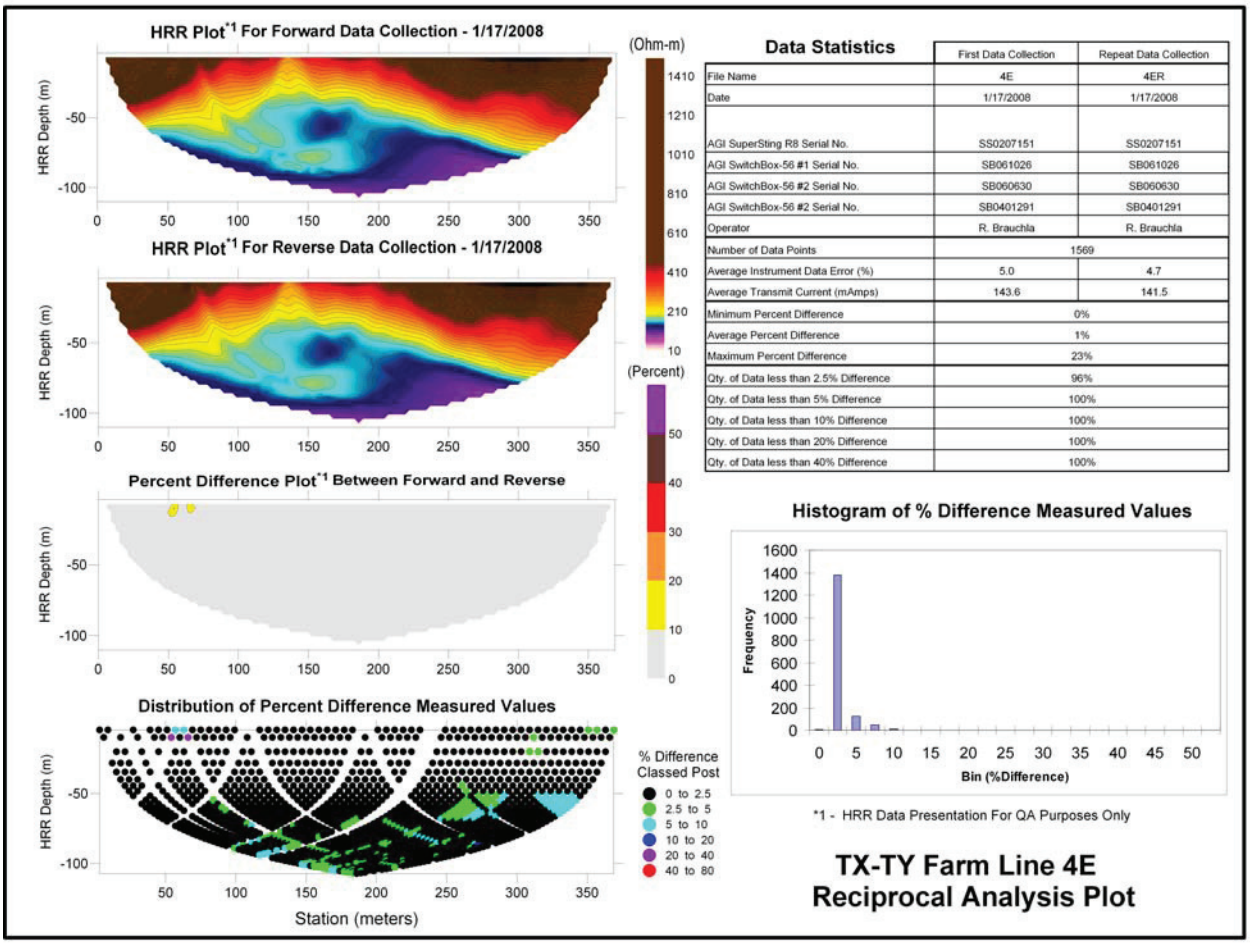

Data Statistics

	First Data Collection	Repeat Data Collection
File Name	4E	4ER
Date	1/17/2008	1/17/2008
AGI SuperSting R8 Serial No.	SS0207151	SS0207151
AGI SwitchBox-56 #1 Serial No.	SB061026	SB061026
AGI SwitchBox-56 #2 Serial No.	SB060630	SB060630
AGI SwitchBox-56 #2 Serial No.	SB0401291	SB0401291
Operator	R. Brauchla	R. Brauchla
Number of Data Points	1569	
Average Instrument Data Error (%)	5.0	4.7
Average Transmit Current (mAmps)	143.6	141.5
Minimum Percent Difference	0%	
Average Percent Difference	1%	
Maximum Percent Difference	23%	
Qty. of Data less than 2.5% Difference	96%	
Qty. of Data less than 5% Difference	100%	
Qty. of Data less than 10% Difference	100%	
Qty. of Data less than 20% Difference	100%	
Qty. of Data less than 40% Difference	100%	

Figure A-18. Line 5E Reciprocal Analysis Plot.

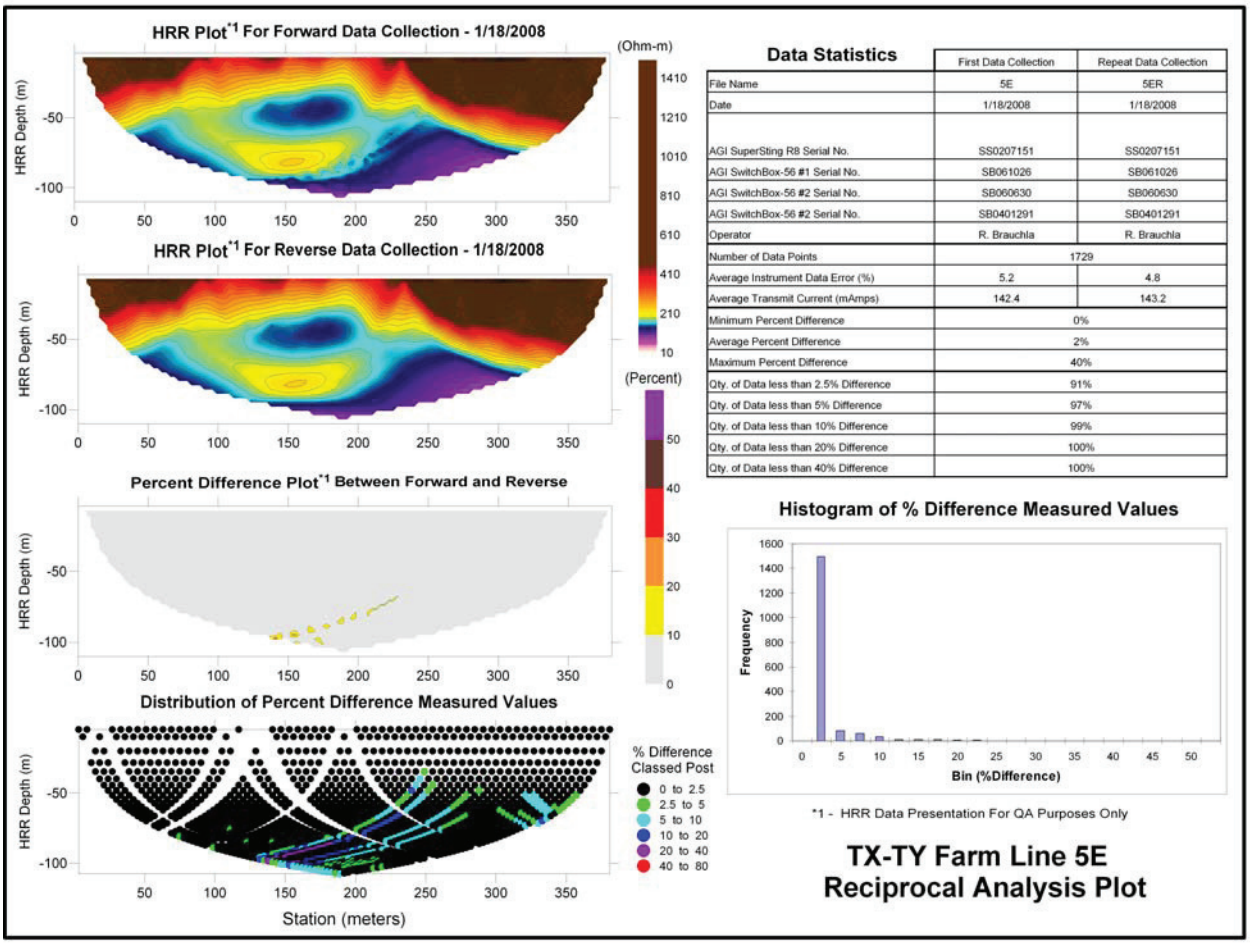

Data Statistics

	First Data Collection	Repeat Data Collection
File Name	5E	5ER
Date	1/18/2008	1/18/2008
AGI SuperSting R8 Serial No.	SS0207151	SS0207151
AGI SwitchBox-56 #1 Serial No.	SB061026	SB061026
AGI SwitchBox-56 #2 Serial No.	SB060630	SB060630
AGI SwitchBox-56 #2 Serial No.	SB0401291	SB0401291
Operator	R. Brauchla	R. Brauchla
Number of Data Points	1729	
Average Instrument Data Error (%)	5.2	4.8
Average Transmit Current (mAmps)	142.4	143.2
Minimum Percent Difference	0%	
Average Percent Difference	2%	
Maximum Percent Difference	40%	
Qty. of Data less than 2.5% Difference	91%	
Qty. of Data less than 5% Difference	97%	
Qty. of Data less than 10% Difference	99%	
Qty. of Data less than 20% Difference	100%	
Qty. of Data less than 40% Difference	100%	

A4.0 DATA ACQUISITION—WELL-TO-WELL SURVEY

Data acquisition for the well-to-well (WTW) survey, which began on October 16, 2007 and was completed on October 17, 2007, collected resistivity data using existing steel-cased wells as current sources and receivers. Because of the significant lengths of steel casing at the well locations, each well was generally modeled as a line source instead of as a point source as traditionally assumed in STS resistivity. The wells were randomly spaced in the survey and not generally distributed along simple lines.

This WTW survey made use of 27 Point Source electrodes, 105 Vadose Zone wells, and 30 Groundwater Wells, totaling 162 electrodes. The individual names of the wells used for the survey are listed in Table A-2.

As with the STS data acquisition, a pole-pole array was used for the WTW survey. Sixteen American Wire Gauge machine tool wires were strung from a central location outside the TX-TY Complex fences to each of the 162 electrodes within the survey area as shown in Figures A-19 and A-20. Wells were prepared in two ways: (1) a small area of rust was removed from the well casing and a wire with a stainless steel strap attached to the casing wall, or (2) small hose clamps were used to attach the wire to monitoring components inside the well casing.

Table A-2. Names of Vadose Zone Wells, Groundwater Wells, Point Source Electrodes Used in Well-to-Well Survey. (2 Sheets)

Well ID	Well ID	Well ID	Well ID	Point Source ID
51-00-03	51-06-10	51-13-05	52-03-12	PSE 1
299-W15-763	51-07-07	51-14-08	52-04-09	PSE 2
51-01-08	51-08-09	51-15-09	52-06-05	PSE 3
51-02-09	51-09-08	51-16-11	51-10-13	PSE 4
51-03-06	51-10-04	51-18-03	L3874	PSE 5
51-04-02	51-11-02	52-01-01	L3875	PSE 6
51-04-10	51-12-01	52-02-05	299-W10-16	PSE 7
51-05-05	51-12-10	52-03-06	299-W10-17	PSE 8
51-06-02	51-13-12	52-04-06	299-W10-2	PSE 9
51-06-12	51-15-04	52-06-04	299-W10-26	PSE 10
51-07-09	51-16-04	51-10-25	299-W10-27	PSE 11
51-08-11	51-17-10	51-00-07	299-W10-4	PSE 12
51-09-10	51-18-07	51-01-04	299-W10-5	PSE 13
51-10-08	52-01-09	51-02-05	299-W11-12	PSE 14
51-11-03	52-02-09	51-03-01	299-W11-13	PSE 15
51-12-04	52-04-02	51-03-11	299-W14-11	PSE 16
51-12-11	52-05-07	51-04-06	299-W14-13	PSE 17
51-14-04	52-06-06	51-05-01	299-W14-14	PSE 18

Table A-2. Names of Vadose Zone Wells, Groundwater Wells, Point Source Electrodes Used in Well-to-Well Survey. (2 Sheets)

51-15-07	51-00-06	51-05-08	299-W14-15	PSE 19
51-16-07	51-01-02	51-06-08	299-W14-16	PSE 20
51-17-11	51-02-02	51-07-03	299-W14-17	PSE 21
51-18-11	51-02-12	51-08-05	299-W14-18	PSE 22
52-02-01	51-03-09	51-09-04	299-W14-19	PSE 23
52-03-03	51-04-05	51-10-01	299-W14-5	PSE 24
52-04-03	51-04-12	51-11-01	299-W14-51	PSE 25
52-06-02	51-05-07	51-11-10	299-W14-53	
51-00-09	51-06-04	51-12-07	299-W14-6	
51-01-06	51-07-01	51-13-08	299-W15-1	
51-02-07	51-07-11	51-14-11	299-W15-11	
51-03-02	51-09-03	51-15-11	299-W15-33	
51-03-12	51-09-12	51-17-02	299-W15-41	
51-04-08	51-10-12	51-18-05	299-W15-64	
51-05-03	51-11-07	52-01-05	299-W15-65	
51-05-10	51-12-05	52-02-06	299-W15-66	
			299-W15-7	

Figure A-19. Deployment of Wire to Connect Monitoring Wells to Resistivity Data Acquisition System.

Figure A-20. Deployment of Wire with All-Terrain Vehicle Outfitted with Wire Spooler.

The wires from the wells were then connected to resistivity distribution panels which are used to organize the 162 electrode wires and to act as a coupler to the SuperSting R8 switchboxes. After the initial (forward) survey at each well pair was completed, a reciprocal data set of resistivity at the same pairs was acquired for quality purposes. The percent difference between each forward and reverse reading was computed and data measurements with a relative percent difference greater than 3% were considered unacceptable and removed before inversion. The average percent difference for all reciprocal data points is approximately 1.5 percent, with a low of 0% and a high of 83%. Figure A-21 shows a histogram of the reciprocal percent difference values for WTW measurements.

The coordinates of each well and point source electrode were measured with an RTK Leica global positioning system to facilitate geo-referencing the data. The spatial layout of the wells and point source electrodes are shown in Figure A-22.

Figure A-21. Histogram Showing Results of Reciprocal Analysis for WTW Measurements.

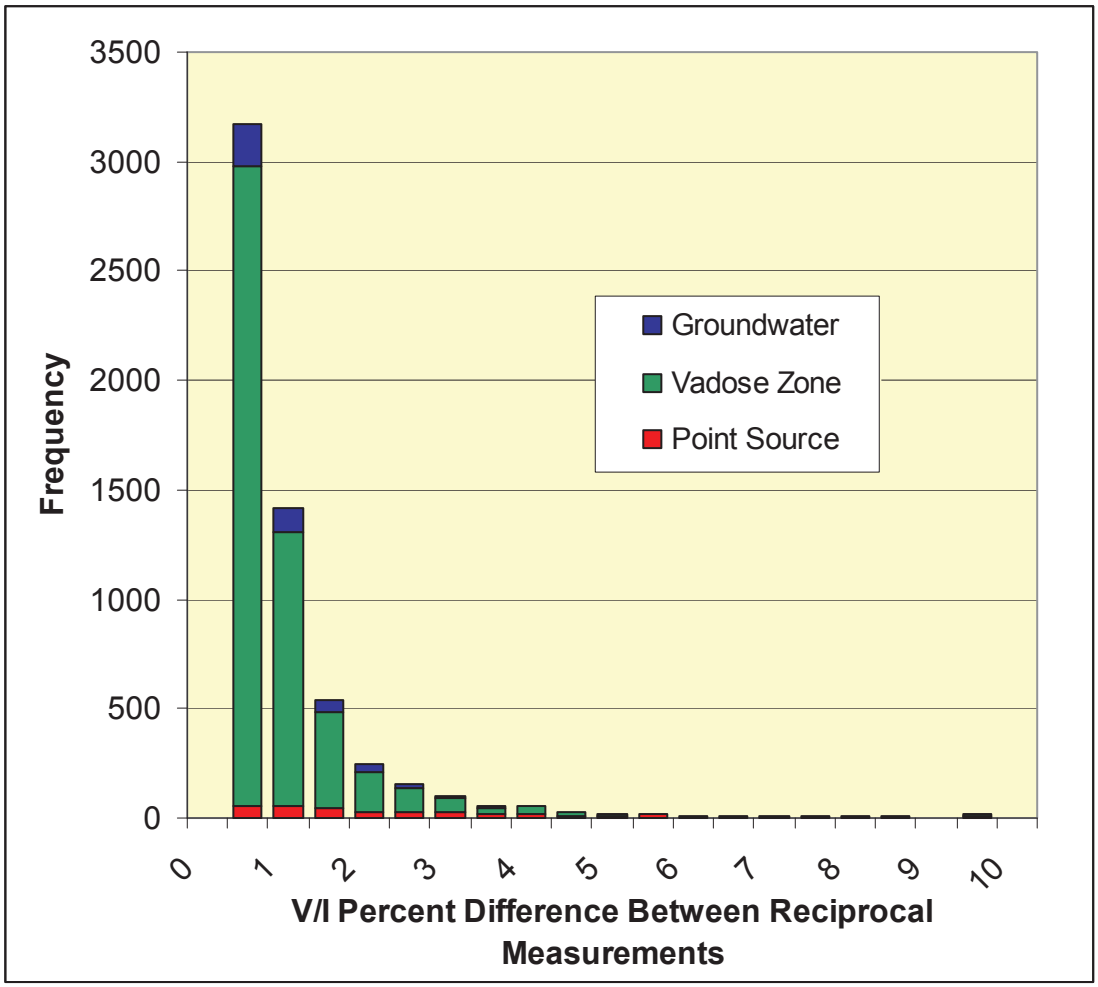

Figure A-22. Well Layout for WTW Resistivity Survey—TX-TY Complex Area.

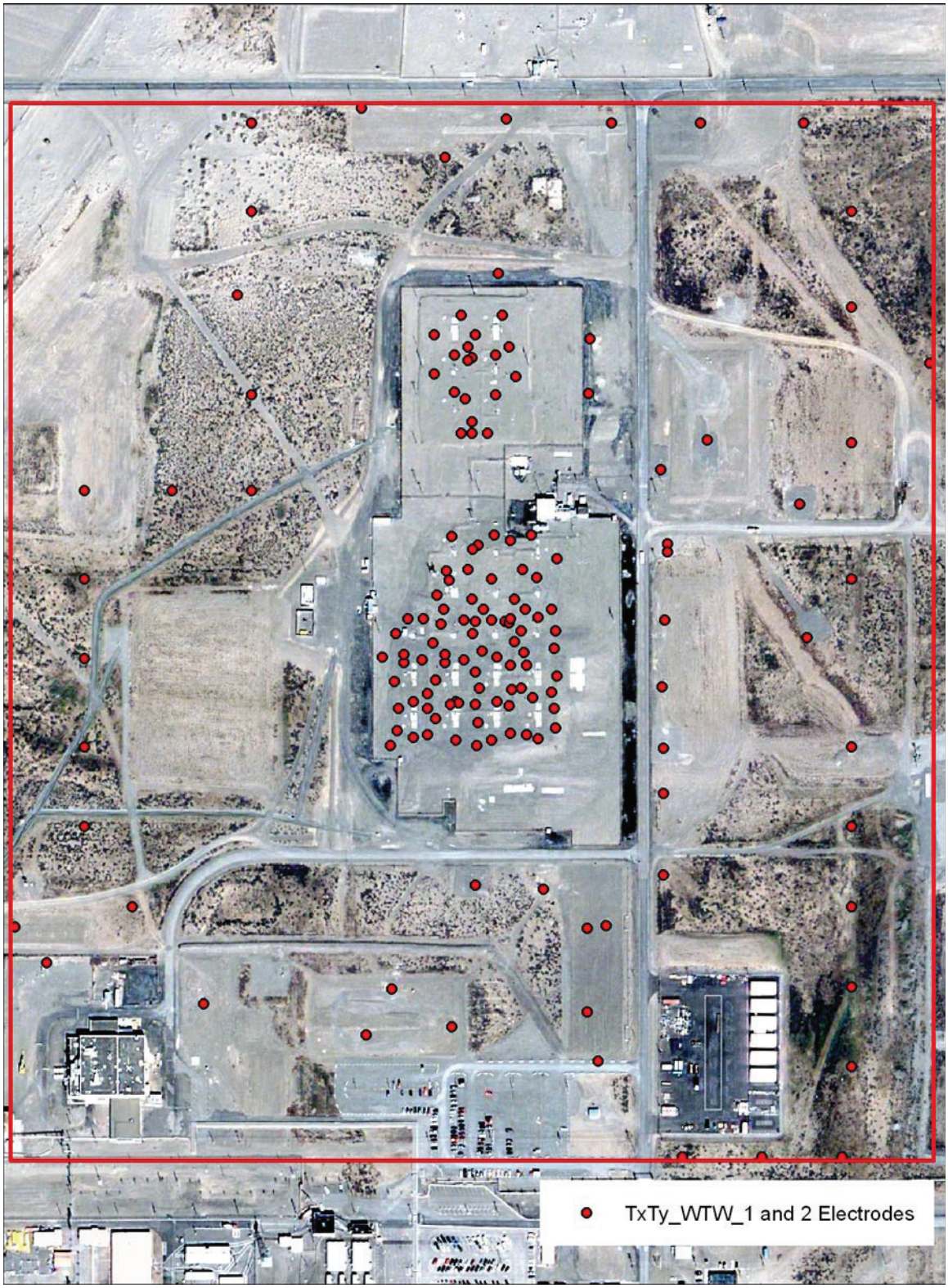

A5.0 REFERENCES

RPP-RPT-28955, 2006, *Surface Geophysical Exploration of T Tank Farm*, Rev. 0, CH2M HILL Hanford Group, Inc., Richland, Washington

This page intentionally left blank

APPENDIX B

DATA PROCESSING AND REDUCTION

This page intentionally left blank.

TABLE OF CONTENTS

B1.0 DATA PROCESSING AND REDUCTION B-1
B1.1 DATA REDUCTION B-1
B1.2 DATA FILTERING STATISTICS FOR TX-TY COMPLEX DATA B-6
B1.3 DATA INVERSION MODELING AND VISUALIZATION B-24
B1.3.1 Geospatial Database Management and Queries B-24
B1.4 INVERSION MODELING B-26
B1.4.1 Inversion Parameters B-28
B1.4.2 Resistivity Visualization B-33
B1.4.3 Resistivity Color Scales B-33
B1.5 REFERENCES B-35

LIST OF FIGURES

B-1. Schematic Flowchart for the SGE Data Acquisition and Processing Steps Contributing to the Analysis and presentation of Resistivity Data B-2
B-2. Example of Noisy Data Removal using Repeat Error (left image) and Electrical Current (right image) B-3
B-3. Example of Data Scatter (Plotted as Linear Pseudo-Section) Before and After Noisy Data Rejection B-3
B-4. Example of Spike Rejection of Transfer Resistance Data for Transmitter Electrode 237 ..... B-4
B-5. Data Filtering Example B-5
B-6. Example HRR section from Line 2E at the TX-TY Complex B-6
B-7. A) Line 1E - Raw Data Density, B) Line 1E – Filtered B-9
B-8. A) Line 1N – Raw Data Density. B) Line 1N – Filtered B-9
B-9. A) Line 2E – Raw Data Density, B) Line 2E – Filtered. B-9
B-10. A) Line 2N – Raw Data Density, B) Line 2N - Filtered B-10
B-11. A) Line 3E – Raw Data Density, B) Line 3E - Filtered B-10
B-12. A) Line 3N – Raw Data Density. B) Line 3N - Filtered B-10
B-13. A) Line 4E – Raw Data Density, B) Line 4E - Filtered B-11
B-14. A) Line 4N – Raw Data Density, B) Line 4N – Filtered B-11
B-15. A) Line 5E – Raw Data Density, B) Line 5E - Filtered B-11
B-16. A) Line 5N – Raw Data Density, B) Line 5N - Filtered B-12
B-17. A) Line 6E – Raw Data Density. B) Line 6E – Filtered B-12
B-18. A) Line 6N- Raw Data Density, B) Line 6N – Filtered B-12

B-19. A) Line 7E – Raw Data Density, B) Line 7E – Filtered B-13
B-20. A) Line 7N – Raw Data Density, B) Line 7N – Filtered B-13
B-21. A) Line 8E – Raw Data Density, B) Line 8E – Filtered B-13
B-22. A) Line 8N – Raw Data Density, B) Line 8N – Filtered B-14
B-23. A) Line 9E – Raw Data Density. B) Line 9E – Filtered B-14
B-24. A) Line 9N – Raw Data Density. B) Line 9N – Filtered B-14
B-25. A) Line 10E – Raw Data Density. B) Line 10E – Filtered B-15
B-26. A) Line 10N – Raw Data Density. B) Line 10N – Filtered B-15
B-27. A) Line 11E – Raw Data Density. B) Line 11E – Filtered B-15
B-28. A) Line 11N – Raw Data Density. B) Line 11N – Filtered B-16
B-29. A) Line 12E – Raw Data Density. B) Line 12E – Filtered B-16
B-30. A) Line 12N – Raw Data Density. B) Line 12N – Filtered B-16
B-31. A) Line 13E – Raw Data Density. B) Line 13E – Filtered B-17
B-32. A) Line 13N – Raw Data Density. B) Line 13N – Filtered B-17
B-33. A) Line 14E – Raw Data Density. B) Line 14E – Filtered B-17
B-34. A) Line 14N – Raw Data Density. B) Line 14N – Filtered B-18
B-35. A) Line 15E – Raw Data Density. B) Line 15E – Filtered B-18
B-36. A) Line 15N – Raw Data Density. B) Line 15N – Filtered B-18
B-37. A) Line 16E – Raw Data Density. B) Line 16E – Filtered B-19
B-38. A) Line 16N – Raw Data Density. B) Line 16N – Filtered B-19
B-39. A) Line 17E – Raw Data Density. B) Line 17E – Filtered B-19
B-40. A) Line 17N – Raw Data Density. B) Line 17N – Filtered B-20
B-41. A) Line 18E – Raw Data Density. B) Line 18E – Filtered B-20
B-42. A) Line 18N – Raw Data Density. B) Line 18N – Filtered B-20
B-43. A) Line 19E – Raw Data Density. B) Line 19E – Filtered B-21
B-44. A) Line 19N – Raw Data Density. B) Line 19N – Filtered B-21
B-45. A) Line 20E – Raw Data Density. B) Line 20E – Filtered B-21
B-46. A) Line 20N – Raw Data Density. B) Line 20N – Filtered B-22
B-47. A) Line 21E – Raw Data Density. B) Line 21E – Filtered B-22
B-48. A) Line 21N – Raw Data Density. B) Line 21N – Filtered B-22
B-49. A) Line 22E – Raw Data Density. B) Line 22E – Filtered B-23
B-50. A) Line 22N – Raw Data Density. B) Line 22N – Filtered B-23
B-51. A) Line 23E – Raw Data Density. B) Line 23E – Filtered B-23
B-52. A) Line 23N – Raw Data Density. B) Line 23N – Filtered B-24
B-53. A) Line 24N – Raw Data Density. B) Line 24N – Filtered B-24

B-54. ERSI ArcView 9.2 Interface with Resistivity Data Plotted by Location on an Aerial Photo of TX-TY Complex B-25

B-55. A) Resistivity data loaded in geospatial database (Lower Window), B) Sample SQL code (Right Window), C) Model domain (blue highlighted data points on aerial photo).....B-26

B-56. Flowchart of the Resistivity Inversion Process.....B-28

B-57. TX-TY Complex Inversion model Resistivity Histograms and Color Values B-34

LIST OF TABLES

B-1. Data Reduction Statistics for all TX-TY Complex HRR lines.....B-7

B1.0 DATA PROCESSING AND REDUCTION

Data processing and reduction steps involve processing and visualization of resistivity and GPS data. The GPS data provide accurate control points and geo-referencing so that the resistivity data can be accurately located relative to trenches, cribs and tank farm features. Data reduction involves the post-acquisition identification and removal of spurious data values that do not conform to the overall data population or that violate potential theory.

B1.1 DATA REDUCTION

The resistivity data are collected along two-dimensional transects in order to best satisfy data processing, site layout logistics and equipment. Data processing is performed on an individual line basis and then combined into a three-dimensional (3D) data set using the GPS data. Figure B-1 presents a flowchart of the data acquisition and processing steps contributing to and resulting in the final analysis and presentation of the HRR data.

Pre-survey and background geophysical properties were acquired using Ground Penetrating Radar, Electromagnetics, and Magnetics surveying to determine the location of subsurface infrastructure or other buried metallic debris. The results of these surveys are presented in two separate reports: *Surface Geophysical Exploration of TX and TY Tank Farms at the Hanford Site: Results of Background Characterization with Ground Penetrating Radar (RPP-RPT-38104)* and *Surface Geophysical Exploration of TX and TY Tank Farms at the Hanford Site: Results of Background Characterization with Magnetics and Electromagnetics (RPP-RPT-36893).*

Each day, individual binary data files are downloaded and exported to a laptop computer where the data are reviewed to ensure adequate data quality before moving the resistivity equipment to the next survey line. This process also allows the operator to refine data acquisition parameters as the survey migrates from one area of the site to another. Each file is parsed into usable columns (e.g., Record No., Date, Current, Normalized Potential, Error, Apparent Resistivity, Geometry, Transmitter Gain) using Excel (Microsoft, Inc.). Numerical and graphical evaluation of the signal-to-noise ratio, percent error, and scatter in collected data in comparison to neighboring lines were conducted as a part of the data inspection process.

After data are downloaded from the resistivity instrument and parsed into a usable spreadsheet format, data filtering techniques are used to identify and remove data spikes or anomalous data caused by data acquisition card instabilities or extraneous current sources. Data filtering is performed by copying the parsed raw data into an Excel (Microsoft, Inc.) data filtering template that contains a series of graphs that show the various data parameters. The process of filtering identifies and eliminates data points, but no data modification (rounding, averaging, smoothing, or splining) is permitted. The rationale is to seek out and remove spurious points that do not conform to the data population or points that violate potential theory.

Figure B-1. Schematic Flowchart for the SGE Data Acquisition and Processing Steps Contributing to the Analysis and presentation of Resistivity Data.

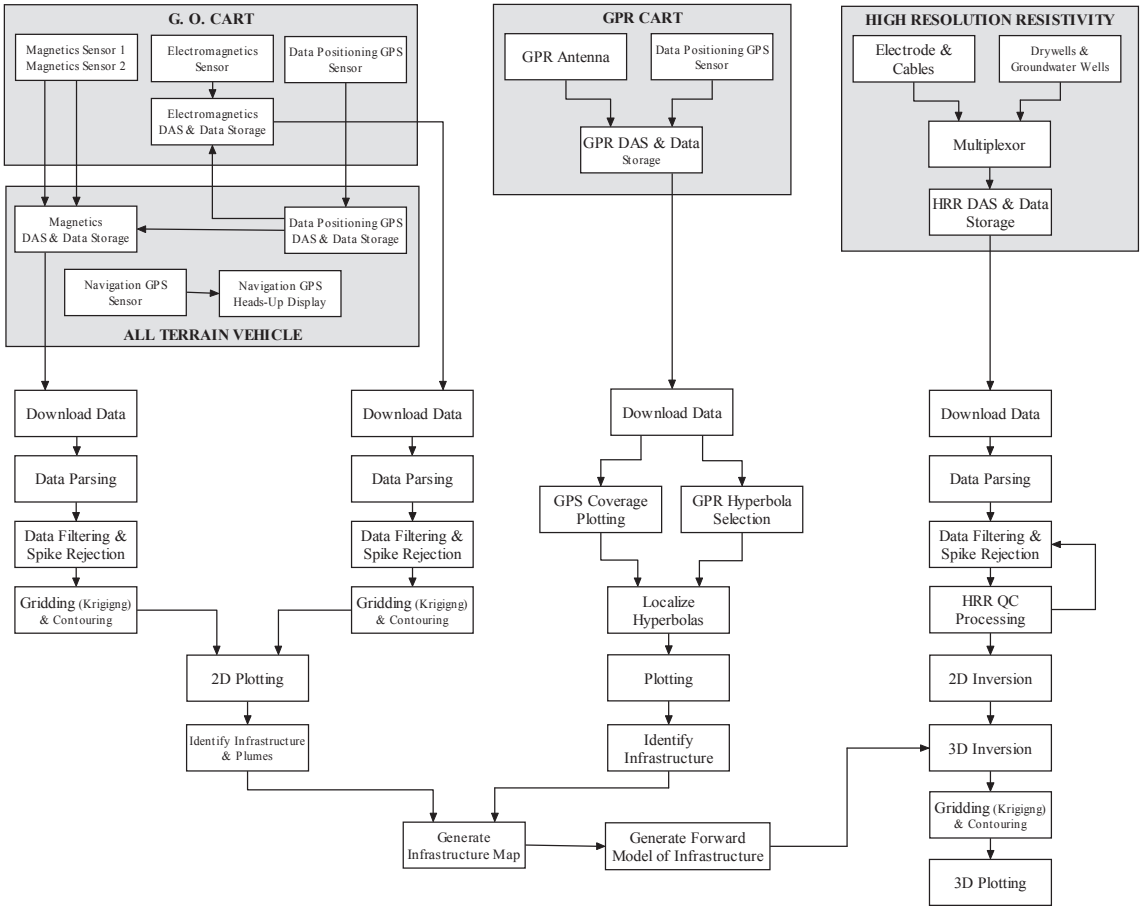

Several data parameters are plotted with respect to the X axis plane along the line (i.e., pseudo-sectional format) to inspect data quality and consistency. Data parameters that are assessed during this step include: apparent resistivity (calculated by the measurement instrument), normalized potential (V/I), repeat error, and electrical current. Auto-filters (filtering technique within Microsoft Excel that easily segregates specific groups of data records based on user criteria, e.g., measured normalized voltage values below 0.001 ohms) are then applied to the data fields. The auto-filtering allows an operator to quickly interrogate a specific data range for each parameter. The data plots for all quality fields are linked to the auto-filters, and only show the resulting data that remains after a filter is applied. To remove any unsatisfactory data points, an operator selects the appropriate auto-filter range, determines which data points do not conform to the surrounding data population or conflict with potential theory, and then deletes the rows that contain the unsatisfactory points.

The following discussion provides a specific example data set to illustrate the general filtering process:

Step 1:

Figure B-2 shows an example of data that are targeted for removal. The low transmitted current produced measured data with high error (in relation to the data population). To ensure that the original data are retained and error removal can be repeated, the raw and edited data are saved to different folders with different file names. Data editing statistics are retained for QA purposes.

Figure B-2. Example of Noisy Data Removal using Repeat Error (left image) and Electrical Current (right image).

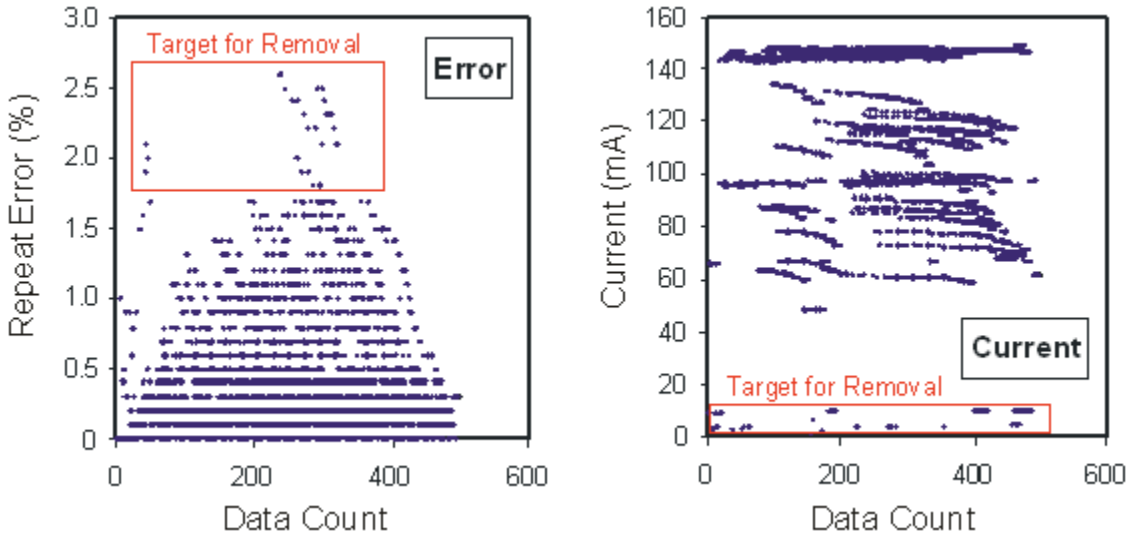

Step 2:

The result of the data removal in Step 1 is shown in Figure B-3. The data are plotted spatially according to the standard pseudo-section methodology. The left plot of Figure B-3 shows the distribution of all measurements and the right plot of Figure B-3 shows the distribution of data after removal of noisy data from Step 1.

Figure B-3. Example of Data Scatter (Plotted as Linear Pseudo-Section) Before and After Noisy Data Rejection.

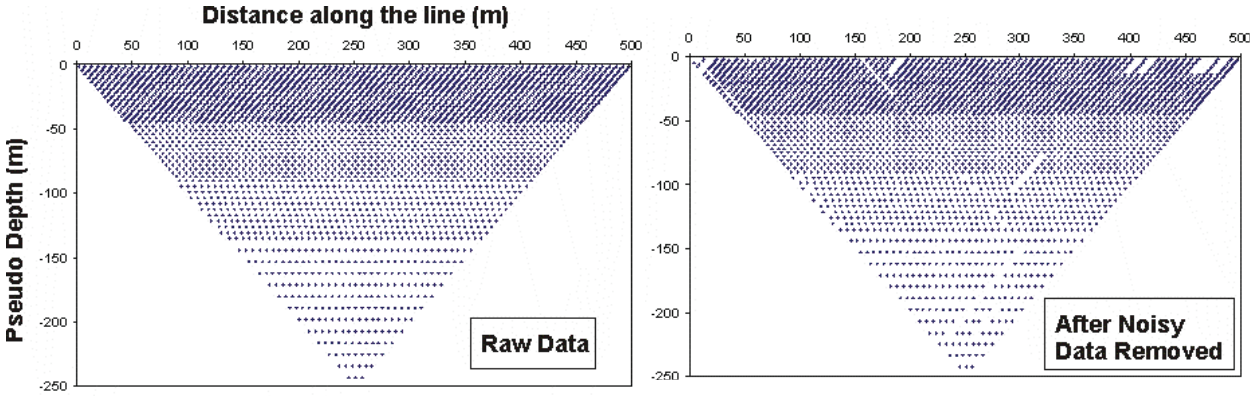

Step 3:

After data rejection is completed based on noise or error, data are evaluated for physical impossibilities as they relate to potential field theory. This step requires that the transfer resistance (V/I) for each transmitter electrode be plotted with all of the receiver electrodes. The plot should show a smoothly varying function as the separation of the transmitter and receiver electrode increases. Large spikes in the function are associated with suspect data points that represent physical impossibilities in natural media. In this case, these data are removed from the overall data set. Figure B-4 demonstrates an example of a data spike that is targeted for removal as it violates potential theory. The process involves individually assessing each data "sweep" based on transmitter and then repeating the process based on each receiver "sweep."

Figure B-4. Example of Spike Rejection of Transfer Resistance Data for Transmitter Electrode 237.

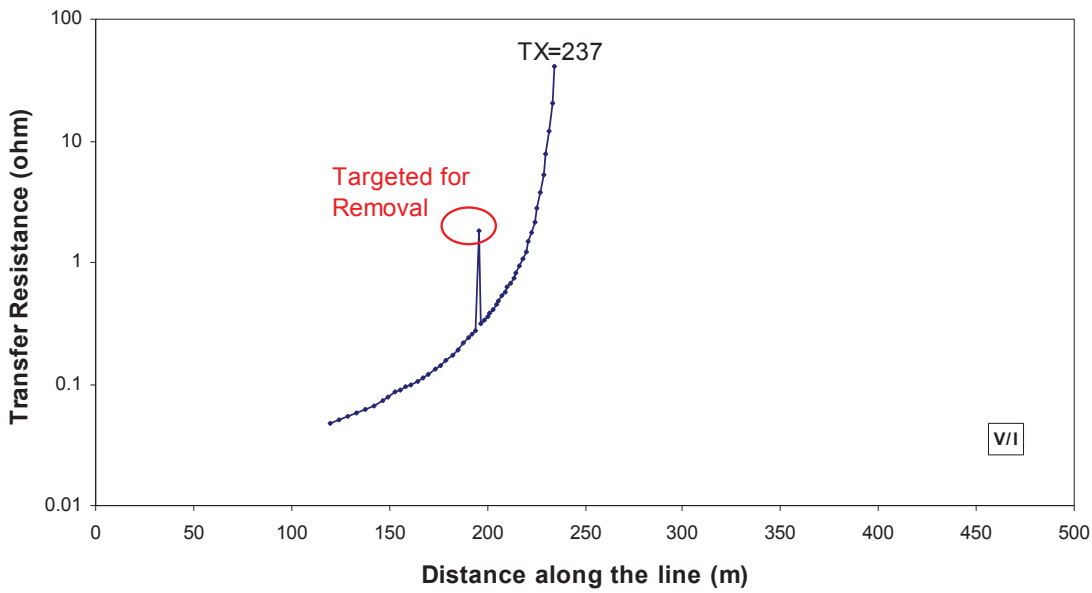

Filtering is accomplished by plotting all receivers associated with a particular transmitter. Using Figure B-5A as a guide, a single transmitter is shown with a series of receivers. The distance between a transmitter-receiver pair will dictate the depth at which the data point is represented. Figure B-5B shows how the entire subsurface is populated when considering all transmitter-receiver pairs. Figure B-5C shows a plot of the actual normalized voltage potential (V/I in ohms [transfer resistance]) associated with a transmitter. Within this plot are two example sets from the TX-TY Complex data acquisition, representing types of spurious data: Line 9N, transmitter number 240 (Tx 240) with all receivers and Line 15E, Tx 234 with all receivers.

In the case of Line 9N, a single spike is evident on only one receiver when transmitting on transmitter number 240. The single point spike violates potential field theory and

therefore is likely due to measurement error. Potential field theory, in summary, states that if the spike would have been from a very resistive layer, it would also have influence on all other measurements at larger separations. This is not the case in Figure B-5C. For filtering, this spike is removed from the data set due to its non-conformance. Often, spikes of this nature are associated with one bad receiver and will carry through a series of transmitters. In such a case, all data from the affected receiver may be removed from the data set. Conversely, these spikes may carry through a series of receivers and may be associated with one transmitter. Line 9N represents a fairly clean data set for TX-TY Farm.

In the case of Line 15E, multiple suspect data points are observed. Little confidence can be placed in these data values for this particular transmitter. As a result, many points at multiple receiver locations would be removed during the filtering. Line 15E represents a relatively noisy data set for TXTY Farm.

Figure B-5D shows how the removal process affects the overall data coverage. The plot representing line 15E shows that approximately 35% of the data are removed. This represents the high end of percent data edited for TX-TY resistivity lines. Line 9N, on the other hand, shows that approximately 3% of the data have been removed, representing a more lightly edited TX-TY representation.

Figure B-5. Data Filtering Example.

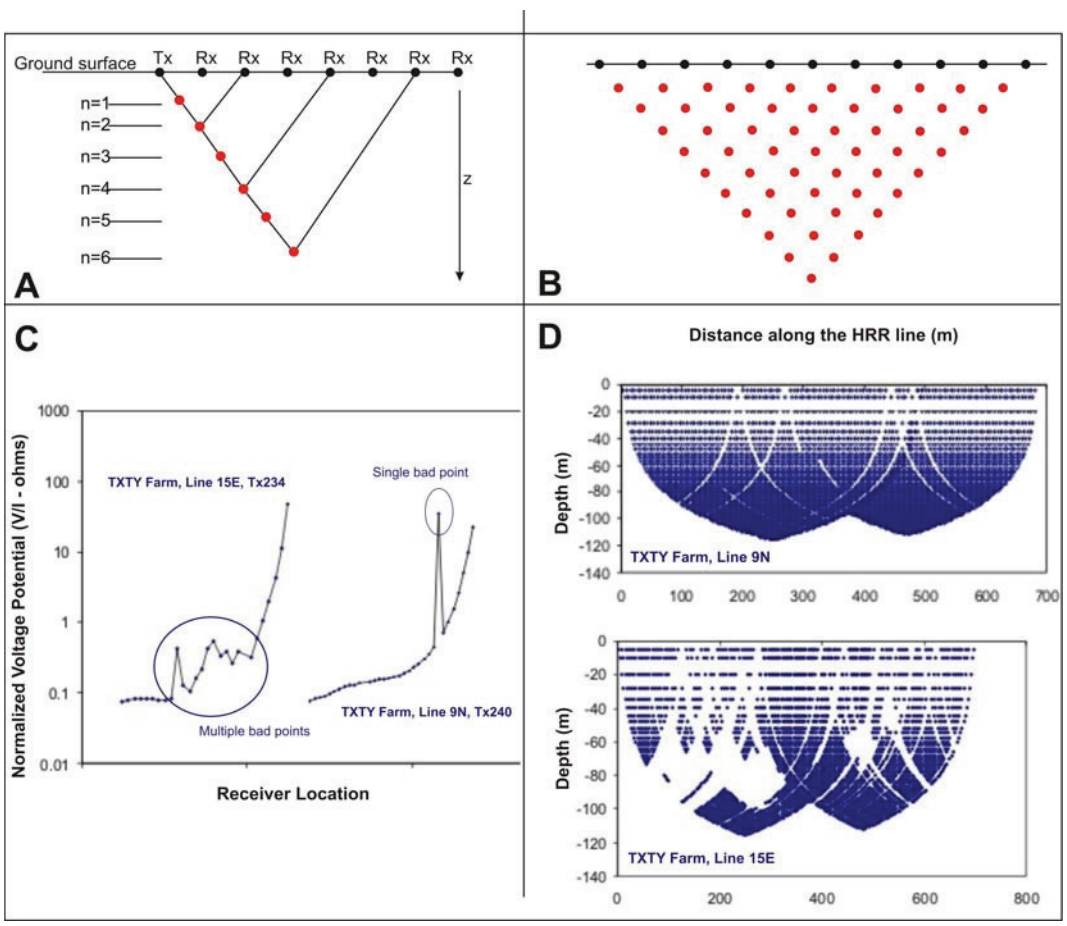

Step 4:

After eliminating all data that are considered low quality, the data are then passed through a processing algorithm that uses a geometric inversion technique. Measured normalized potential values are converted to an apparent resistivity at a depth that represents the highest sensitivity. The depth is a logarithmic function of electrode spacing. The HRR routine places the measured apparent resistivity value at a depth below ground surface that best represents its location.

Step 5:

The data are then plotted as HRR color-contoured cross-sections in Surfer® (Golden Software, Inc). The plot can be used as a quality check of data acceptability and data coverage, while also providing an approximation to the depth of the target. Figure B-6 displays an example of a contoured cross section produced for Line 2E.

Figure B-6. Example HRR section from Line 2E at the TX-TY Complex.

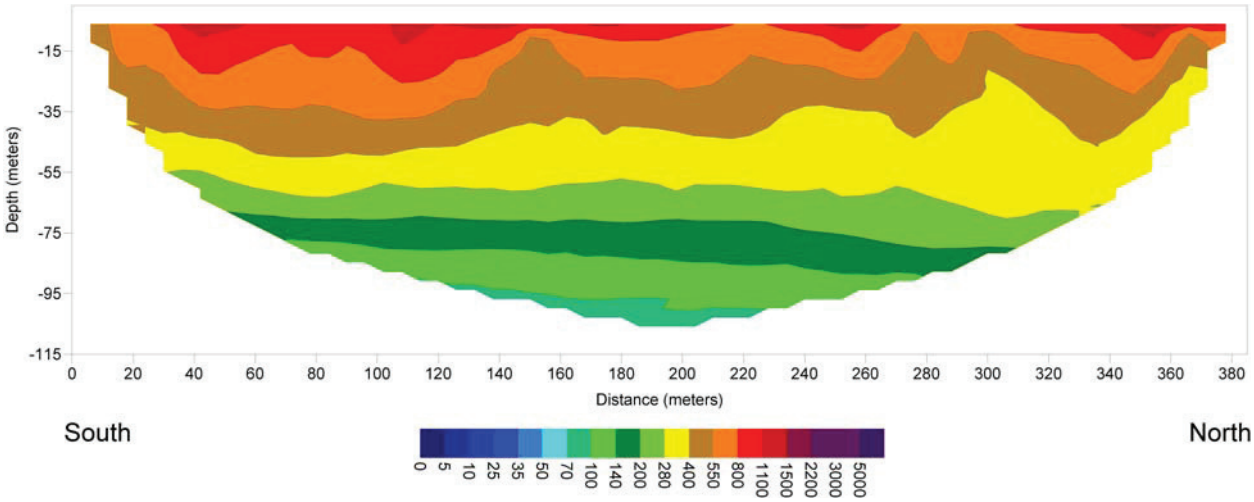

B1.2 DATA FILTERING STATISTICS FOR TX-TY COMPLEX DATA

The TX-TY Complex Data were filtered for inversion and data reduction statistics, such as the number of data points removed and error cutoff value, were recorded. Table 1 displays statistics for data reduction performed on all forty-seven TX-TY Complex resistivity lines. Column A provides the line number and Column B lists the number of raw data points before removal of any spurious data. Column C lists the number of data points remaining following filtering performed as described in Steps 1 through 3 above. Column D lists the percent data removed from the raw dataset, with a minimum percentage of 0% removed and a maximum of approximately 38%.

® Surfer is a registered trademark of Golden Software, Inc., Golden, Colorado.

The repeatable error cut-off value used in data removal is provided in Column E of Table B-1. The error value is a statistic calculated in data processing performed by the SuperSting resistivity instrument. The error cut-off value describes the value at which all greater percent error values, (i.e. those that did not conform to the data population or were associated with spurious data) were removed from the data set. The minimum current value at which data associated with all lesser current values were removed is given in Column F within Table B-1.

Table B-1. Data Reduction Statistics for all TX-TY Complex HRR lines. (2 Sheets)

A	B	C	D	E	F
Line Number	No. of Data Points	No. of Data Points – Filtered	Percent Data Removed (%)	Repeat Error Cut-off (%)	Current Cut-off Values (mA)
01E_STS	1955	1571	19.6	*N/A	*N/A
01N_STS	884	765	13.5	16	*N/A
02E_STS	1953	1438	26.4	10	*N/A
02N_STS	885	774	12.5	12	*N/A
03E_STS	1898	1593	16.1	15	*N/A
03N_STS	885	736	16.8	20	*N/A
04E_STS	1900	1630	14.2	20	*N/A
04N_STS	903	903	0.0	*N/A	*N/A
05E_STS	1896	1729	8.8	25	*N/A
05N_STS	4976	4797	3.6	30	*N/A
06E_STS	1891	1806	4.5	*N/A	*N/A
06N_STS	5410	5196	4.0	30	*N/A
07E_STS	4863	3808	21.7	30	*N/A
07N_STS	5168	4983	3.6	30	*N/A
08E_STS	6335	3881	38.7	30	*N/A
08N_STS	5590	4846	13.3	40	*N/A
09E_STS	5783	3742	35.3	27	*N/A
09N_STS	5151	4980	3.3	*N/A	*N/A
10E_STS	5785	4171	27.9	30	*N/A
10N_STS	5007	4639	7.3	40	*N/A
11E_STS	5861	4086	30.3	30	*N/A
11N_STS	5069	4572	9.8	45	*N/A
12E_STS	5799	4832	16.7	30	97
12N_STS	5249	4938	5.9	35	*N/A
13E_STS	5954	5138	13.7	30	81
13N_STS	5178	4152	19.8	37	*N/A

Table B-1. Data Reduction Statistics for all TX-TY Complex HRR lines. (2 Sheets)

A	B	C	D	E	F
Line Number	No. of Data Points	No. of Data Points – Filtered	Percent Data Removed (%)	Repeat Error Cut-off (%)	Current Cut-off Values (mA)
14E_STS	5233	4227	19.2	28	*N/A
14N_STS	4944	4288	13.3	22	*N/A
15E_STS	5807	3732	35.7	15	*N/A
15N_STS	5797	4640	20.0	20	*N/A
16E_STS	4994	4413	11.6	*N/A	*N/A
16N_STS	5623	4897	12.9	20	96
17E_STS	4676	4488	4.0	31	*N/A
17N_STS	5623	4363	22.4	29	*N/A
18E_STS	4658	4394	5.7	*N/A	*N/A
18N_STS	3169	2005	36.7	29	97
19E_STS	4743	4502	5.1	20	*N/A
19N_STS	3248	2546	21.6	27	*N/A
20E_STS	4785	4605	3.8	29	*N/A
20N_STS	3213	2694	16.2	24	*N/A
21E_STS	4739	4436	6.4	30	*N/A
21N_STS	2968	2576	13.2	27	*N/A
22E_STS	4995	4540	9.1	27	*N/A
22N_STS	3103	2622	15.5	28	*N/A
23E_STS	4760	4219	11.4	29	*N/A
23N_STS	3160	3067	2.9	23	*N/A
24N_STS	3163	2839	10.2	27	*N/A

* Data were not filtered based on this parameter.

Plots that help visualize the effect of data reduction and decimation on the original raw data population are provided in Figures B-7 through B-53. For each line there are two associated figures. Plot A shows the raw data density, plotted as a pseudo-section. Plot B displays the same pseudo-section after the data has been filtered per Steps 1 through 3 above.

Figure B-7. A) Line 1E - Raw Data Density, B) Line 1E – Filtered.

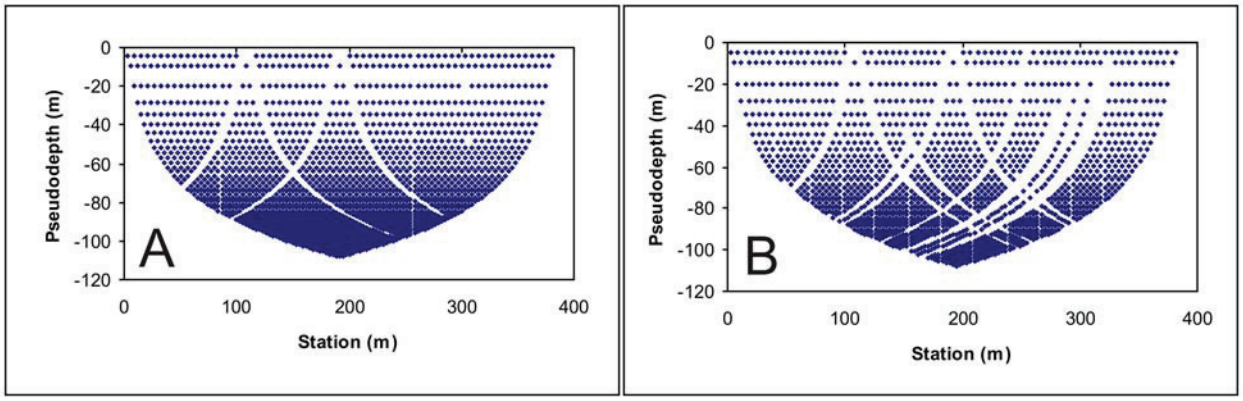

Figure B-8. A) Line 1N – Raw Data Density. B) Line 1N – Filtered.

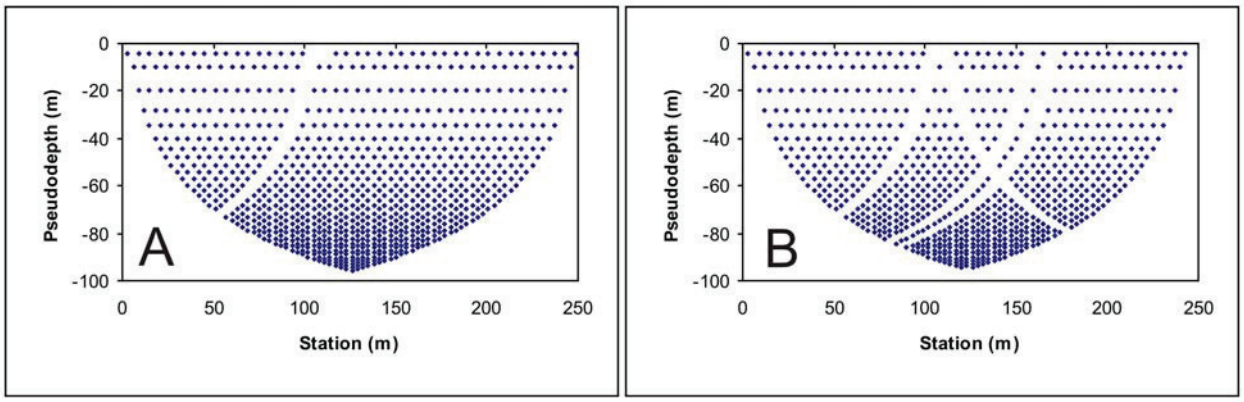

Figure B-9. A) Line 2E – Raw Data Density, B) Line 2E – Filtered.

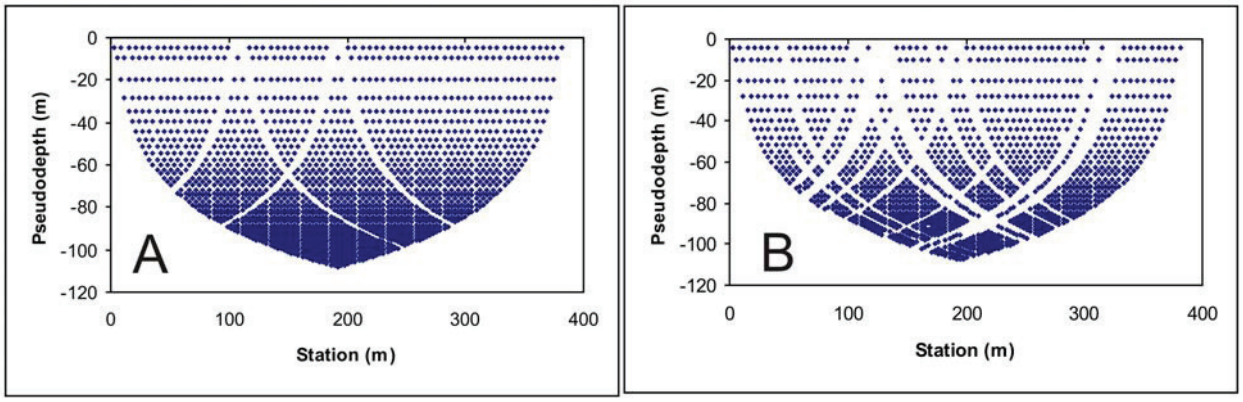

Figure B-10. A) Line 2N – Raw Data Density, B) Line 2N - Filtered.

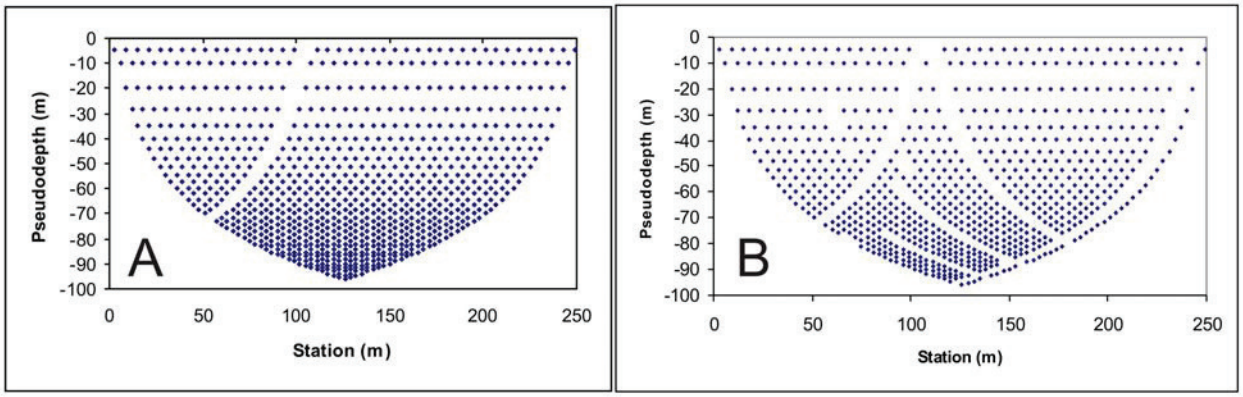

Figure B-11. A) Line 3E – Raw Data Density, B) Line 3E - Filtered.

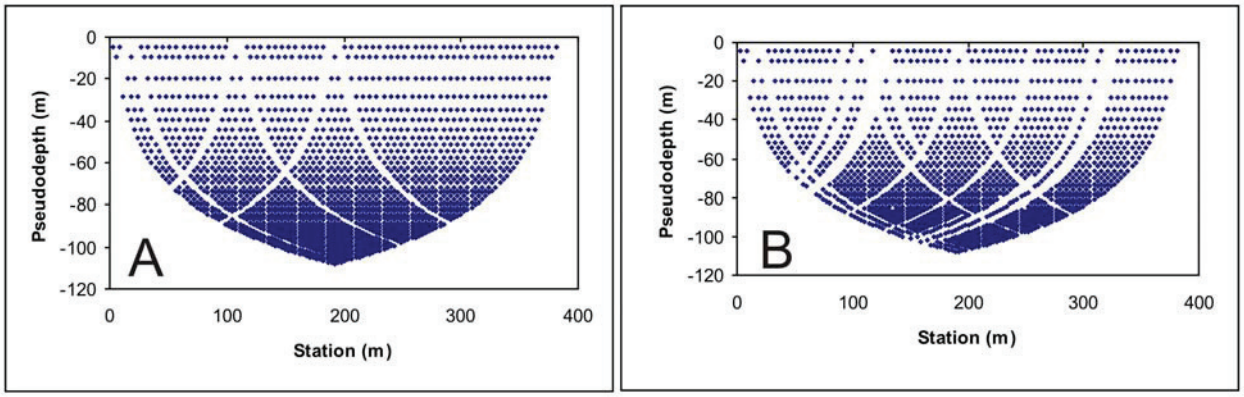

Figure B-12. A) Line 3N – Raw Data Density. B) Line 3N - Filtered.

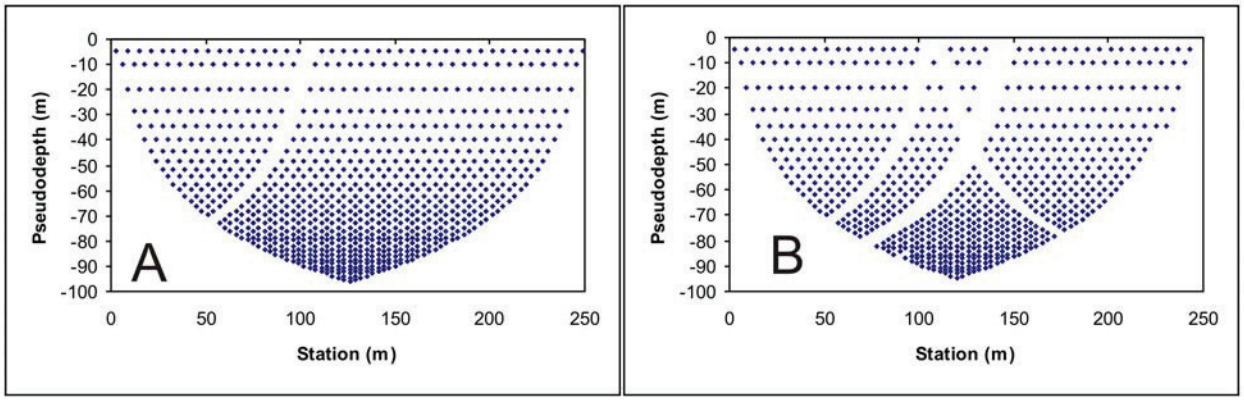

Figure B-13. A) Line 4E – Raw Data Density, B) Line 4E - Filtered.

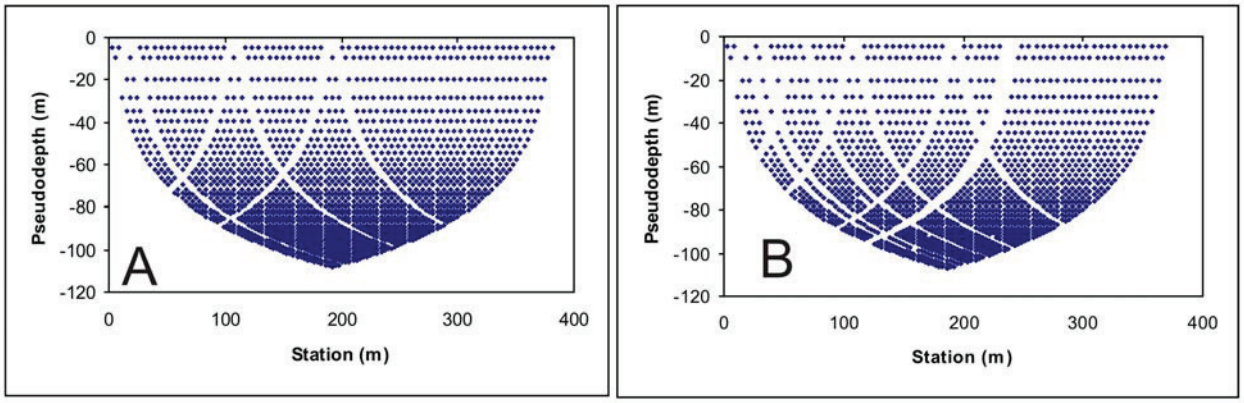

Figure B-14. A) Line 4N – Raw Data Density, B) Line 4N – Filtered.

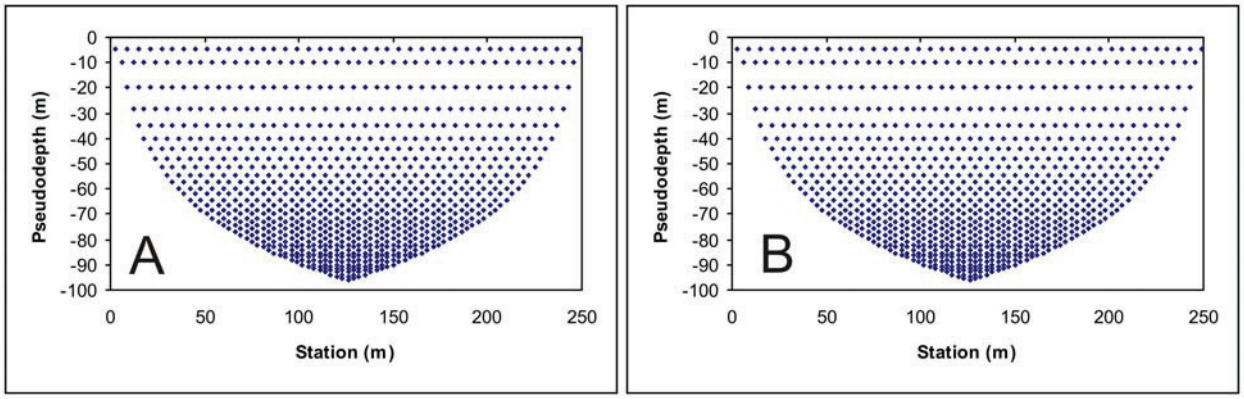

Figure B-15. A) Line 5E – Raw Data Density, B) Line 5E - Filtered.

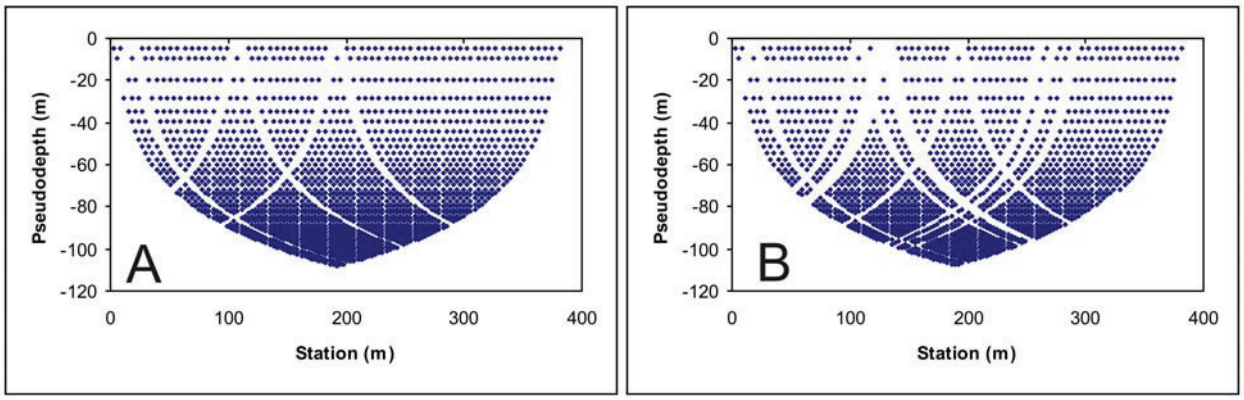

Figure B-16. A) Line 5N – Raw Data Density, B) Line 5N - Filtered.

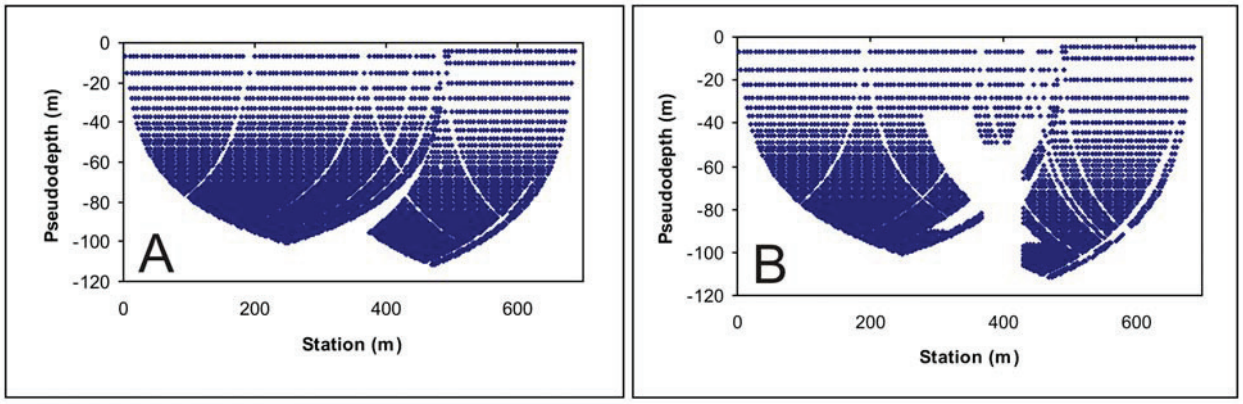

Figure B-17. A) Line 6E – Raw Data Density. B) Line 6E – Filtered.

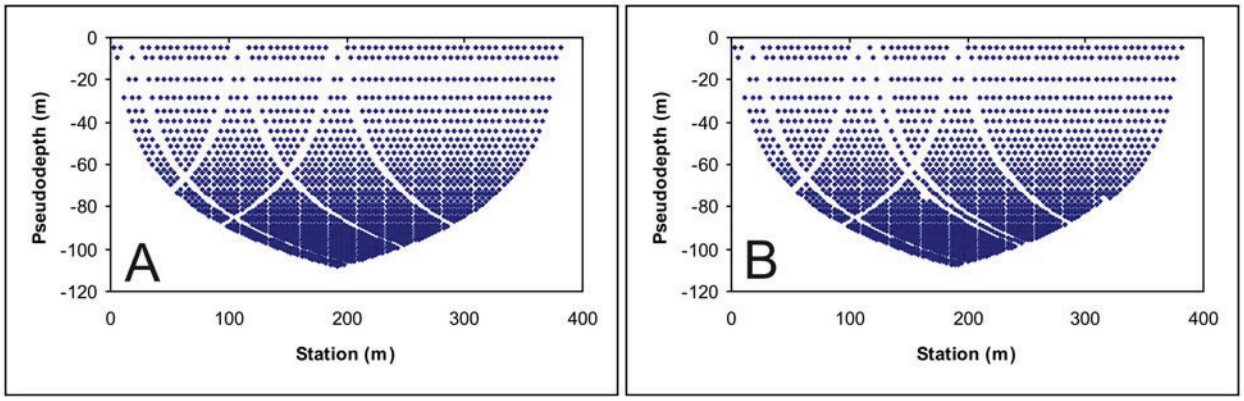

Figure B-18. A) Line 6N- Raw Data Density, B) Line 6N – Filtered.

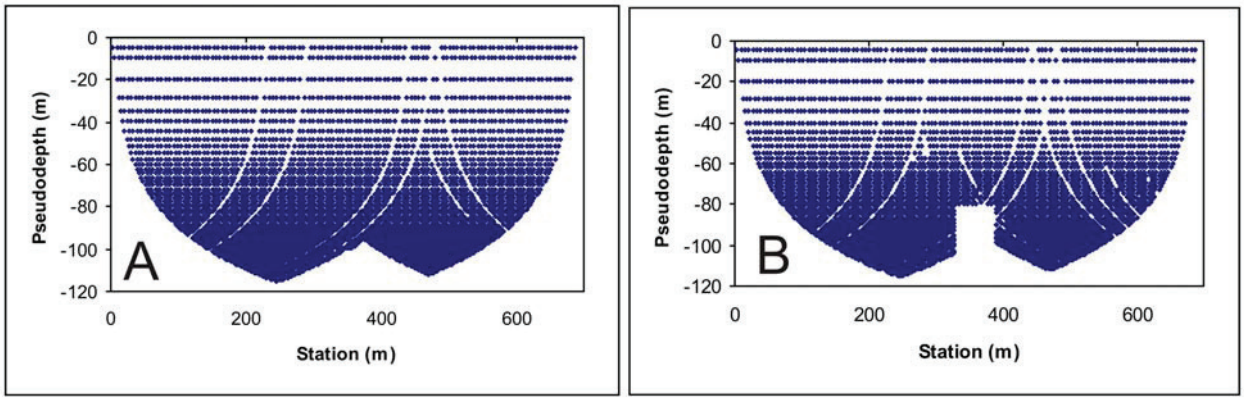

Figure B-19. A) Line 7E – Raw Data Density, B) Line 7E – Filtered.

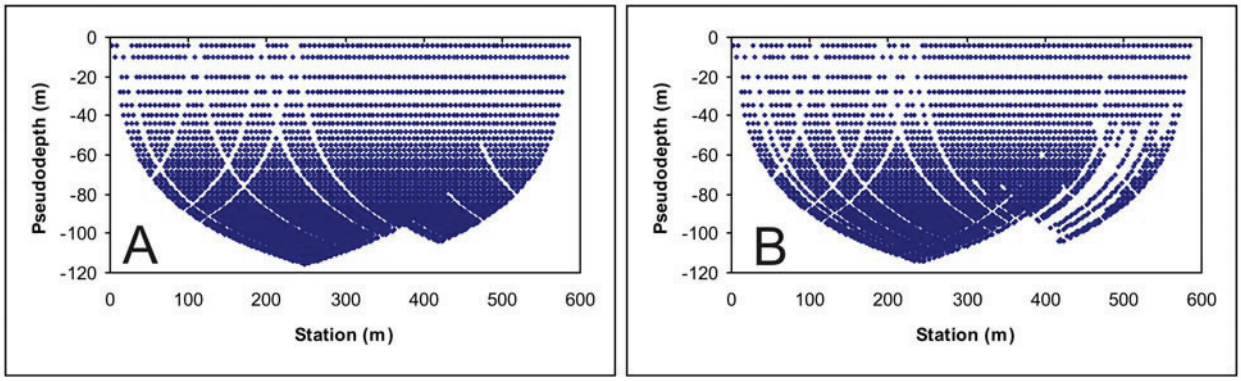

Figure B-20. A) Line 7N – Raw Data Density, B) Line 7N – Filtered.

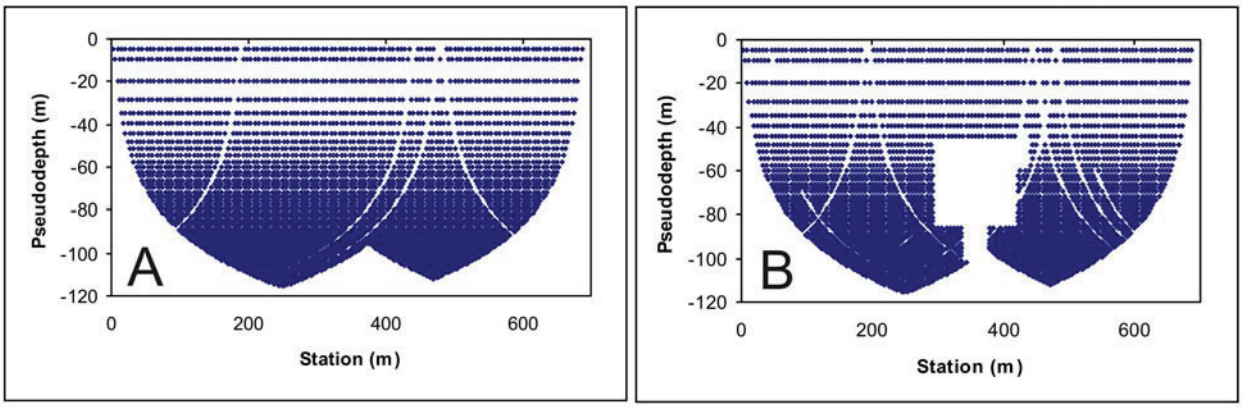

Figure B-21. A) Line 8E – Raw Data Density, B) Line 8E – Filtered.

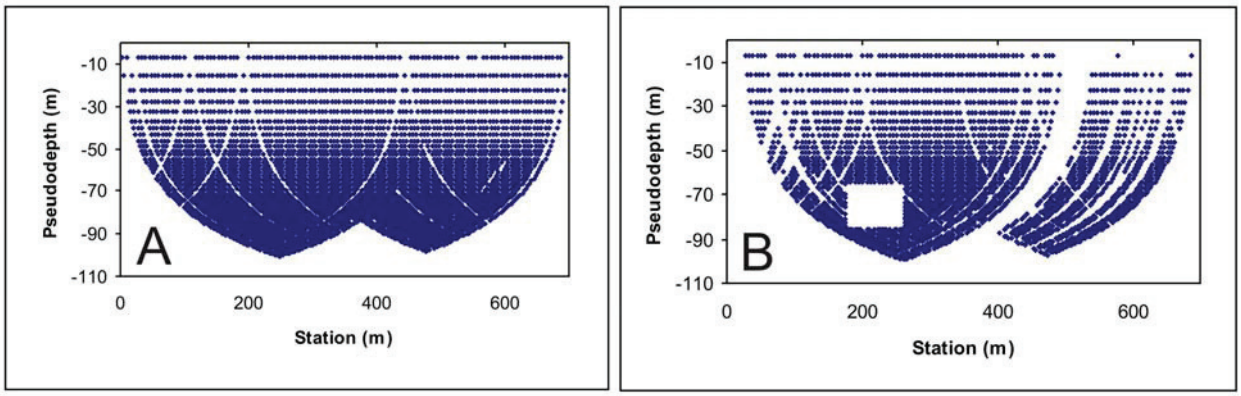

Figure B-22. A) Line 8N – Raw Data Density, B) Line 8N – Filtered.

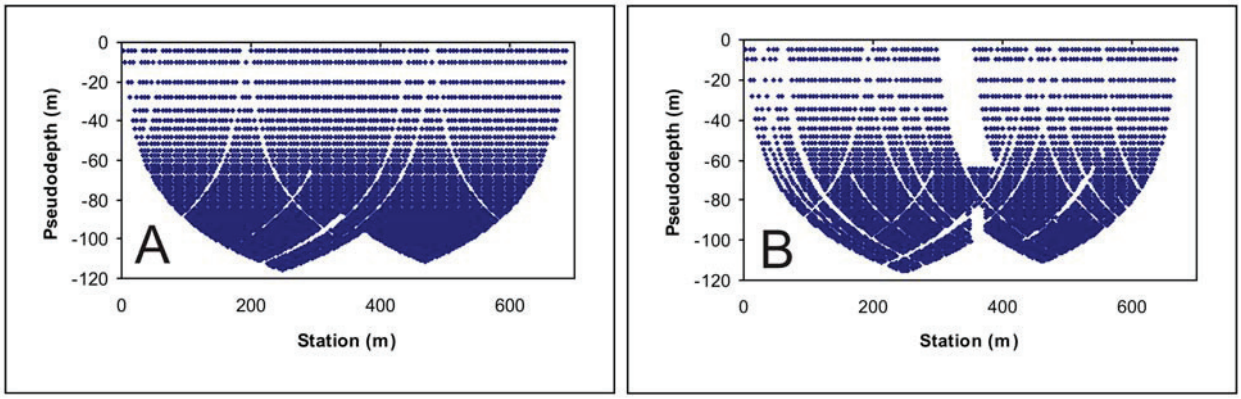

Figure B-23. A) Line 9E – Raw Data Density. B) Line 9E – Filtered.

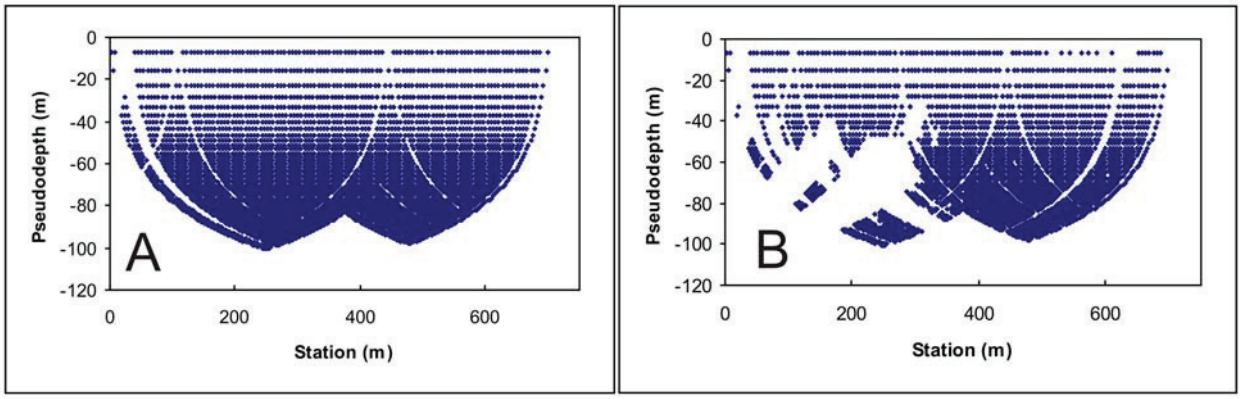

Figure B-24. A) Line 9N – Raw Data Density. B) Line 9N – Filtered.

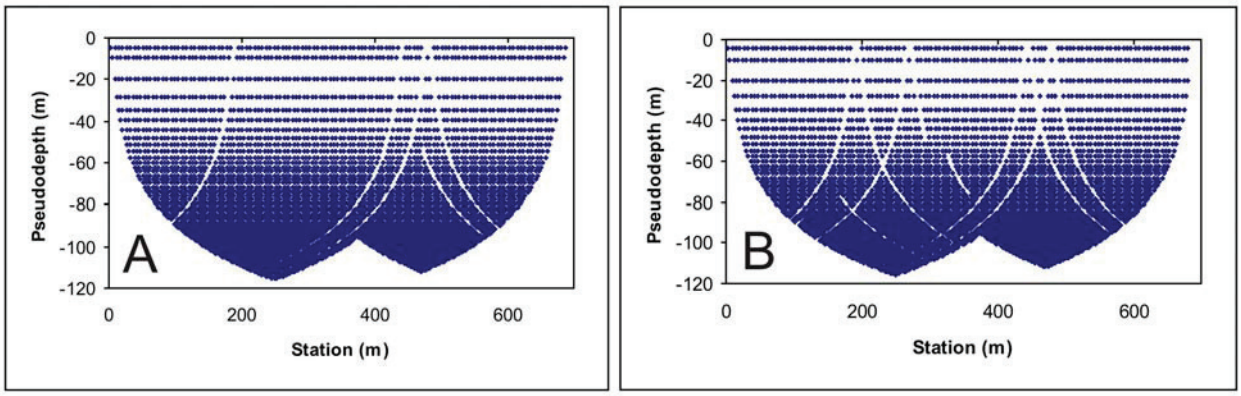

Figure B-25. A) Line 10E – Raw Data Density. B) Line 10E – Filtered.

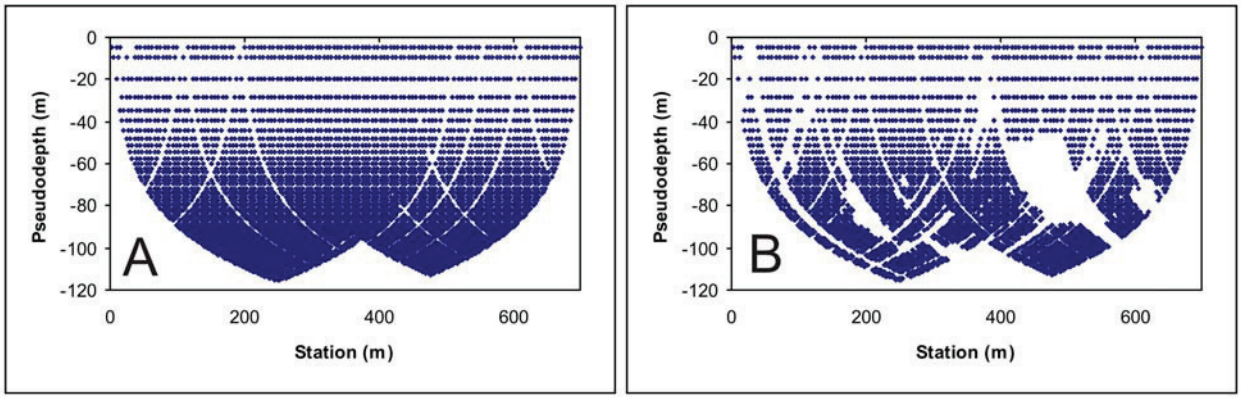

Figure B-26. A) Line 10N – Raw Data Density. B) Line 10N – Filtered.

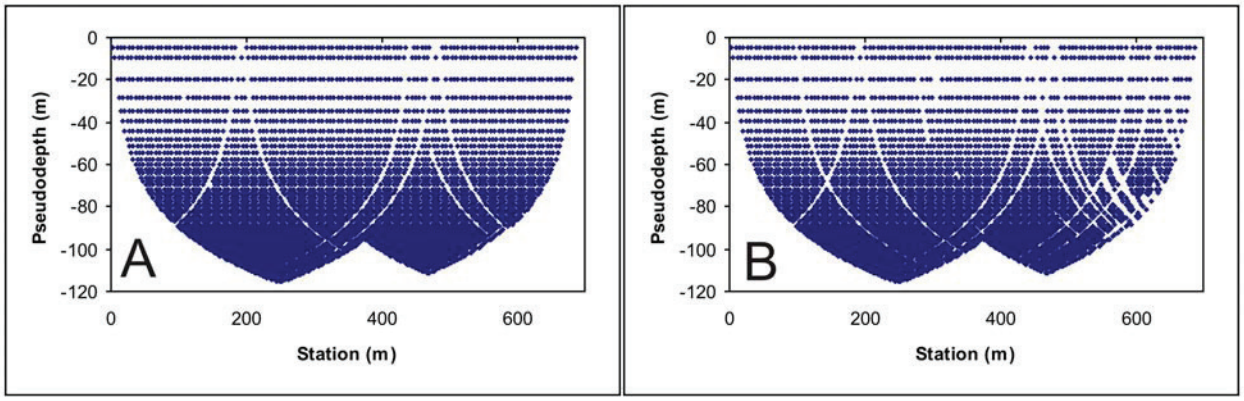

Figure B-27. A) Line 11E – Raw Data Density. B) Line 11E – Filtered.

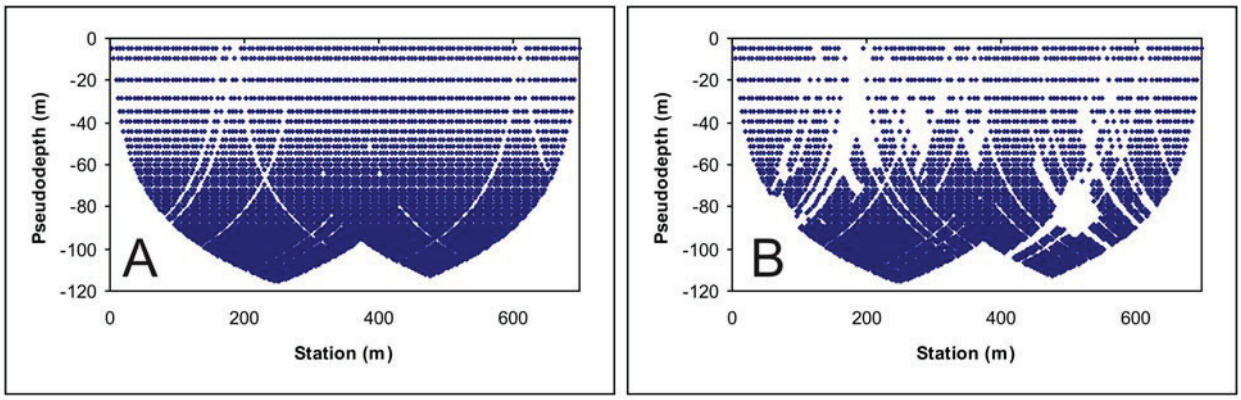

Figure B-28. A) Line 11N – Raw Data Density. B) Line 11N – Filtered.

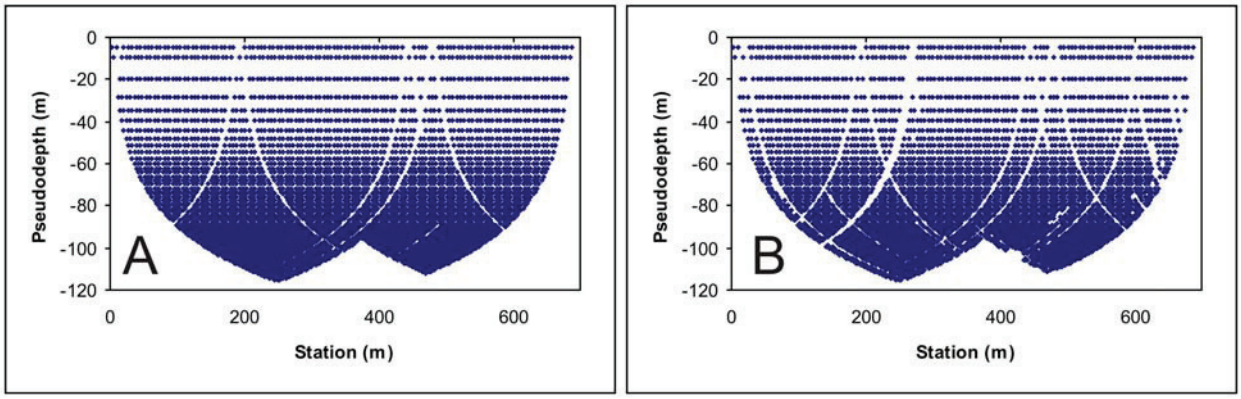

Figure B-29. A) Line 12E – Raw Data Density. B) Line 12E – Filtered.

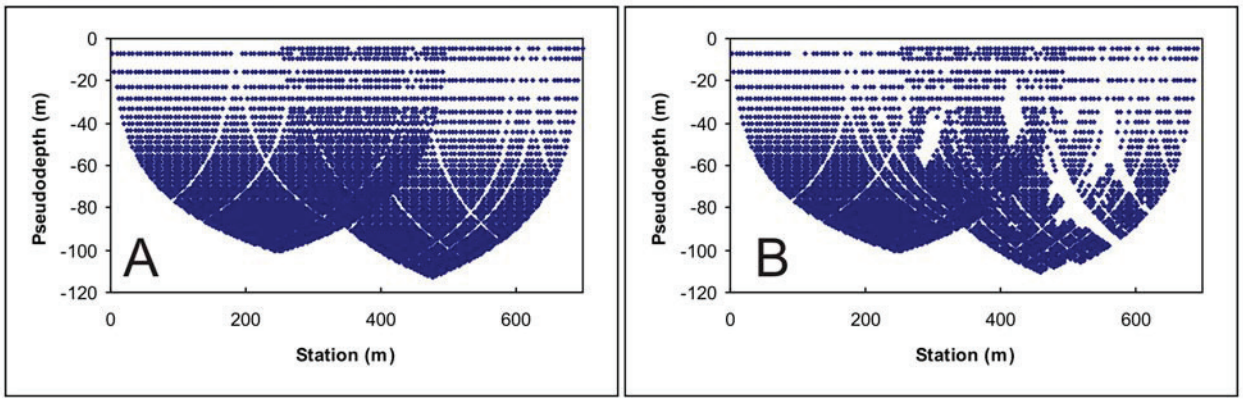

Figure B-30. A) Line 12N – Raw Data Density. B) Line 12N – Filtered.

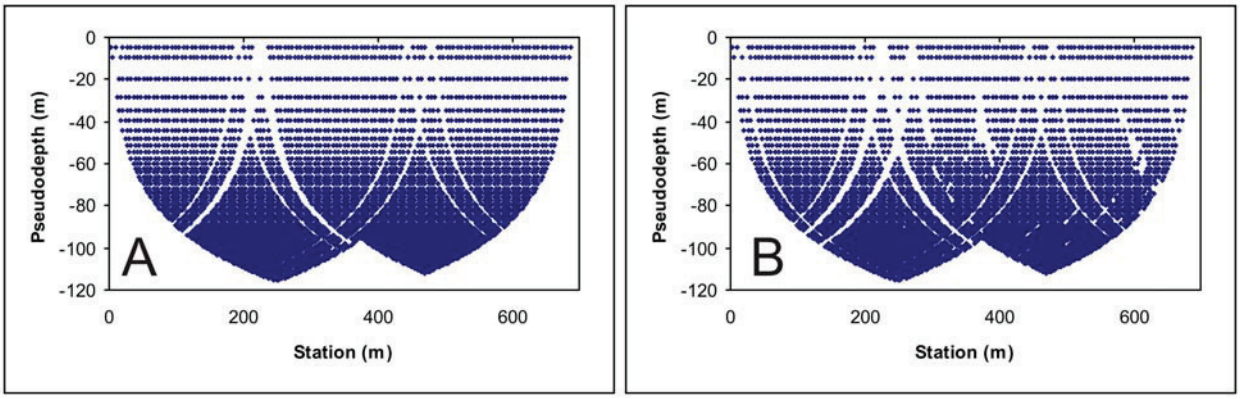

Figure B-31. A) Line 13E – Raw Data Density. B) Line 13E – Filtered.

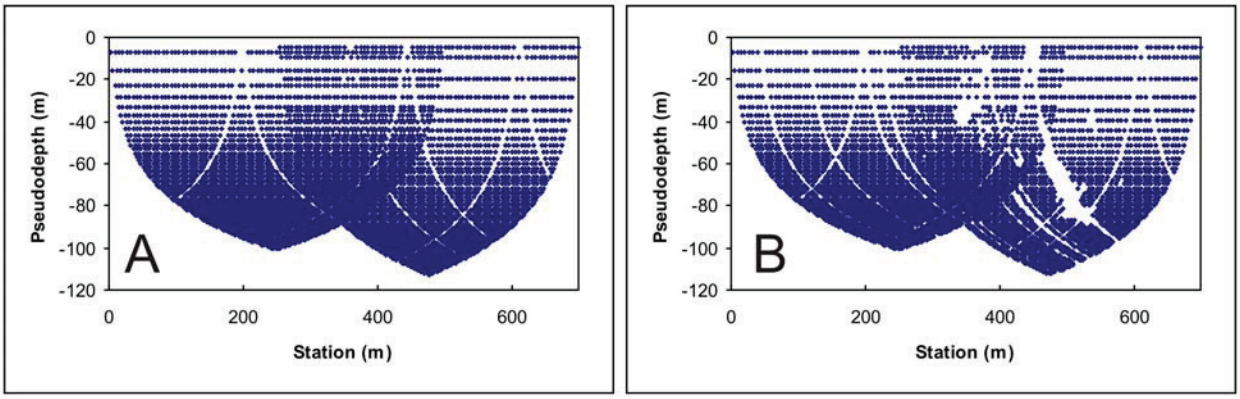

Figure B-32. A) Line 13N – Raw Data Density. B) Line 13N – Filtered.

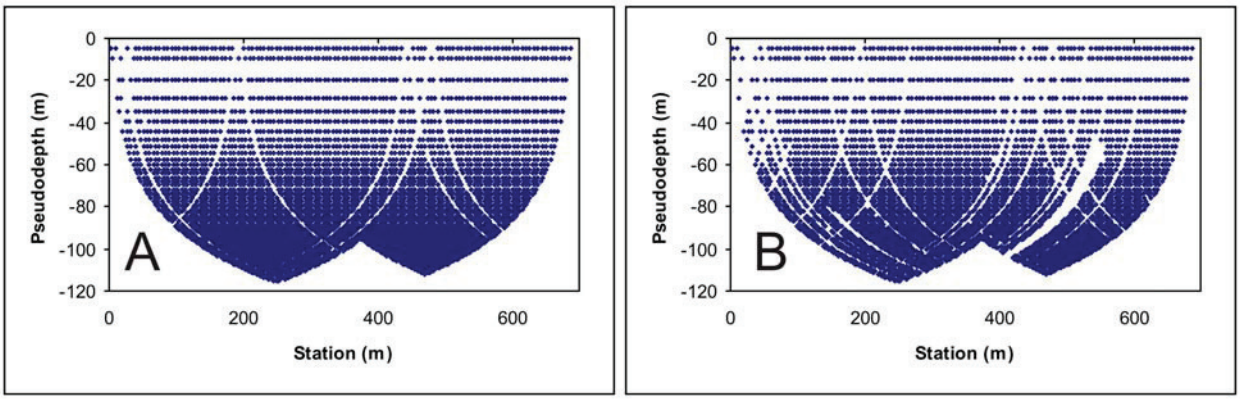

Figure B-33. A) Line 14E – Raw Data Density. B) Line 14E – Filtered.

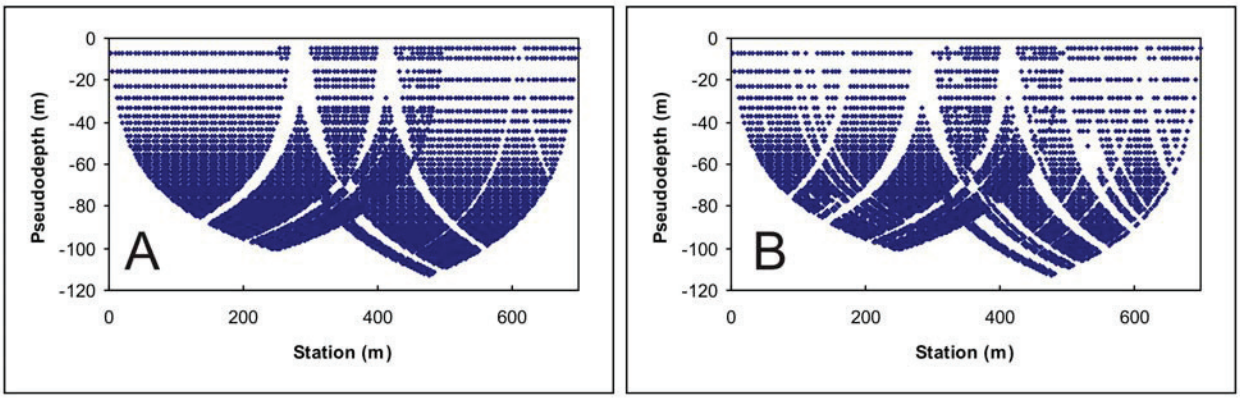

Figure B-34. A) Line 14N – Raw Data Density. B) Line 14N – Filtered.

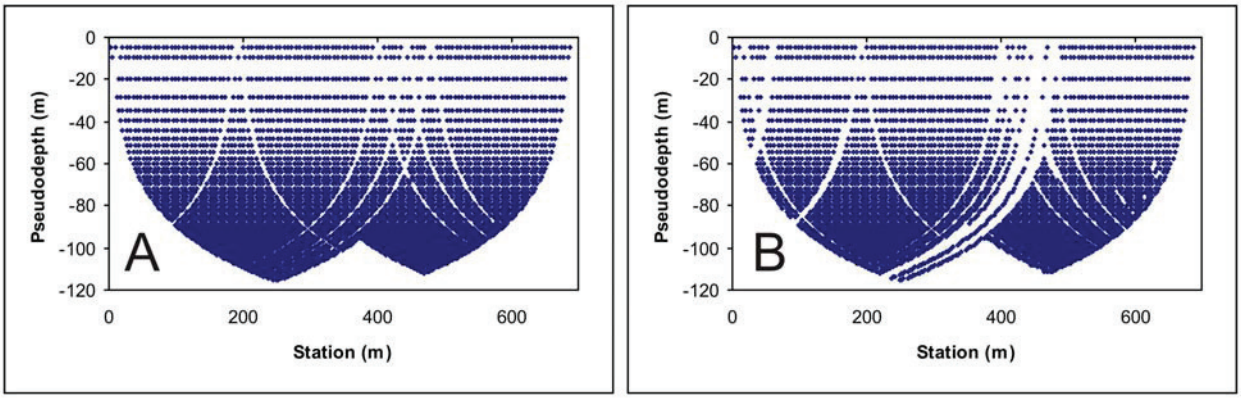

Figure B-35. A) Line 15E – Raw Data Density. B) Line 15E – Filtered.

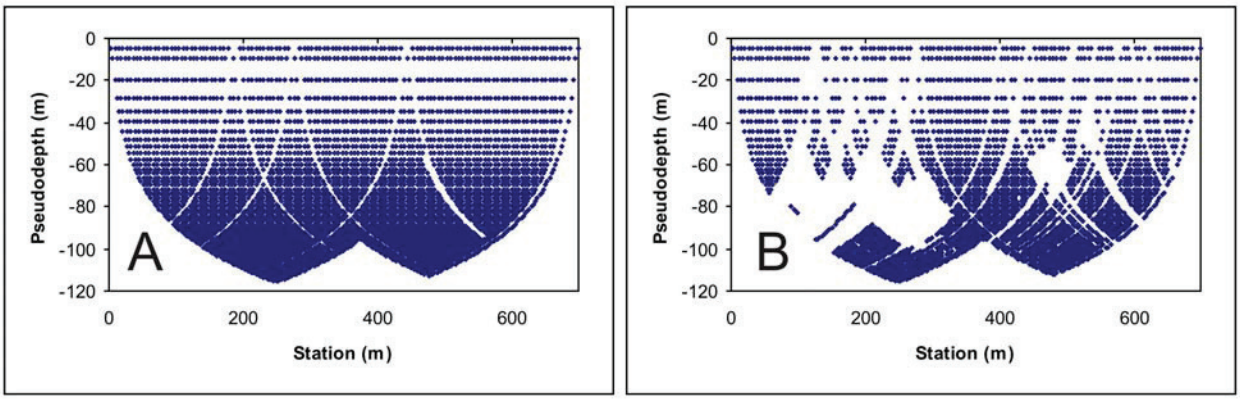

Figure B-36. A) Line 15N – Raw Data Density. B) Line 15N – Filtered.

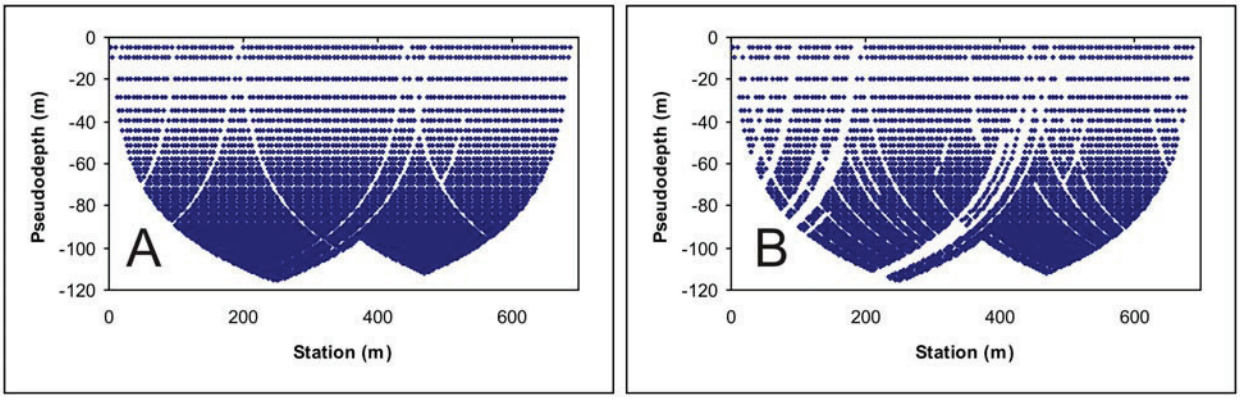

Figure B-37. A) Line 16E – Raw Data Density. B) Line 16E – Filtered.

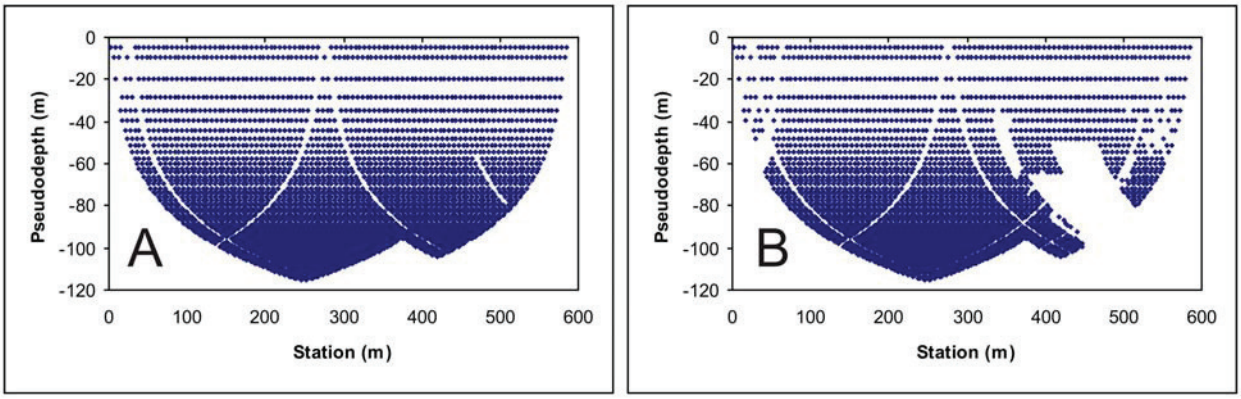

Figure B-38. A) Line 16N – Raw Data Density. B) Line 16N – Filtered.

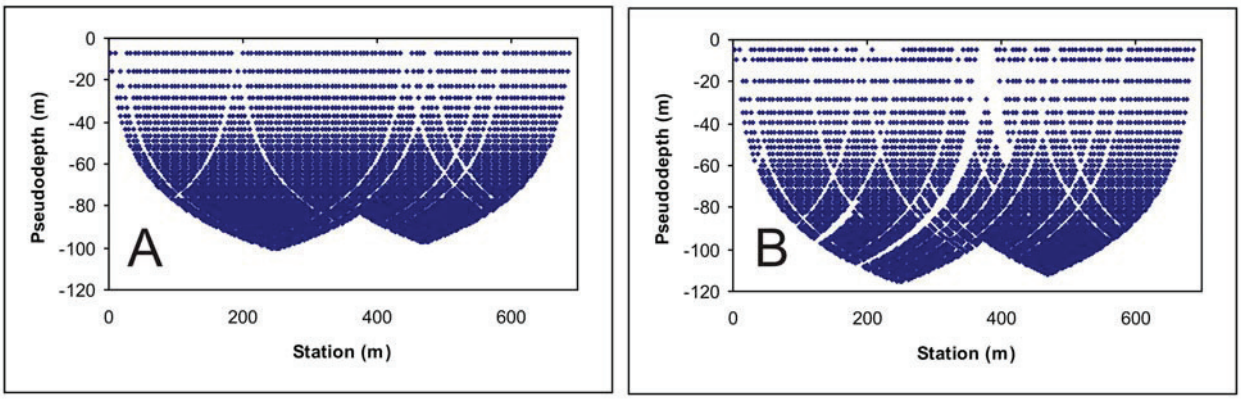

Figure B-39. A) Line 17E – Raw Data Density. B) Line 17E – Filtered.

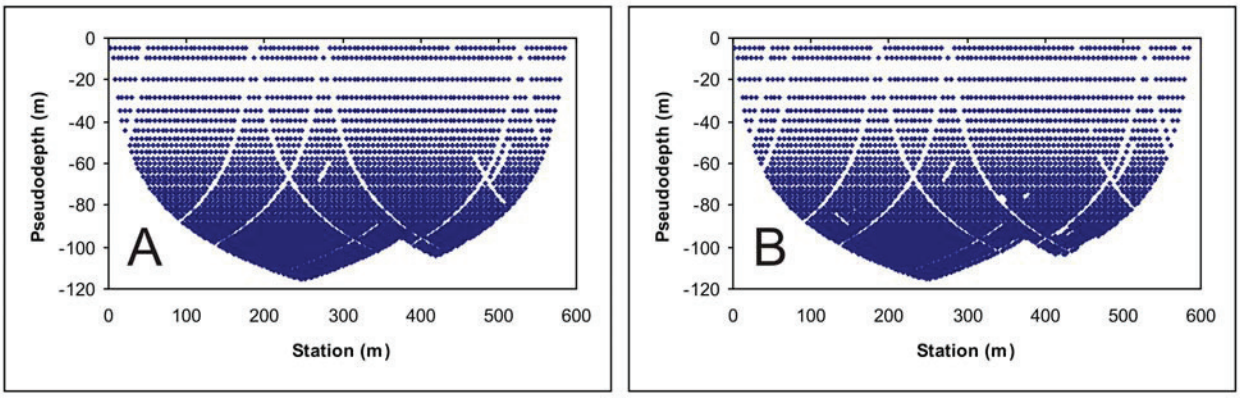

Figure B-40. A) Line 17N – Raw Data Density. B) Line 17N – Filtered.

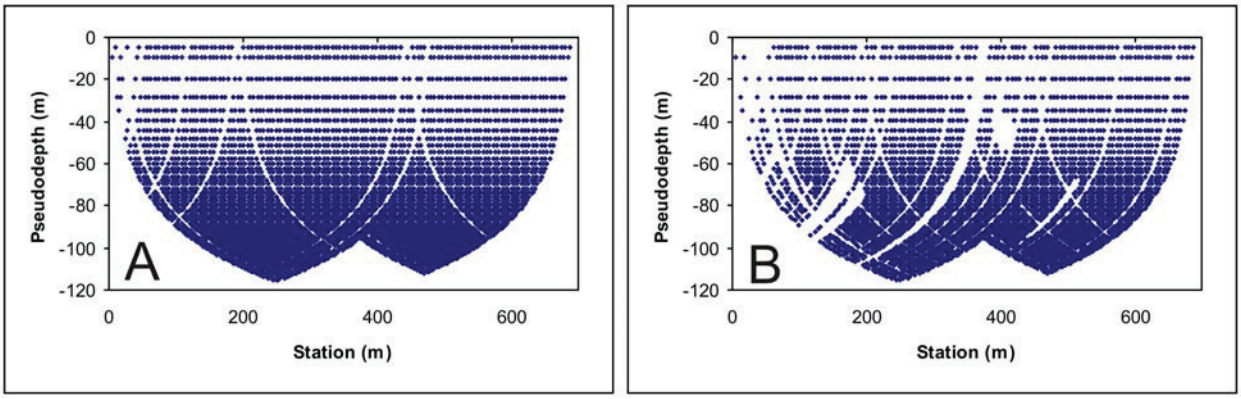

Figure B-41. A) Line 18E – Raw Data Density. B) Line 18E – Filtered.

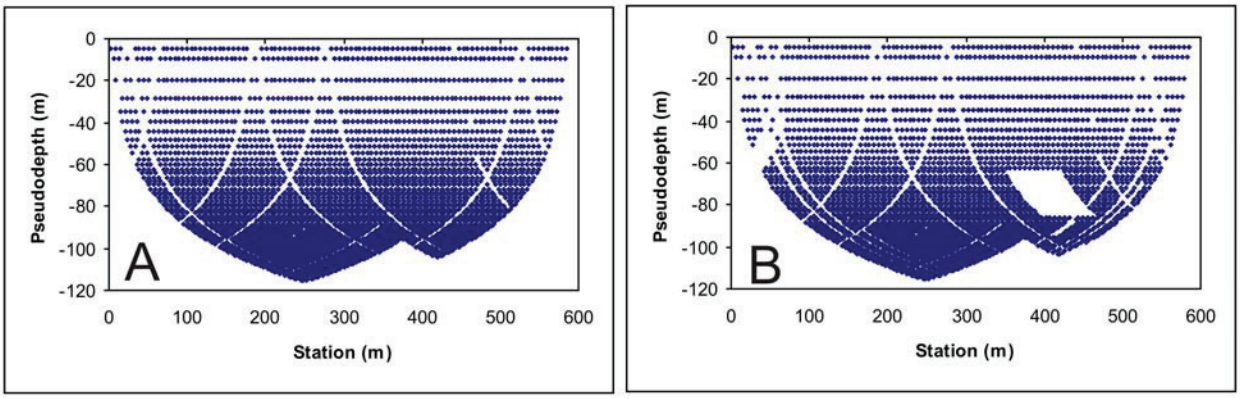

Figure B-42. A) Line 18N – Raw Data Density. B) Line 18N – Filtered.

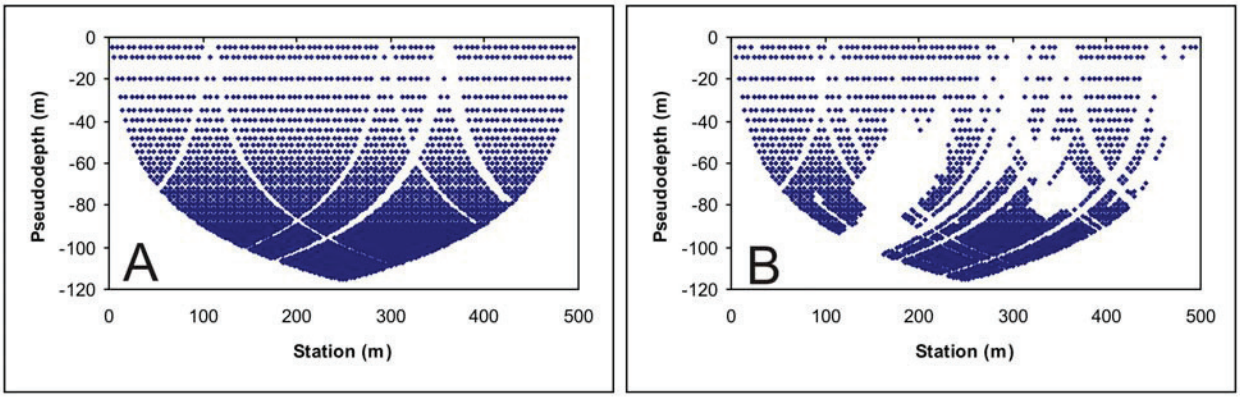

Figure B-43. A) Line 19E – Raw Data Density. B) Line 19E – Filtered.

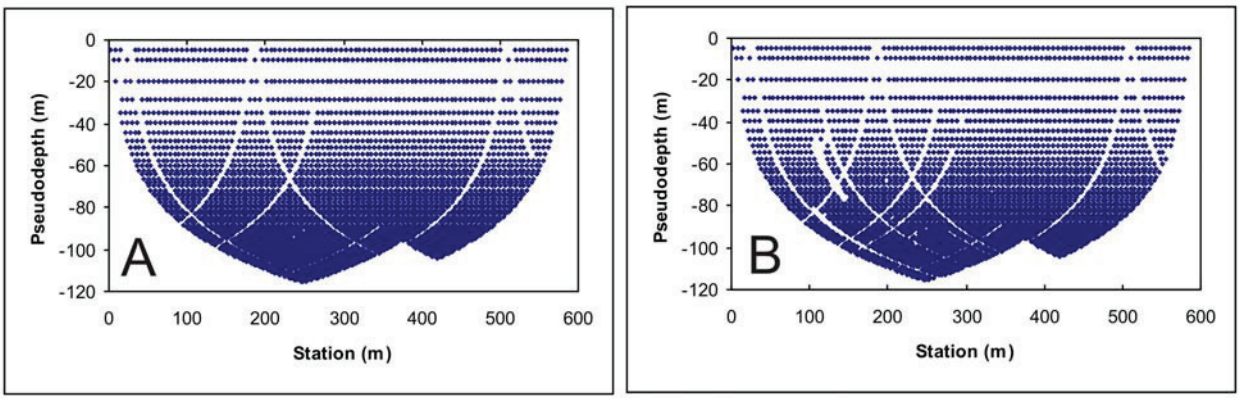

Figure B-44. A) Line 19N – Raw Data Density. B) Line 19N – Filtered.

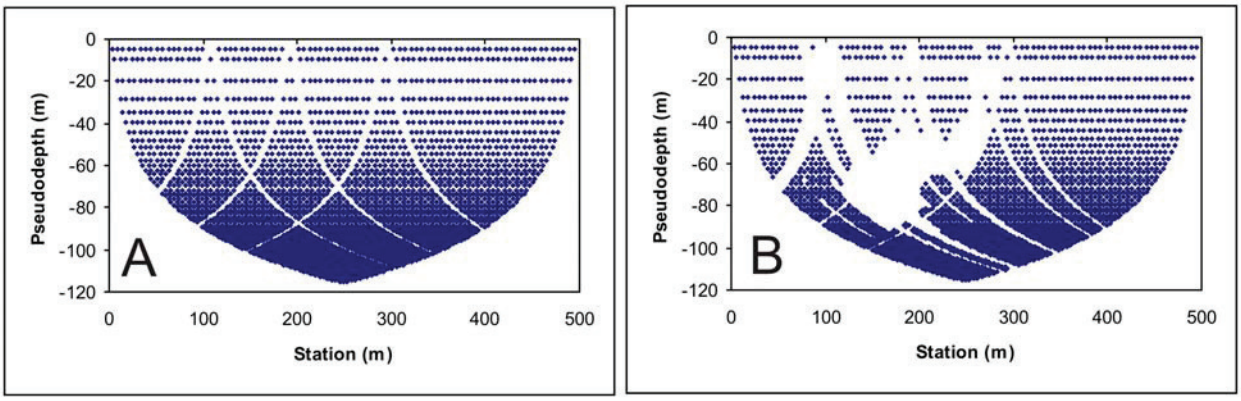

Figure B-45. A) Line 20E – Raw Data Density. B) Line 20E – Filtered.

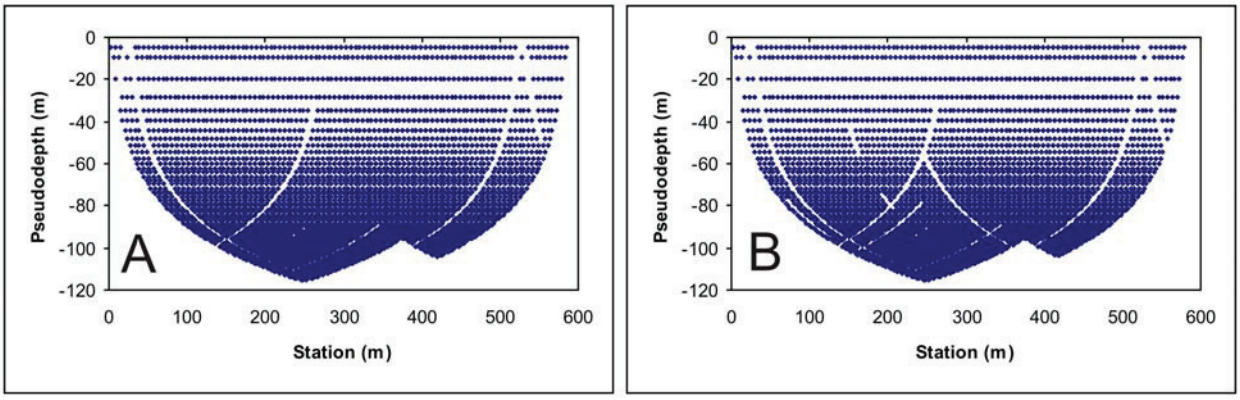

Figure B-46. A) Line 20N – Raw Data Density. B) Line 20N – Filtered.

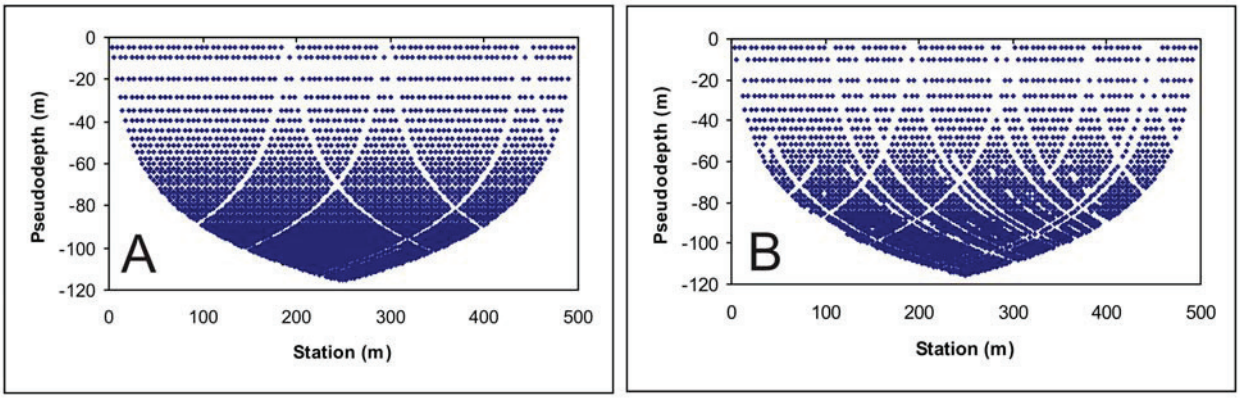

Figure B-47. A) Line 21E – Raw Data Density. B) Line 21E – Filtered.

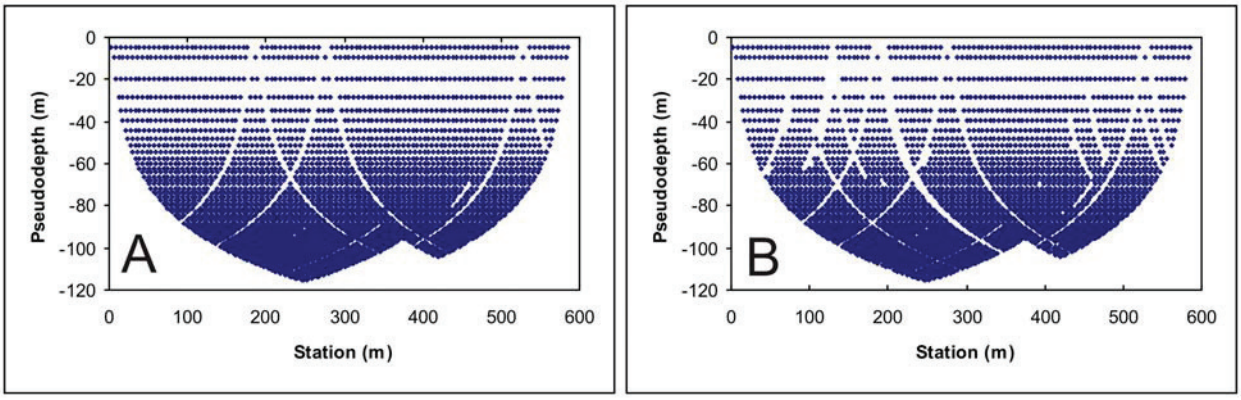

Figure B-48. A) Line 21N – Raw Data Density. B) Line 21N – Filtered.

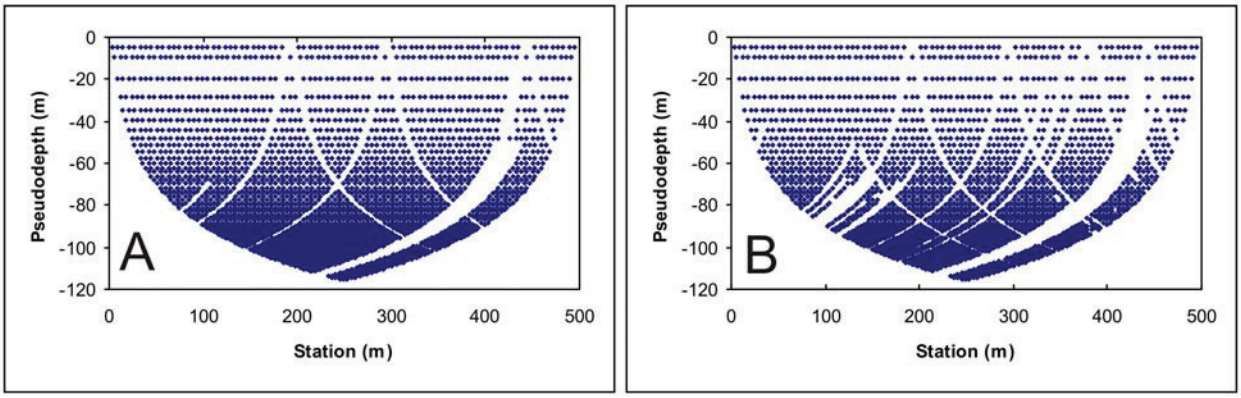

Figure B-49. A) Line 22E – Raw Data Density. B) Line 22E – Filtered.

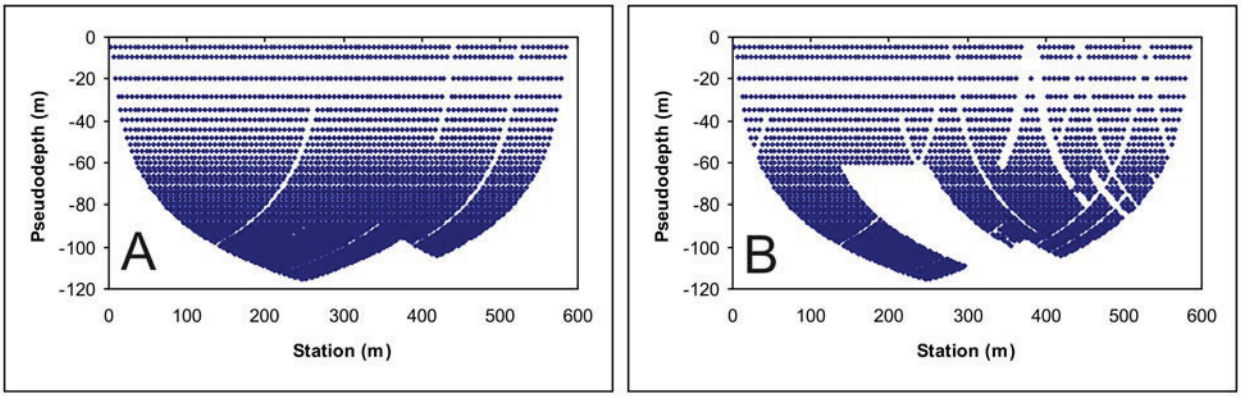

Figure B-50. A) Line 22N – Raw Data Density. B) Line 22N – Filtered.

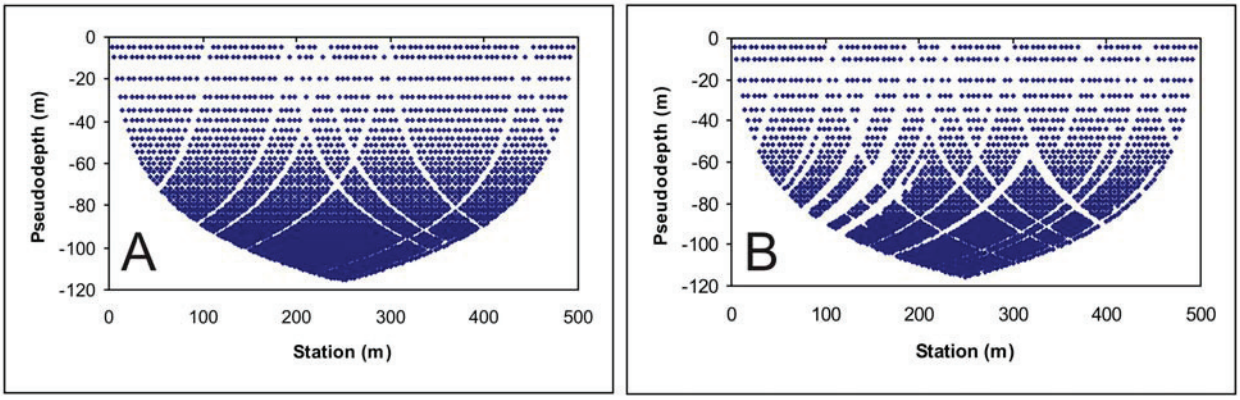

Figure B-51. A) Line 23E – Raw Data Density. B) Line 23E – Filtered.

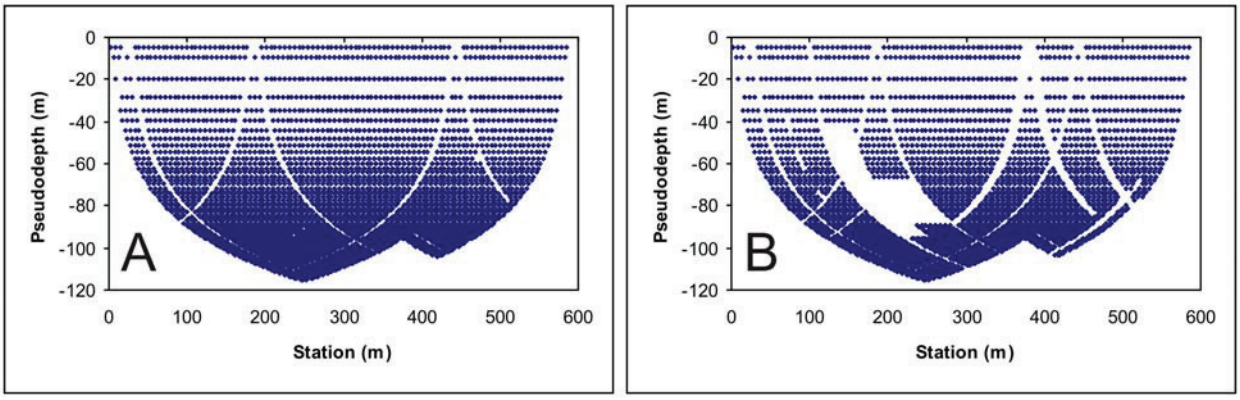

Figure B-52. A) Line 23N – Raw Data Density. B) Line 23N – Filtered.

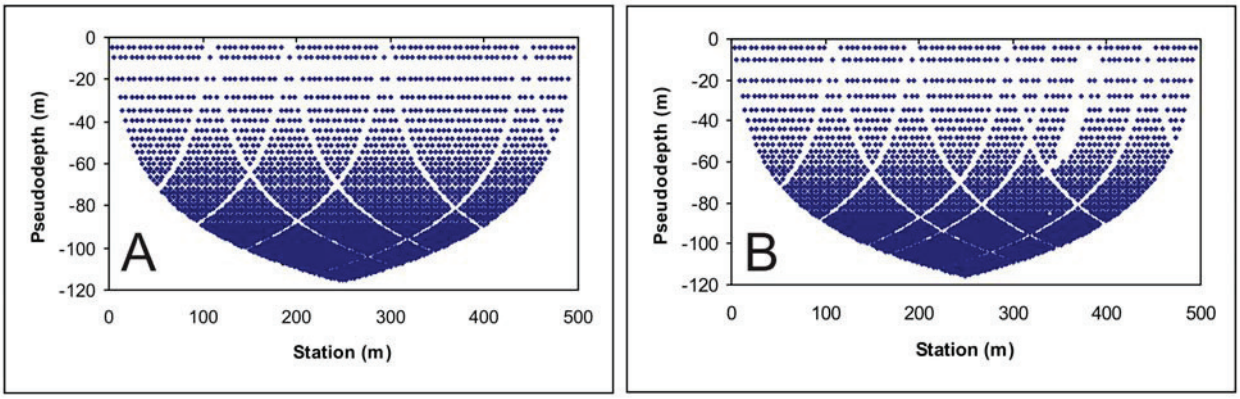

Figure B-53. A) Line 24N – Raw Data Density. B) Line 24N – Filtered.

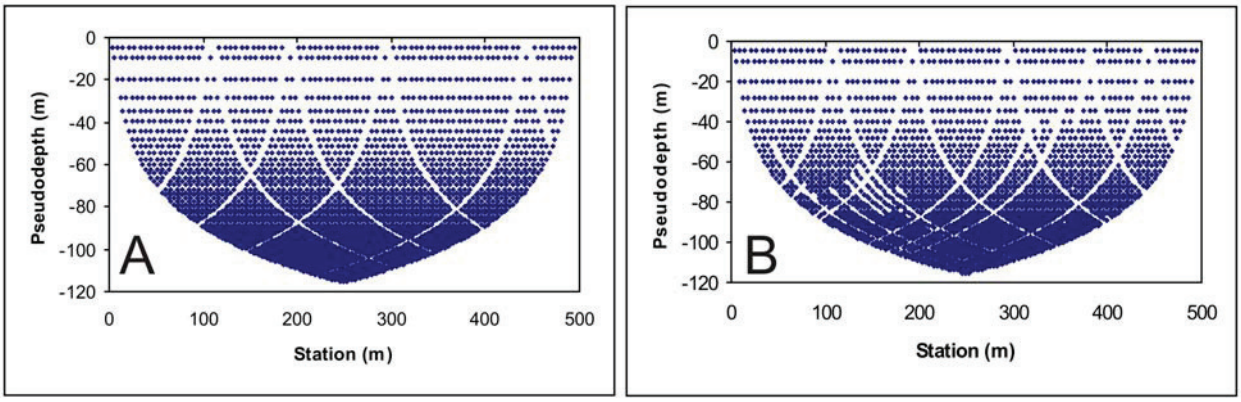

B1.3 DATA INVERSION MODELING AND VISUALIZATION

B1.3.1 Geospatial Database Management and Queries

The filtered data sets from each line are used as input in the inversion modeling process. To facilitate the preparation of these data sets, all TX-TY Complex resistivity data were loaded into a geospatial database running in ESRI ArcView 9.2. This database facilitates examination and evaluation of the quality control of the line layout and electrode spacing. Consistent and correct line layout and electrode coordinates are critical to the efficient functioning of three-dimensional finite difference and finite element inversion algorithms such as those used by the EarthImager series. The ESRI ArcView 9.2 interface with resistivity data plotted by location on an aerial photo of the TX-TY Complex site is illustrated in Figure B.54.

Figure B-54. ERSI ArcView 9.2 Interface with Resistivity Data Plotted by Location on an Aerial Photo of TX-TY Complex.

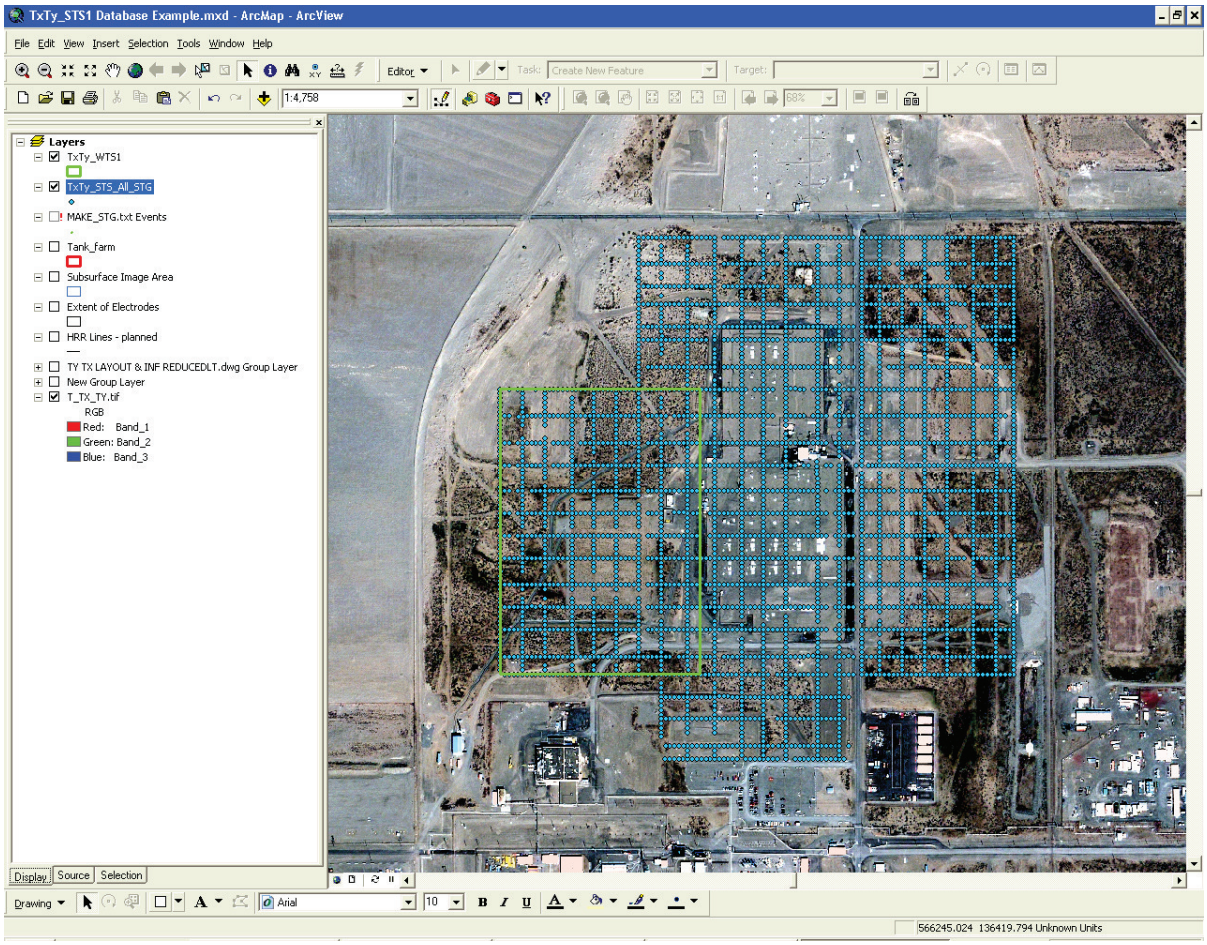

ArcView 9.2 implements an SQL (Structured Query Language) interactive development environment (See Figure B.55) to facilitate the development of database queries. These SQL queries extract data based on any combination of spatial limits (x,y,z), measured data and acquisition parameters.

Figure B-55. A) Resistivity data loaded in geospatial database (Lower Window), B) Sample SQL code (Right Window), C) Model domain (blue highlighted data points on aerial photo).

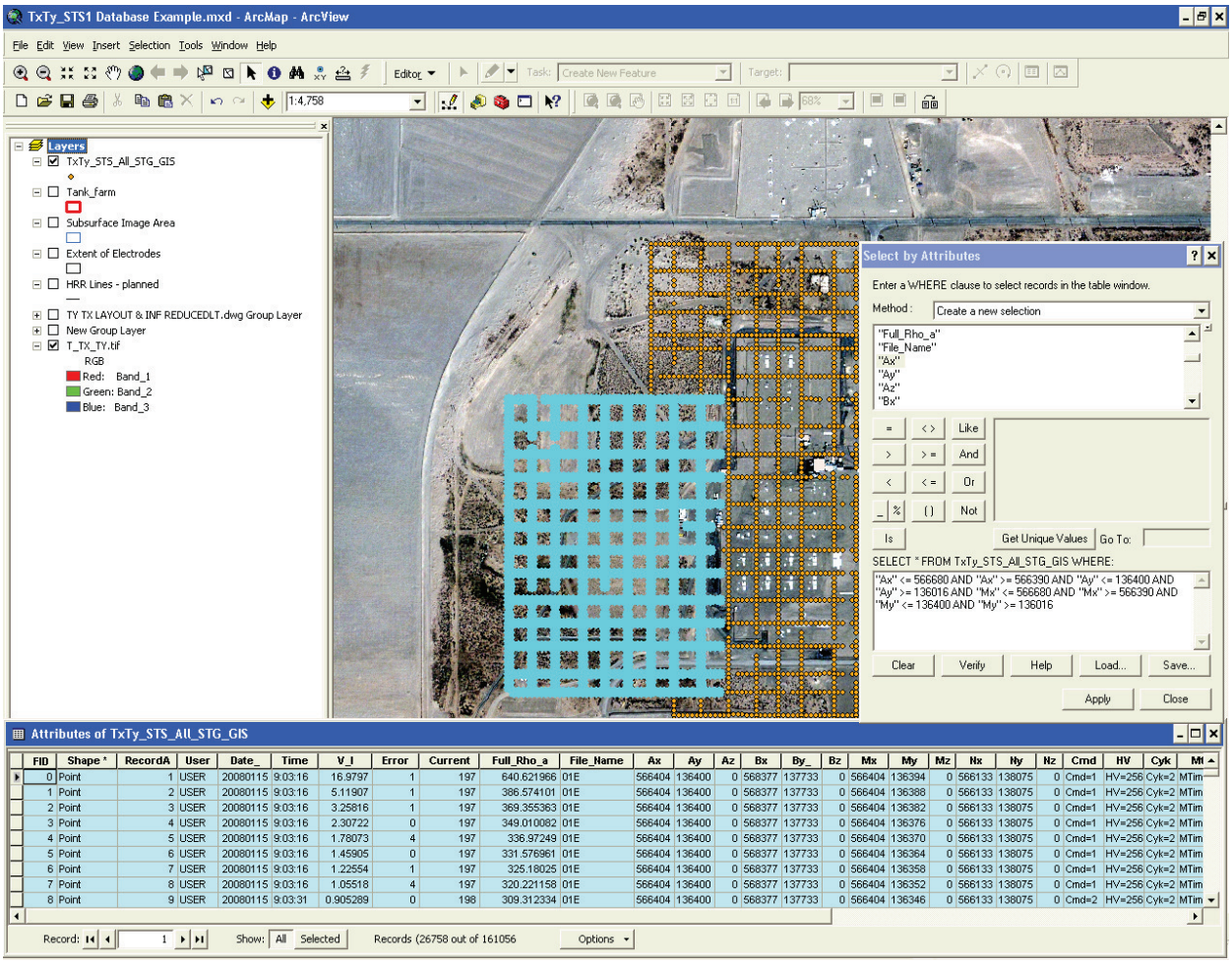

Queried model domains are exported from the geospatial database as ASCII format which is used by EarthImager2D[1], EarthImager3D[1] and EarthImager3DCL[1].

B1.4 INVERSION MODELING

Popular use of RES2DINV/RES3DINV series of resistivity inversion codes has led both professional and academic users to regard these codes as industry standard software.

The EarthImager series are designed to replicate the inversion results achievable with the RES2DINV/RES3DINV inversion codes by using the same optimization algorithm while integrating efficiently with Microsoft Windows®, adding a user friendly interface, and allowing more complex model parameters. A comprehensive comparison of the RES2DINV / RES3DINV

[1] EarthImager2D, EarthImager3D and EarthImager3DCLare trademarks of Advanced Geosciences, Inc., Austin, TX.
® Microsoft Windows is a registered service mark of Microsoft Corporation.

to the EarthImager 2D / 3D series can be viewed in Verification and Testing of the EarthImager Series of Electrical Resistivity Inversion Codes - A Benchmark Comparison (RPP-RPT-34730).

In general, the automated inversion process for both RES2DINV/RES3DINV and EarthImager 2D/3D inversion codes proceeds as described in the following 5 steps. These steps are also shown graphically in a flowchart provided in Figure B-56.

1. The study site's voltage data has been measured and is discretized into grid nodes using a finite difference or finite element mesh. The meshing parameters used in either method to design the computational grids are dependent on electrode spacing used in site-specific data acquisition.

2. The inversion will set out to estimate the true resistivity at every grid node. An initial estimate of the subsurface properties is made based on the literal translation of the pseudo-section to a true resistivity, a constant value, or some other distribution from *a priori* information. A forward model run with these initial estimates is made to obtain the distribution of voltages in the subsurface. The root-mean-square (RMS) error is calculated between the measured voltage and the calculated voltage resulting from the forward run.

3. Based on the degree of model fit to field measurements, the initial estimate of resistivity is changed to improve the overall model fit and the forward model with the updated estimates is rerun. The iterative method linearizes a highly nonlinear problem using Newton's method. Using this method, the inversion code essentially solves the linearized problem to obtain the change in modeled resistivity (Δm) for the next iteration.

4. The resistivity model is updated using the general formula $m_{i+1} = m_i + \Delta m$, where m_{i+1} is the resistivity in a model cell at the next iteration, and the m_i is the current value.

5. Steps 3 and 4 are repeated until the RMS error change between successive iterations is less than 10 percent.

Figure B-56. Flowchart of the Resistivity Inversion Process.

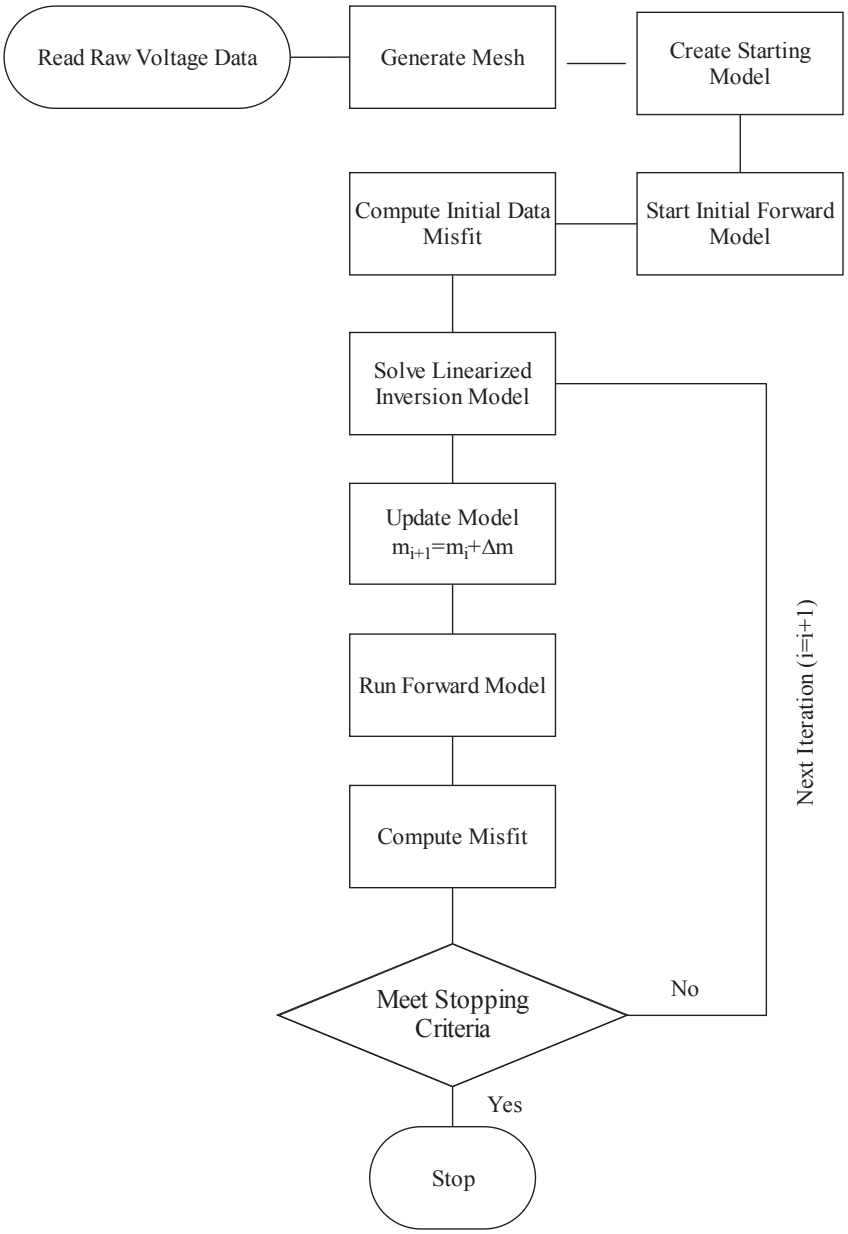

B1.4.1 Inversion Parameters

Inversion software use a series of user defined parameters to control the direction of the inversion modeling process. The following section contains a brief description of the inversion parameters used with the EarthImager inversion software. Due to naming conventions and slightly different inversion mechanisms within the codes, the comparison between RES2DINV and EarthImager 2D required contacting the code authors for additional information and confirmation of parameter incorporation. Unfortunately, both AGI and Geotomo, Inc. regarded

certain parameters as proprietary information and expert judgment was used to fill in missing information. In several cases, this expert judgment included sensitivity analyses that aimed to minimize the difference in the resistivity inversion results between the two codes.

B1.4.1.1 Boundary Condition Type and Limit. The core mesh is a finite difference mesh with the same domain limits set to the maximum distance between electrodes. The boundary mesh is a continuum of the core mesh at some distance outside of the measured region and contains the boundary condition and the remote electrodes for the pole-pole array. Numerical artifacts in the core mesh are minimized when the boundary condition is set far enough away from the current sources and sinks so that field gradients are constant at the boundaries.

EarthImager uses a homogenous Neumann boundary condition (i.e., specified current density) for the surface layer, which has no current flow through air. This is equivalent to an insulating boundary condition. Equation 3 describes the Neumann boundary condition as applied to surface resistivity inversion model:

$$\rho^{-1}(s)\eta \cdot \nabla\Psi = J(s) \tag{3}$$

Where:

ρ	=	resistivity of the area to be imaged
Ψ	=	electrical potential (i.e., voltage)
s	=	core mesh area
J(s)	=	current density.

The value of the Dirichlet boundary condition for the bottom and sides is proprietary, but is likely a constant voltage of zero based on common usage in electrical and groundwater models and the unsupported reasoning for values other than zero. The boundary conditions for RES2DINV are proprietary as well.

The damping and stabilization parameters are defined in EarthImager 2D separately from RES2DINV. The stabilizing factor is described by AGI as a Lagrange multiplier that balances data misfit and model constraints (see Equation 2) with the effect of smoothing the adjacent values of resistivity by minimizing the second spatial derivative. AGI recommends setting this parameter to 10 for data collected on surface electrodes. AGI states that the damping factor suppresses the effect of small Eigen values of the Hessian matrix (derivative of the Jacobian Matrix with respect to the model parameters) and speeds up convergence at early stages of inversion(AGI, 2007a; AGI, 2007b). Within EarthImager 2D, the damping factor automatically defaults to the same value as the stabilizing factor, but can change to have a unique value. The effect of both parameters is explored during the V&T process through sensitivity analyses, which aims to find the best representative value for comparison with RES2DINV. The exact implementation of these factors is proprietary (AGI, 2007a; AGI, 2007b).

B1.4.1.2 Damping Factor for RES2DINV. The damping factors for RES2DINV include values for the initial, minimum, and first layer. These parameters are defined differently than the EarthImager 2D code and the exact implementation of these factors is proprietary (Loke, 2006). Each of these parameters can be automatically optimized by RES2DINV so that a minimum

RMS model fit error is achieved. These parameters are automatically optimized during the V&T process.

B1.4.1.3 Initial Condition of Inversion Model. An initial value is needed to start the calculation of the partial differential equation of the predicted value at a given point in the domain of the solution. The starting value for both EarthImager 2D and RES2DINV is a homogenous pseudo-section, set to the average apparent resistivity of the measured data.

B1.4.1.4 Inversion Method. Both the EarthImager 2D and RES2DINV support the L_2 normalized damped least-squares inversion objective function (Equation 2). Compared to the damped least-squares method with no normalization or with L_1 normalization (or robust inversion), the L_2 normalization is optimal at resolving naturally smooth varying electrical properties as expected for conductive plumes and most hydrologic problems (Dahlin and Zhou 2004; Loke 2003 et al. 2003; "Inversion of magnetotelluric data for 2D structure with sharp resistivity-contrast" [deGroot-Hedlin and Constable 2004]; and deGroot-Hedlin and Constable 1990). The L_2 normalization objective function is less likely to over fit smooth field measured data thus reflecting the true conductive plume boundaries (deGroot-Hedlin and Constable 1990).

HGI uses the pole-pole electrode configuration due to its high signal strength at the deepest exploration depths relative to other array types, while collecting the widest horizontal coverage for a given array length ("A comparison of smooth and blocky inversion methods in 2D electrical imaging surveys" [Loke et al. 2001] and Robain et al. 1999). The L_2 normalization also appears to work well in conjunction with the pole-pole array (deGroot-Hedlin and Constable 1990). For the benchmark testing, the L_2 normalization option is held constant in order to focus on problems and environments similar to SGE sites.

B1.4.1.5 Inversion Stop Criteria. A compatible inversion stop criteria between EarthImager 2D and RES2DINV is the percentage change in the RMS error. EarthImager 2D and RES2DINV use slightly different definitions of RMS error. EarthImager 2D uses a weighted RMS (Equation 4), where small errors of measured transfer resistance (d_{meas}) have a higher weight in the RMS error computation than those with large d_{meas}.

$$RMS_{AGI} = \sqrt{\sum_{i=1}^{N} \frac{\left(d_{pred} - d_{meas}\right)^2}{\frac{d_{meas}}{N}}} \times 100 \tag{4}$$

The RMS error used in RES2DINV is defined in Equation 5. When RES2DINV completes an inversion (i.e., when the RMS is less than 5 percent), the difference in the logarithms of the measured and calculated apparent resistivity values will be similar to the relative error.

$$RMS = \sqrt{\sum_{i=1}^{N} \frac{\left(\log\left(d_{meas}\right) - \log\left(d_{pred}\right)\right)^2}{N}} \times 100 \tag{5}$$

Where:

d_{meas} = measured apparent resistivity
d_{pred} = predicted apparent resistivity
N = the number of measurements.

If the change of RMS error between two successive inversion iterations is less than the selected value, then the inversion codes will stop. Using an RMS change stop criteria of 5 to 10 percent is recommended by both AGI and Geotomo, Inc. for field-measured surface data sets with 5 percent as the default value in both codes. In general, the percent change stop condition of 5% stops both AGI and Geotomo codes as the model RMS values plateau.

B1.4.1.6 Inverted Value. EarthImager 2D inverts transfer resistance (V/I) during the model updates, whereas RES2DINV inverts the apparent resistivity. Transfer resistance and ρ_a are equivalent quantities that can be converted back and forth using a geometric factor. However, the different inverted value is significant for WTW problems, where the geometric factor to convert transfer resistance to apparent resistivity does not exist.

B1.4.1.7 Inverted Output. The inverted output from RES2DINV and EarthImager 2D do not overlap exactly for the same input data because the mesh (model cell) design is different for each program. To allow for code-to-code and code-to-concept (i.e., comparison of inversion results to starting conceptual model), RMS error calculations, all data were re-interpolated onto a common 3- by 3-foot (1- by 1-meter) rectilinear mesh. The nearest neighbor exact interpolator was used to preserve the original resolution of the inversion mesh. The RMS percent errors and grids are calculated using MATLAB®.

B1.4.1.8 Jacobian Matrix Calculation. The Jacobian Matrix is the matrix of all first-order partial derivatives of a vector-valued function relative to the model parameter. This calculation provides the best linear approximation to a differentiable function near a given point. The quasi-Newton or partial Jacobian Matrix calculation is a method of slightly lower accuracy, but requires less computational power ("Practical techniques for 3D resistivity surveys and data inversion" [Loke 1996a] and "Methods for calculating Fréchet derivatives and sensitivities for the non-linear inverse problem: a comparative study" [McGillivray 1990]). RES2DINV offers the option to enable the full Jacobian Matrix calculation using the Gauss-Newton method with each model update. EarthImager 2D uses the full Jacobian Matrix calculation without choice for a partial Jacobian. The full Jacobian Matrix is calculated for each iteration in both codes during the V&T.

B1.4.1.9 Model-Fitting Error. The model-fitting error is the RMS error (see Equations 4 and 5) between the measured apparent resistivity and the model predicted apparent resistivity. The error is minimized between each successive model iteration and used as a stop condition. Both RES2DINV and EarthImager 2D use this statistic as a measure of data match.

B1.4.1.10 Model Layer Thickness Increase with Depth. The sensitivity of surface resistivity decreases with distance from the electrodes. A telescoping mesh is applied by both RES2DINV

® MATLAB is a registered trademark of The MathWorks, Inc.

and EarthImager 2D so that lower layers are not over resolved by the inversion process. The telescoping mesh layer thickness increases by a factor of 1.1 in both codes.

B1.4.1.11 Mesh and Solver Type. RES2DINV and EarthImager 2D incorporate finite difference and finite element mesh designs in the 2D versions of their codes. Finite difference and finite element methods solve for electrical properties by breaking the problem area (i.e., domain) into many small elements (e.g., squares as in the finite difference or triangles, tetrahedra, etc. in finite element) and solving the equation for each element (all electrical properties are assumed constant or linearly variable within an element). The finite element method discretizes the model domain optimally for complex topographic surfaces as expected when resistivity is measured over hills and valleys. The finite difference method discretizes the model domain into block elements, which are significantly faster to compute during the inversion process. The finite difference and finite element approximation leads to an implicit set of equations that must be solved using linear algebra.

The finite difference method is used for the V&T in both codes as this is an optimal method for the SGE sites, which are relatively flat and involve large computationally intensive model domains. EarthImager uses the Cholesky Decomposition method to solve the set of equations formulated during the finite differencing. The solver type used by RES2DINV is proprietary, though it is very likely to be either the Cholesky Decomposition or the Conjugate Gradient solver. Both the Cholesky Decomposition and Conjugate Gradient solver are numerically equivalent, robust, and stable methods. The Cholesky Decomposition solver is generally faster and requires more memory than the Conjugate Gradient method (*Matrix Computations* [Golub and van Loan 2006]).

B1.4.1.12 Model Depth of Investigation. The deepest model layer as calculated from the array type and electrode geometry using an empirical method was proposed by Edwards (1977). EarthImager 2D uses a proprietary parameter called Depth Factor. Through experimentation, it was determined that a depth factor of 1.45 produces an equivalent exploration depth to RES2DINV for a pole-pole array with 16-foot (5-meter) electrode spacing. This equivalent Depth Factor and array geometry is used for all intercode comparisons.

B1.4.1.13 Model Nodes. The number of model nodes per electrode spacing controls the density of the model mesh. A mesh with more than four nodes per electrode spacing is probably finer than the resolution of the resistivity method, but reduces numerical approximation errors within the mathematical model relative to coarser grids. Four nodes per electrode spacing are used in both EarthImager 2D and RES2DINV codes for this study.

B1.4.1.14 Model Resistivity Limits. The upper and lower resistivity limits are based on the reasonably expected values for a particular field area. These limits are imposed in order to reduce the chance of equivalent solutions that are outside the bounds of the true material properties. EarthImager 3DCL allows an upper and lower limit to be set in resistivity units (ohm-m). RES2DINV uses an upper and lower limit factor that is multiplied by the average apparent resistivity of the pseudo-section. The user manual for RES2DINV describes the limits as a soft constraint, which is not strictly applied. Both EarthImager 3DCL and RES2DINV codes were set to the default resistivity limits of 1 and 10,000 ohm-m.

B1.4.1.15 RES2DINV Automated Parameter Optimization. RES2DINV offers the option of optimizing damping parameters during inversion. This optimization method solves for the damping parameters that result in the lowest over all RMS error between the measured (e.g., field or synthetic) and predicted apparent resistivity. Optimizing inversion parameters based on reducing the model fit, RMS error is a common strategy to improve model resolution in industry ("Two- and three-dimensional electrical resistivity imaging at a heterogeneous remediation site" [Bentley and Gharibi 2004]; "Geostatistical reconstruction of gaps in near-surface electrical resistivity data" [Cornacchiulo and Amvrossios 2004]; "A 3-D resistivity investigation of a contaminated site at Lernacken, Sweden" [Dahlin et al. 2002a]; "Continuous resistivity profiling to delineate submarine groundwater discharge; examples and limitations"[Day-Lewis et al. 2006]; "Extending Electromagnetic Methods to Map Coastal Pore Water Salinities" [Greenwood et al. 2006]; Loke et al. 2003; "A case study of the reliability of multielectrode earth resistivity testing for geotechnical investigations in karst terrains.; Engineering and environmental impacts of karst" [Roth et al. 2002]; LaBrecque et al. 1996; and "Full 3-D inversion of electromagnetic data on PC" [Sasaki 2001]).

B1.4.2 Resistivity Visualization

Two-dimensional inversion data are represented in color contour cross-section form using Surfer® (Golden Software, Inc). Three-dimensional inversion data are interpolated and visualized using Rockworks (Rockware, Inc). Examples of these plots are found in Appendix A and the Results section of this report (Section 3.0).

B1.4.3 Resistivity Color Scales

A consistent color scale was developed for TX-TY Complex based on analysis of all modeled data. The color scale is comprised of a continuous spectrum of colors similar to a rainbow. This spectrum uses cool colors (blue) to represent lower values and hot colors (red) to represent higher values. Color bins were calculated using the log binning algorithm (Loke and Baker, 1995). Figure B-57 shows a histogram of all data collected at TX-TY Complex with an overlay of all associated resistivity values and color bins. The histogram of resistivity values from TX-TY Complex exhibits a log normal distribution which can be difficult to visualize using a linear color scale. The log binning method improves color differentiation by placing a higher number of contrasting color bins where values are clustered, such as the 0-100 ohm-m range (Figure B-57).

Resistivity inversion model output from EarthImager3DCL is often visualized using an iso-contour method in Rockworks. In this method, a smaller number of semi-transparent color bins are used to highlight specific target locations and shapes. These plots will have a color key denoting the unique iso-contour values and colors.

® Surfer is a registered trademark of Golden Software, Inc., Golden, CO.

Figure B-57. TX-TY Complex Inversion model Resistivity Histograms and Color Values.

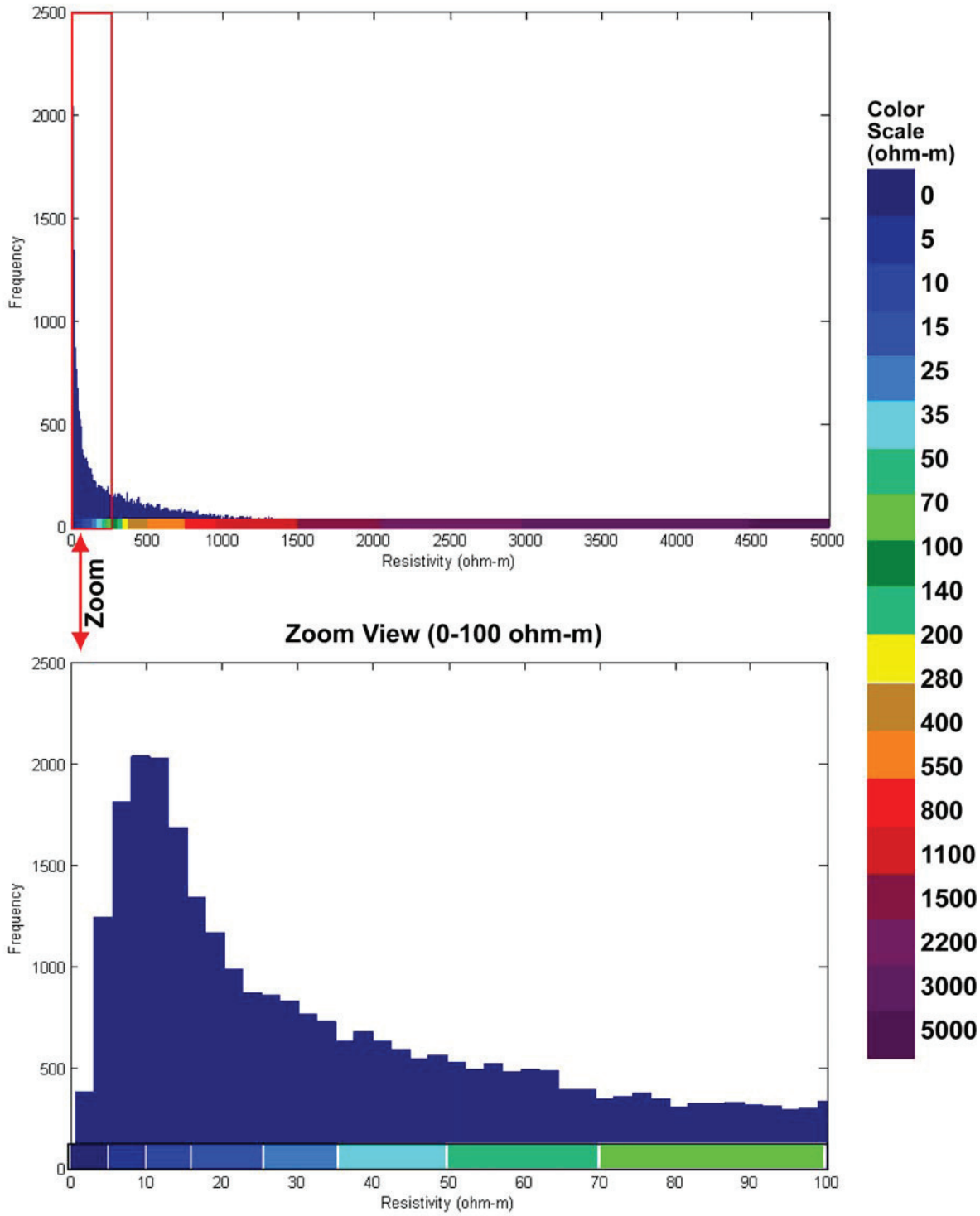

B1.5 REFERENCES

AGI, 2007a. Instruction Manual for EarthImager 2D Version 2.0.7 Resistivity and IP Inversion Software. Advanced Geosciences, Inc., 12700 Volente Rd., FM 2769, Bldg A, Austin, Texas 78726.

AGI, 2007b. Instruction Manual for EarthImager 3D Version 1.3.9 Resistivity and IP Inversion Software. Advanced Geosciences, Inc., 12700 Volente Rd., FM 2769, Bldg A, Austin, Texas 78726.

Bentley, L.R. and M. Gharibi, 2004, "Two- and three-dimensional electrical resistivity imaging at a heterogeneous remediation site," *Geophysics*, 69(3): 674-680.

Dahlin, T., C. Bernstone, and M.H. Loke, 2002a, "A 3-D resistivity investigation of a contaminated site at Lernacken, Sweden," *Geophysics*, 67(6): 1692-1700.

Dahlin T. C. and Zhou, B., 2004, "A numerical comparison of 2D resistivity imaging with 10 electrode arrays," *Geophysical Prospecting*, 52(5): 379-398.

Day-Lewis, F.D. et al., 2006, "Continuous resistivity profiling to delineate submarine groundwater discharge; examples and limitations," *The Leading Edge*, 25(6): 724-728.

deGroot-Hedlin, C. and Constable, S., 1990, "Occam's inversion to generate smooth, two-dimensional models from magnetotelluric data," *Geophysics*, 55(12): 1613-1624.

de Groot-Hedlin, C. and Constable, S., 2004. Inversion of magnetotelluric data for 2D structure with sharp resistivity contrasts. Geophysics, 69(1): 78-86.

Edwards, L. S., 1977, "A Modified Pseudo-Section for Resistivity and IP," *Geophysics*, 43(5): 1020-1036.

Gill, P.E. and Murray, W., 1978. Algorithms for the solution of the nonlinear least-squares problem. SIAM Journal of Numerical Analysis, 15(5): 977-992.

Golub, G.H. and C.F. van Loan, 1996, *Matrix Computations*, Third Edition, John Hopkins University Press, 694 p.

Greenwood, W.J., S.E. Kruse, and P.W. Swarzenski, 2006, "Extending Electromagnetic Methods to Map Coastal Pore Water Salinities," *Ground Water*, 44(2): 292-299.

LaBrecque, D.J., M. Miletto, W. Daily, A. Ramirez, and E. Owen, 1996, "Effects of noise on Occam's inversion of resistivity tomography data," *Geophysics*, 61(2): 538.

Levenberg, K., 1944. A Method for the Solution of Certain Non-Linear Problems in Least Squares. Quarterly of Applied Mathematics, 2: 164-168.

Loke, M.H. and R.D. Barker. 1995. Least-squares deconvolution of apparent resistivity pseudosections. *Geophysics, Vol. 60, No. 6; 1682-1690.*

Loke, M.H. and R.D. Barker, 1996, "Practical techniques for 3D resistivity surveys and data inversion," *Geophysical Prospecting*, 44(3): 499-523.

Loke, M.H., I. Acworth, and T. Dahlin, 2001, "A comparison of smooth and blocky inversion methods in 2D electrical imaging surveys," Procs. ASEG 15th Geophysical Conference and Exhibition, August 2001, Brisbane, Australia.

Loke, M.H., Acworth, I. and Dahlin, T., 2003, "A comparison of smooth and blocky inversion methods in 2D electrical imaging surveys," *Exploration Geophysics*, 34(3): 182-187.

Marquardt, D., 1963. An Algorithm for Least-Squares Estimation of Nonlinear Parameters. SIAM Journal of Applied Mathematics, 11: 431-441.

McGillivray, R. and D.W. Oldenburg, 1990, "Methods for calculating Fréchet derivatives and sensitivities for the non-linear inverse problem: a comparative study," *Geophysical Prospecting*, 38(5): 499-524.

Robain, H. et al., 1999, "Location of infinite electrodes in pole-pole electrical surveys: Consequences for 2D imaging," *Journal of Applied Geophysics*, 41(4): 313-333.

Roth, M.J.S., J.R. Mackey, C. Mackey, and J.E. Nyquist, 2002, "A case study of the reliability of multielectrode earth resistivity testing for geotechnical investigations in karst terrains.; Engineering and environmental impacts of karst," *Engineering Geology*, 65(2-3): 225-232.

Sasaki, Y., 2001, "Full 3-D inversion of electromagnetic data on PC," *Journal of Applied Geophysics*, 46(1): 45-54.

APPENDIX C

DATA ARCHIVAL

This page intentionally left blank.

TABLE OF CONTENTS

C1.0 RAW DATA 1

C2.0 LINE INFORMATION 1

LIST OF FIGURES

C-1: HGI HRR Field Form (page 1). 2
C-2: HGI HRR Field Form (page 2). 3
C-3. HGI HRR Field Form (page 3) 4
C-4. Line Processing Form 5

This page intentionally left blank.

For the TX-TY Complex SGE survey, both raw resistivity data and survey line information were archived using database and GIS software. Raw resistivity data are stored in both the original Sting file format as downloaded from the instrument and in parsed Excel (Microsoft, Inc.) files in designated raw data folders on the HGI server. Raw resistivity data were also input into GIS software, providing a secondary means of storage. Survey line information pertaining to project, location, line set-up, file name, instrument settings, and survey conditions were recorded for each resistivity line section and later imported into a project specific database.

C1.0 RAW DATA

Each day, individual raw data files, as downloaded from the instrument, are exported to a field laptop computer. The files are placed in designated raw data folders on the HGI server for each survey line and remain unaltered. Each raw resistivity file is then parsed into usable columns (e.g., Record No., Date, Current, Normalized Potential, Error, Apparent Resistivity, Geometry, Transmitter Gain) using Excel (Microsoft, Inc.) and stored within a separate data folder.

All raw data parameters recorded by the SuperSting resistivity instrument and stored within the Sting file were input into a GIS geospatial database using ArcMap 9.2 (ESRI). All raw data recorded in the Sting file were geo-referenced using GPS positions by linking transmitting locations with measured resistivity parameters. Data parameters include V/I value, Error, Current, Rho-a, and Transmitter, Receiver, and Infinite electrode locations.

C2.0 LINE INFORMATION

General information regarding each line section is recorded by HGI operators during field data acquisition on an HGI HRR Field Form template. The template was created with Microsoft Word. General line information includes Job Number, Site Location, Line ID and Section of the survey. Electrode information such as Total Number of Electrodes, Start and End Electrode Number, Type of Electrode, Spacing and Units, and any Skipped Electrodes are also recorded. Array information includes Command File Name and Generator used, Type of Array, Transmit Direction and Roll Along information. Equipment information such as Model and Serial Number, Switchbox Configuration, and Cable Configuration are entered into the form. Instrument Configuration Settings recorded include Cable Address Setup, Measurement Settings and Remote Electrode Information. Additional line notes such as Environmental and Weather Conditions, Infrastructure Location, and Equipment Failures are also entered into the form. Figure 1 shows the HGI HRR Field Form used for gathering survey information.

Following completion of each full line survey, all separate line segments must be combined into a single line for editing, processing and inversion. A Line Processing Form template, created using Microsoft Word, is used to record Job Number, Line ID, Site Location, Number of Sting Files acquired for each resistivity line, File Names, File Locations, Total Line Length, and Start and End Coordinates of the line. The number of data points per Sting file, combined raw data points per line, and number of data points remaining after filtering are also recorded on this form. Figure 2 displays the Line Processing Form used to combine all information for each resistivity line.

All data fields in each of the above forms have designated bookmarks that can be called by an import module within Microsoft Access. When the code is initiated, all fields of the Field Form or Line Processing Form are directly imported to various Access tables. Once imported to Access, data are easily extracted with user-written queries in whatever form is required.

A collection of completed field forms for all survey lines is included in this report in an attached CD.

Figure C-1: HGI HRR Field Form (page 1).

HGI hydroGEOPHYSICS

HGI HRR FIELD FORM

GENERAL		
Select Existing Job Number: **Or, Enter New Job Number**	**Project Site:**	**Line ID:** **Section:**
Date:	**Start Time (Military Time):**	**End Time (Military Time):**
Field Manager:		**Sting File Name:**

ELECTRODE		
No. Electrodes: **Depth of Penetration:**	**Start Electrode:** Station Number Direction: XCoord: YCoord:	**End Electrode:** Station Number Direction: XCoord: YCoord:
Electrode Type:	**Min. Electrode Spacing:** **Max. Electrode Spacing:**	**Layout Units:**
Skipped Electrodes (Include Electrode Number and Reason for Skipping):		

ARRAY	
Command File Name:	**Command File Generator:**
Array Type:	**Transmit Direction:**
Roll Along?	**Roll-along Electrodes** (in relation to entire line): **Start Electrode:** **End Electrode:**

EQUIPMENT	
Rx/Tx Model:	**Rx/Tx Serial No.:** **Rental? Enter Serial No.:**

Figure C-2: HGI HRR Field Form (page 2).

Switchbox Configuration:

Box	Switchbox Serial No.	Switch box Model	Board/Serial 1 (electrodes)	Board/Serial 2 (electrodes)	Board/Serial 3 (electrodes)	Board/Serial 4 (electrodes)
1	Select S/N: Rental? Enter S/N:					
2	Select S/N: Rental? Enter S/N:					
3	Select S/N: Rental? Enter S/N:					
4	Select S/N: Rental? Enter S/N:					
5	Select S/N: Rental? Enter S/N:					
6	Select S/N: Rental? Enter S/N:					

Smart Cable Configuration:

No. Electrodes per Roll:

No. Electrodes per Cable Section:

No. Cable Sections:

CONFIGURATION SETTINGS

Cable Address Setup:	Section AddrL AddrH	Section AddrL AddrH	Section AddrL AddrH
Section AddrL AddrH	5	10	15
1	6	11	16
2	7	12	17
3	8	13	18
4	9	14	19

Measurement Settings:			**Remote Locations:**
Cycles:	Separate Pot.:	Start X:	TxXCoord:
Max Error:	Measure Mode:	Start Y:	TxYCoord:
Max Repeat:	Address Table:	Start Z:	TxZCoord:
Max Current:	Measure Units:	Distributed vs. SwitchBox:	RxXCoord:
Measure Time:	Scaling Factor:	1Chn or 8 Chn:	RxYCoord:
			RxZCoord:
			Remote Continuity:
			Rx to Tx: Ω
			Tx to Rx: Ω

Figure C-3. HGI HRR Field Form (page 3).

PRE OPERATIONAL CHECKLIST
Checklist ☐ **Set Date/Time** ☐ **Pass Receiver Test** ☐ **Pass Relay Test** ☐ **Pass Contact Resistance Test**
LINE NOTES
Environmental/Weather Conditions:
Line Notes (Infrastructure Location, etc.):
EQUIPMENT FAILURES
Description of Equipment Failure and Resolution of Failure:

Figure C-4. Line Processing Form.

HGI hydroGEOPHYSICS

HGI LINE PROCESSING

Job Number: **Site:**	**Line ID:** **Total Line Length:**
StartX StartY StartZ	**EndX EndY EndZ**

Total Number of Sting Files:

Sting File	Number of Data Points	Zip File Location	Coordinate File Location	Processed File Location

Total Number of Raw Data Points:

Total Number of Edited Data Points:

This page intentionally left blank.

APPENDIX D

BACKGROUND GEOPHYSICAL PROPERTIES

This page intentionally left blank.

TABLE OF CONTENTS

D1.0 GROUND PENETRATING RADAR 1

D2.0 MAGNETIC GRADIOMETRY AND EM INDUCTION 6

LIST OF FIGURES

D-1. GPR Coverage – TX and TY Tank Farm Area 2

D-2. Estimated Locations of TX Farm Infrastructure based on Interpreted Linear Features and Depths Developed from GPR Hyperbola Picks 4

D-3. Estimated Locations of TY Farm Infrastructure based on Interpreted Linear Features and Depths Developed from GPR Hyperbola Picks 5

D-4. Magnetic Gradiometry and EM Induction Coverage at the TX and TY Farm Area 7

D-5. Vertical Magnetic Gradient Results 9

D-6. Electromagnetic Induction Results, Showing Electrical Conductivity 10

D-7. Data Acquisition Lines and Linear features identified from the G 11

This page intentionally left blank.

A main objective for geophysical surveying of background geophysical properties is to define the subsurface with regard to the presence and extent of metallic infrastructure and debris. The presence of subsurface metal may interfere with electrical resistivity measurements, which are being conducted to help define electrolytic anomalies due to increased moisture or salt content within the vadose zone.

The scope of the geophysical surveying included data acquisition, processing, and visualization of GPR (in-farm), and the collection of electromagnetic induction and magnetic gradiometry (ex-farm) data around the TX and TY Farms. This appendix summarizes the results of the surveys. Full reports on these efforts can be found in RPP-38104, *Surface Geophysical Exploration of TX and TY Tank Farms at the Hanford Site: Results of Background Characterization with Ground Penetrating Radar* and RPP-36893, *Surface Geophysical Exploration of TX and TY Tank Farms at the Hanford Site: Results of Background Characterization with Magnetics and Electromagnetics*.

D1.0 GROUND PENETRATING RADAR

Data acquisition was conducted using a Noggin 250 Smart Cart system (Sensors and Software, Mississauga, ON), which included a GPR system (transmitting and receiving antennae, battery, and energy source) and digital output display, both housed on a fiberglass cart. The Smart Cart was outfitted with a Leica 1200 RTK GPS unit (Leica Geosystems AG, Heerbrugg, Switzerland) for geo-referencing of data and a heads-up display/GPS light bar (Ag Leader Technology, Ames, IA) to allow real-time navigation while traversing the area. Data coverage included a total of 30.42 line-kilometers throughout the tank farms. Total aerial coverage of the GPR survey was approximately 15.95 acres.

The full report describing the results of the GPR survey can be found in RPP-38104, *Surface Geophysical Exploration of TX and TY Tank Farms at the Hanford Site: Results of Background Characterization with Ground Penetrating Radar*. A summary of the GPR survey coverage area for TX and TY farm areas can be viewed in Figure D-1, which was created by plotting the GPS data recorded by the GPR datalogger. Gaps shown in data coverage were due to surficial obstacles or extreme terrain that prevented Smart Cart access to some areas.

Correlation of the data collected in the GPR survey with known tank farm infrastructure was evaluated in a series of steps. First, all GPR data were processed to record the location and depth of GPR anomalies, called “hyperbola picks.” The hyperbola picks for each line within a grid were merged into a grid specific data file for each tank farm. Two-dimensional, plan-view plots were generated from the spatial locations of the GPR anomalies within the summary pick data file. Each anomaly is represented in these plots by a colored circle, where the colors represent a range of depths. For example, the shallowest GPR hyperbola picks, from 0-2 ft below ground surface, are represented by dark blue. A total of six depth classes (a group of data points conforming to similar depths beneath the ground surface) are used for plotting, and colors for the classes were chosen so that picks similar in depth placed in an adjacent class could be grouped together more easily.

Figure D-1. GPR Coverage – TX and TY Tank Farm Area.

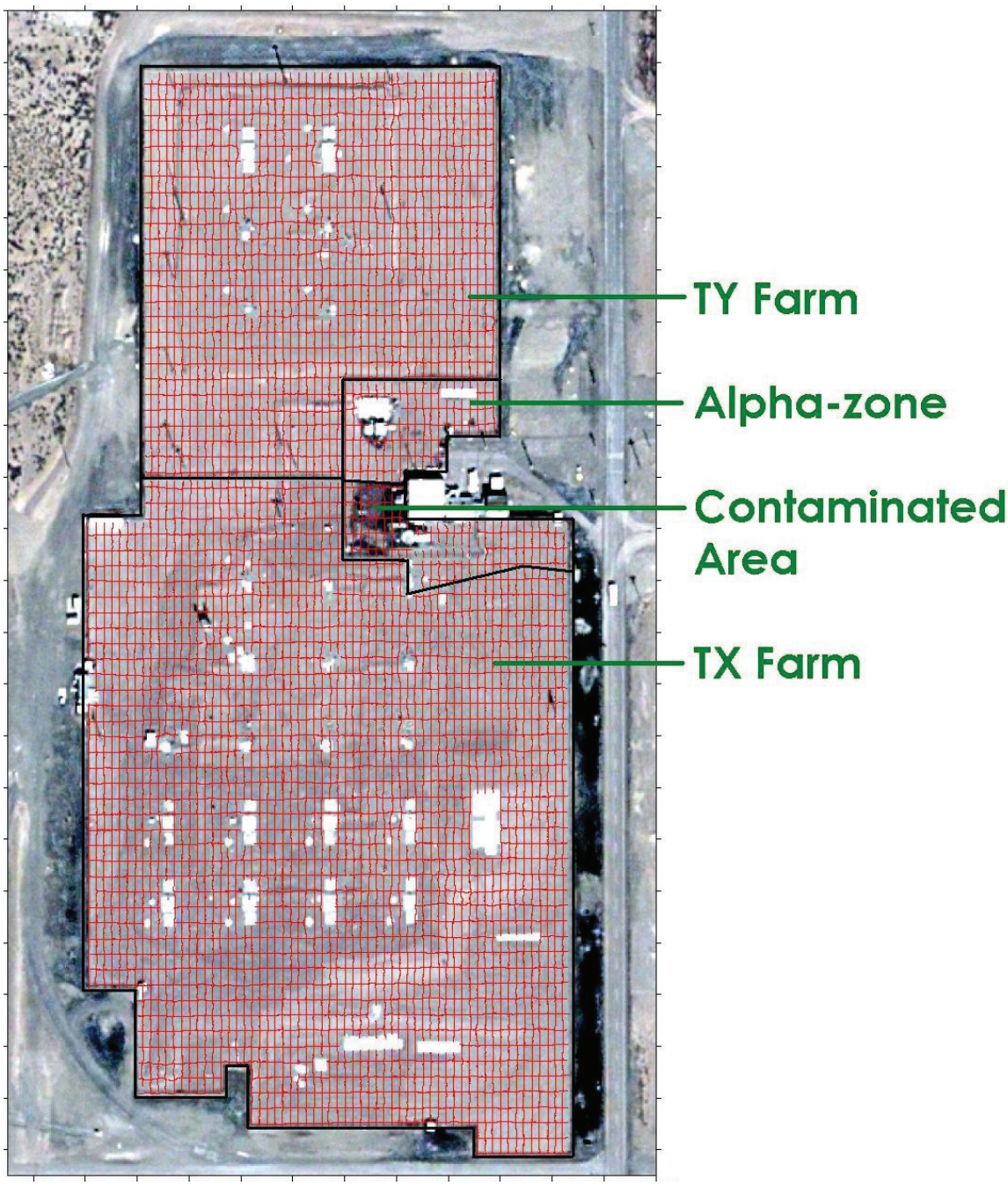

The plots of GPR hyperbola picks were then reviewed by comparing neighboring GPR picks of similar depth in order to identify continuous linear features in the data collected. With precise measurements, a GPR hyperbola pick corresponding to a known metallic linear feature such as a pipe should be located directly at the metallic feature location. However, due to imperfect GPS geo-referencing (the GPS is accurate to ± 0.5 to 1.0 meters), potential spatial offsets of the GPR pick with known metallic feature locations were observed. The offset typically correlates with

the direction of travel, giving the linear pipe feature a herringbone effect. Where this occurred, a linear feature was placed at the average location between the offset picks. The interpretation of all picks forms a set of linear features, which are subsequently digitized in Surfer software (Golden Software, Inc, Golden, CO).

A depth was assigned to each identified linear feature by considering the depths of all picks used to interpret each feature and using an average of those depths. Interpretations of these potential linear feature locations are plotted as solid straight lines and include the estimated depth of the feature at each GPR hyperbola pick location.

GPR anomaly picks that are interpreted as occurring in a linear pattern at similar depths are thought to correlate as subsurface metallic linear features, and are likely due to pipe infrastructure. Linear features interpreted from GPR hyperbola picks and corresponding depths in the TX and TY tank farm areas are provided in Figure D-2 through Figure D-4. The linear features and depths, shown in the plots, are interpreted as being representative of the potential pipe locations and depths in these tank farm areas.

Figure D-2. Estimated Locations of TX Farm Infrastructure based on Interpreted Linear Features and Depths Developed from GPR Hyperbola Picks.

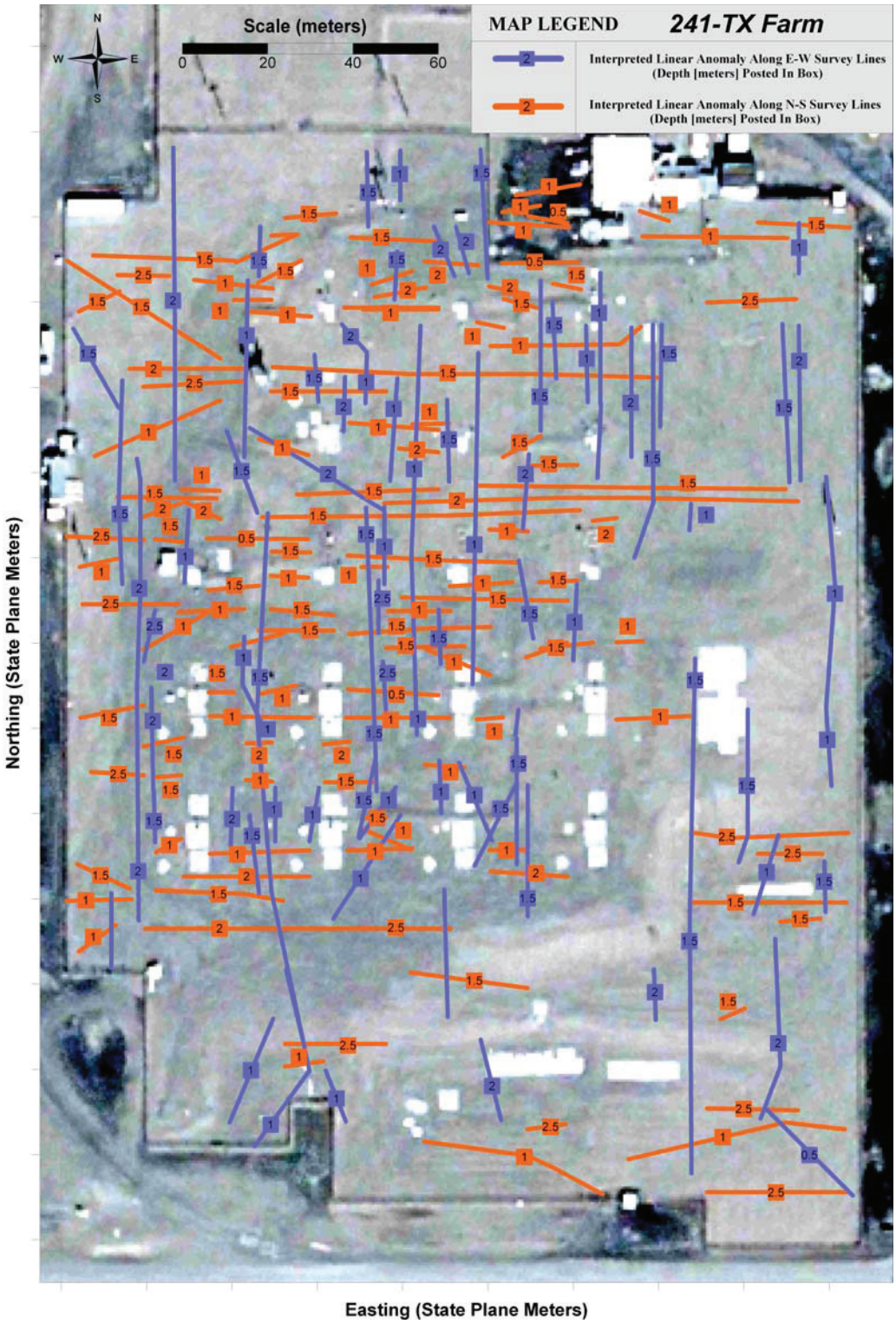

Figure D-3. Estimated Locations of TY Farm Infrastructure based on Interpreted Linear Features and Depths Developed from GPR Hyperbola Picks.

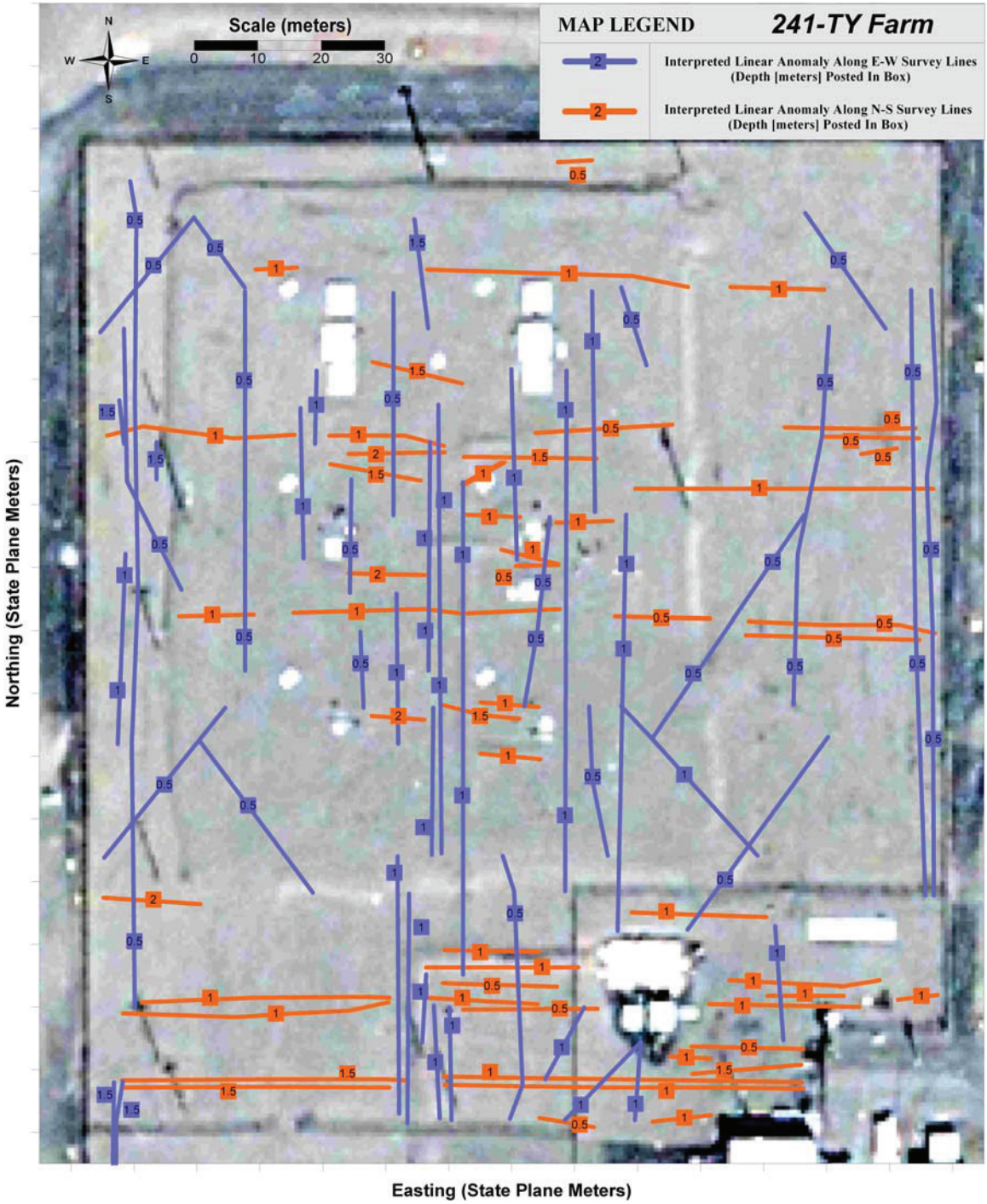

D2.0 MAGNETIC GRADIOMETRY AND EM INDUCTION

TX and TY Farm area characterization was also conducted by attaching the electromagnetic (EM) induction and magnetic gradiometry instruments to a Geophysical Operations Cart (G.O.Cart TM) (hydroGEOPHYSICS, Inc, Tucson, AZ), which included an ATV and a fiberglass towed trailer. The G.O.Cart TM was outfitted with a GPS for geo-referencing of data and to allow tracking of its location while traversing the area.

Data coverage included a total of approximately 82 acres over five main focus areas: the eastern cribs (216-T-26 through 216-T-28), northern cribs (216-T-36-13 and T216-T-13), south tile field (216-T-19), western trenches (216-T-21 through 216-T-25), and the area directly west of the TX farm.

A full discussion of the EM induction and magnetic gradiometry characterization of the TX and TY Farm area can be found in RPP-RPT-36893 *Surface Geophysical Exploration of TX and TY Tank Farms at the Hanford Site: Results of Background Characterization with Magnetics and* Electromagnetics. A summary of the EM induction and magnetic gradiometry survey coverage area for TX and TY Farm can be viewed in Figure D-4, which was created by plotting the GPS data recorded by the data logger. Gaps in GPS coverage are due to surficial obstacles or extreme terrain that prevented data collection access to some areas for data collection with the G.O. Cart.

Figure D-4. Magnetic Gradiometry and EM Induction Coverage at the TX and TY Farm Area.

The magnetic data were processed and plotted spatially to assist in delineation of subsurface features. The features show up as extremely high and low amplitude values of the magnetic field, relative to the background field. Figure D-5 shows the results of the vertical magnetic gradient, presented as contours of the amplitude. The background field is represented by yellow hues and the high and low amplitudes are red and blue hues, respectively. Several linear features can be seen in the plot that likely represent subsurface steel pipes.

Similarly, the EM induction data were processed and plotted spatially. The results are displayed in Figure D-6. High electrical conductivity as measured by inductive phenomenon distinguish subsurface features from background. Contours of the conductivity data, shown in Figure D-6, show some features that are not found in the magnetic gradient data in Figure D-5. Both techniques are valuable in assessing subsurface infrastructure features.

The interpreted EM induction and magnetic gradiometry data, shown in Figure D-7 were used in this study in multiple ways. First, the interpreted data was used to assist and guide the direct resistivity data acquisition. Additionally, results of the EM and magnetic survey and associated interpreted linear feature or pipe locations were used in the interpretation of resistivity inversion modeling results. Comparison of inversion results with plots of interpreted features based on the EM and magnetic data allows for consideration of the potential effects of these artifacts in the interpretations of inverted resistivity results. If, for example, a low resistivity target is seen directly beneath a grouping of several pipes, then the resistivity results should be viewed carefully with anticipated uncertainty in an interpreted electrolytic conduction phenomenon.

Figure D-5. Vertical Magnetic Gradient Results.

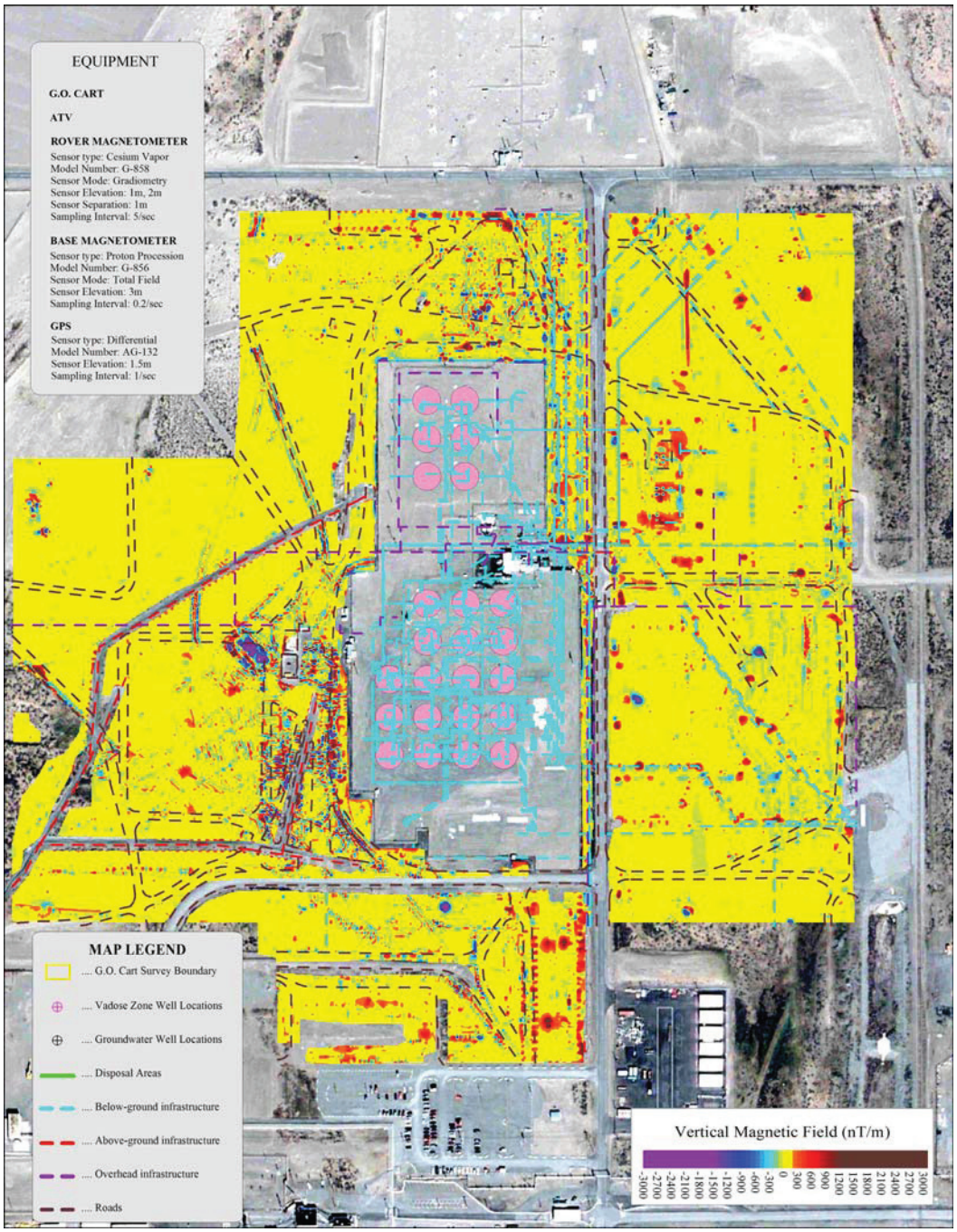

Figure D-6. Electromagnetic Induction Results, Showing Electrical Conductivity.

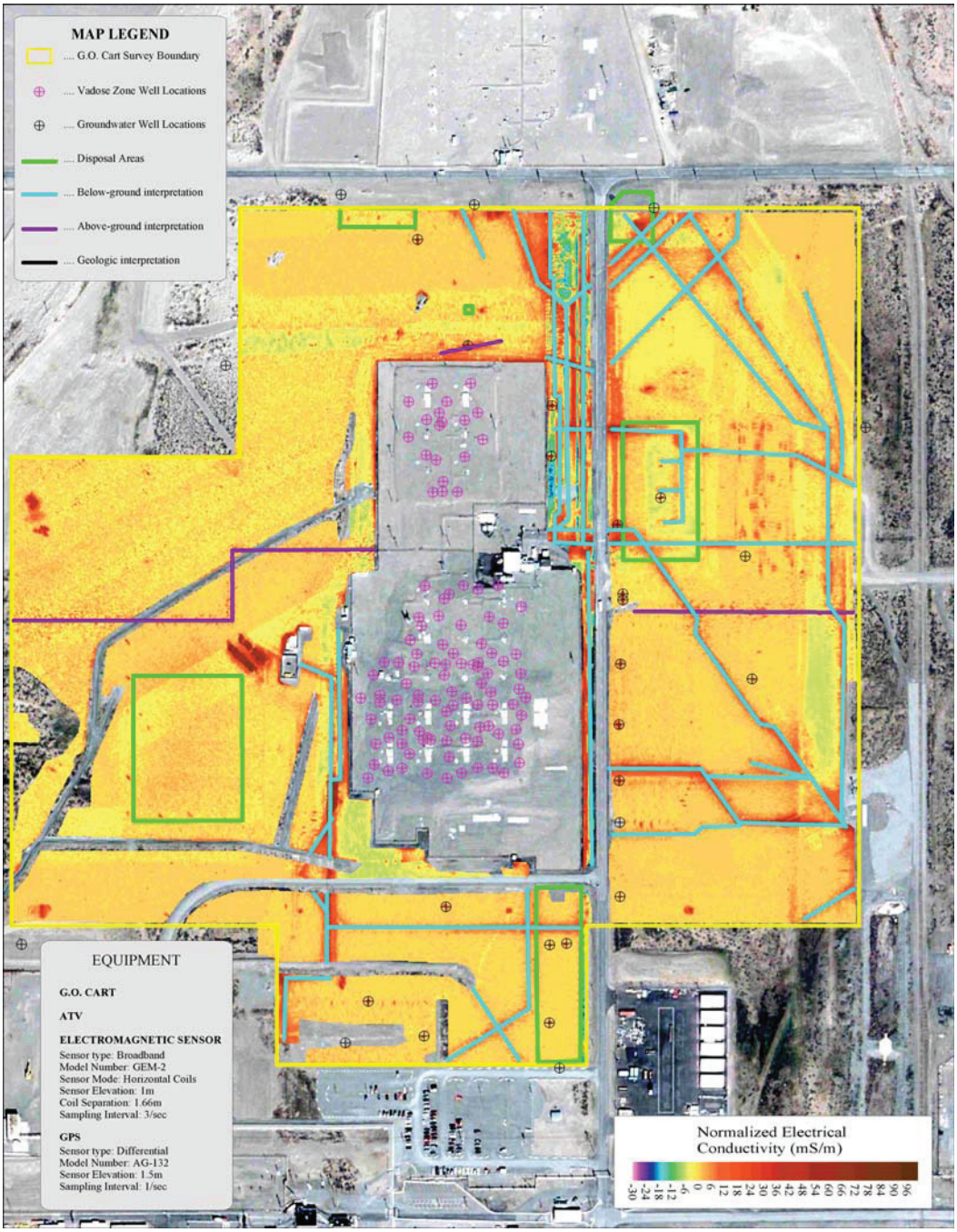

Figure D-7. Data Acquisition Lines and Linear features identified from the G.O.Cart Survey.

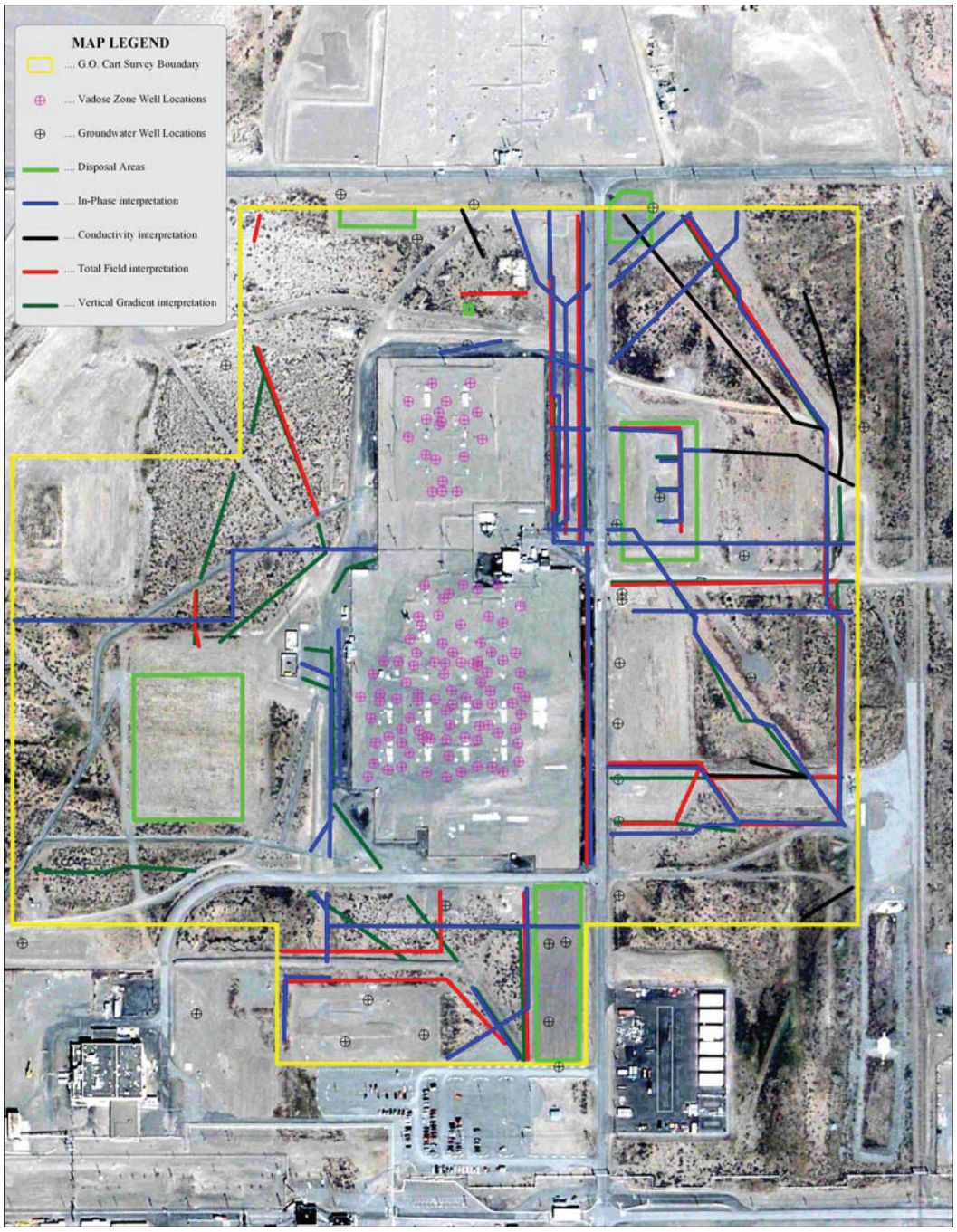

This page intentionally left blank.

APPENDIX E

DATA PROCESSING AND REDUCTION

This page intentionally left blank.

TABLE OF CONTENTS

E1.0 2D INVERSIONS E-1

LIST OF FIGURES

E-1. Line 1E 2D Resistivity Inversion Results E-2
E-2. Line 2E 2D Resistivity Inversion Results E-3
E-3. Line 3E 2D Resistivity Inversion Results E-4
E-4. Line 4E 2D Resistivity Inversion Results E-5
E-5. Line 5E 2D Resistivity Inversion Results E-6
E-6. Line 6E 2D Resistivity Inversion Results E-7
E-7. Line 7E 2D Resistivity Inversion Results E-8
E-8. Line 8E 2D Resistivity Inversion Results E-9
E-9. Line 9E 2D Resistivity Inversion Results E-10
E-10. Line 10E 2E Resistivity Inversion Results E-11
E-11. Line 11E 2D Resistivity Inversion Results E-12
E-12. Line 12E 2D Resistivity Inversion Results E-13
E-13. Line 13E 2D Resistivity Inversion Results E-14
E-14. Line 14E 2D Resistivity Inversion Results E-15
E-15. Line 15E 2D Resistivity Inversion Results E-16
E-16. Line 16E 2D Resistivity Inversion Results E-17
E-17. Line 17E 2D Resistivity Inversion Results E-18
E-18. Line 18E 2D Resistivity Inversion Results E-19
E-19. Line 19E 2D Resistivity Inversion Results E-20
E-20. Line 20E 2D Resistivity Inversion Results E-21
E-21. Line 21E 2D Resistivity Inversion Results E-22
E-22. Line 22E 2D Resistivity Inversion Results E-23
E-23. Line 23E 2D Resistivity Inversion Results E-24
E-24. Line 1N 2D Resistivity Inversion Results E-25
E-25. Line 2N 2D Resistivity Inversion Results E-26
E-26. Line 3N 2D Resistivity Inversion Results E-27
E-27. Line 4N 2D Resistivity Inversion Results E-28
E-28. Line 5N 2D Resistivity Inversion Results E-29
E-29. Line 6N 2D Resistivity Inversion Results E-30
E-30. Line 7N 2D Resistivity Inversion Results E-31

E-31. Line 8N 2D Resistivity Inversion Results E-32
E-32. Line 9N 2D Resistivity Inversion Results E-33
E-33. Line 10N 2D Resistivity Inversion Results E-34
E-34. Line 11N 2D Resistivity Inversion Results E-35
E-35. Line 12N 2D Resistivity Inversion Results E-36
E-36. Line 13N 2D Resistivity Inversion Results E-37
E-37. Line 14N 2D Resistivity Inversion Results E-38
E-38. Line 15N 2D Resistivity Inversion Results E-39
E-39. Line 16N 2D Resistivity Inversion Results E-40
E-40. Line 17N 2D Resistivity Inversion Results E-41
E-41. Line 18N 2D Resistivity Inversion Results E-42
E-42. Line 19N 2D Resistivity Inversion Results E-43
E-43. Line 20N 2D Resistivity Inversion Results E-44
E-44. Line 21N 2D Resistivity Inversion Results E-45
E-45. Line 22N 2D Resistivity Inversion Results E-46
E-46. Line 23N 2D Resistivity Inversion Results E-47
E-47. Line 24N 2D Resistivity Inversion Results E-48

E1.0 2D INVERSIONS

Two-dimensional (2D) resistivity data for the surface-to-surface (STS) survey were collected at surface electrodes laid out along orthogonal surface lines using a pole-pole array. The electrodes were spaced at 20 feet (6 meters) apart within each line, with parallel resistivity lines spaced approximately 30 meters apart.

Data were collected along a total of 47 lines. Lines 1E through 23E were oriented in a south-north direction. Lines 1N through 24N were oriented in a west-east direction. North-south data collection began just west of the TX trenches, extended through and past the TX-TY tank farm and selected waste sites north and south of the farm area, then across selected waste sites to the east. East-west data collection began at selected waste sites south of the TX tank farm boundary and progressed north through the TX-TY tank farm and selected waste sites west and east of the farm area, then through selected waste sites to the north. Wastes sites outside of the tank farm areas investigated to the west include the TX Trenches (216-T-21 through 216-T-25), to the south include the 216-T-19 crib and tile field and the 216-Z-7 crib, to the east include the TY Cribs (216-T-26 through 216-T-28) and the 216-T-31 french drain, and to the north include the 216-T-36 crib and 216-T-13 trench.

The STS resistivity data were filtered to remove noisy data (discussed in section B.1 of Appendix B) and the dataset collected at each line was then inverted using RES2DINV. Section B.3 of Appendix B outlines all 2D inversion parameters and methodology used. The convergence curve and the final RMS value are provided for reference on each 2D inversion plot, along with location of the line with respect to the orthogonal grid.

The two-dimensional inversion results are represented in color contour cross-section form using Surfer® (Golden Software, Inc). A consistent color scale, developed for TX-TY Complex based on analysis of all modeled data, is used for all lines. The color scale is comprised of a continuous spectrum of colors similar to a rainbow. This spectrum uses cool colors (blue) to represent lower values and hot colors (red) to represent higher values. A discussion on the development of this color scale is provided in section B.3.4 of Appendix B.

Also included in the plots is an annotation layer, plotted at the top of the cross section, presenting line features compiled from multiple sources. A geospatial database, containing CAD maps of known infrastructure and other area features, was used to automatically generate intersection points along each resistivity line. Layers of interest include pipelines, trench lines, electrical lines, roads, waste site boundaries and line intersections with other resistivity lines. This information was combined with and compared to in-field observations, collected and noted on field forms by HGI field personnel while traversing lines in the field. The final step was to quality check these

® Surfer is a registered trademark of Golden Software, Inc., Golden, CO.

locations using aerial photos of the TX-TY farm area overlain with GPS points of each electrode location.

Figures E-1 through E-23 provide graphical representation of the 2D inversion results for the north-south lines and Figures E-24 through E-47 for the east-west lines.

Figure E-1. Line 1E 2D Resistivity Inversion Results.

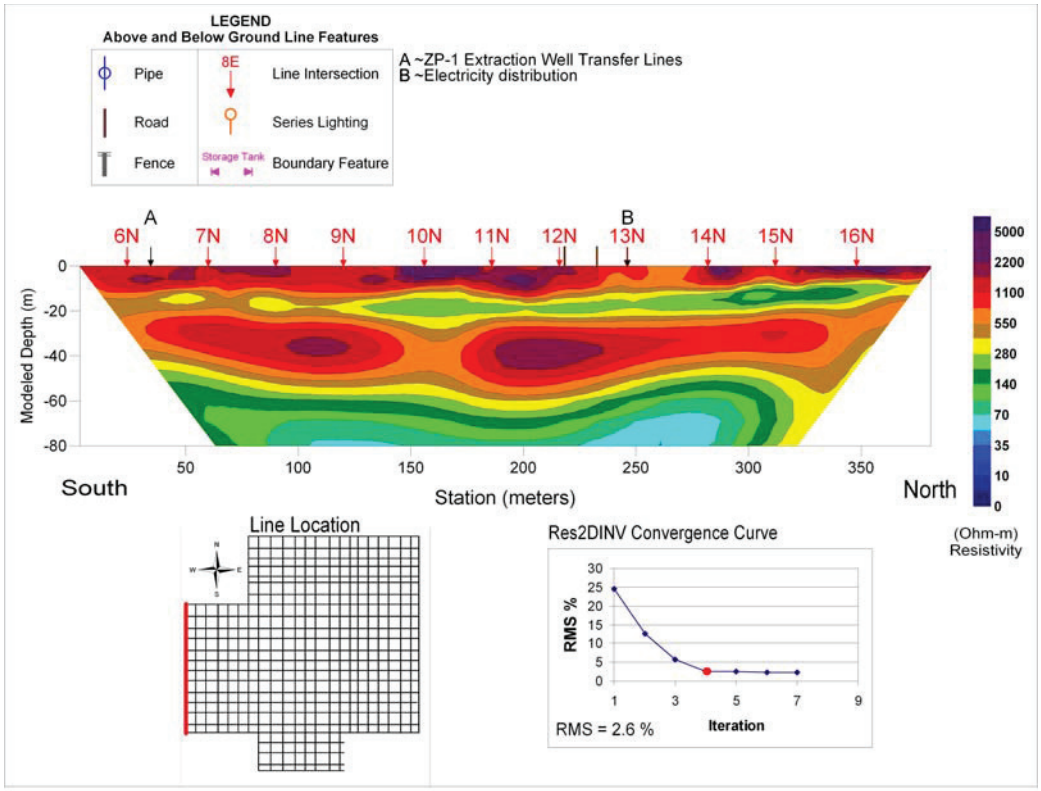

Figure E-2. Line 2E 2D Resistivity Inversion Results.

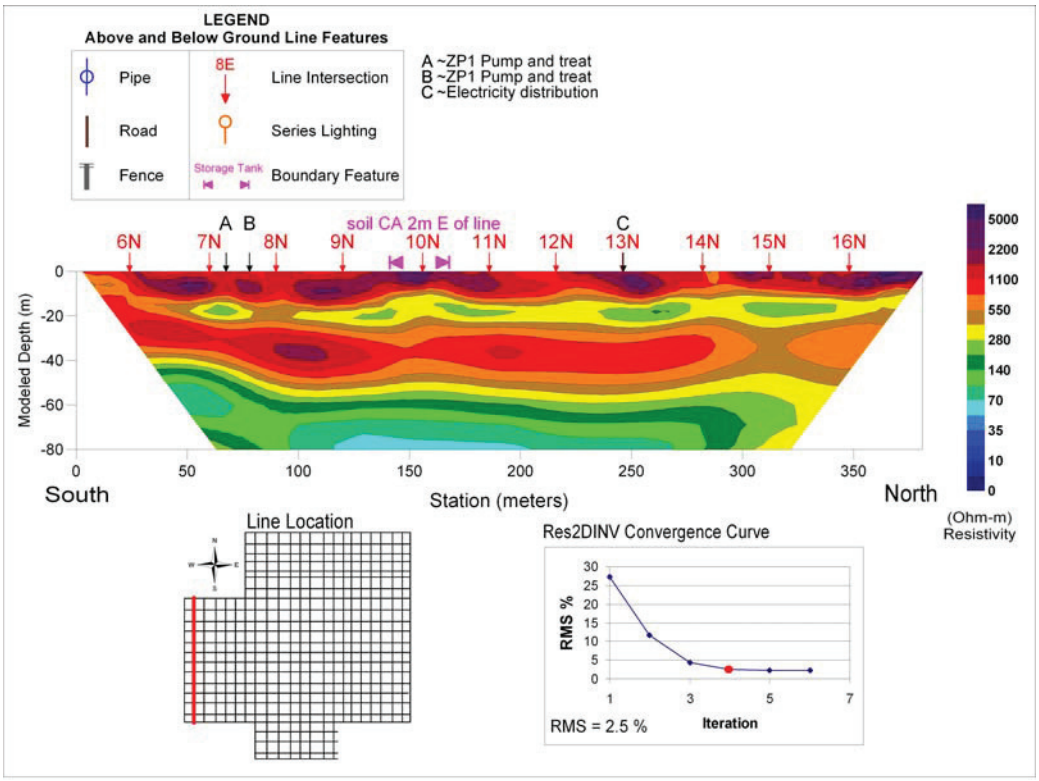

Figure E-3. Line 3E 2D Resistivity Inversion Results.

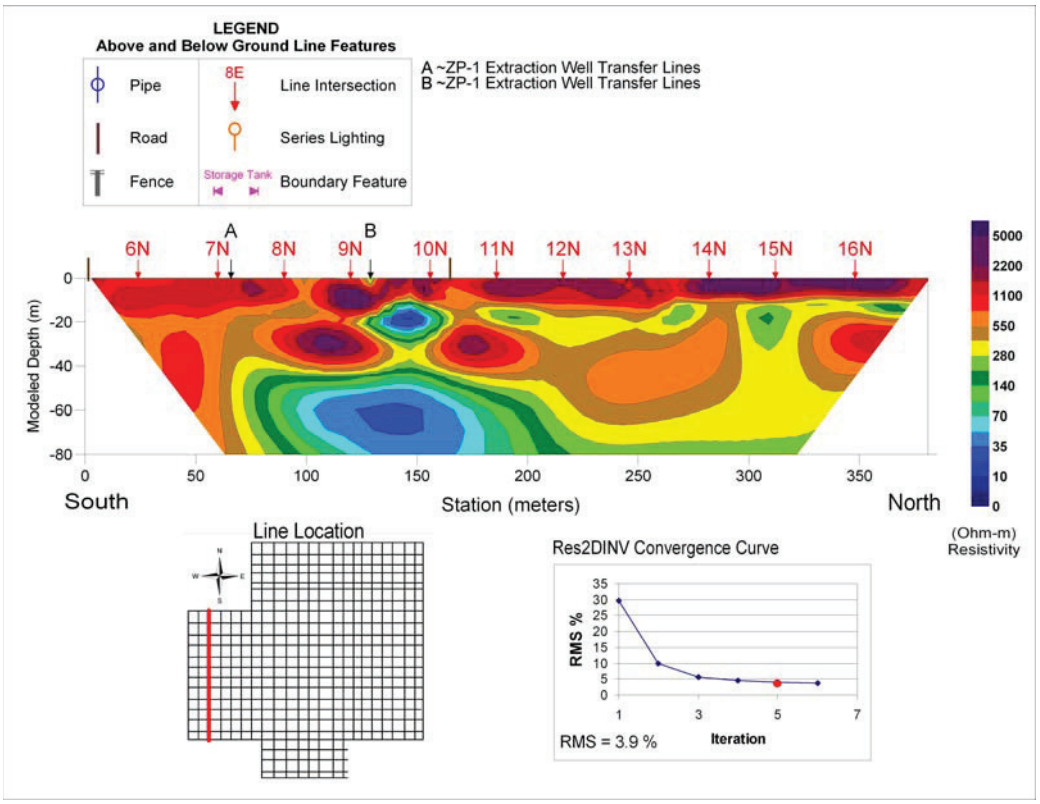

Figure E-4. Line 4E 2D Resistivity Inversion Results.

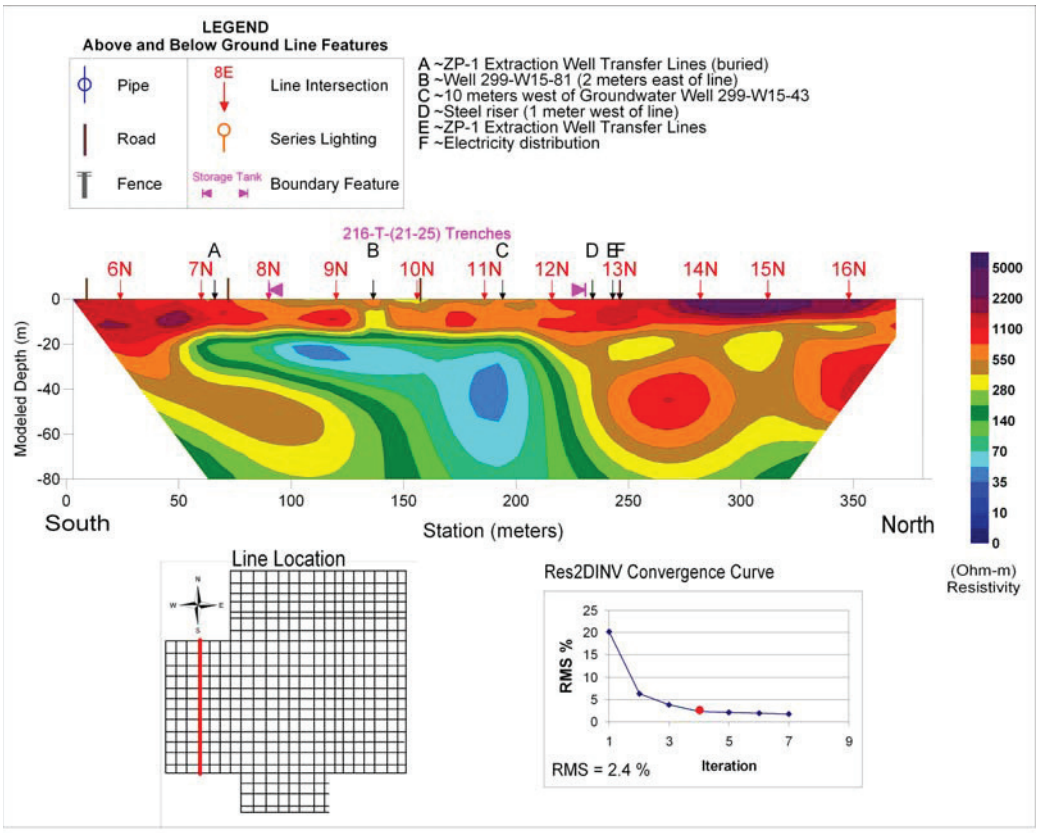

Figure E-5. Line 5E 2D Resistivity Inversion Results.

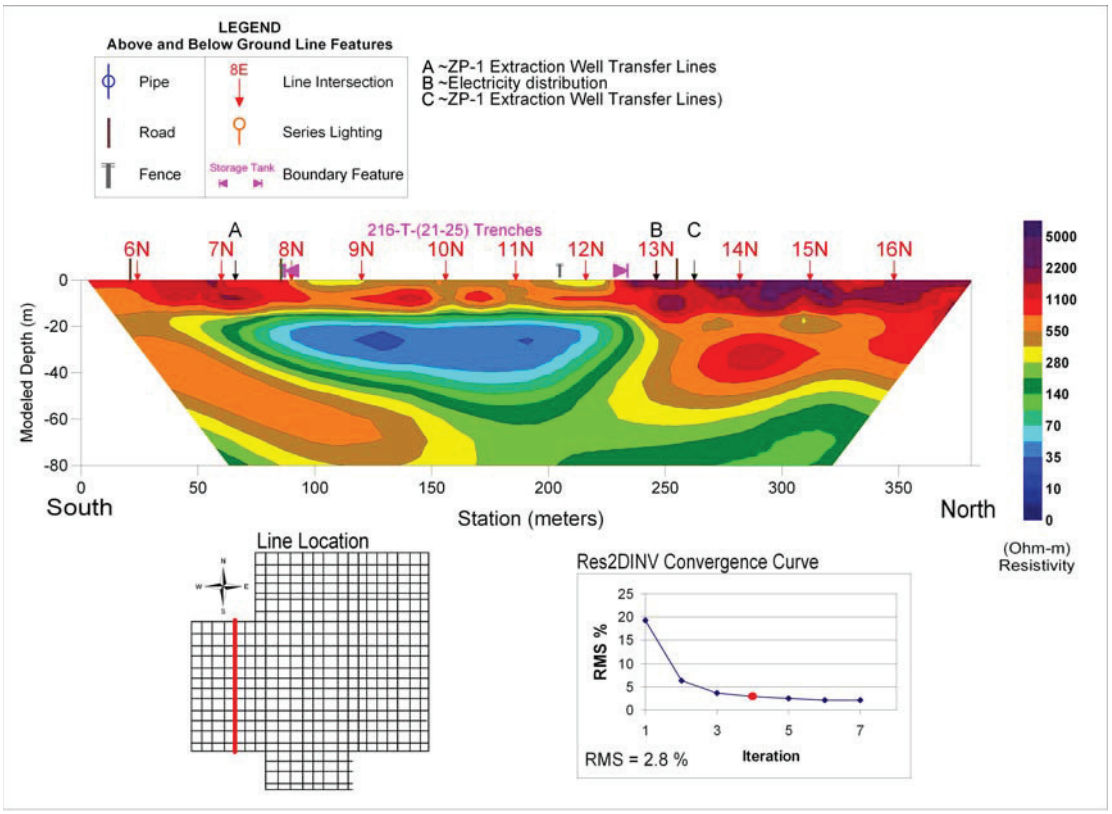

Figure E-6. Line 6E 2D Resistivity Inversion Results.

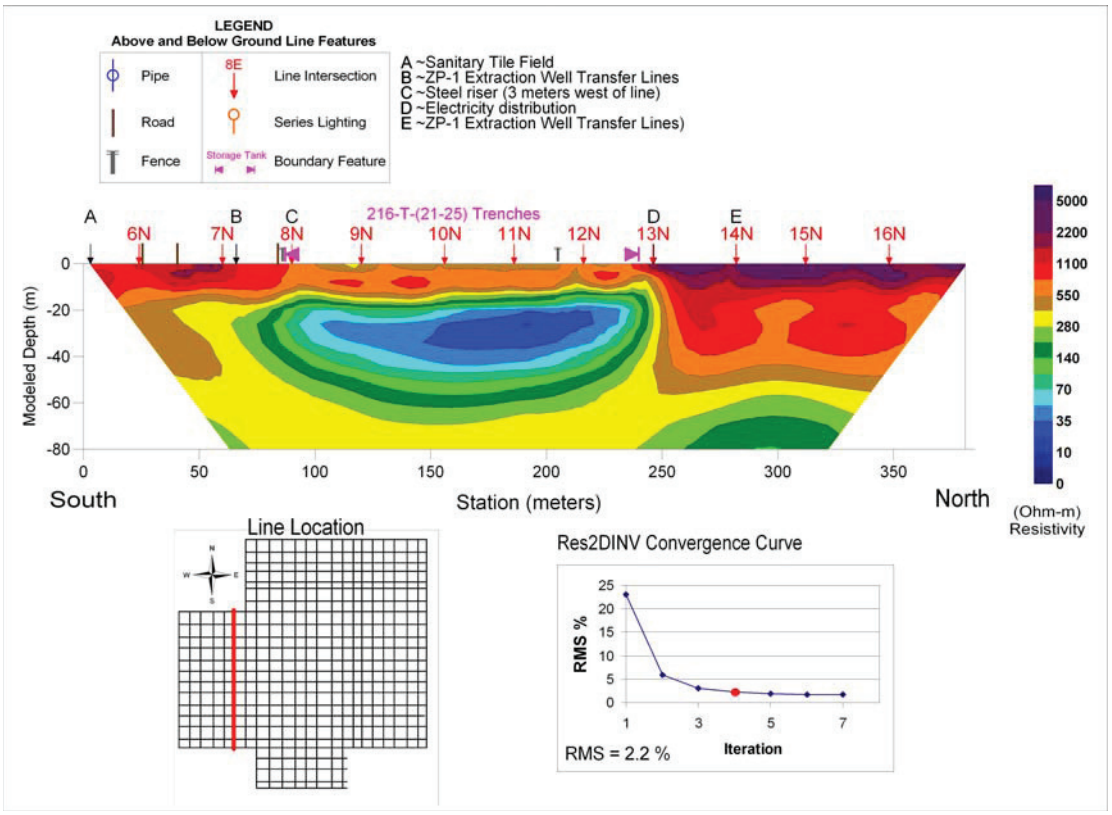

Figure E-7. Line 7E 2D Resistivity Inversion Results.

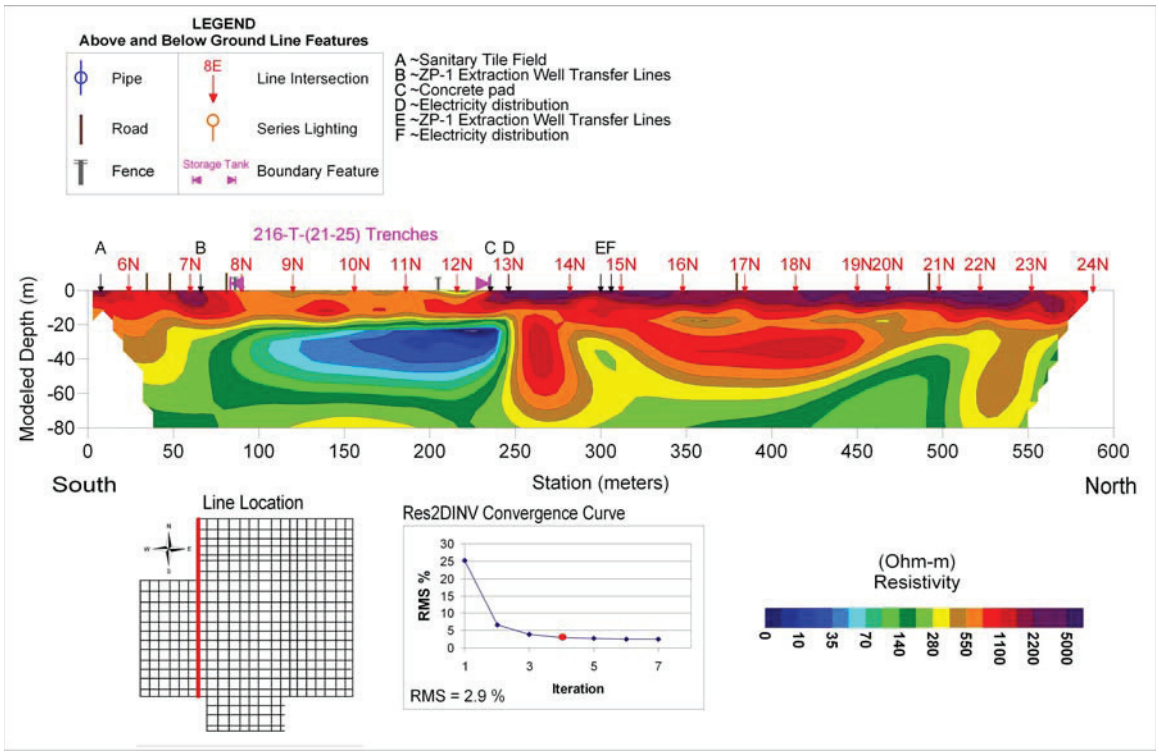

Figure E-8. Line 8E 2D Resistivity Inversion Results.

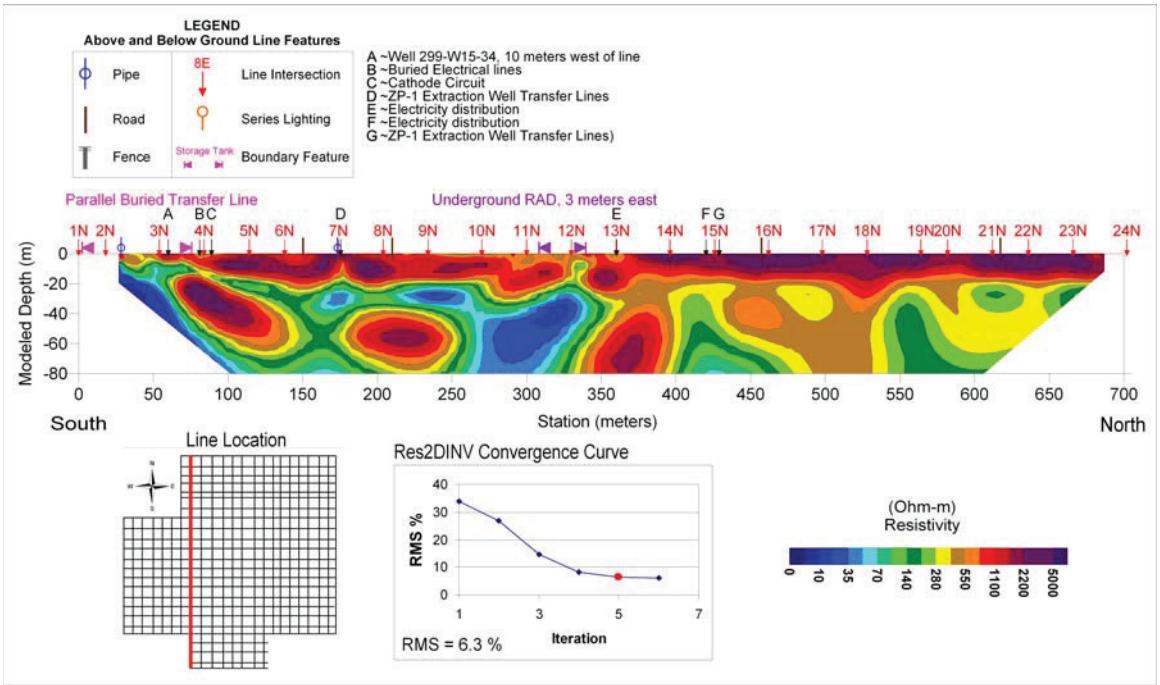

Figure E-9. Line 9E 2D Resistivity Inversion Results.

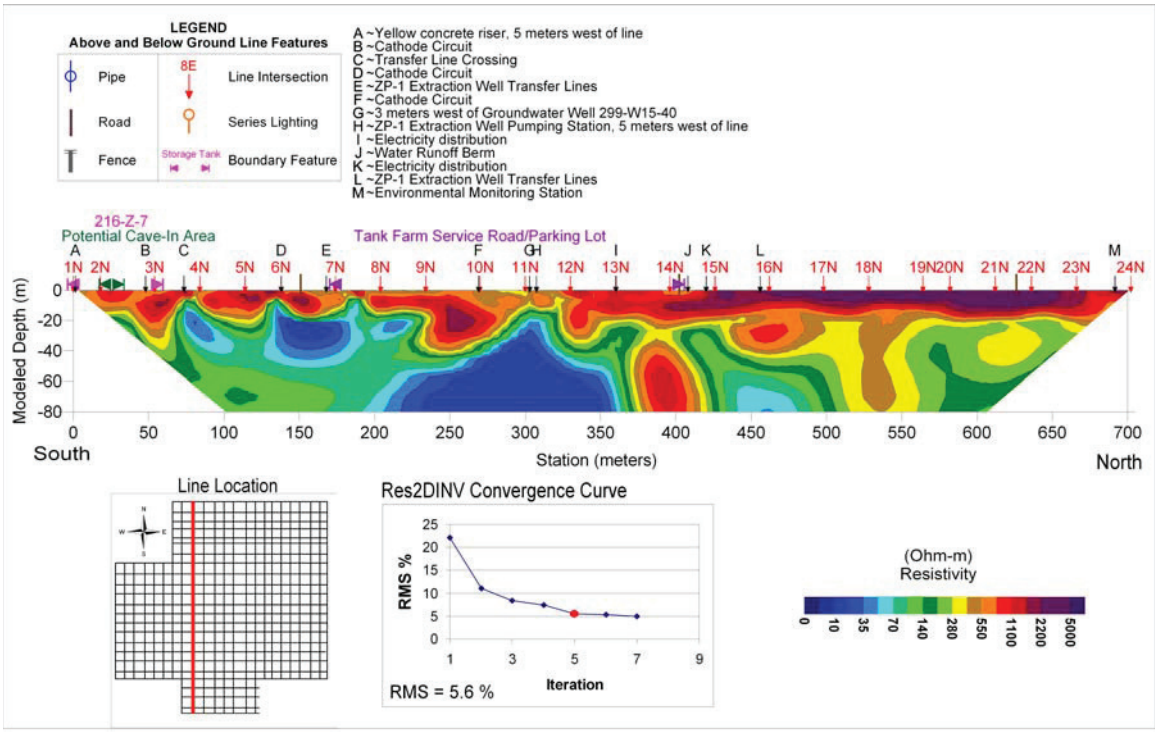

Figure E-10. Line 10E 2E Resistivity Inversion Results.

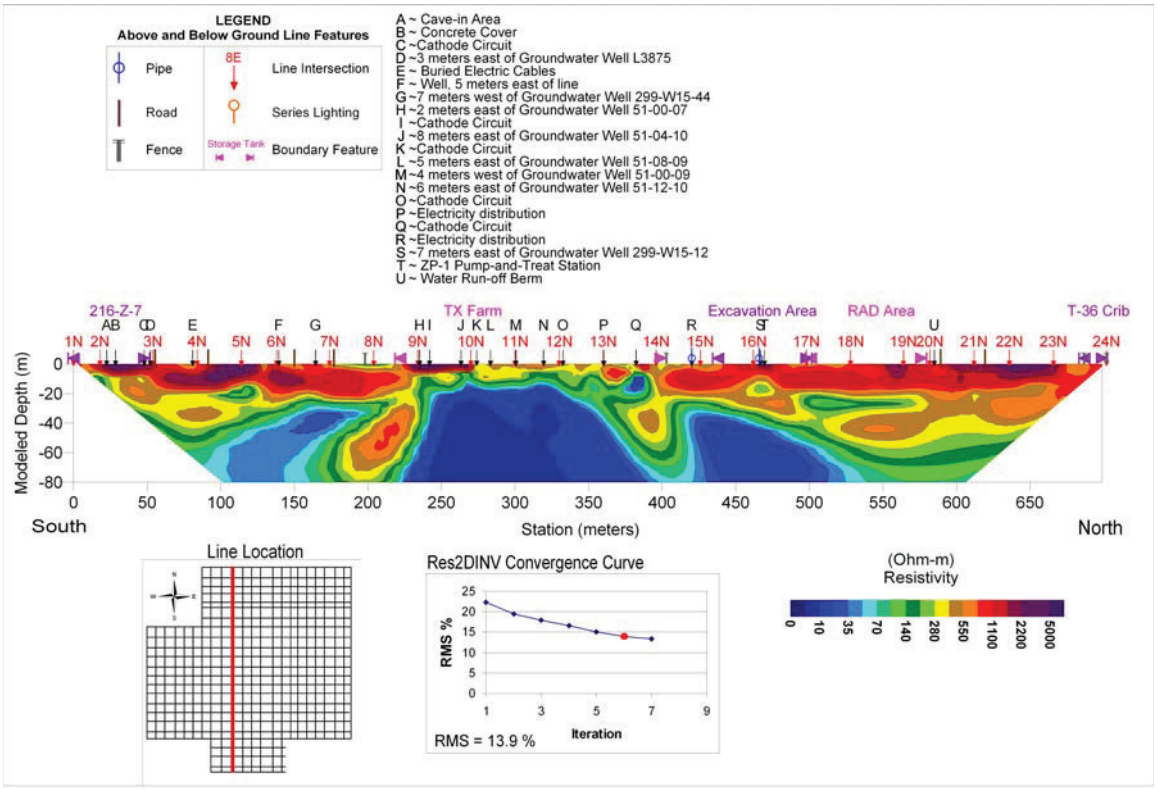

Figure E-11. Line 11E 2D Resistivity Inversion Results.

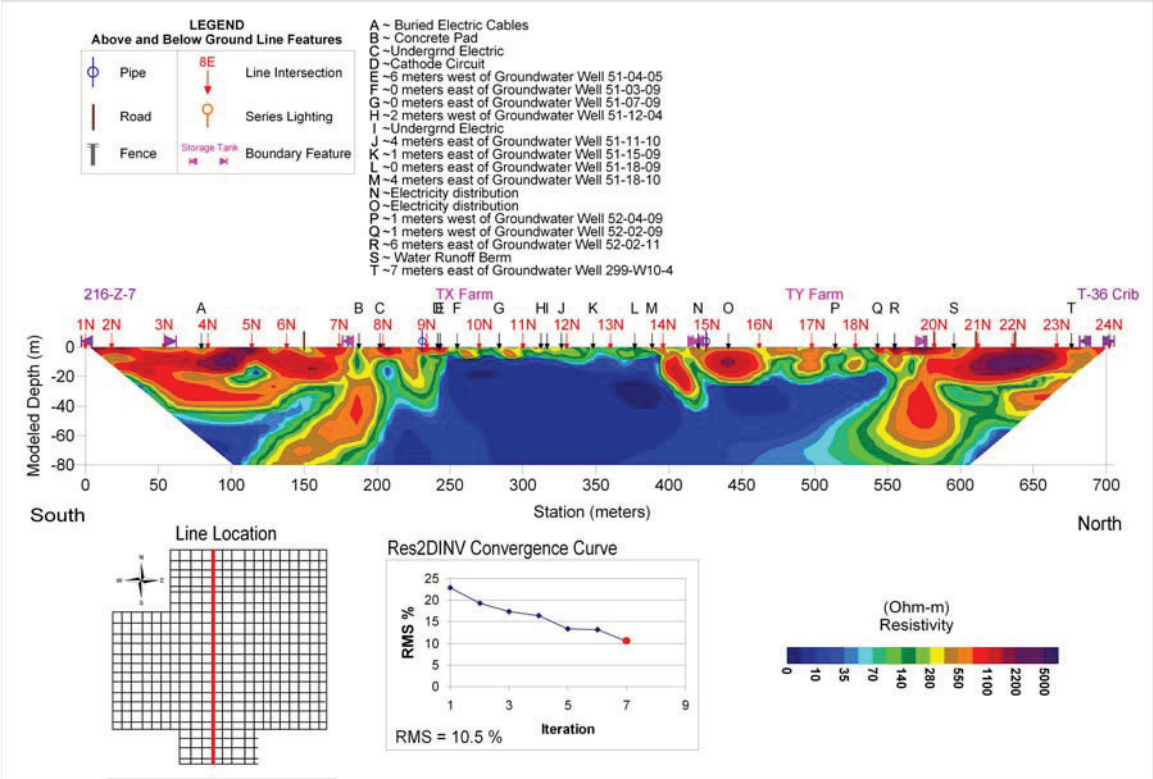

Figure E-12. Line 12E 2D Resistivity Inversion Results.

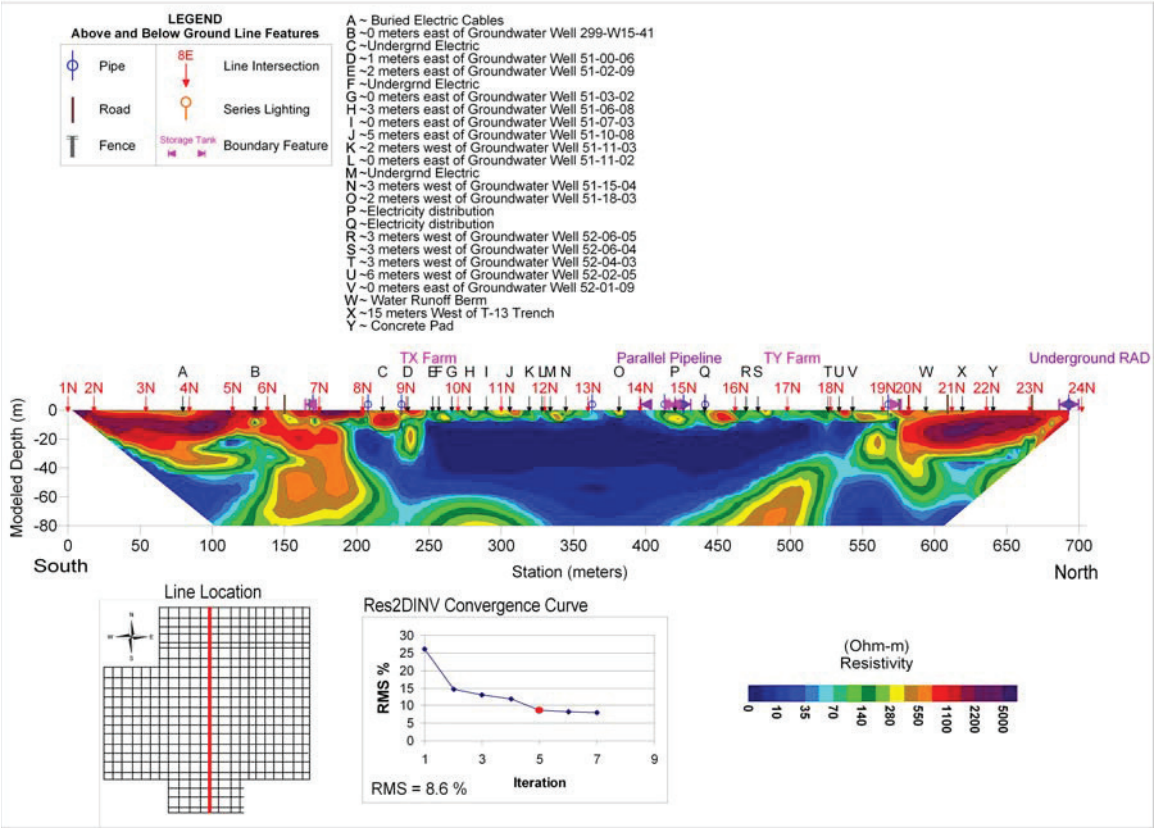

Figure E-13. Line 13E 2D Resistivity Inversion Results.

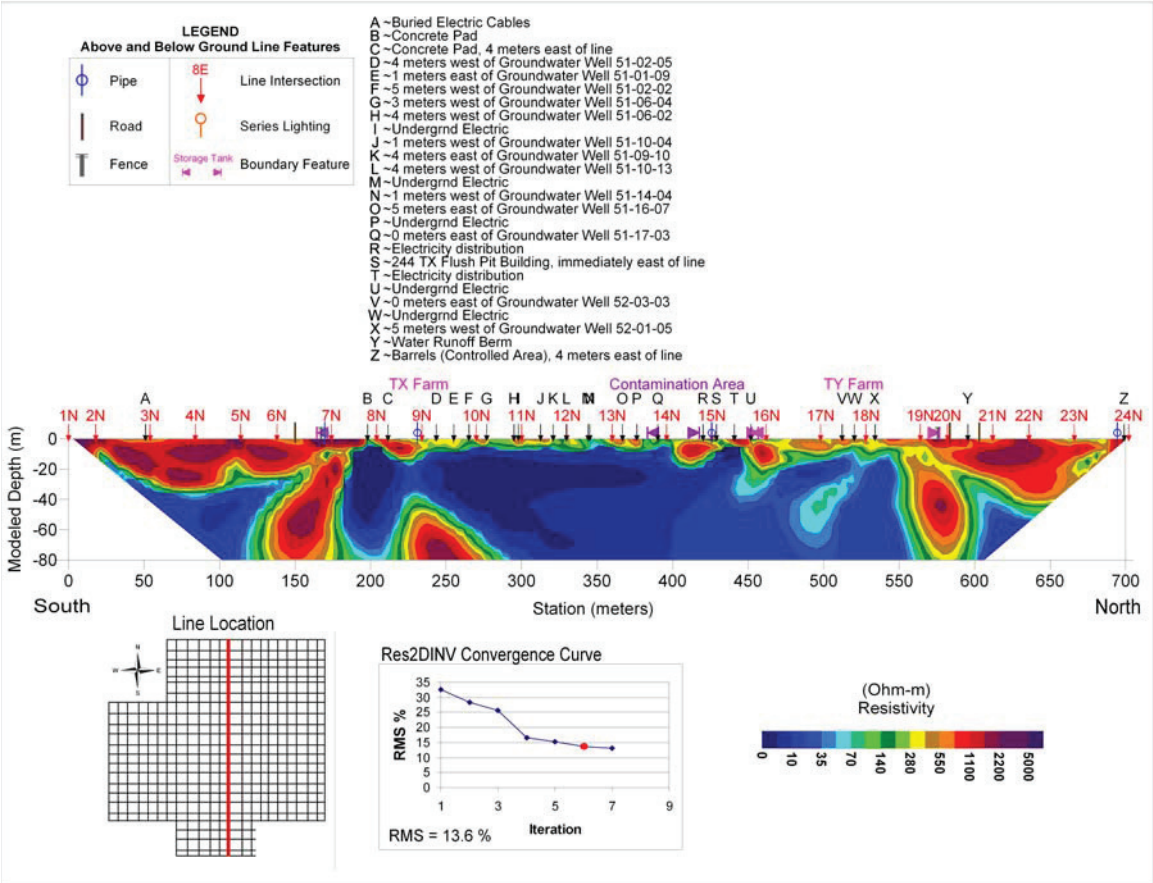

Figure E-14. Line 14E 2D Resistivity Inversion Results.

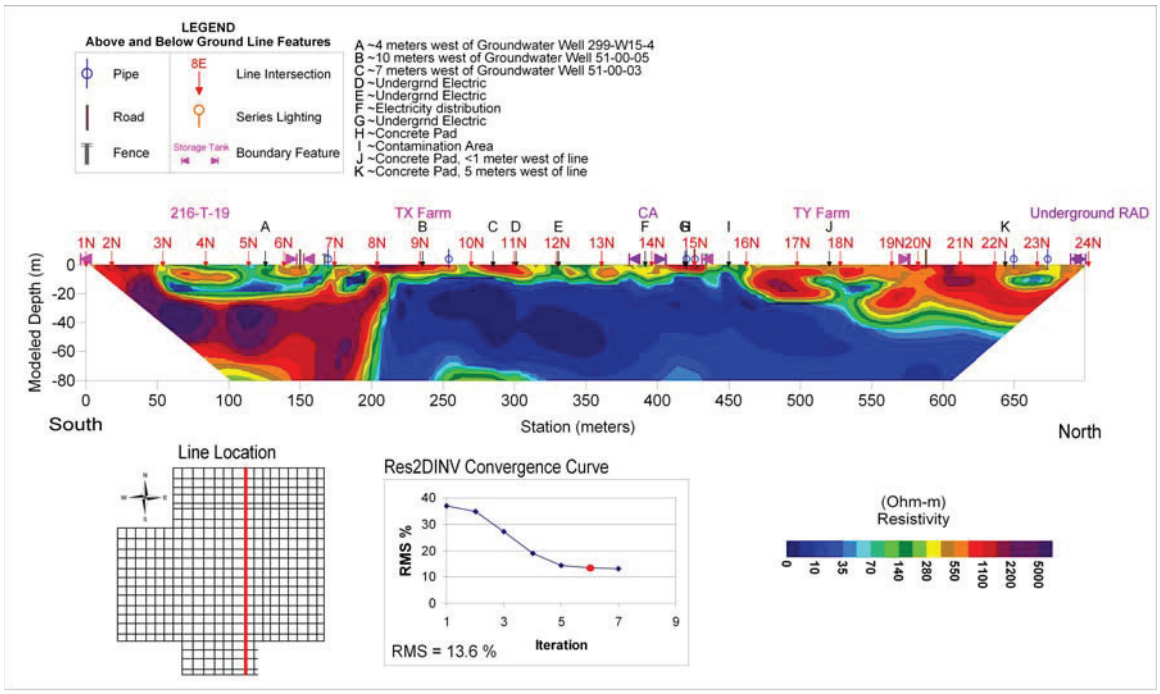

Figure E-15. Line 15E 2D Resistivity Inversion Results.

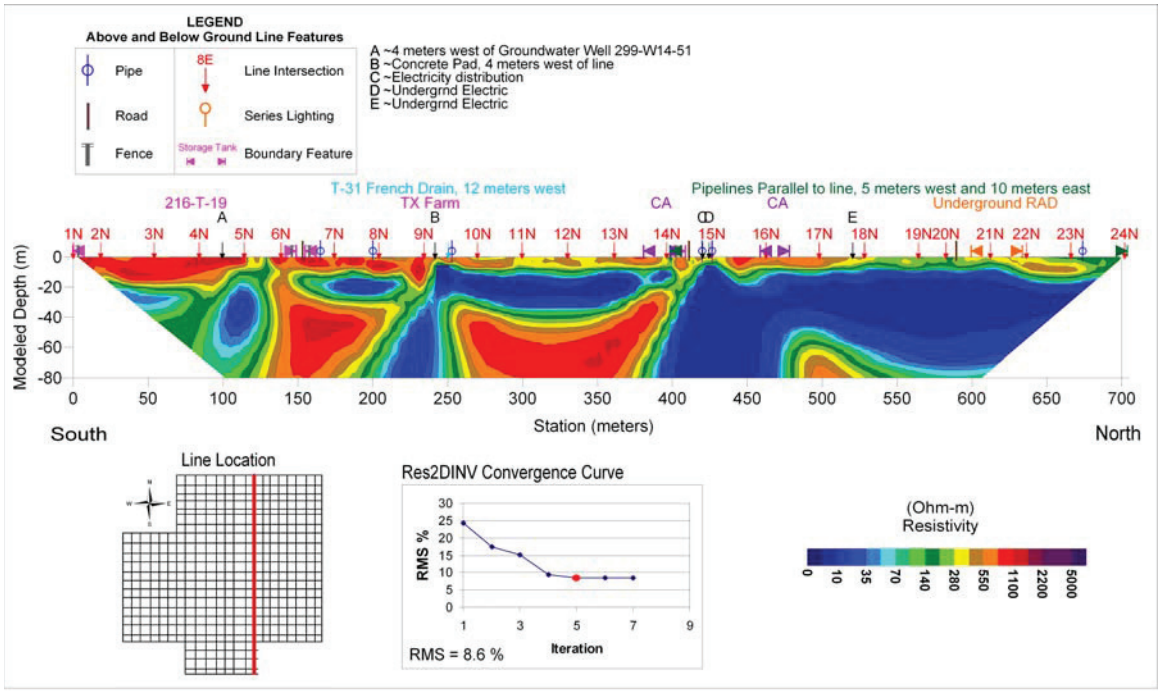

Figure E-16. Line 16E 2D Resistivity Inversion Results.

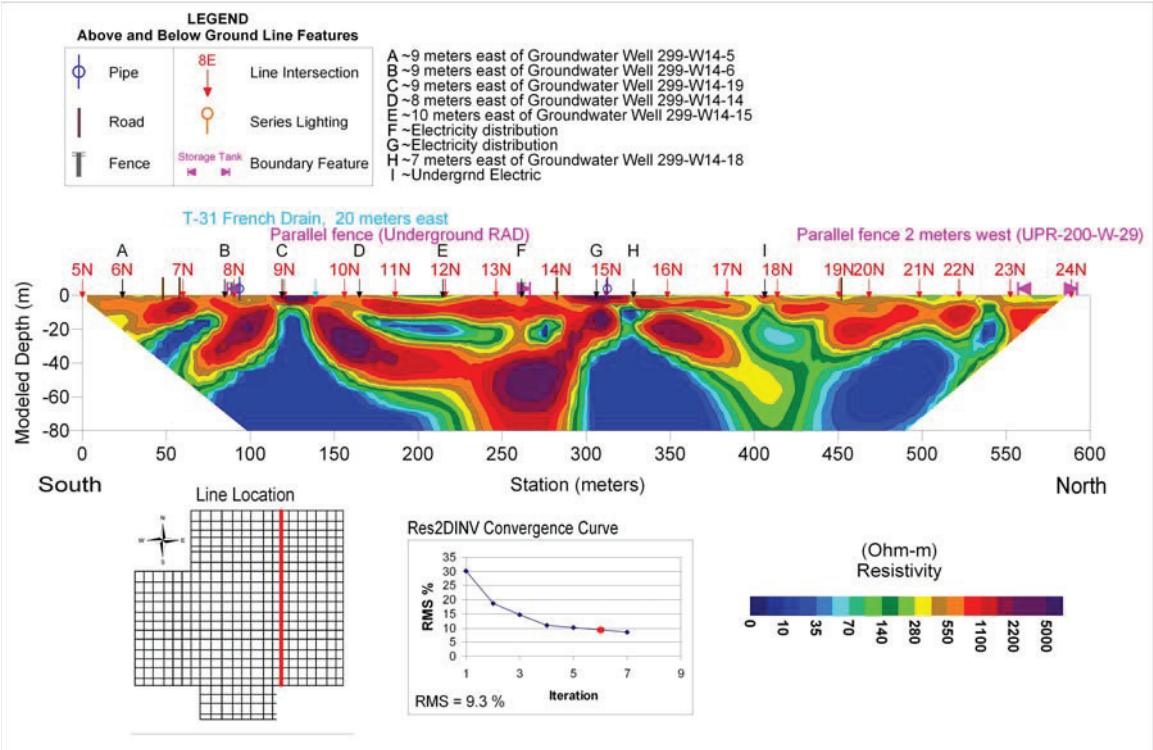

Figure E-17. Line 17E 2D Resistivity Inversion Results.

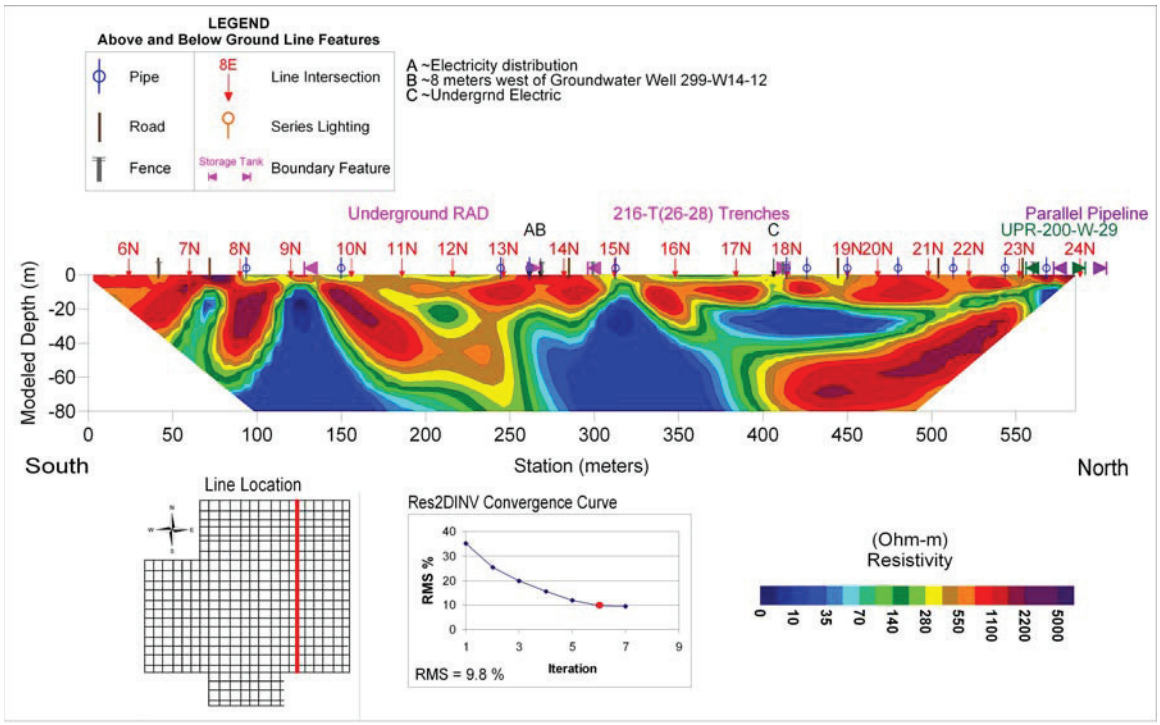

Figure E-18. Line 18E 2D Resistivity Inversion Results.

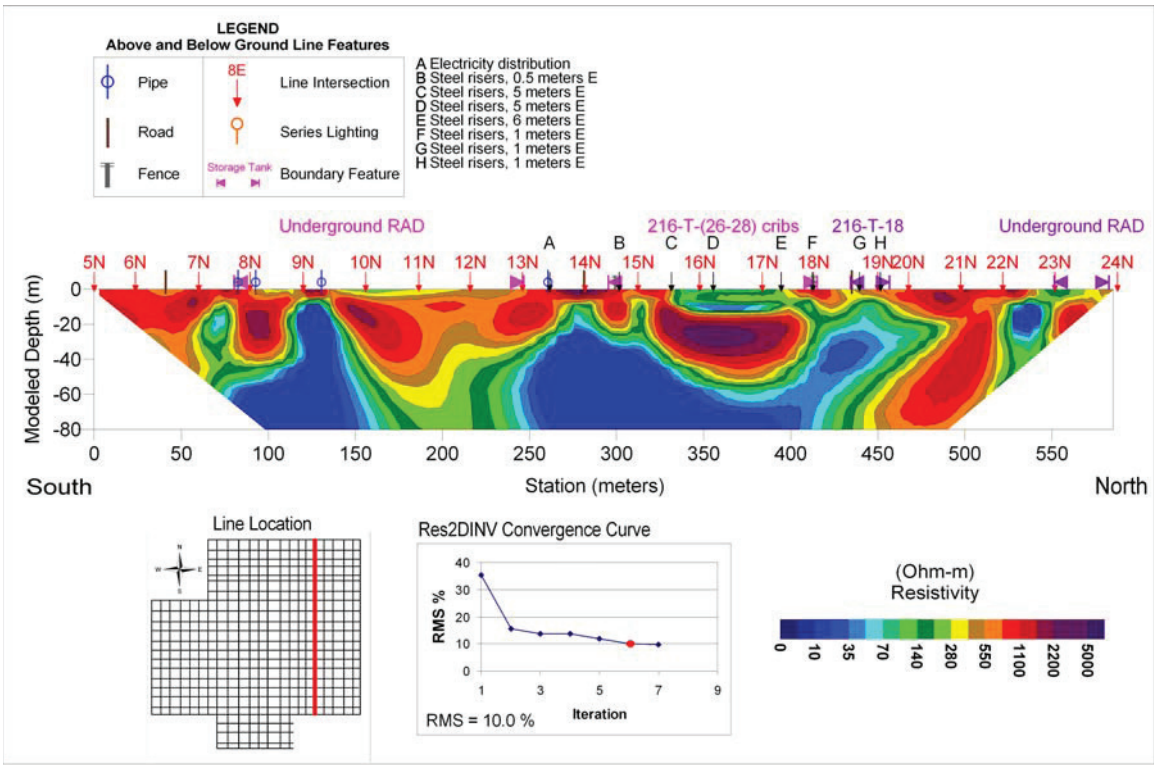

Figure E-19. Line 19E 2D Resistivity Inversion Results.

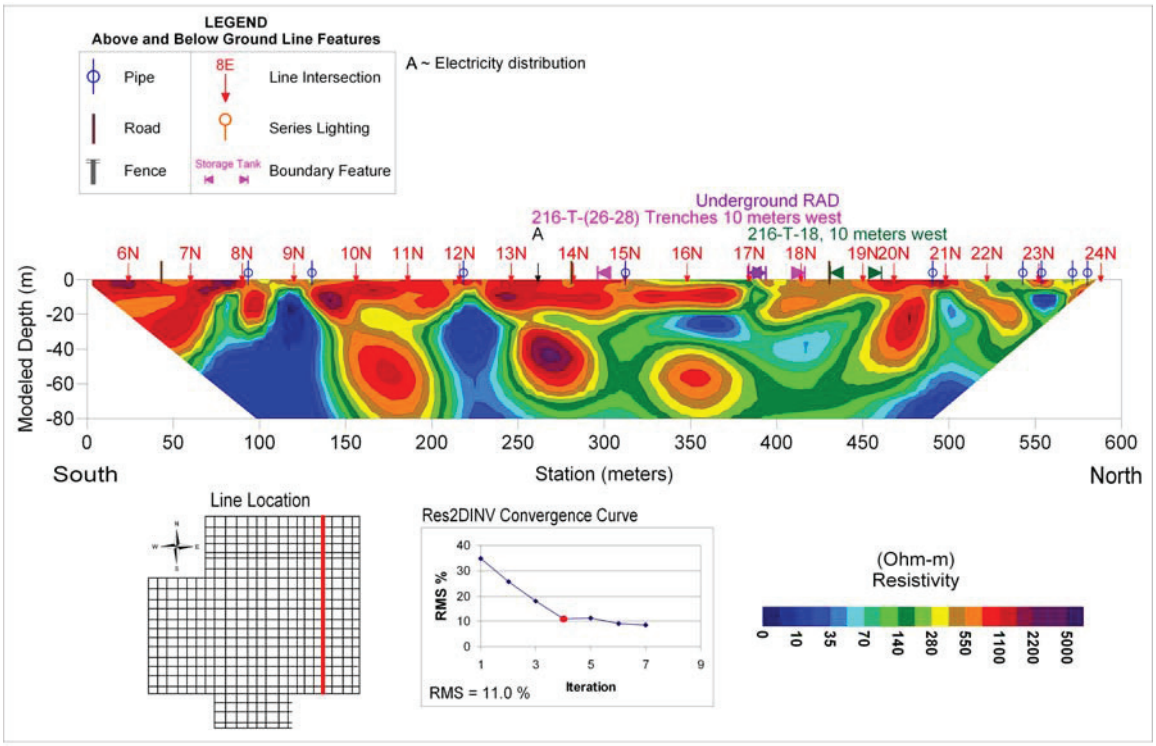

Figure E-20. Line 20E 2D Resistivity Inversion Results.

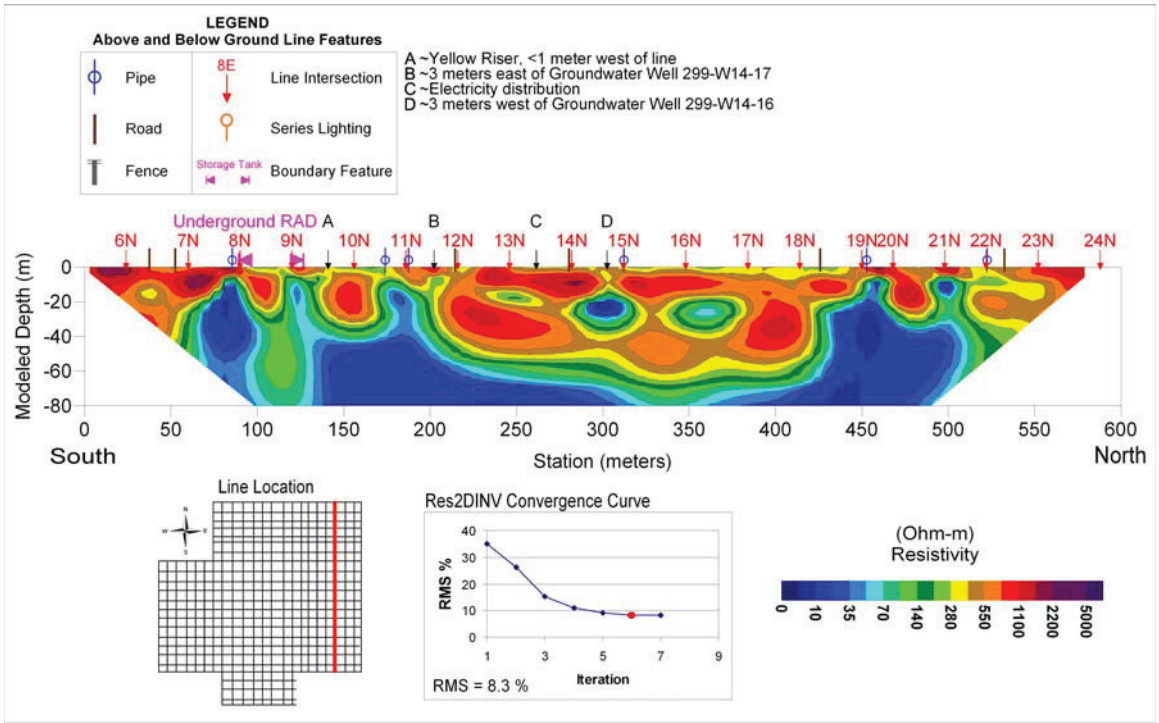

Figure E-21. Line 21E 2D Resistivity Inversion Results.

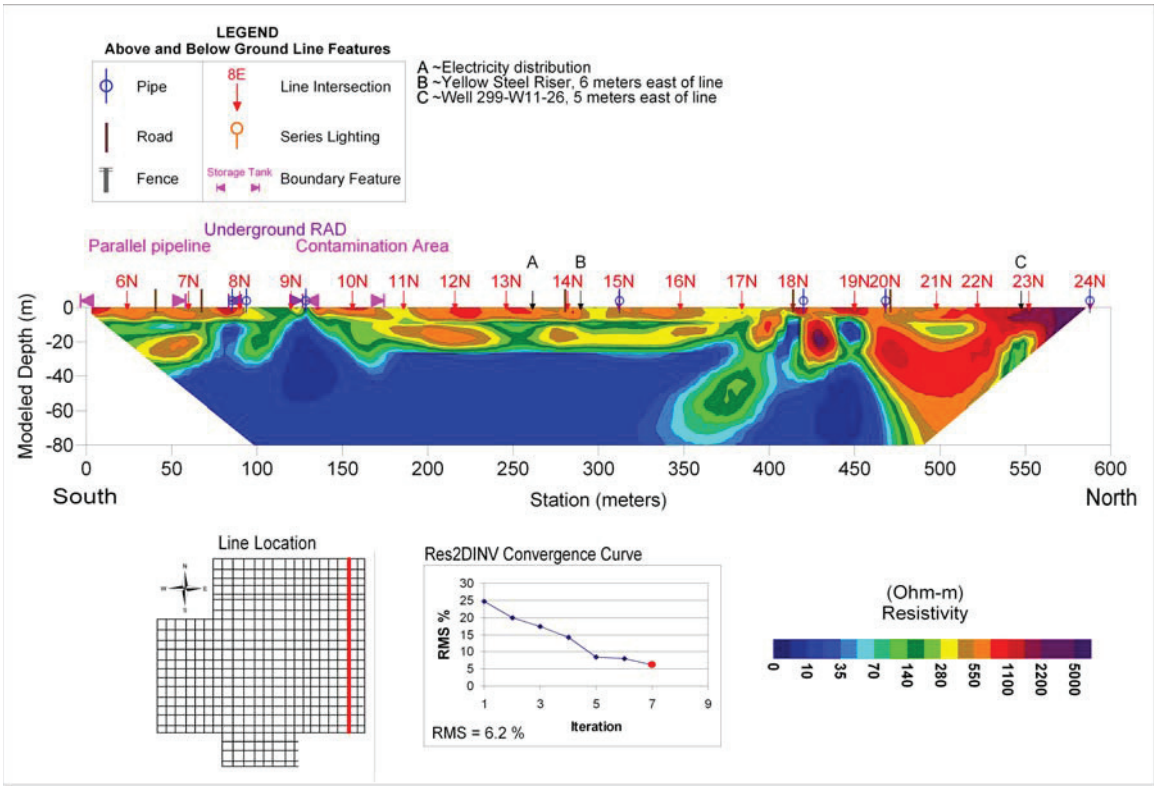

Figure E-22. Line 22E 2D Resistivity Inversion Results.

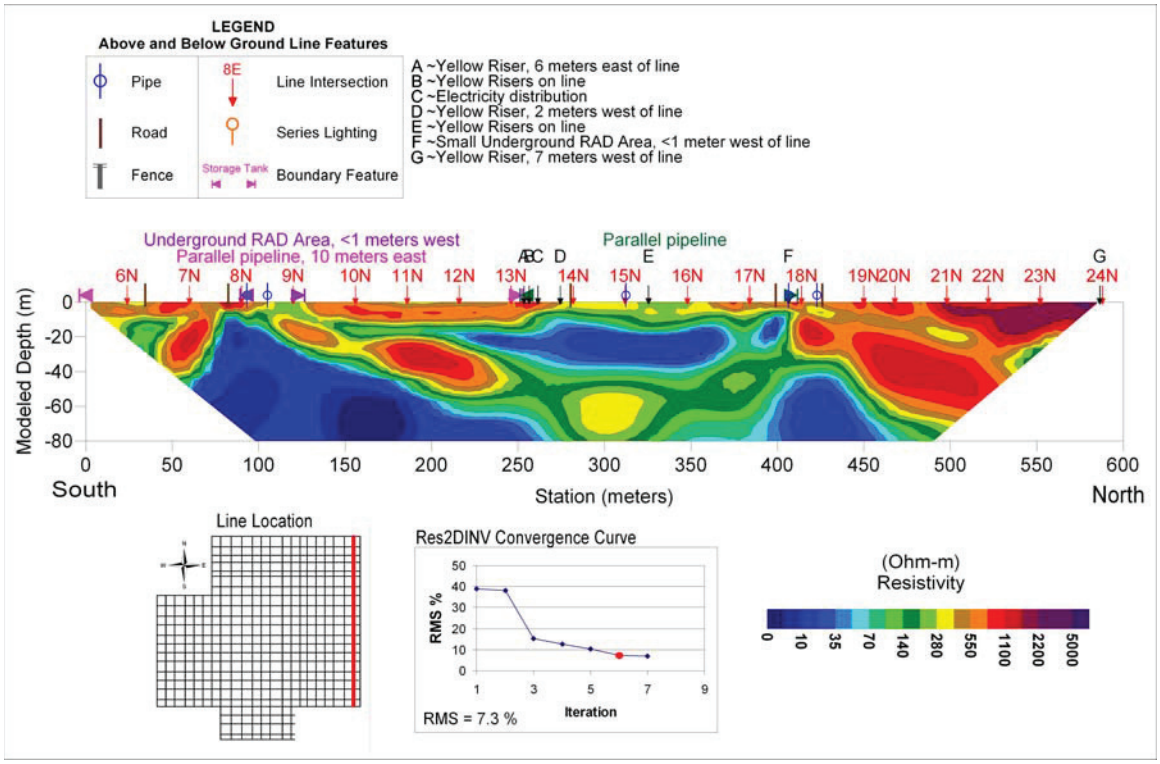

Figure E-23. Line 23E 2D Resistivity Inversion Results.

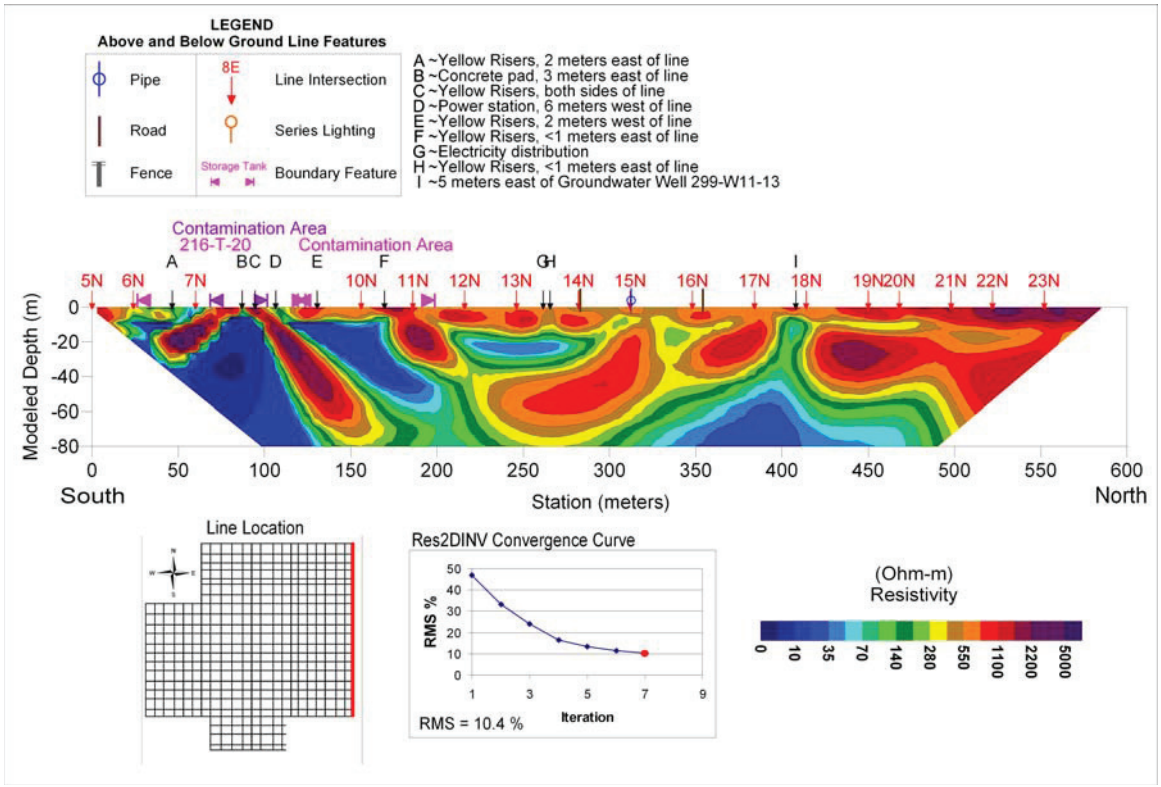

Figure E-24. Line 1N 2D Resistivity Inversion Results.

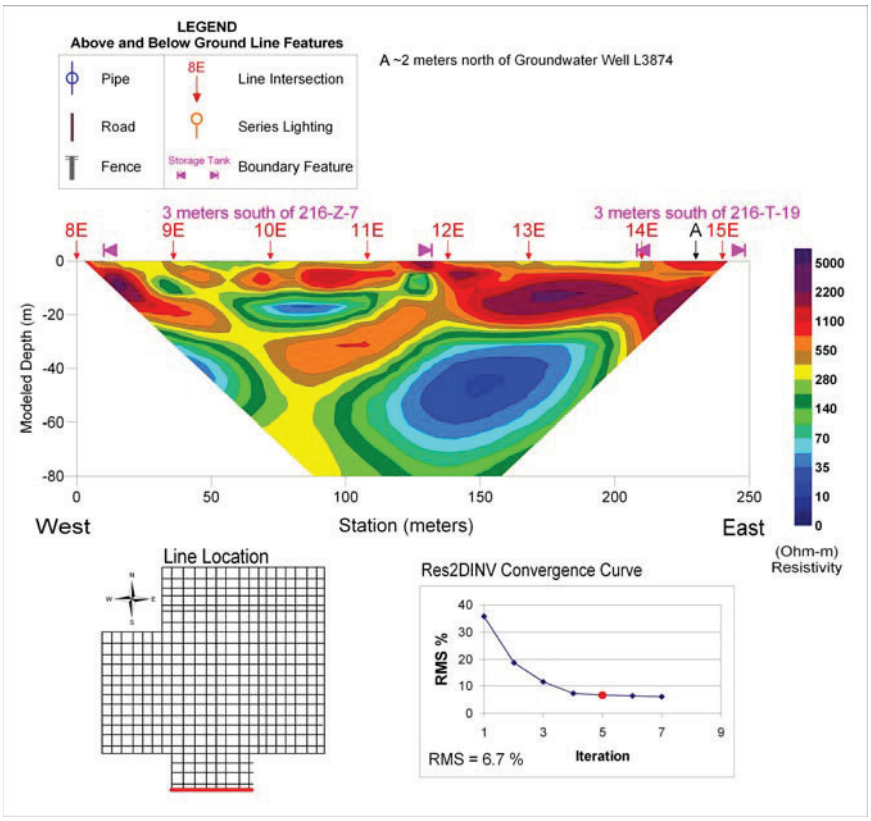

Figure E-25. Line 2N 2D Resistivity Inversion Results.

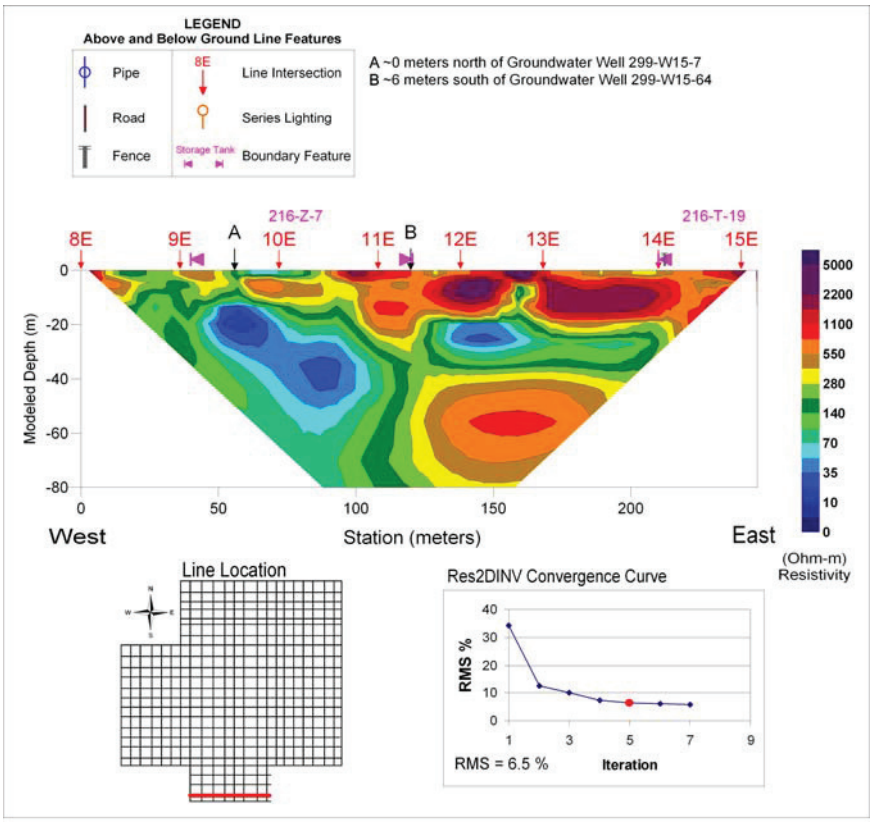

Figure E-26. Line 3N 2D Resistivity Inversion Results.

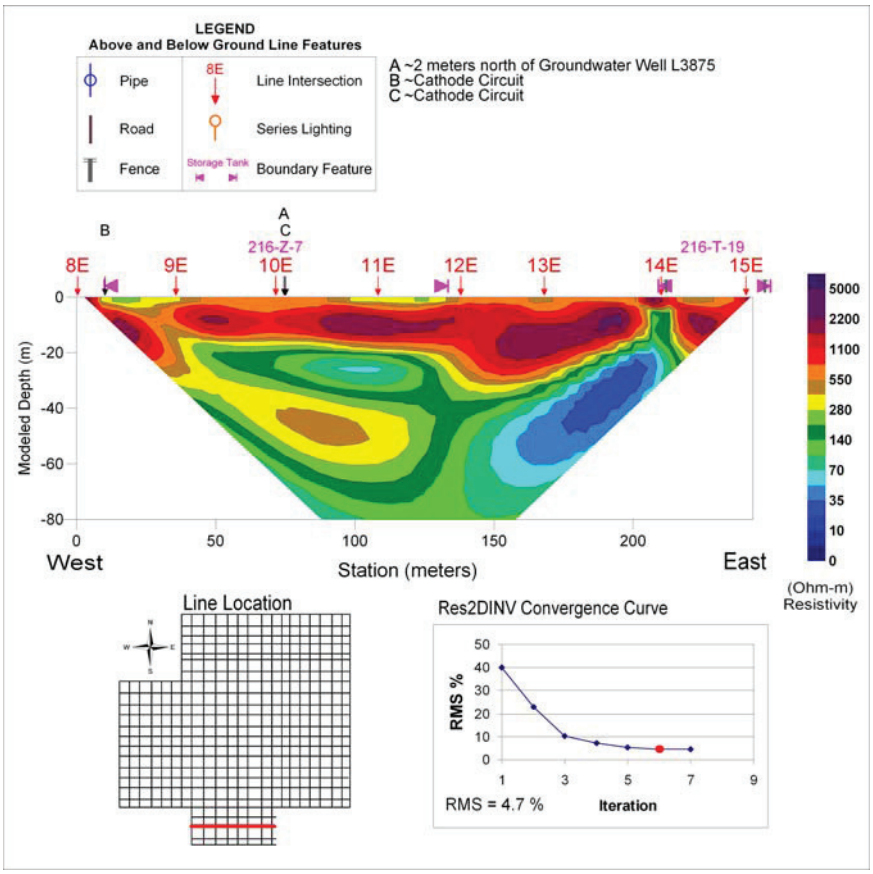

Figure E-27. Line 4N 2D Resistivity Inversion Results.

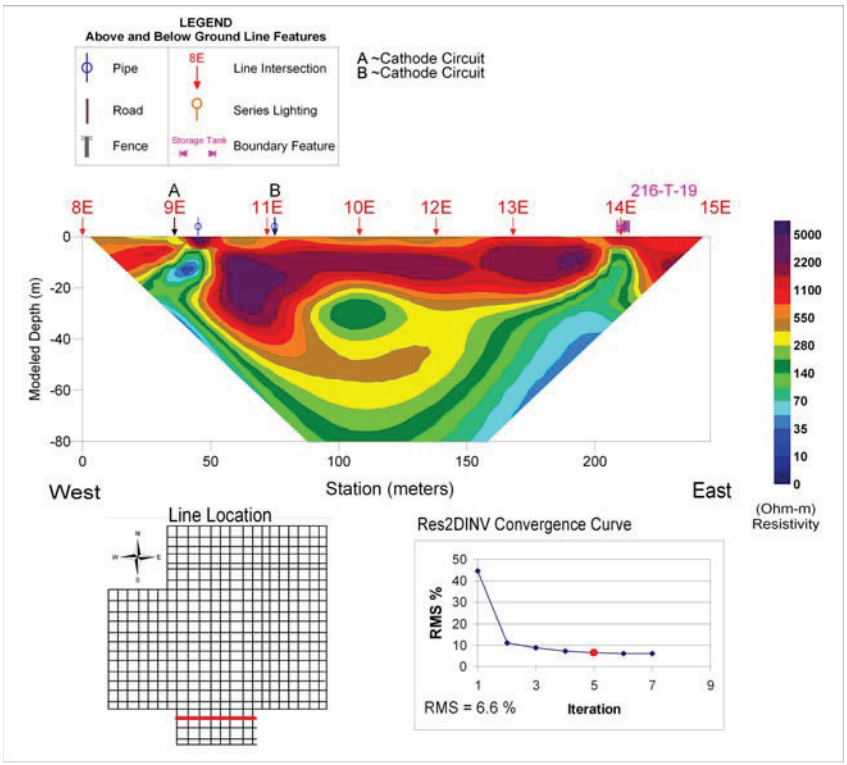

Figure E-28. Line 5N 2D Resistivity Inversion Results.

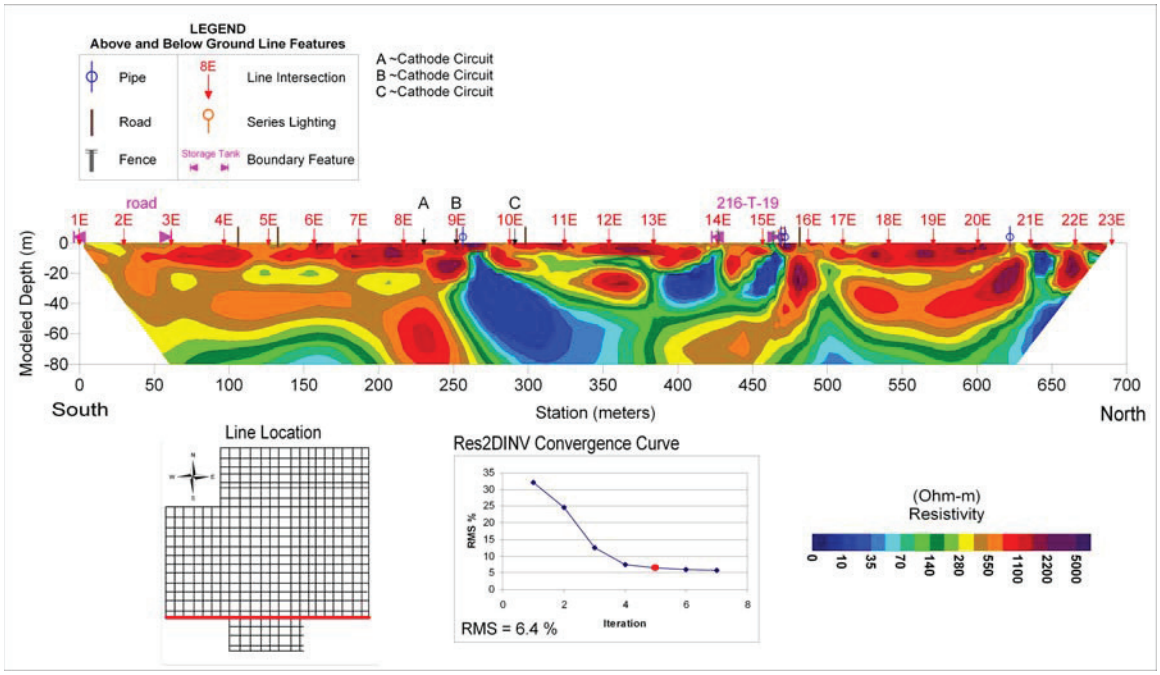

Figure E-29. Line 6N 2D Resistivity Inversion Results.

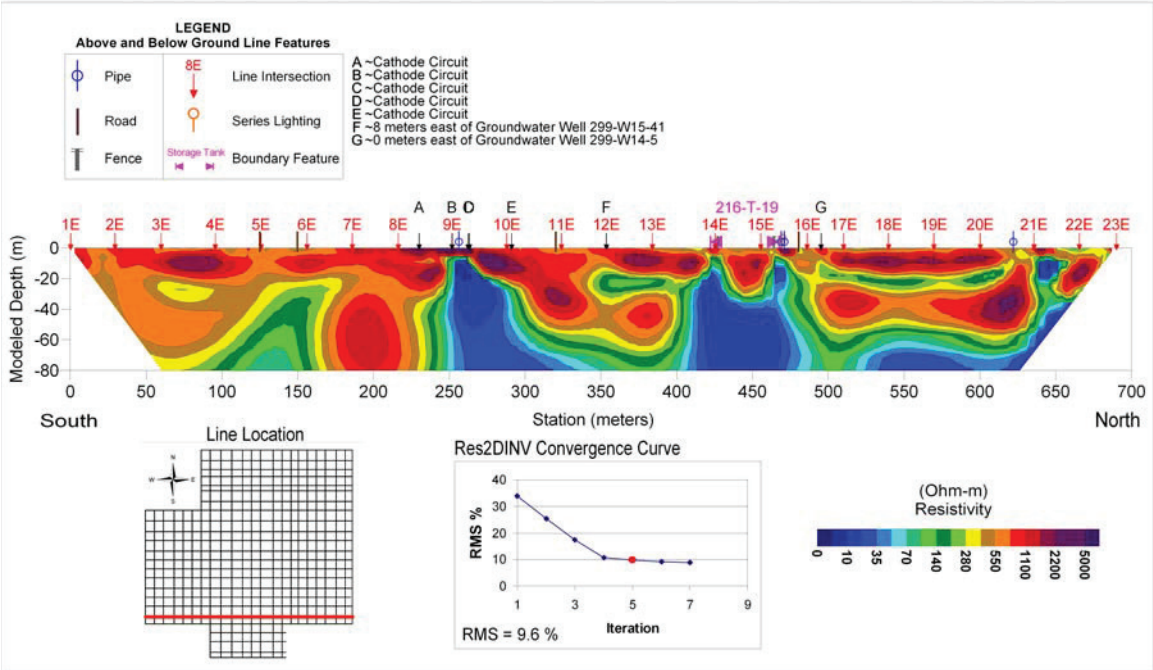

Figure E-30. Line 7N 2D Resistivity Inversion Results.

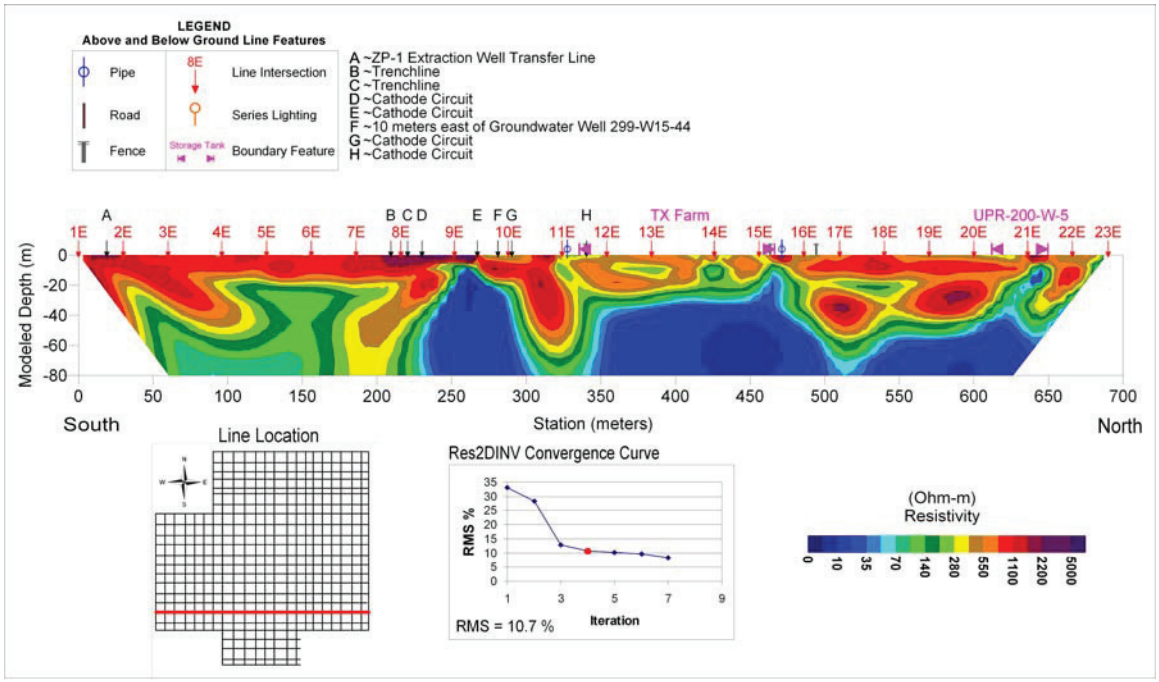

Figure E-31. Line 8N 2D Resistivity Inversion Results.

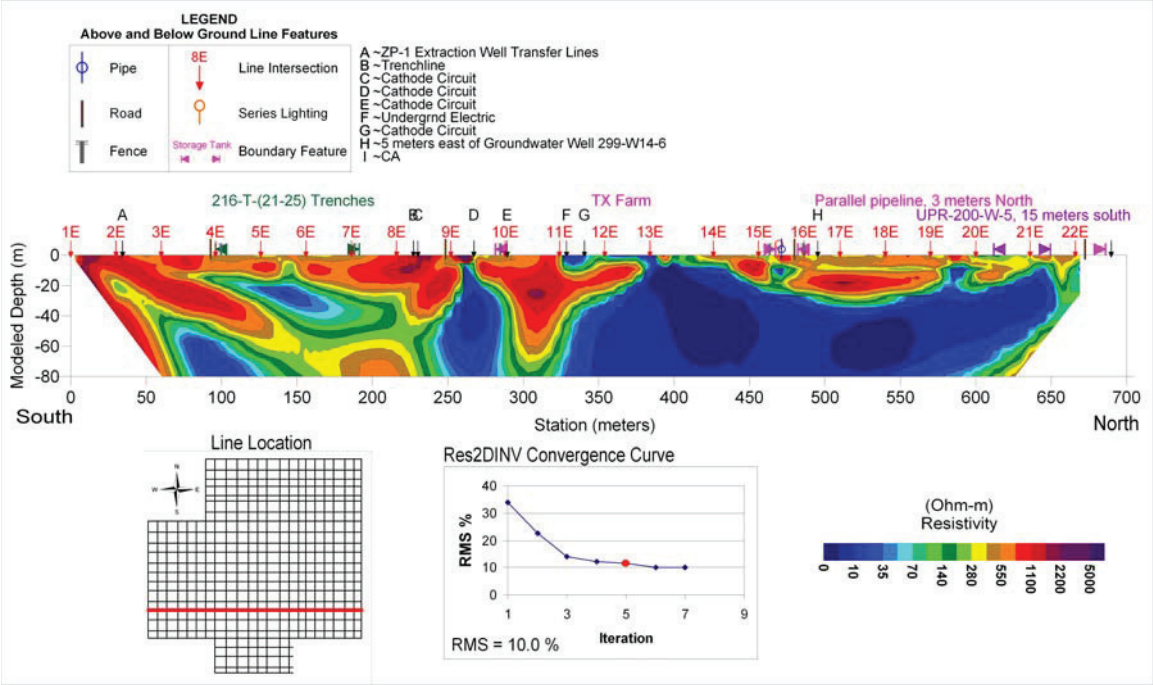

Figure E-32. Line 9N 2D Resistivity Inversion Results.

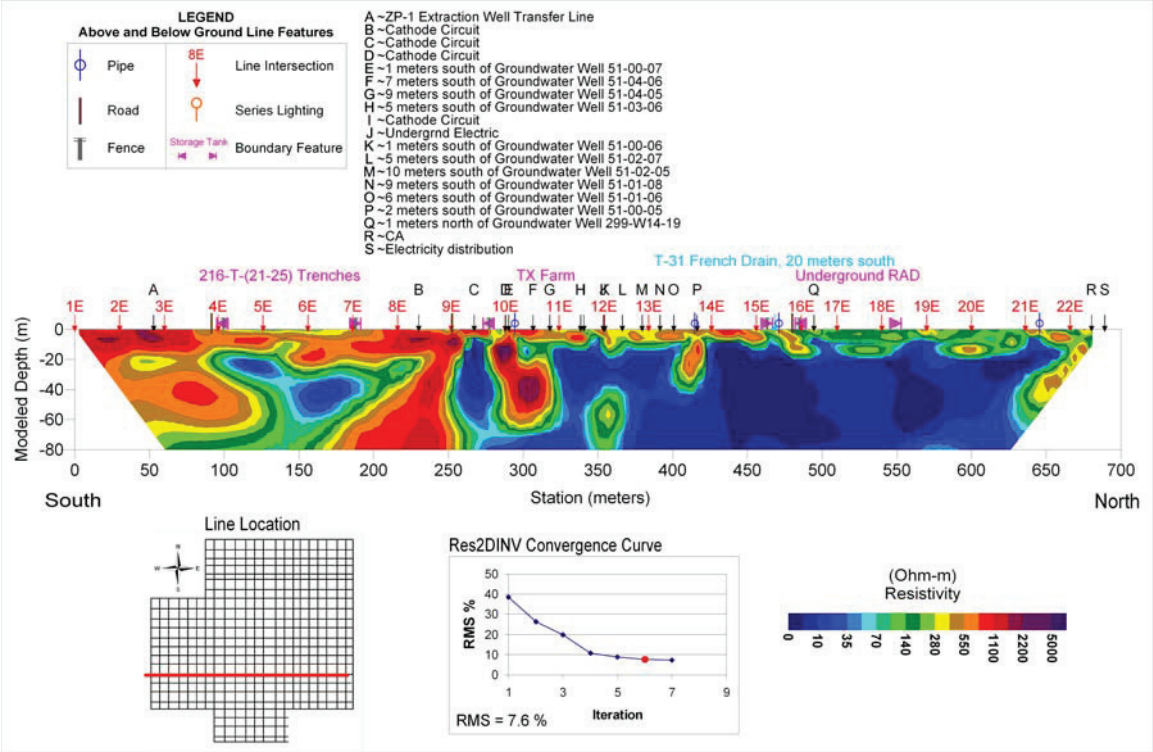

Figure E-33. Line 10N 2D Resistivity Inversion Results

.

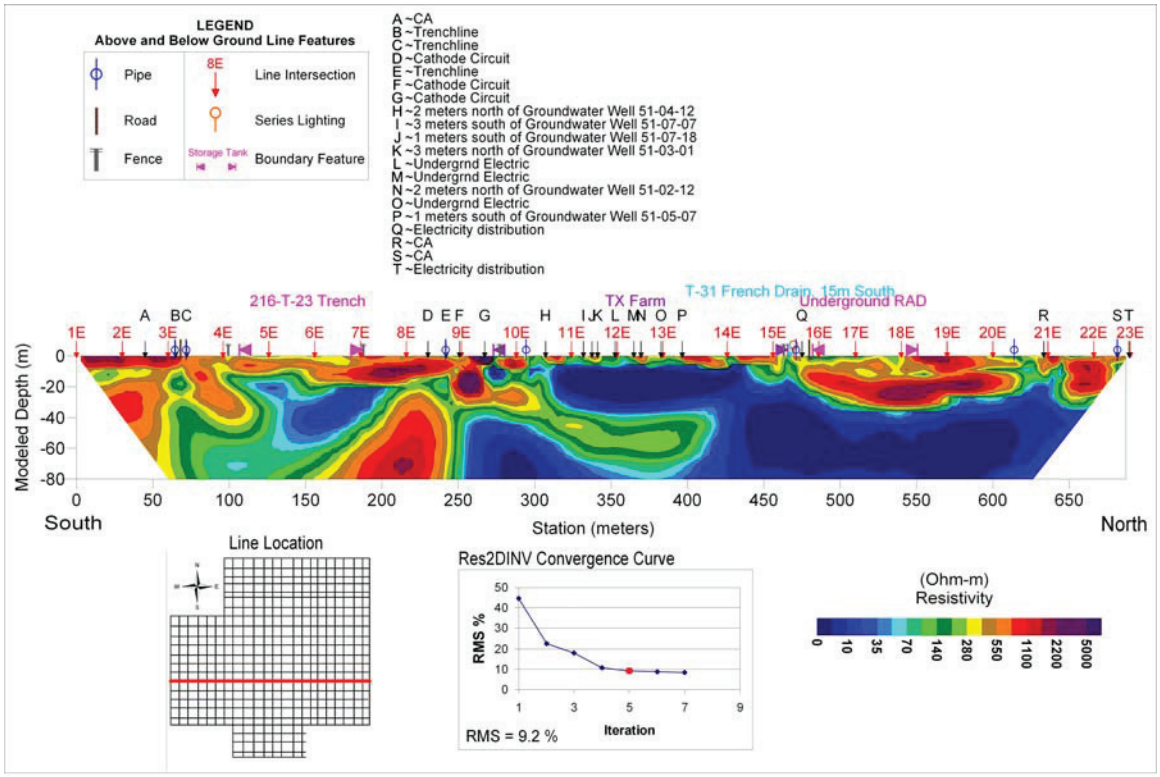

Figure E-34. Line 11N 2D Resistivity Inversion Results.

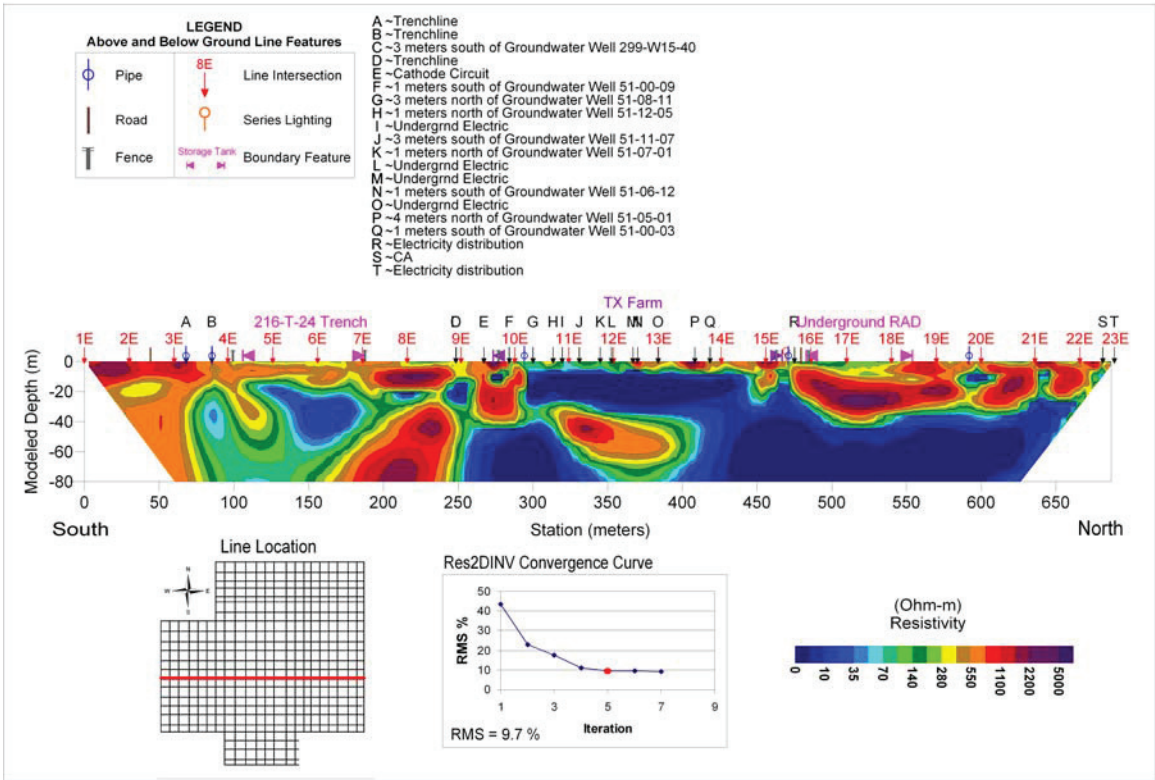

Figure E-35. Line 12N 2D Resistivity Inversion Results.

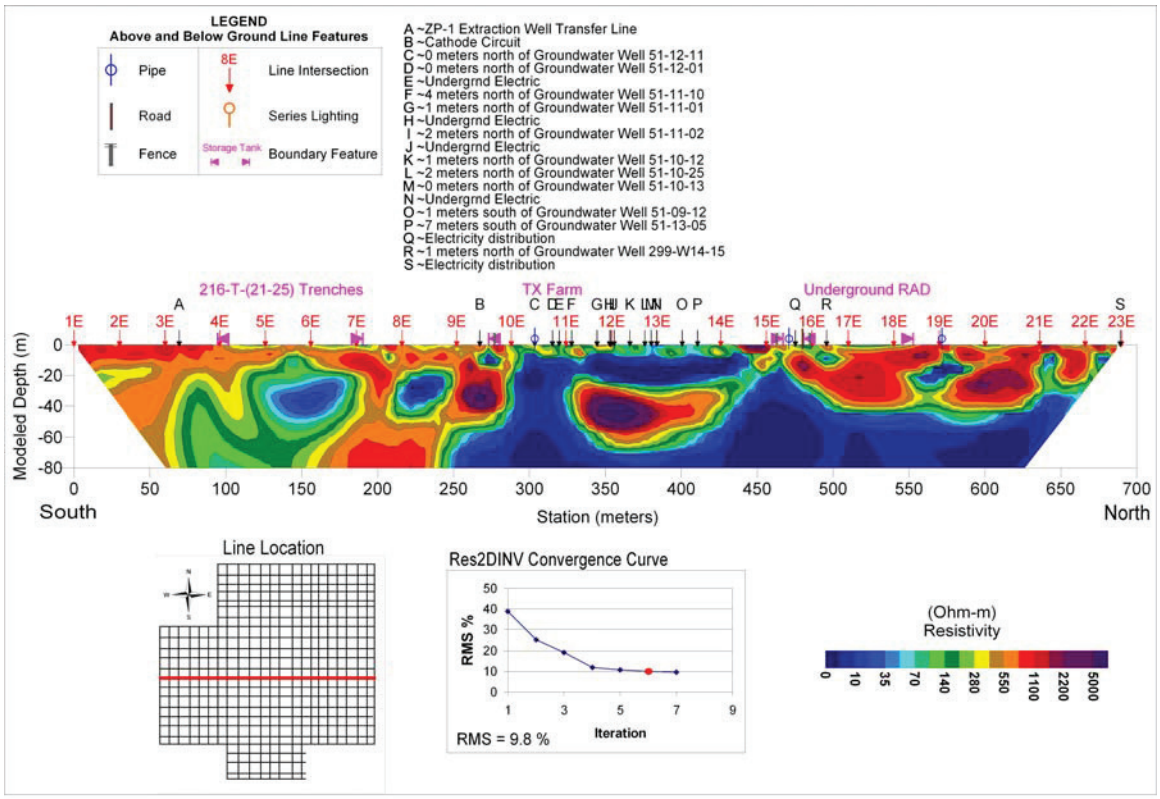

Figure E-36. Line 13N 2D Resistivity Inversion Results.

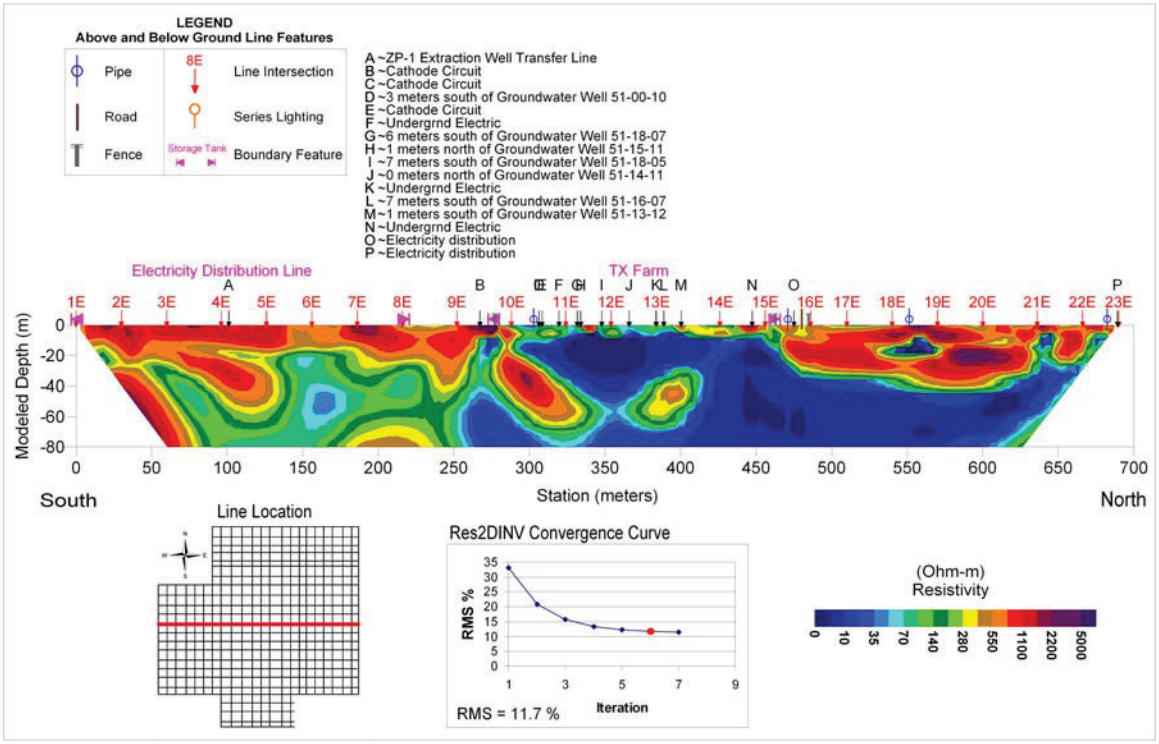

Figure E-37. Line 14N 2D Resistivity Inversion Results.

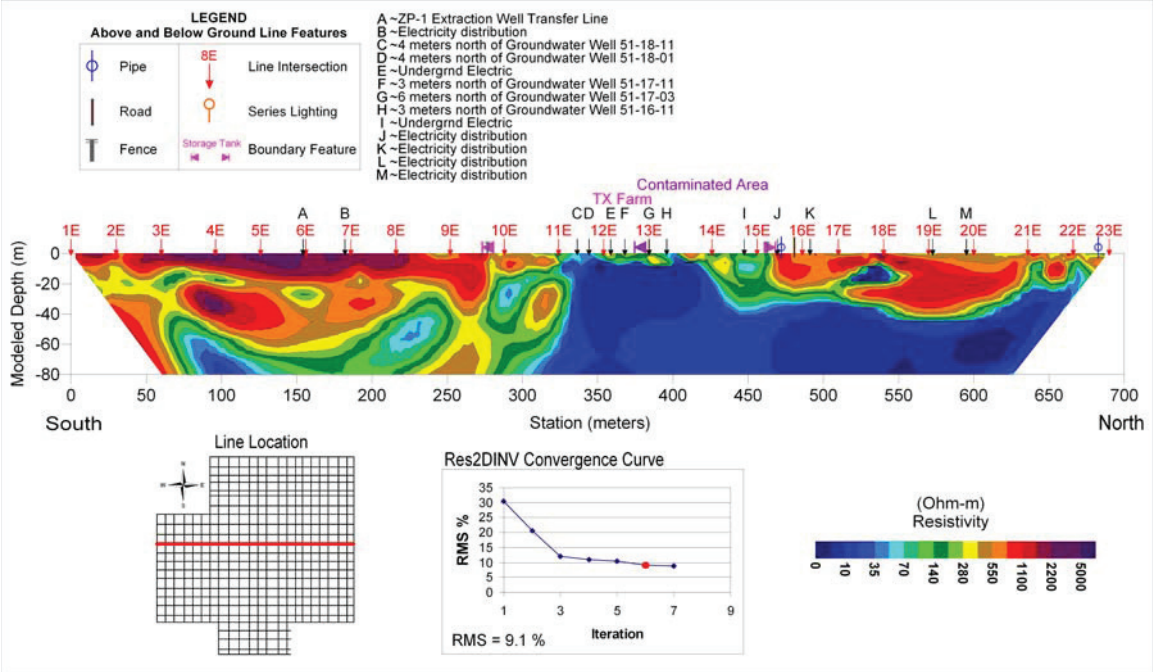

Figure E-38. Line 15N 2D Resistivity Inversion Results.

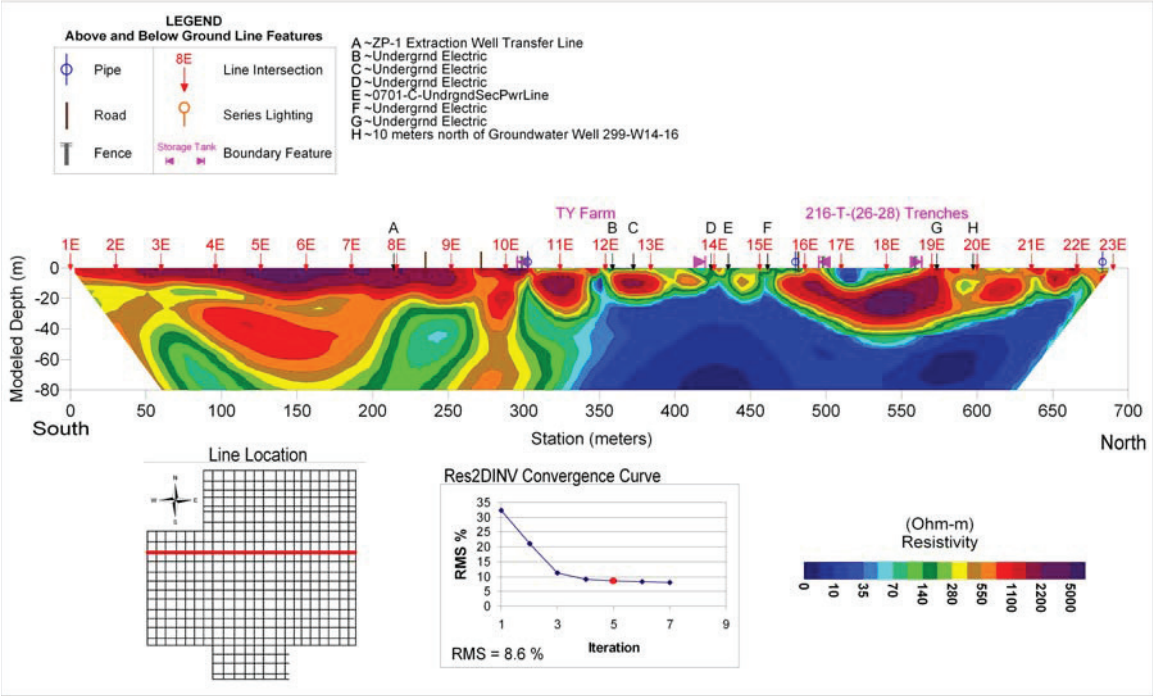

Figure E-39. Line 16N 2D Resistivity Inversion Results.

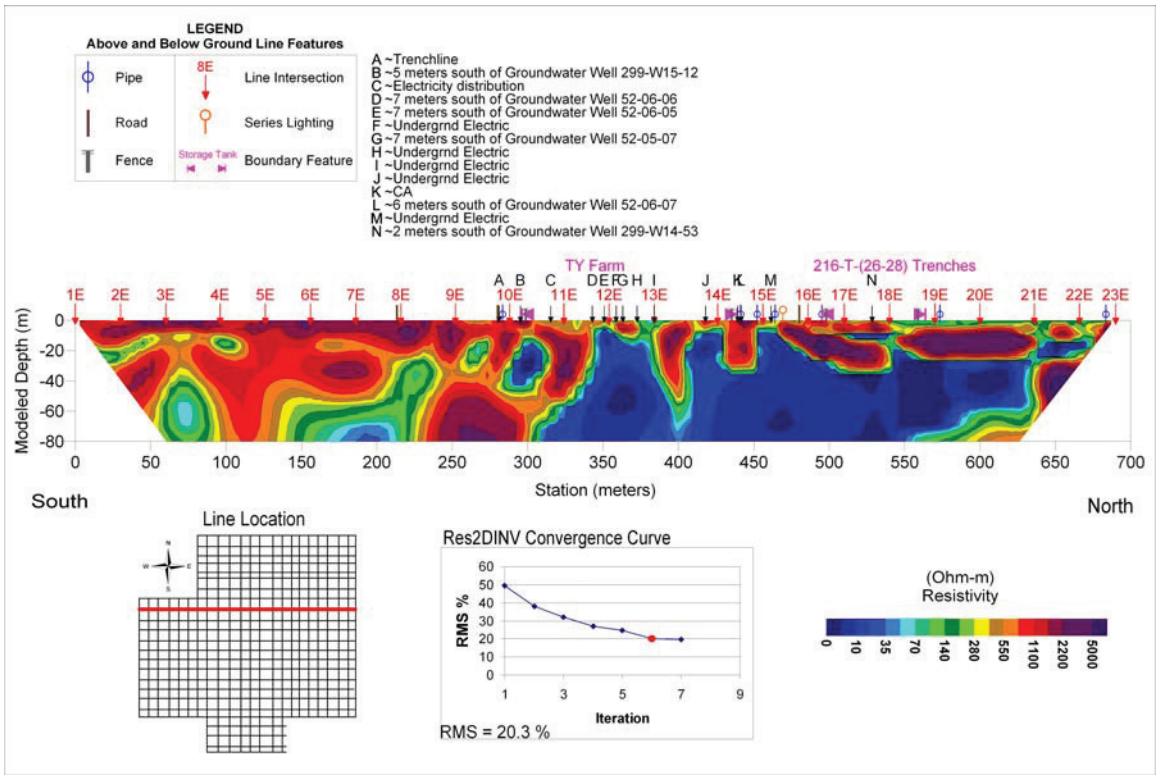

Figure E-40. Line 17N 2D Resistivity Inversion Results.

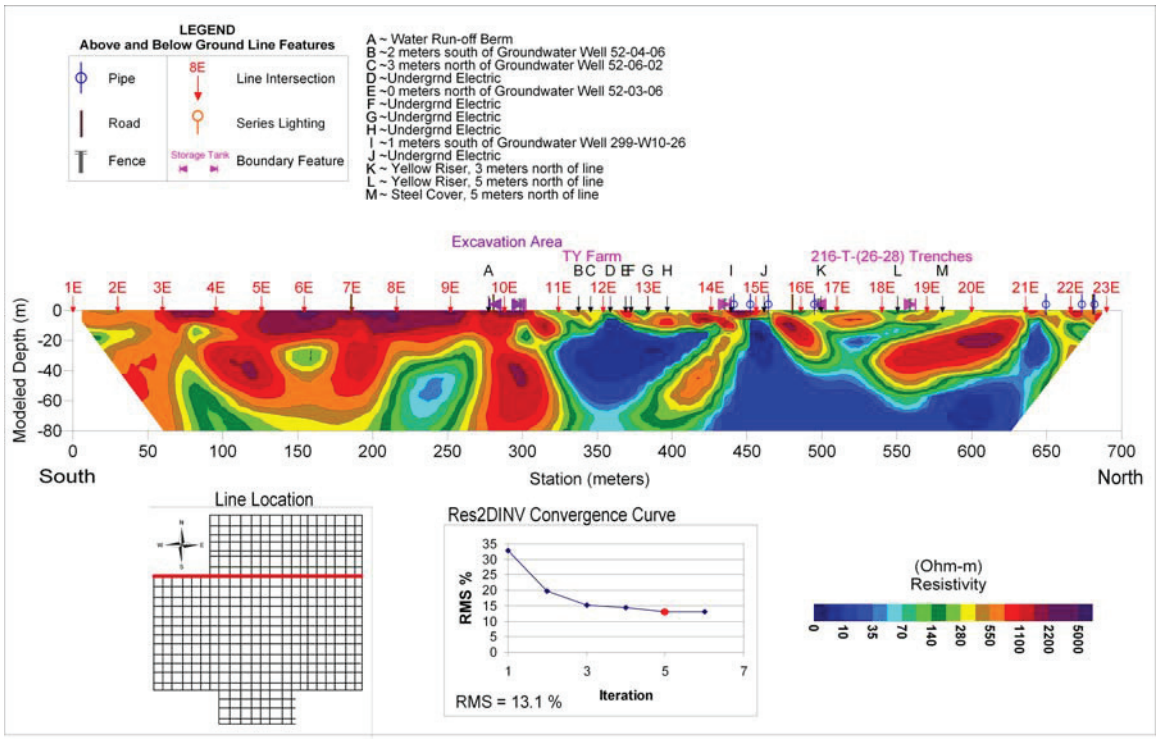

Figure E-41. Line 18N 2D Resistivity Inversion Results.

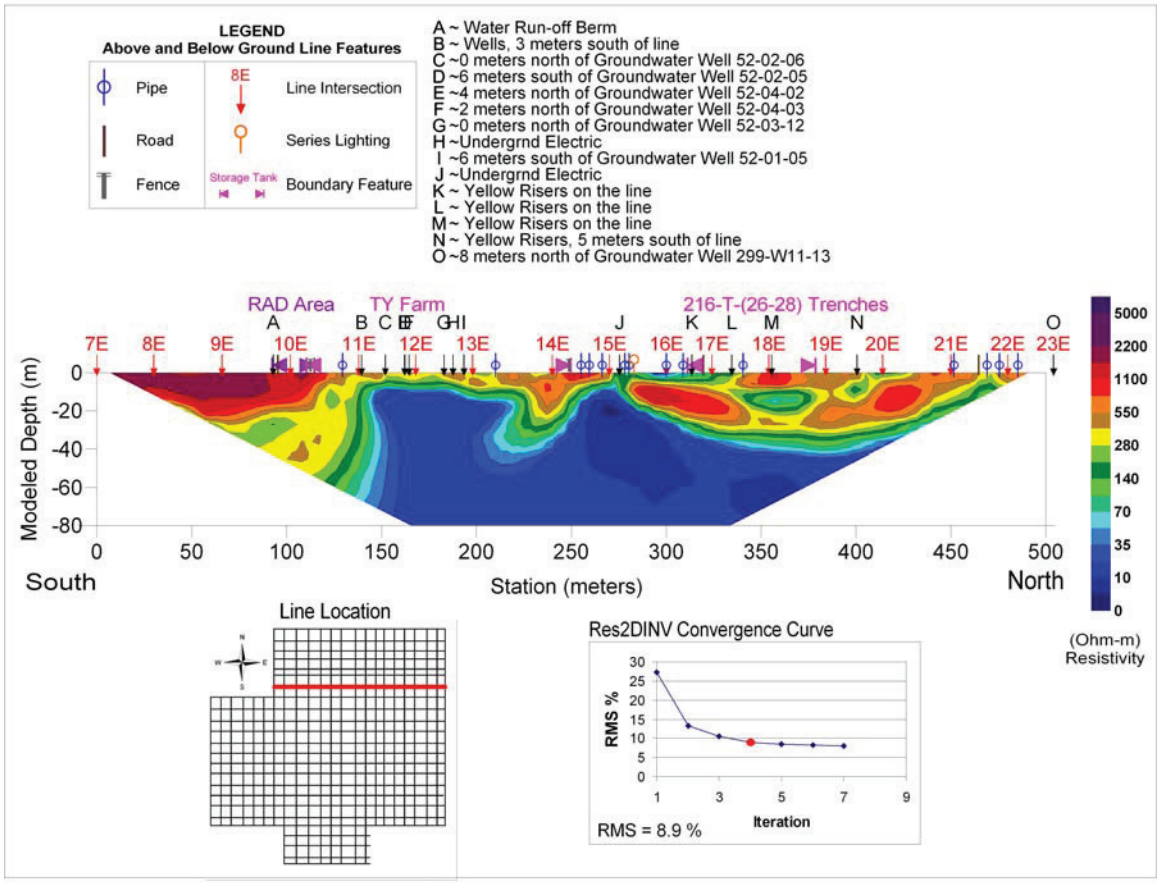

Figure E-42. Line 19N 2D Resistivity Inversion Results.

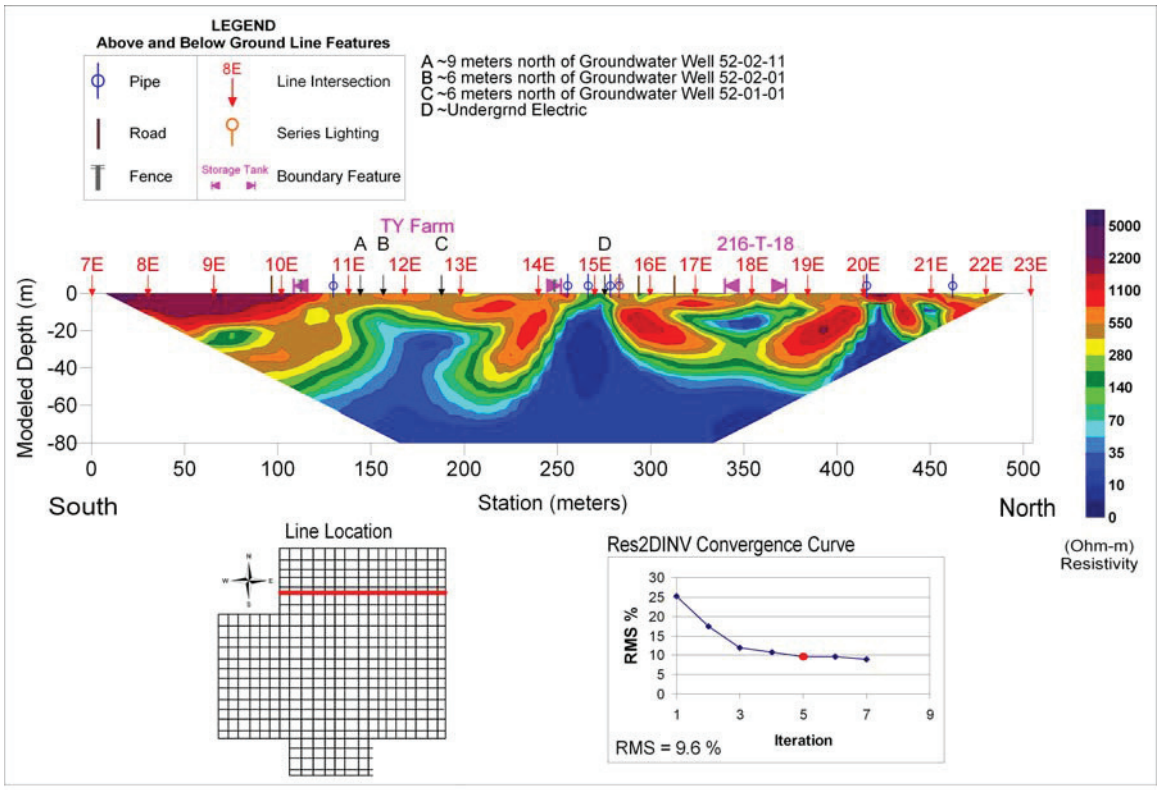

Figure E-43. Line 20N 2D Resistivity Inversion Results.

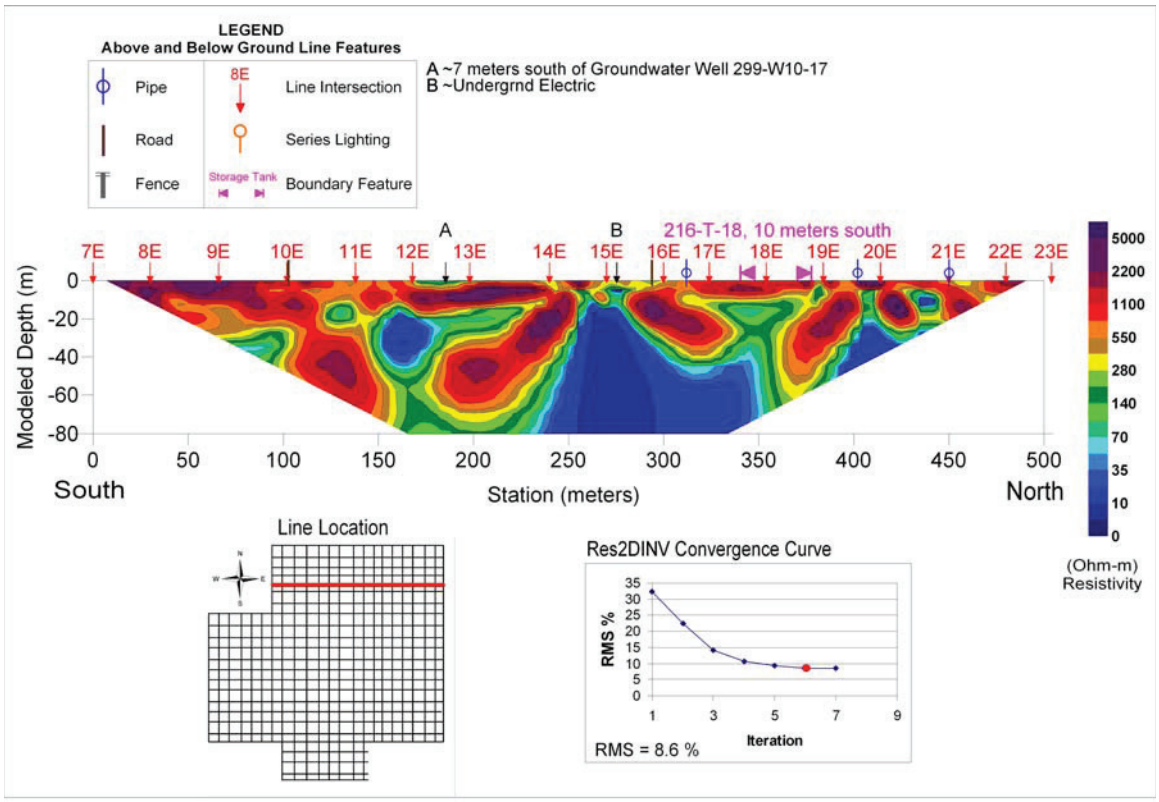

Figure E-44. Line 21N 2D Resistivity Inversion Results.

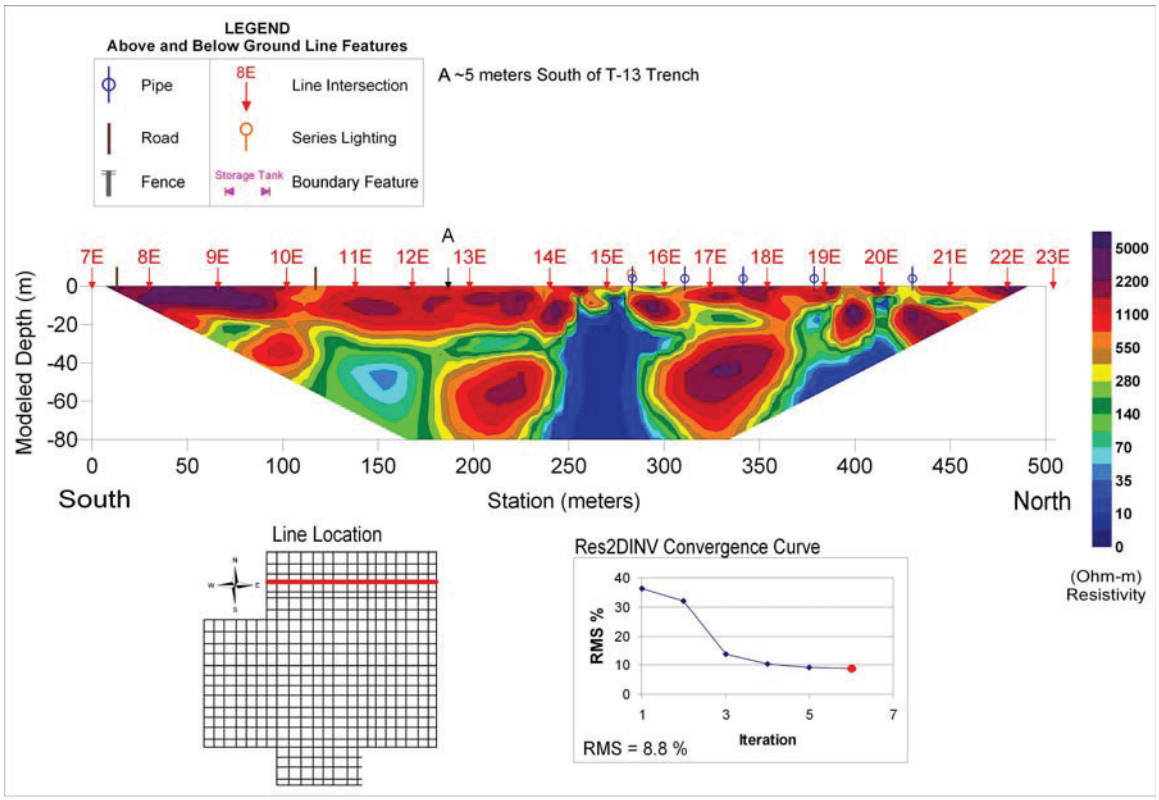

Figure E-45. Line 22N 2D Resistivity Inversion Results.

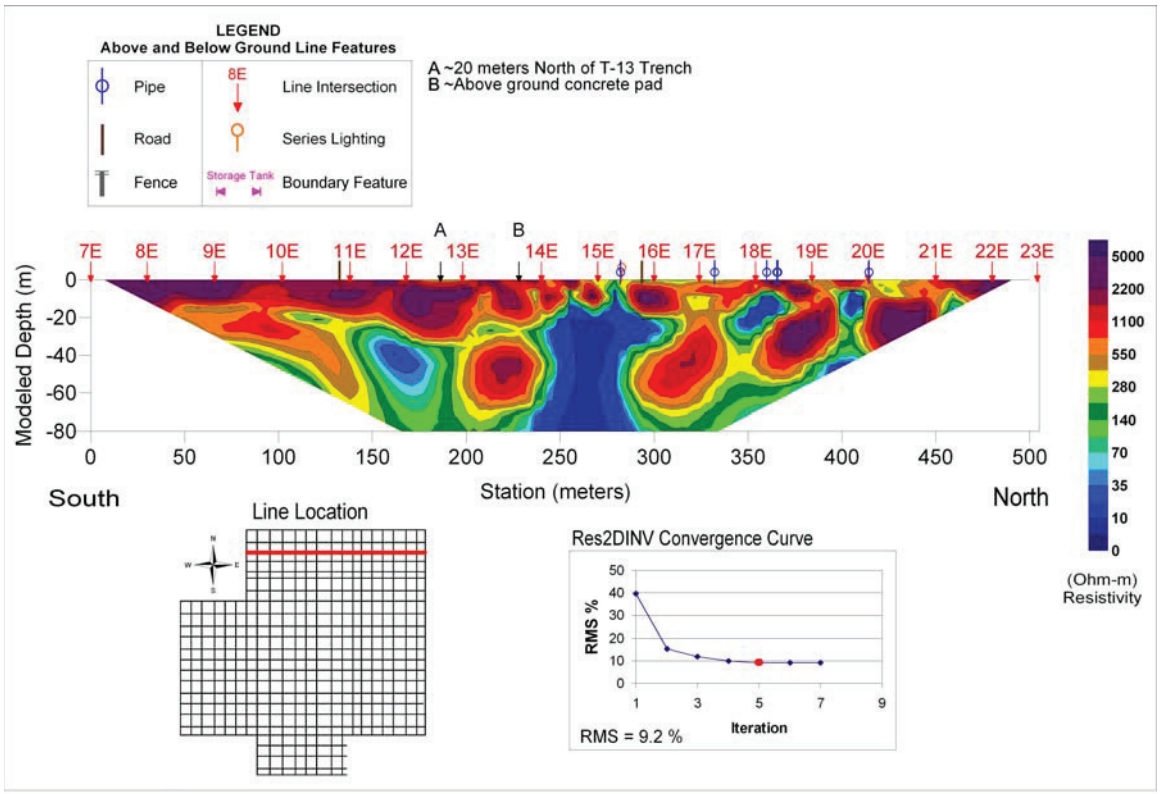

Figure E-46. Line 23N 2D Resistivity Inversion Results.

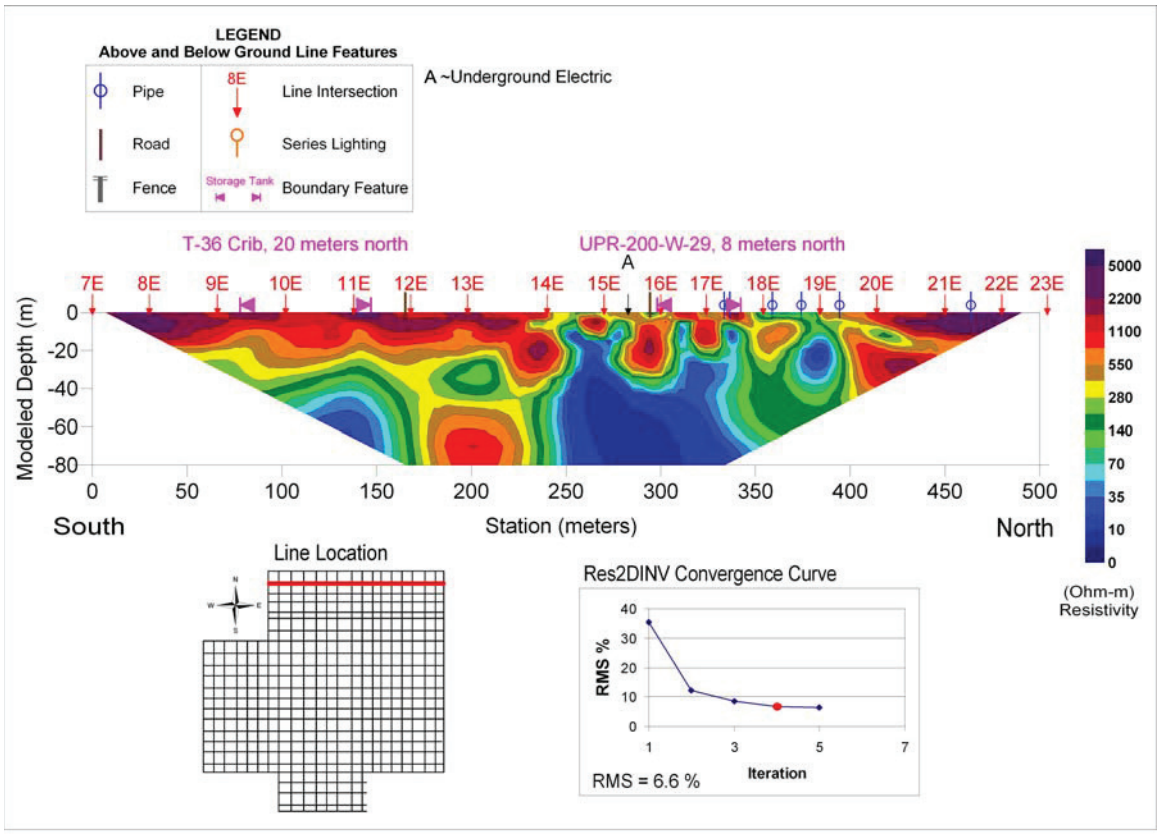
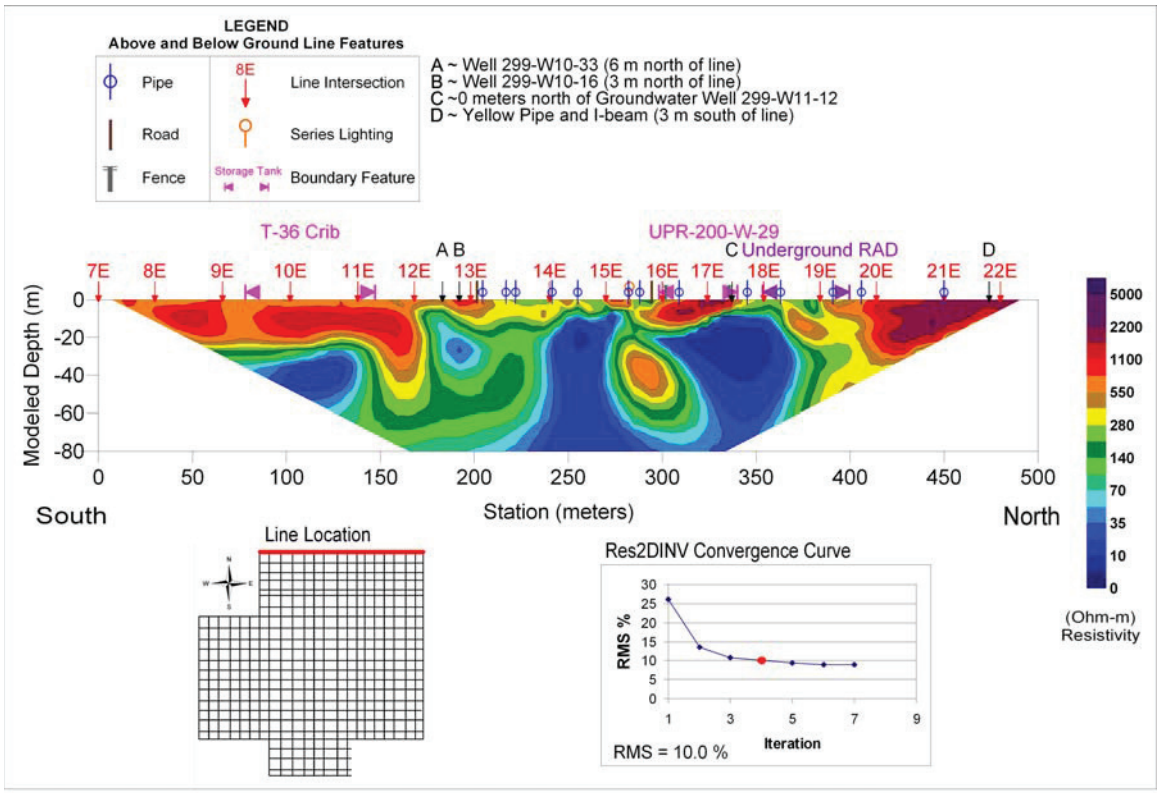
Figure E-47. Line 24N 2D Resistivity Inversion Results.